THE PREDICTION OF METAL FLOW AND PROPERTIES IN THREE-DIMENSIONAL FORGINGS USING THE FINITE-ELEMENT METHOD

by

Ian Pillinger

A Thesis submitted in supplication

for the degree of Ph.D.

Department of Mechanical Engineering,

University of Birmingham.

December, 1983.

Errata

Page 118, the last sentence in the first paragraph should read:

"To this end, during the solution of the stiffness equations, for all iterations after the first, any component of displacement which has a prescribed incremental value is assumed to have a prescribed value of zero."

Page 126, the last sentence of the penultimate paragraph should read:

"If the value of p is greater than one, the hypothetical-elastic generalised stress in the element does not exceed the yield value at the end of the increment by more than 20%."

SYNOPSIS

A knowledge of the flow occuring in metal-forming processes is of great industrial importance, and the finite-element technique is the only form of deformation analysis which can predict the flow of the material.

The examination of forging operations requires a full elastic-plastic treatment to be used. This thesis is concerned with an elastic-plastic, finite-element program which has been developed to investigate three-dimensional examples of this process.

The fundamental theory of the finite-element method is first introduced, and then the finite-element program is described in detail.

The deformation, and distributions of hardness and die-interface pressure, predicted by this technique for the unlubricated upsetting of a rectangular block are compared with experimental results, and found to be in broad agreement, the differences being attributed to the incorrect imposition of very high friction by the friction-layer technique used in the analysis.

With a corrected form of the friction technique, the finite-element program predicts results for the axisymmetric friction-ring test and a new three-dimensional friction test which are in good agreement with experimental findings up to deformations of approximately 30%; the friction-layer technique used successfully in previous axisymmetric treatments appears to be unsuitable for three-dimensional formulations when large deformations are considered.

The finite-element program developed here is shown to be capable of modelling an example of a more complicated three-dimensional forging, that of an automobile connnecting rod. The experimental measurements of deformation and hardness for an aluminium con rod forged using graphite lubrication are found to be in good agreement with the finite-element predictions obtained assuming sticking-friction conditions but not with the results of a zero-friction idealisation.

Finally, suggestions are made for the future development of this technique.

In Memory of Laurie Legg

AKNOWLEDGEMENTS

I should like to thank the Science and Engineering Research Council for funding this research, and Professor S.A. Tobias for the use of the facilities of the Department of Mechanical Engineering.

My thanks are also due to Mr. A. Downing and Mr. B. Beighton for performing much of the experimental work discussed in this thesis, to Mr. P.R. Bower, Mr. A. Jarvis and Dr. T.A. Dean for their help in making the designs of the con-rod forging die and preforms a reality, and to the staff of the Centre for Computing and Computer Science at Birmingham, and the University of Manchester Regional Computer Centre, for the use of computer facilities and the unfailing source of help on computing matters.

I am grateful to Dr. P. Bate for several fruitful discussions concerning some of the techniques described in this thesis, and to my colleagues, Mrs. S.E. Stuteley and Liu Cai, for acting as uncomplaining guinea pigs - their comments and suggestions were invaluable.

I am also grateful to Acheson Ltd. for providing, free of charge, the lubricant used in some of the experimental work, and to Austin-Rover Cars who supplied information about, and practical examples of, the con-rod forgings considered towards the end of this work.

Finally, I should like to express my most sincere gratitude to my supervisors, Dr. P. Hartley, Dr. C.E.N. Sturgess and Professor G.W. Rowe, for all the advice and encouragement offered during the course of this research.

CONTENTS

TABLE OF NOMENCLATURE

For convenience, the symbols used in this thesis are listed together here in alphabetical order. (The numbers in parentheses refer to the section in which the symbol is first introduced or defined.)

a — substitution for $g(\Delta \underline{\delta}^{eJ\prime})^2$ (3.2.4.2.1), angle of rotation during combined extension and rotation of a body (Appendix A).

$[B_n^{\epsilon}], [B_n^{q}], [B_n^{b}], [B_n^{\phi}]$ — matrices relating nodal displacement to strain, displacement gradient, bulk strain and element dilatation respectively (2.1.2).

$[B_n]$ — matrix relating nodal displacement to strain assuming zero rotation of material (3.2.3.1).

b — substitution for $3\underline{\sigma}'^{T}[M]\,\Delta \underline{\sigma}^{eJ\prime}$ (3.2.3.3), estimated angle of rotation during combined extension and rotation of a body (Appendix B).

c — substitution for $g(\underline{\sigma}')^2$ (3.2.4.2.1).

CONF — convergence factor for iterative procedure (3.2.3.1.2).

[D] — elastic, incremental stress-strain matrix (3.2.3).

$[D_n]$ — incremental stress-strain matrix for element n (2.1.1.4).

$[D^p]$ — elastic-plastic, incremental stress-strain matrix (3.2.3).

d — distance from primary (1y) to secondary (2y) specified boundary surface (3.2.1.2.1), number of degrees of freedom per node, (Appendix C).

$\underline{d}$ — global vector of nodal displacement (2.1.2).

$\underline{d}_I$ — vector of displacement at node I (3.2.1.1.2).

$\Delta \underline{d}^{(i)}$ — vector increment of global displacement for ith iteration (3.2.3.1).

$\Delta \underline{d}_n^{(i)}$ vector increment of nodal displacement for element n, during ith iteration (3.2.3.1).

$\underline{d}_n$ vector of displacement at nodes of element n (2.1.1.1).

E Young's modulus (3.2.3).

e empirically-determined lower limit of proportionality in strain-hardening function (3.2.4.2.1), extension (or shortening) of unit cube during combined extension and rotation (Appendix B).

$\underline{\varepsilon}$ vector of linearised co-rotational (LCR) engineering strain at a point = $(\varepsilon_{xx}, \varepsilon_{yy}, \varepsilon_{zz}, \varepsilon_{xy}, \varepsilon_{yz}, \varepsilon_{zx})^T$ in Cartesian frame (2.1.1.4).

$[\varepsilon]$ tensor of linearised co-rotational (LCR) strain (2.1.1.3.2).

$\bar{\varepsilon}$ accumulated, generalised strain at centroid of an element at the beginning of a deformation step (3.2.6.1).

$\hat{\underline{\varepsilon}}$ bulk-strain vector (2.1.1.5).

$\Delta\varepsilon_b$, $\Delta\underline{\varepsilon}'$ increments in bulk and deviatoric strain (2.1.1.5).

$\Delta\underline{\varepsilon}^{cd}$ vector increment of strain modified for constant-dilatation technique (2.1.1.5).

$[\Delta\varepsilon^{cr}]$ tensor of incremental co-rotational strain (2.1.1.3.1).

$\Delta\underline{\varepsilon}^{II}$ vector of incremental strain during plastic part of deformation step (3.2.4.2.2).

$\Delta\underline{\varepsilon}^{IIe}$, $\Delta\underline{\varepsilon}^{IIp}$, vectors of elastic and plastic components of deviatoric strain during plastic part of deformation step (3.2.4.2.2.1).

$\bar{\varepsilon}^f$ accumulated, generalised strain at centroid of an element at the end of a deformation step (3.2.6.1).

$[\Delta\varepsilon^L]$ tensor of incremental Lagrangian (right Cauchy-Green) strain (3.2.4.1).

$\Delta\underline{\varepsilon}^p$, $\bar{\varepsilon}^p$ incremental plastic-strain vector, accumulated generalised plastic strain (3.2.3).

$\bar{\varepsilon}^{p_f}$ accumulated, generalised plastic strain at the end of a deformation step (3.2.4.3).

$[\Delta\varepsilon^{\infty}]$ tensor of infinitesimal increment of strain (Appendix B).

f force acting on rotated body (Appendix A).

$f(\Delta m)$ final yield stress expressed as a function of plastic-proportionality factor (3.2.4.2.2.1).

$\underline{f}$ global vector of nodal force (2.1.2).

$\underline{f}_I$ vector of force at node I (3.2.1.1.2).

$\Delta\underline{f}^{(i)}$ vector increment of global force for ith iteration (3.2.3.1).

$\underline{f}_n$ vector of force at nodes of element n (2.1.1.1).

$\Delta\underline{f}_n^{(i)}, \Delta\underline{f}^{(i)}$ vector increments of equilibrating nodal force for nth element and whole mesh, respectively (3.2.3).

f_x component of force in x direction acting on rotated body (Appendix A).

G rigidity modulus (3.2.4.2.1).

$g(\underline{\sigma}')$ generalised-stress function = $(\frac{3}{2}\underline{\sigma}'^{T}[M]\underline{\sigma}')^{\frac{1}{2}}$ (3.2.3).

$\underline{\nabla}$ gradient-operator vector (2.1.1.1).

H' slope of curve of Y against plastic strain (3.2.3).

$h(\bar{\varepsilon}^{p})$ strain-hardening function (3.2.4.2.2.1).

$h_0 \ldots h_5$ empirically-determined constants of strain-hardening function (3.2.4.2.1).

I local or global node number (2.1.2).

$[I]$ 3x3 unit matrix (2.1.1.3).

: operation of inner tensor product (2.1.1.1).

J local or global node number (2.1.2).

$[J_n]$ Jacobian matrix for element n (2.1.2).

$[K]$ global stiffness matrix (2.1.2).

$[K_n]$ stiffness matrix for element n (2.1.2).

k shear-yield stress (3.2.1.2.2.1).

κ bulk modulus (2.1.1.5).

k_{ij} entry in row i, column j of [K] (2.2).

$[k_{IJ}]$ 3x3 submatrix of [K], relating force at node I to displacement at node J (3.2.1.1.2).

LCR abbreviation for linearised co-rotational (incremental strain) (2.1.1.3.2).

$[L_n^{\varepsilon}],[L^q],[L_n^b],[L_n^{\phi}]$ operator matrices (2.1.1.6).

$\Delta\lambda$ plastic-proportionality factor in Prandtl-Reuss equations (3.2.3).

l_i,m_i,n_i direction cosines of rotated ith axis with respect to the unrotated x, y and z axes respectively (2.1.1.3.1).

l_X,m_X,n_X direction cosines of local X axis with respect to global x, y and z axes. Similarly for local Y and Z axes (3.2.1.1.2).

[M] 'engineering' matrix (3.2.3).

m friction factor (3.2.1.2.2.1).

Δm plastic-proportionality factor in mean-normal method (3.2.4.2.2.1).

N_I shape function of local coordinates for node I (2.1.2).

$[N_n]$ = $(N_1\,[I]\quad N_2\,[I]\ \ldots\ N_8\,[I])$ interpolating matrix for displacement (2.1.2).

n element number (2.1.1.1).

ν,ν_e,ν_p Poisson's ratio; values used in $[D_n]$ matrices for elastic and plastic elements respectively (2.1.1.6, 3.2.5).

p proportion of increment necessary to cause the hypothetical-elastic generalised stress in a given element to exceed the yield stress by 20%; the minimum value thereof for all elements (3.2.3.3).

ϕ_n dilatation (volume strain) of element n (2.1.1.5).

[Q] incremental-displacement gradient tensor = $\delta\Delta u_j/\delta x_i$ (2.1.1.1)

$\underline{q}$ vector of incremental-displacement gradient (2.1.1.4).

[R] rotational transformation matrix of direction cosines; rotation of material (2.1.1.3.1), rotation of boundary conditions (3.2.1.1.2).

REF reference value of modulus of incremental displacement arrays during iterative procedure (3.2.3.1.2).

r proportion of deformation step before yield occurs at a given point (3.2.4.2).

SMM stiffness-matrix multiplier used to modify the stiffness matrices of friction-layer elements (3.2.1.2.2.2).

S_x, S_y, S_z gradients of hydrostatic stress in x, y and z directions, respectively (3.2.4.4.1).

S_x^A, S_y^A, S_z^A values of S functions at point A. Similarly B (3.2.4.4.2).

s substitution for $\frac{2}{3}\bar{\sigma}^2(1+\frac{2}{3}(1+\nu)H'/E)$ (3.2.3).

[s] nominal (Piola-Kirchhoff I) stress tensor (2.1.1.1).

σ value of normal component of stress in the x' direction during combined extension and rotation (Appendix A).

$\underline{\sigma}$ vector of Cauchy stress at a point,

= $(\sigma_{xx}, \sigma_{yy}, \sigma_{zz}, \sigma_{xy}, \sigma_{yz}, \sigma_{zx})^T$ in Cartesian frame (2.1.1.5).

$[\sigma]$ Cauchy-stress tensor (2.1.1.2).

$\bar{\sigma}$ generalised stress = $g(\underline{\sigma}')$ (3.2.3).

$\underset{\sim}{\sigma}'$ vector of deviatoric stress half-way through plastic part of a deformation step (3.2.4.2.2.1).

$\hat{\underline{\sigma}}'$ vector of hypothetical-elastic deviatoric stress half-way through plastic part of a deformation step (3.2.4.2.2.1).

$\Delta\underline{\sigma}'$ change in deviatoric Cauchy stress during a deformation step (3.2.4.3).

$\underline{\sigma}', \sigma_h$ deviatoric-stress vector, hydrostatic stress (3.2.3).

σ_h^A value of hydrostatic stress at point A, similarly at point B (3.2.4.4.1).

$\underline{\sigma}'_I$ deviatoric stress vector at node I (3.2.4.4.2).

$\Delta\underline{\sigma}^{(i)}$ change in Cauchy stress during the ith iteration (3.2.3.1).

$\underline{\sigma}^{IJ}$, vector of deviatoric stress (in current frame) at end of elastic part of the deformation step (3.2.4.2.1).

$\Delta\underline{\sigma}^{J}$ vector of Jaumann increment of Cauchy stress (2.1.1.4).

$[\Delta\sigma^{J}]$ tensor of Jaumann increment of Cauchy stress (2.1.1.2).

$\Delta\underline{\sigma}^{eJ}$, hypothetical-elastic Jaumann increment of deviatoric stress (3.2.3.3).

$\Delta\underline{\sigma}^{IJ}$, vector of Jaumann increment of stress during elastic part of a deformation step (3.2.4.2.1).

$\Delta\underline{\sigma}^{IIJ}$, vector of Jaumann increment of stress during plastic part of a deformation step (3.2.4.2.2.1).

$\underline{\sigma}^{f}$, vector of deviatoric Cauchy stress (i.e. in reference frame) at end of a deformation step (3.2.4.3).

$\overline{\sigma}^{f}$ generalised stress at centroid of an element at the end of a deformation step (3.2.6.1).

$\underline{\sigma}^{R}$, vector of deviatoric stress (in current frame) at the end of a deformation step (3.2.4.3).

$[T_n]$ Jaumann-correction matrix (2.1.1.4).

$\underline{u}$ vector of displacement at a point (2.1.2).

$[U_n]$ Jaumann-correction matrix (2.1.1.4).

u_x, u_y, u_z components of displacement in x, y and z directions respectively (2.1.1.4).

$[V]$ deformation tensor (2.1.1.3.1).

V_n volume of element n (2.1.1.5).

v relative interfacial velocity (3.2.1.2.2.1).

$[W]$ matrix transforming the stress vector to give the components in a rotated axis system (3.2.4.3).

w_i Gaussian weighting factor for ith sample point (2.1.2).

$\underline{x}$ position vector of a point in reference coordinates (2.1.1.3.1).

x_i global axis, i=1,3 (3.2.4.4.2).

$\underline{x}_n$ vector of global coordinates of nodes of element n (2.1.2).

X,Y,Z coordinates of a point in local axis system (2.1.2).

x,y,z coordinates of a point in Cartesian global or reference frame (2.1.1.1).

x',y',z' coordinates of a point in current reference frame (Appendix A).

x^A, y^A, z^A global coordinates of point A. Similarly B (3.2.4.4.1).

Y axial yield stress in simple tension (3.2.3).

Y^o, Y^f initial and final values of yield stress during deformation step (3.2.3.3, 3.2.4.2.2.1).

INTRODUCTION

The operations which may be applied to metal work-pieces in order to change their shape are conveniently divided into those which add material, such as welding, those which remove material, such as the various forms of machining and those which cause the work-piece to deform by the application of force. The advantage of the last type of process is that not only can economies be effected in the amount of material of the original work-piece, as compared to a metal-removal process, but when performed in the cold state, the variation of material properties with the extent of flow can be harnessed to give superior distributions of characteristics, such as hardness, throughout the finished article.

Forging is the name given to a particular set of metal-deformation processes in which the work-piece is deformed by pressing or hammering it between plane or shaped dies. Forging operations range from upsetting (carried out between plane dies) and cogging (upsetting of part of the billet at a time), to closed- and open-die processes (where the dies contain impressions of the desired shape of the article), and variations such as backward extrusion (indentation or cup forming).

Forging is often carried out in several stages. In order to determine the number, type and extent of deformation of these stages, it is desirable to know:

a) the working load,

b) the pattern of flow,

c) the resulting material properties,

for any operation which could form part of the forging sequence. Experience in forging can often supply an answer to the design problem, but not necessarily the best one. Experience may be of no

help when confronted with a totally unfamiliar type of forging or an exotic material.

The required information can be obtained experimentally, but it is time-consuming and costly, perhaps prohibitively so, to investigate even a few of the possible variations in forging conditions for each stage.

For these reasons, analytical techniques are of great value for examining forging operations.

An estimate of the forging load can be obtained by quite simple means, such as an upper-bound analysis, but the only analytical method which provides information about the flow of the material and the resulting properties, without making prior assumptions about the deformation pattern, is the finite-element technique.

As will be described later, the finite-element method has been successfully used to investigate forging processes which can be simulated by a two-dimensional model, either plane strain or axisymmetric. This thesis considers the application of the method to those examples of forging operations which cannot be thus simplified and have to be treated in a fully three-dimensional way.

Chapter One is a brief survey of some of the literature relating to metal-forming. The following chapter presents, in general terms, the finite-element theory relevant to the present work, while Chapter Three describes in detail the finite-element program which has been developed to examine examples of three-dimensional, plastic deformation.

Chapter Four considers briefly a previous application of the program to the radial expansion of thick tubes under internal pressure and then compares, with the results of experiment, the finite-element predictions for the deformation and distributions of hardness in simply-upset rectangular blocks.

The modification made to the method of modelling friction is described in Chapter Five and finite-element results are obtained for the axisymmetric ring test. A new experimental test is proposed which is sensitive to the level of friction on surfaces where material is flowing in more than one direction. Finite-element analyses of this deformation are performed with different values of the friction factor.

In Chapter Six, the finite-element program is shown to be capable of performing the analysis of a more complicated example of a three-dimensional deformation, namely the forging of a connecting rod.

Finally, the work considered in the thesis is summarised and suggestions are given for future research.

CHAPTER ONE

A BRIEF SURVEY OF THE RELEVANT LITERATURE

1.1 METAL-FORMING RESEARCH

Metal-deformation processes, of which forging is an example, are of great industrial importance and have been studied by numerous workers using experimental or analytical techniques.

1.1.1 Experimental Methods

It is not intended to present a comprehensive survey of all the experimental work which has been carried out in metal forming, since this topic is dealt with elsewhere (for example, reference 1). Instead, the following is a brief introduction to some of the techniques which can be used to study forming operations.

Perhaps the most obvious piece of information to obtain for a forging process is the variation of the deforming load with the extent of the deformation (reduction in height, punch stroke etc.), since this will determine the size of plant required to perform the operation. Measurement of the punch force presents no difficulty, although the work-piece may have to be scaled down or modelled in a material with low yield stress in order to reduce the maximum load to within the limits of laboratory equipment.

In addition to the total punch force, it is important to know the variation of pressure across the interface between the die and the work-piece because the dies must be capable of withstanding any large, localised stresses. Several techniques are available to measure die pressure, none of which is easy to perform.

The most common method uses pin load-cells. These measure

pressure (strictly force acting on a small but finite area) by detecting the axial strain in small pins which fit snugly into recesses in the die with their ends flush with the die surface (fig. 1.1).

Nagamatsu, Murota and Jimma (2,3) and Nagamatsu and Takuma (4) have used this technique to measure the distribution of pressure, during upsetting, across the die-contact surfaces of axisymmetric, plane-strain and rectangular billets, respectively (figs. 1.2,1.3)

The use of pin load-cells is generally restricted to deformations in which the pressure is relatively low since, otherwise, the material of the billet tends to be extruded between the pin and the wall of the recess. To overcome this difficulty, Daneshi and Hawkyard (5) sandwiched a series of strain gauges between the two halves of a split platen, near to the surface in contact with the work-piece, and arranged so that they measured strain in the axial direction (fig. 1.4). The gauges were calibrated in terms of pressure on the surface and extrusion of the work-piece into the gap was prevented by placing a spring-steel shim between die and billet. This arrangement could be used at much higher pressures than pin load-cells, but the results were subject to considerable scatter (fig. 1.5).

An experimental procedure devised by Brouha et al (6) enabled the velocity of the material across the die interface and the pressure to be measured at the same time. Small pieces of ruby were embedded in the top of a cylindrical billet and viewed, during simple upsetting, through a transparent diamond or sapphire top platen, using a mercury-discharge light (fig. 1.6). The rubies fluoresced in this light and could easily be tracked throughout the deformation. The interfacial pressure was obtained by measuring the shifts in a characteristic re-emission frequency of the previously-calibrated rubies (fig. 1.7).

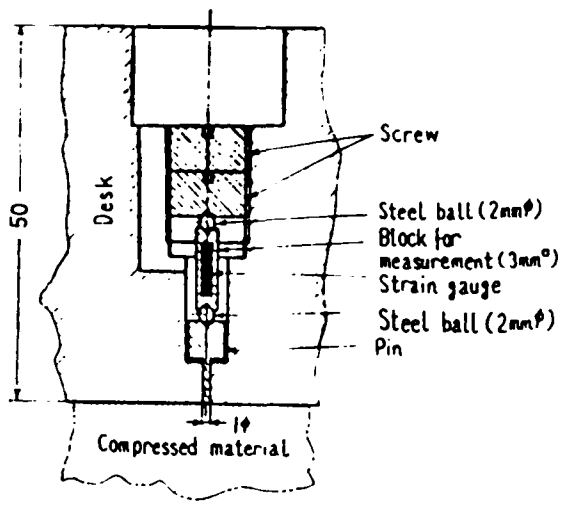

FIG. 1.1

PIN LOAD-CELL

(REF. 3)

FIG. 1.2

VARIATION OF PRESSURE ACROSS DIE/CYLINDER INTERFACE DURING SIMPLE UP-SETTING

h_o = HEIGHT/DIAMETER RATIO

(REF. 2)

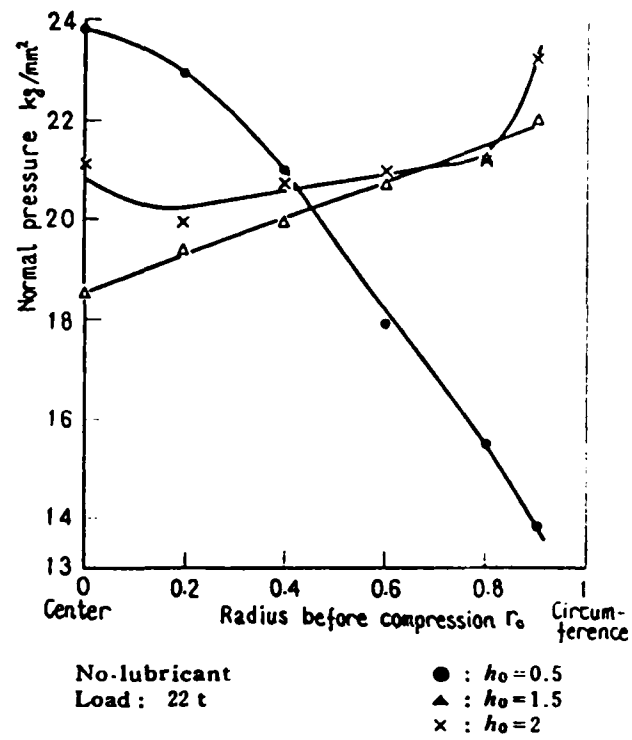

FIG. 1.3

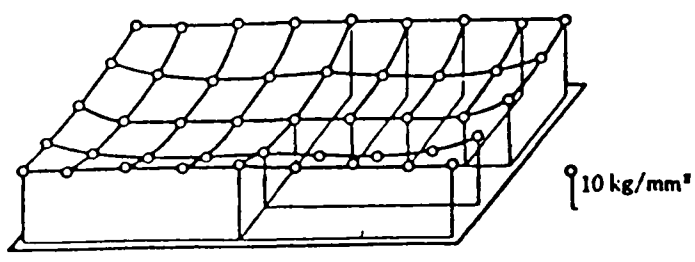

VARIATION OF PRESSURE ACROSS DIE / BLOCK INTERFACE DURING SIMPLE UP-SETTING. BLOCK 20 x 20 x 40 mm, NO LUBRICANT

(REF. 4)

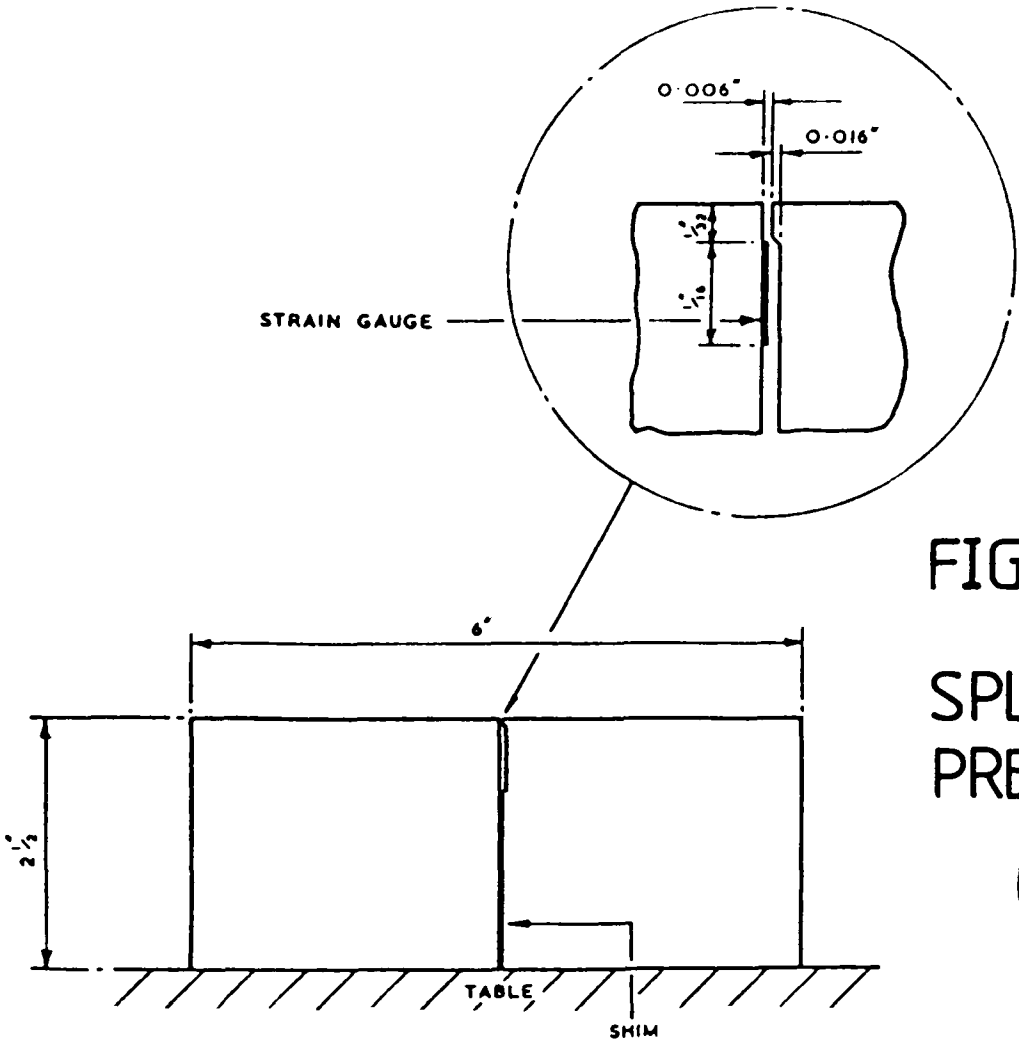

FIG. 1.4

SPLIT-PLATEN PRESSURE CELL

(REF. 5)

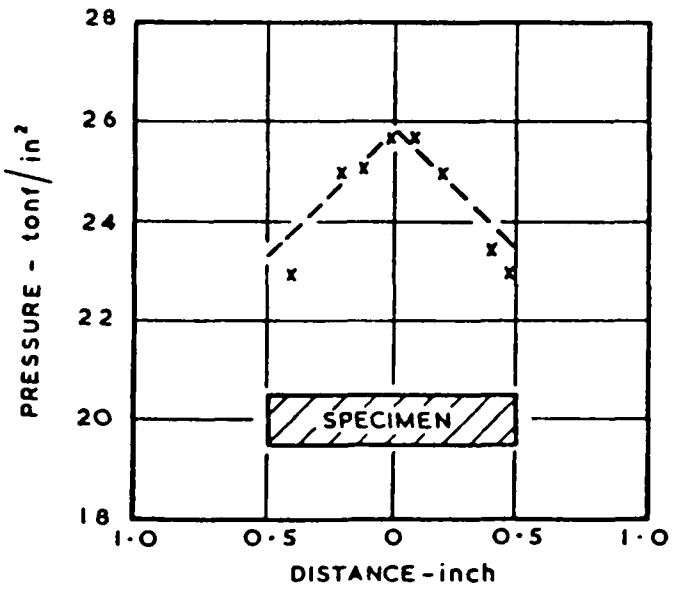

FIG. 11. Pressure distribution on major axes of a rectangular specimen 3 in. by 1 in. and 0·2 in. thick, lubricated with lead foil

FIG. 1.5

VARIATION OF PRESSURE ACROSS TOP OF RECTANGULAR BILLET DURING UPSETTING

(REF. 5)

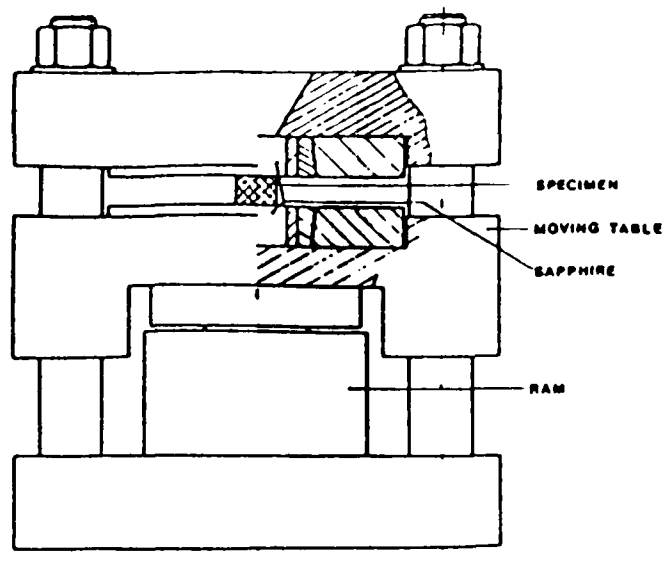

FIG. 1.6

DIE-SET WITH TRANSPARENT PLATENS (REF. 6)

Fig. 7. Measured hydrostatic stress distribution for D/h=6 at various deformations. Fig. 7a shows the measured stresses versus the radii of the ruby positions near to the x-axis and Fig. 7b those near the y-axis from Fig. 6.
The inset of Fig. 7a is a plot of the deformation versus total load.

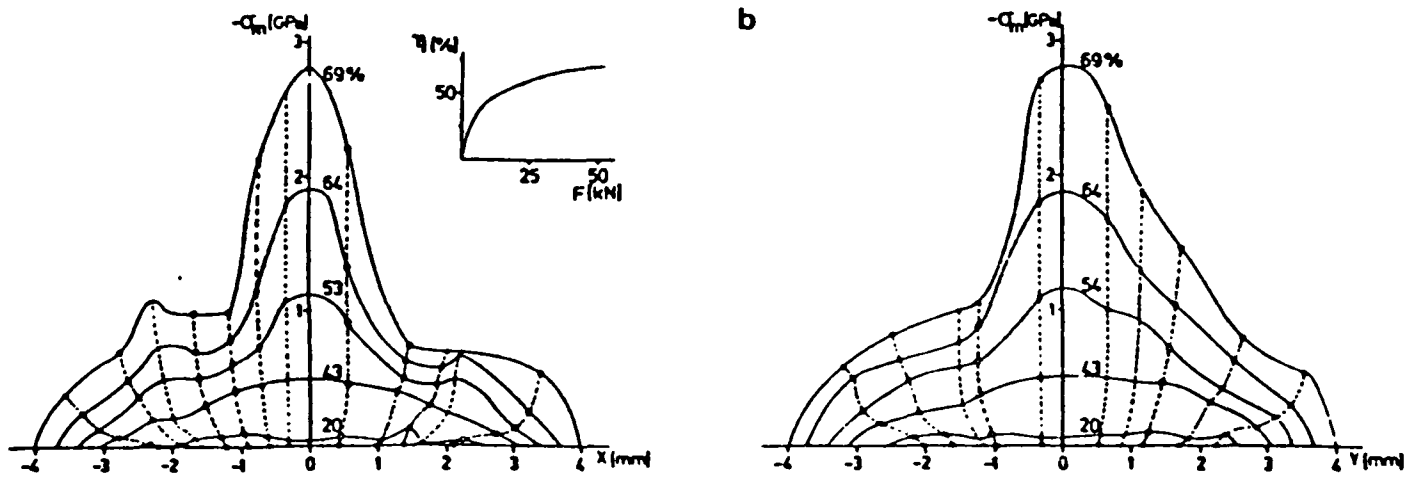

FIG. 1.7

DISTRIBUTION OF PRESSURE ACROSS TOP OF CYLINDRICAL BILLET DURING UPSETTING (REF. 6)

The pattern of metal flow occurring during a deformation process will obviously determine the shape of the forged article, but it will also influence the properties of the work-piece. For example, when forging is carried out below the re-crystallisation temperature (7) of the material, the hardness at any given point will depend upon the extent of localised plastic-straining. Similarly, the susceptibility to fracture and corrosion will depend on how the material deformed (8).

Various methods have been developed to investigate the flow of material during a deformation. The simplest requires the deformed billet to be sectioned and the exposed surfaces etched (9). This can clearly indicate areas of low and high deformation (fig. 1.8), including lines of flow, but the information is of a qualitative nature - actual values of material parameters, such as plastic strain, cannot be calculated.

These quantities can be measured if the billet is sectioned before it is deformed and a grid is marked on one of the mating surfaces (fig. 1.9). The grid may be photo-etched, printed or engraved, and in the last case the incisions may be filled with some material of a contrasting colour. (As an alternative to sectioning, the billet may be drilled and have fine wires inserted through the holes, or may be itself composed of blocks of different colour (10).)

The coordinates of points of the grid can then be compared at stages throughout the deformation in order to calculate incremental components of displacement, and hence strain, in the plane under consideration. Summation of these increments gives total strain while deviatoric stress may be calculated using the Lévy-Mises flow rule (7). This technique, part experimental and part numerical, is known as visioplasticity.

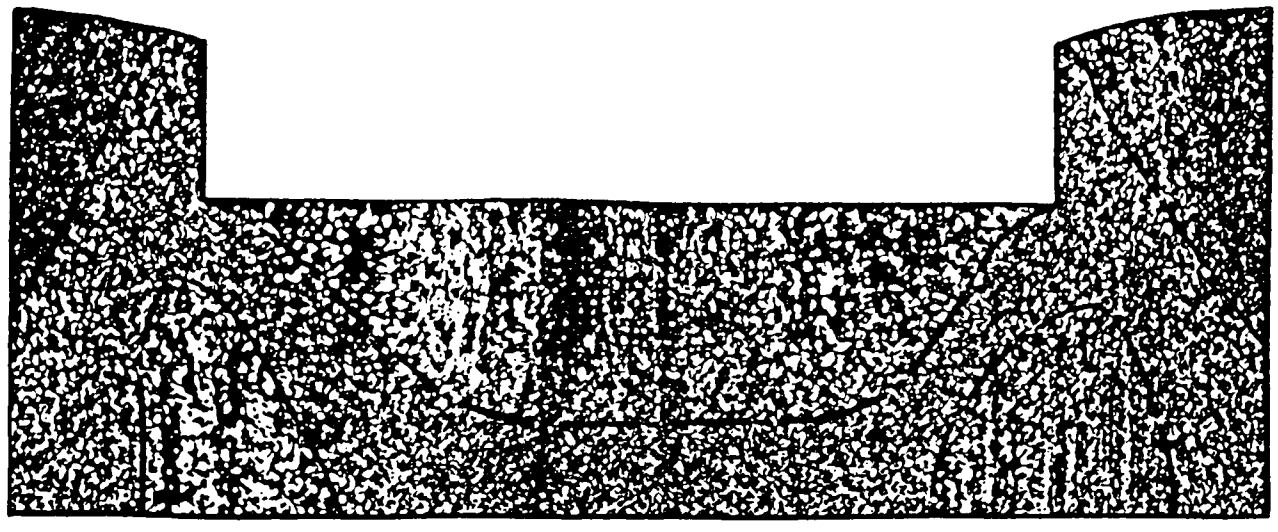

Fig. 11. Etched specimen showing grain structure and approximate limits of regions with little deformation.

FIG. 1.8

BACKWARD-EXTRUSION SPECIMEN AFTER SECTIONING AND ETCHING (REF. 9)

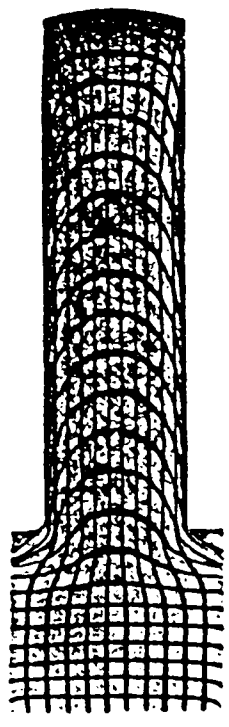

FIG. 101.—Flow shown by distortion of co-ordinate net pattern. Direct extrusion of tin at 100° C., using lubrication.

FIG. 1.9

FORWARD-EXTRUSION SPECIMEN SHOWING DEFORMED GRID (REF. 10)

Savings in the cost of tooling and of press equipment can be made if the visioplasticity tests are conducted using material with a low yield stress. Various materials such as paraffin wax, plastics or the softer metals like lead or tin have been used but the most successful substitute is Plasticine. This modelling material has similar stress-strain characteristics to hot mild-steel or cold, pure aluminium (11). It has been widely used to examine processes such as extrusion (1), rolling (12, fig. 1.10) and upsetting (13, fig. 1.11)

The sectioning method, however, is not universally applicable since the section must be one which remains plane throughout the deformation, e.g. a plane of symmetry. Also, the two halves of the billet must not separate during the process, so that only highly constrained deformations can be studied e.g. plane-strain operations or forging of a billet in a container.

The technique which uses wire inserts does not suffer from these restrictions, but the production of such specimens is very difficult.

Visioplasticity, if carried out incrementally, can give values of the deviatoric components of stress. The generalised or equivalent stress can also be found directly at any position in the billet by sectioning the deformed work-piece and performing hardness tests on the exposed surfaces (14). The distributions of hardness values are often compared with analytically predicted results (fig. 1.12).

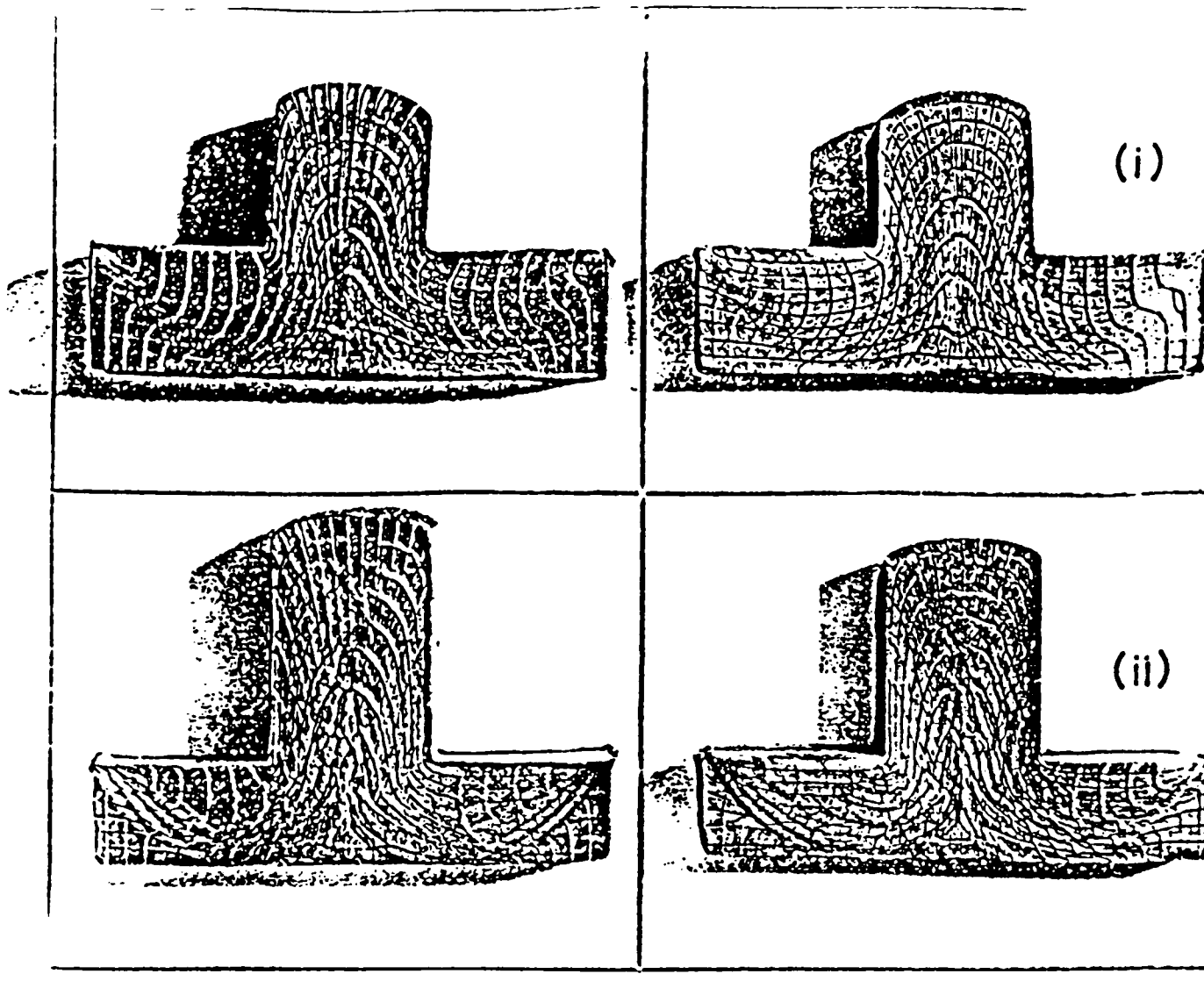

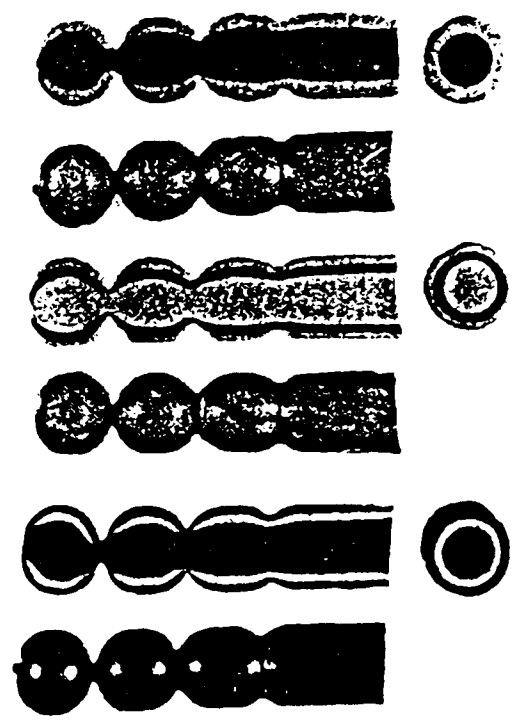

Rolled Plasticine bars.

FIG. 1.10

EXAMPLES OF USE OF PLASTICINE — EXTRUSION AND BALL ROLLING (REF. 1, 12)

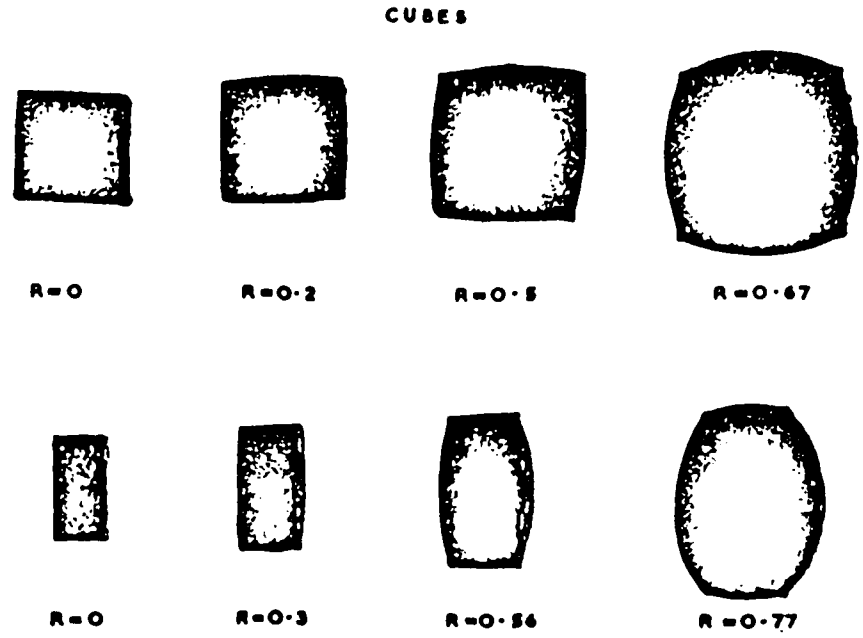

Dynamically upset cubes and rectangular prisms for different fractional reductions.

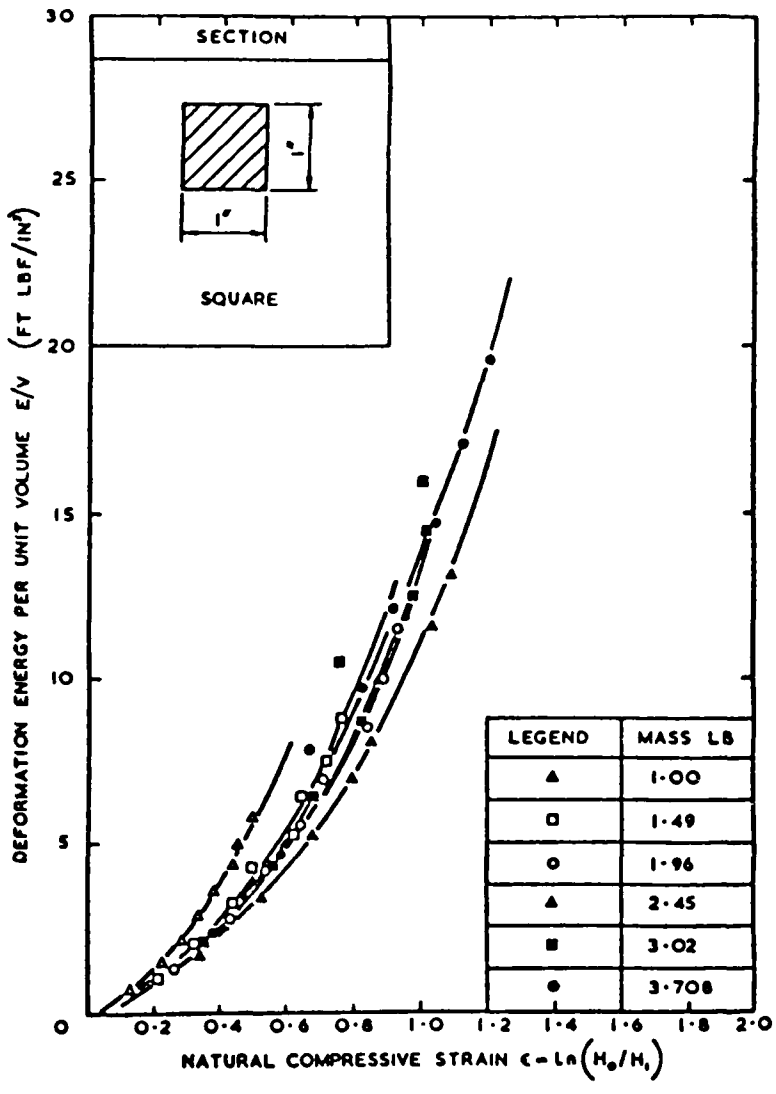

Relation between deformation energy per unit volume and natural compressive strain for cubes.

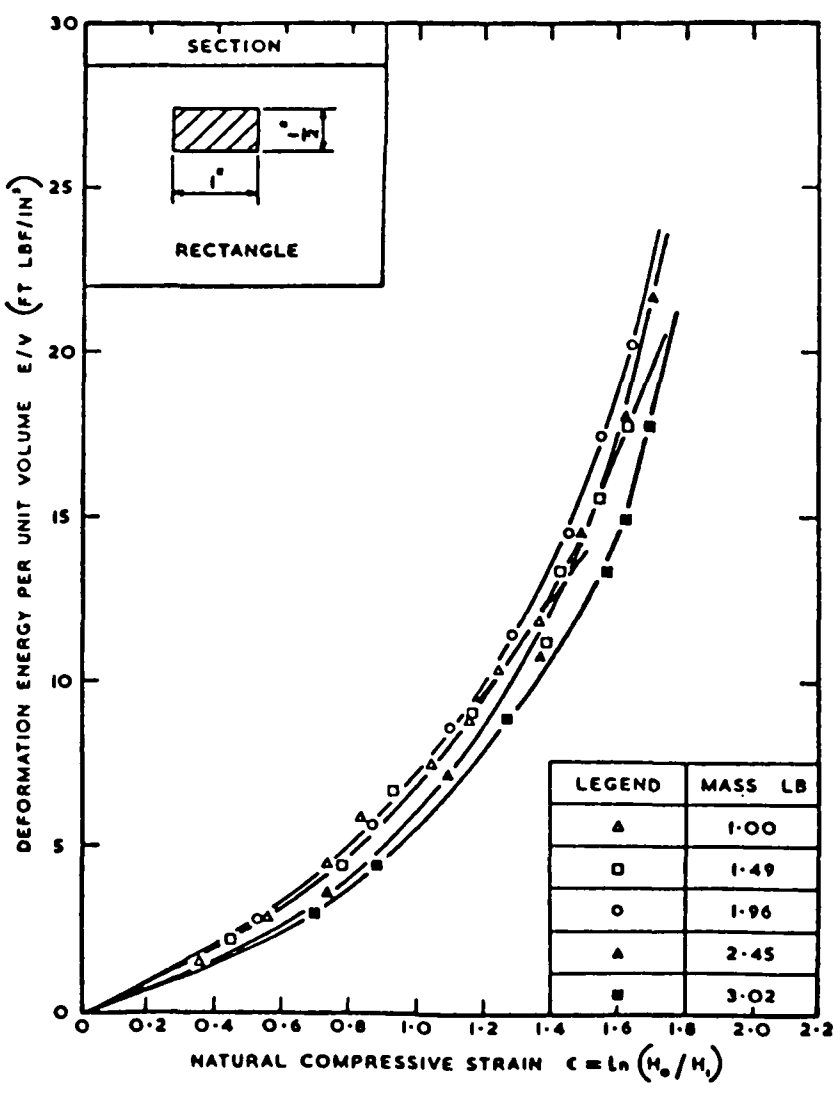

Relation between deformation energy per unit volume and natural compressive strain for rectangular prisms.

FIG. 1.11

DYNAMIC UPSETTING OF PLASTICINE BLOCKS (REF. 13)

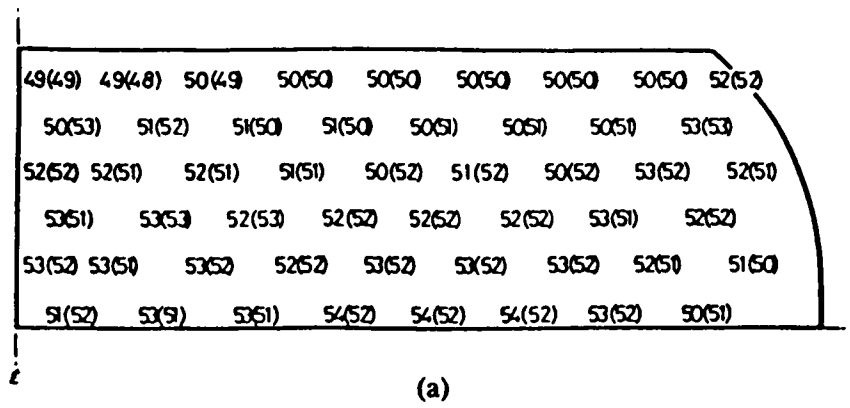

(a)

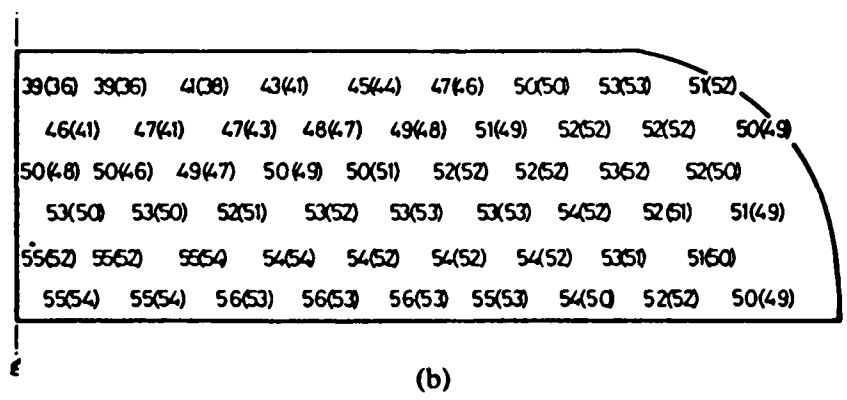

(b)

Comparison of predicted and experimental (in parentheses) hardness distributions (a) low friction ($m = 0{\cdot}1$) (b) high friction ($m = 0{\cdot}7$).

FIG. 1.12

DISTRIBUTIONS OF HARDNESS ACROSS DIAMETRAL SECTION OF UPSET CYLINDER (REF. 14)

1.1.2 Numerical Methods

These include upper-bound, slab and weighted-residual methods as well as slip-line-field techniques and treatments using piecewise interpolation functions.

An upper-bound solution is obtained by choosing a flow-velocity field, in two or three dimensions (15), for the deforming body which satisfies both the boundary conditions and the requirement of material incompressibility, and calculating the power dissipated through the rate of work of deformation in domains of the body, and through the rate of shearing work done between the domains, using their relative velocities and a constant value of shear yield stress. This power represents an upper bound to the power dissipated in the actual work-piece, and the velocity field which leads to the smallest value of power is the closest to the true solution (fig. 1.13). The minimisation can be carried out automatically using a linear-programming method if the power is expressed as a linear function of velocity components (16). Computer packages are available (17).

This is a valuable method for rapid assessment of working loads and can be perfomed incrementally, but it requires some prior assumption about the deformation pattern. It can predict neither the details of the distribution of flow nor any elastic deformation.

The method of slab (or stress) analysis is particularly suited to highly constrained processes, such as closed-die forging, where the geometry of the work-piece is largely pre-determined. As in the upper-bound technique, the body is divided into domains (or 'unit zones') but these are chosen not only to minimise power but also to be aligned with a principal stress direction, and are assumed to deform homogeneously (fig. 1.14). The equations of equilibrium in these regions then allow stress in the work-piece and the total deforming

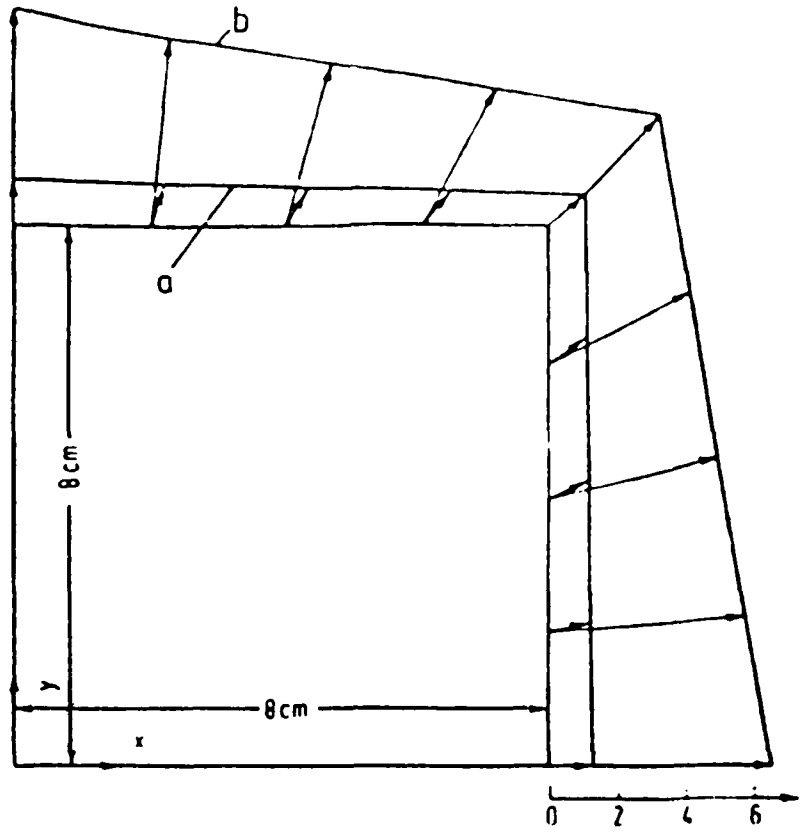

HORIZONTAL VELOCIY VECTORS ON TOP (a) AND MID-HEIGHT (b) PLANES OF 8x8x1 cm BLOCK DURING UPSETTING (REF. 15)

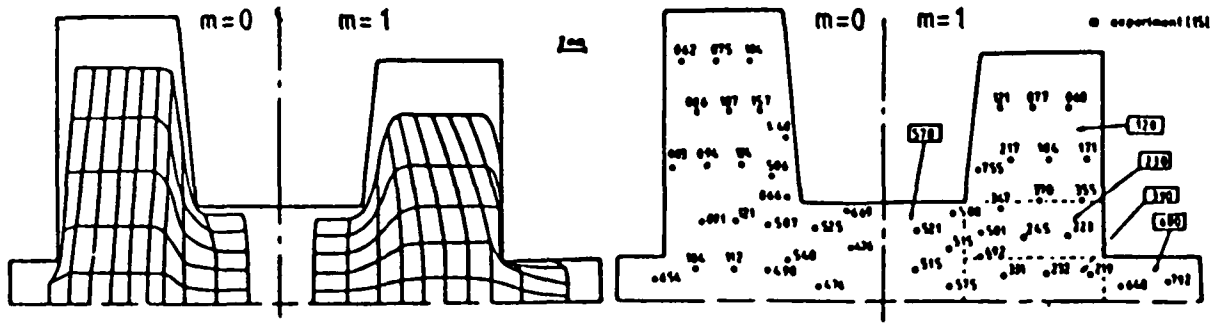

DISTORTION OF GRID AND DISTRIBUTION OF STRAIN IN FORGED AXISYMMETRIC SPECIMEN (REF. 17)

FIG. 1.13

UPPER-BOUND SOLUTIONS

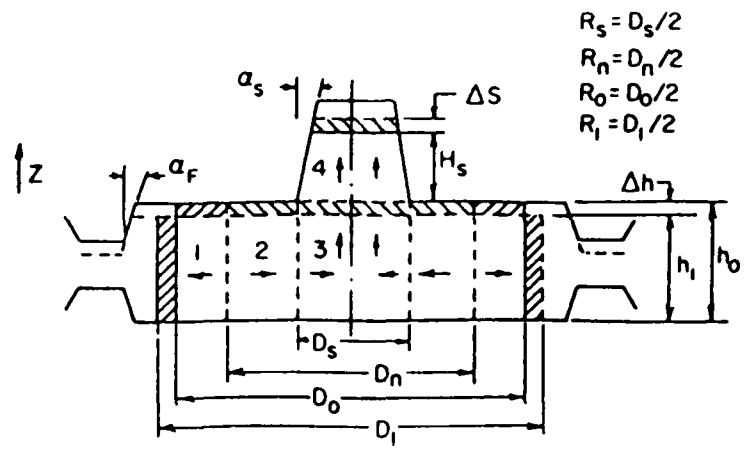

UPSETTING STAGE DURING FORGING IN THE DIES

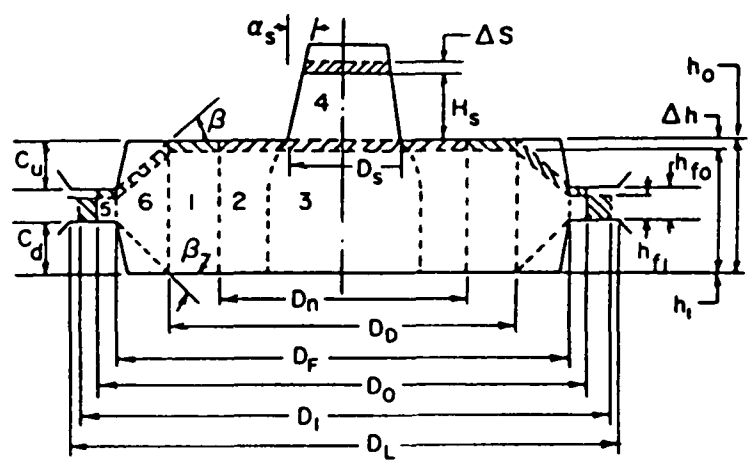

DEFORMATION ZONES AND METAL FLOW DURING THE FILLING STAGE

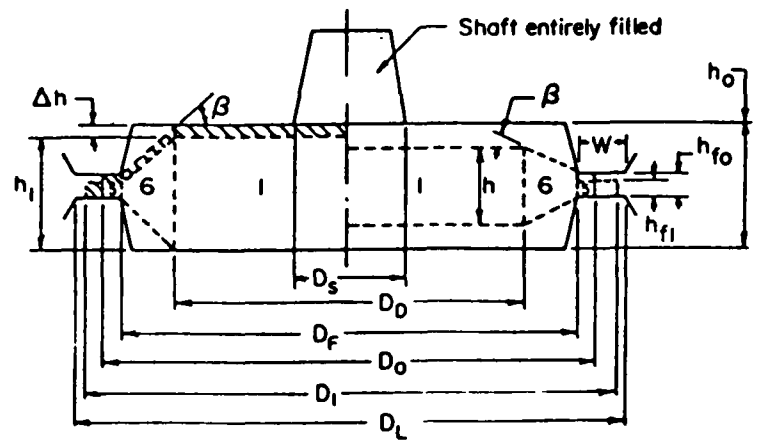

a. Metal Flow by Sliding

b. Metal Flow by Shearing

DEFORMATION ZONES AND METAL FLOW DURING THE END STAGE

FIG. 1.14

SLAB ANALYSIS OF CLOSED-DIE AXISYMMETRIC FORGING (REF. 18)

load to be evaluated from the condition of zero stress normal to a free surface. When the deformation pattern depends on the position of a flow divide, this can be determined by requiring that the stress at this divide is the same whichever free surface is used to start the calculation. A fuller description of the method is given by Altan (18).

The method of weighted residuals is also related to that of upper bounds. In the former treatment, however, the velocity is approximated by a linear combination of functions chosen so that the velocity satisfies the boundary conditions but not necessarily the differential equations of the system. A residual function is obtained by substituting the approximate velocities into the differential equations. The aim is to choose the coefficients of the linear combination in order to minimise the residual in some prescribed manner.

The minimisation can be carried out in a number of ways, for example by requiring the approximation to satisfy the differential equations at a finite number of points of the region, or to satisfy these equations, on average, over a finite number of sub-domains, or to lead to a least-square error over the whole region. The coefficients are generally evaluated as the unknowns of a set of simultaneous equations and the approximation is improved by including more terms in the linear combination. The method is reviewed by Finlayson and Scriven (19).

Slip-line-field analysis is essentially a graphical method of determining material flow (fig. 1.15), although it can be computerised (1). It requires even more care in its use than does the upper-bound method, since a kinematically-admissible velocity field must be found which also satisfies the conditions of stress equilibrium. It is severely restricted by the assumptions of plane-strain deformation and

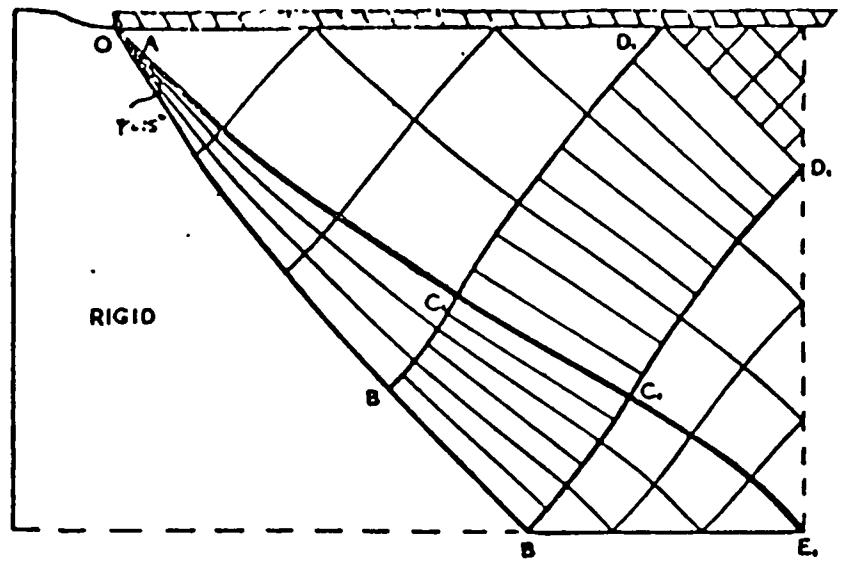

I. $\frac{w}{h}$ =1·386.

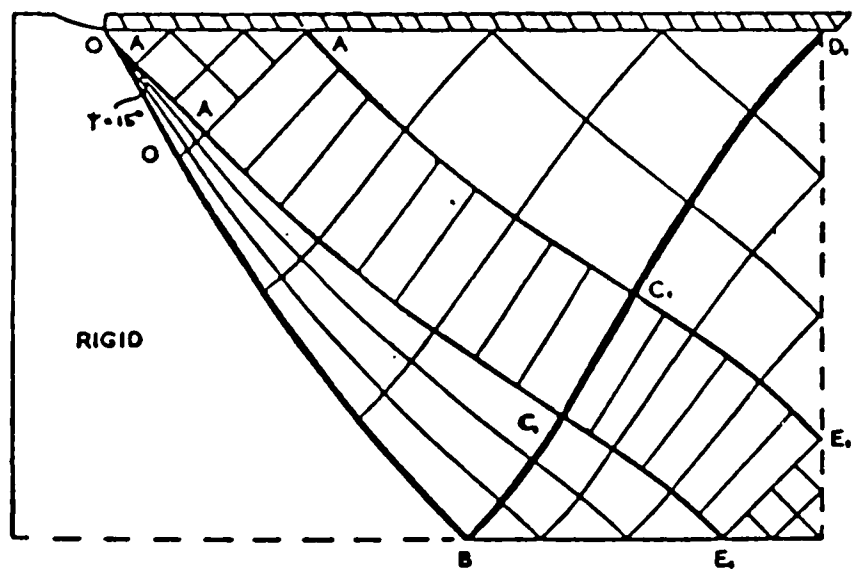

II. $\frac{w}{h}$ =1·443.

FIG. 1.15

SLIP-LINE FIELDS FOR COMPRESSION BETWEEN SMOOTH DIES (REF. 11)

of a non-hardening material although attempts have been made to overcome both of these deficiencies. Details of this method may be found in the literature (20,21,7).

All the numerical methods considered so far have serious disadvantages since they generally neglect elastic deformation, require previous knowledge of the flow pattern and may be restricted to idealised types of deformation. These disadvantages are not shared by the last class of numerical techniques discussed here in which the velocity in the functional for power is approximated by a continuous, piecewise linear function of the velocity at a finite number of points of the body. In particular:

a) the result can be made, in principle, to approximate the 'true' solution as closely as one pleases,

b) the methods are not restricted to any particular geometry - two- and three-dimensional solutions are equally feasible,

c) it is possible to incorporate into the formulation any desired elastic or plastic properties and the variation of these properties with temperature, strain or strain rate,

d) the techniques are fully-predictive in finding displacement or velocity fields which are compatible with the boundary conditions while satisfying equilibrium and minimising potential energy.

Piecewise interpolation techniques can adopt either finite-element or finite-difference approaches. These two methods are broadly similar, and indeed Kunar and Minowa (22) have shown that they give identical results for certain discretisations of the body, and only differ in the way the solution is performed. In a finite-element analysis, the integration of infinitesimal power is implicit in the formulation and a stiffness relationship between the displacement (or velocity) and the force at points of the body is obtained which is solved by matrix methods. In the finite-difference approach, no stiffness relationship

is obtained and the integration is carried out explicitly as the solution proceeds.

Finite-difference methods have been used a great deal to examine geomechanical problems (23), where their ability to model dynamic effects, by considering mass to be concentrated at nodes, is important. They can analyse deformations involving large displacement (24), and have recently been applied to metal forming (25). Some examples are given in fig. 1.16.

Although there is little to choose between the finite-element and the finite-difference techniques in terms of computational effort and accuracy of solution, the author considers the stiffness formulation of the finite-element approach to be more convenient and this method has been selected for the work considered in this thesis.

Finite-element research is reviewed in the remaining sections of this chapter.

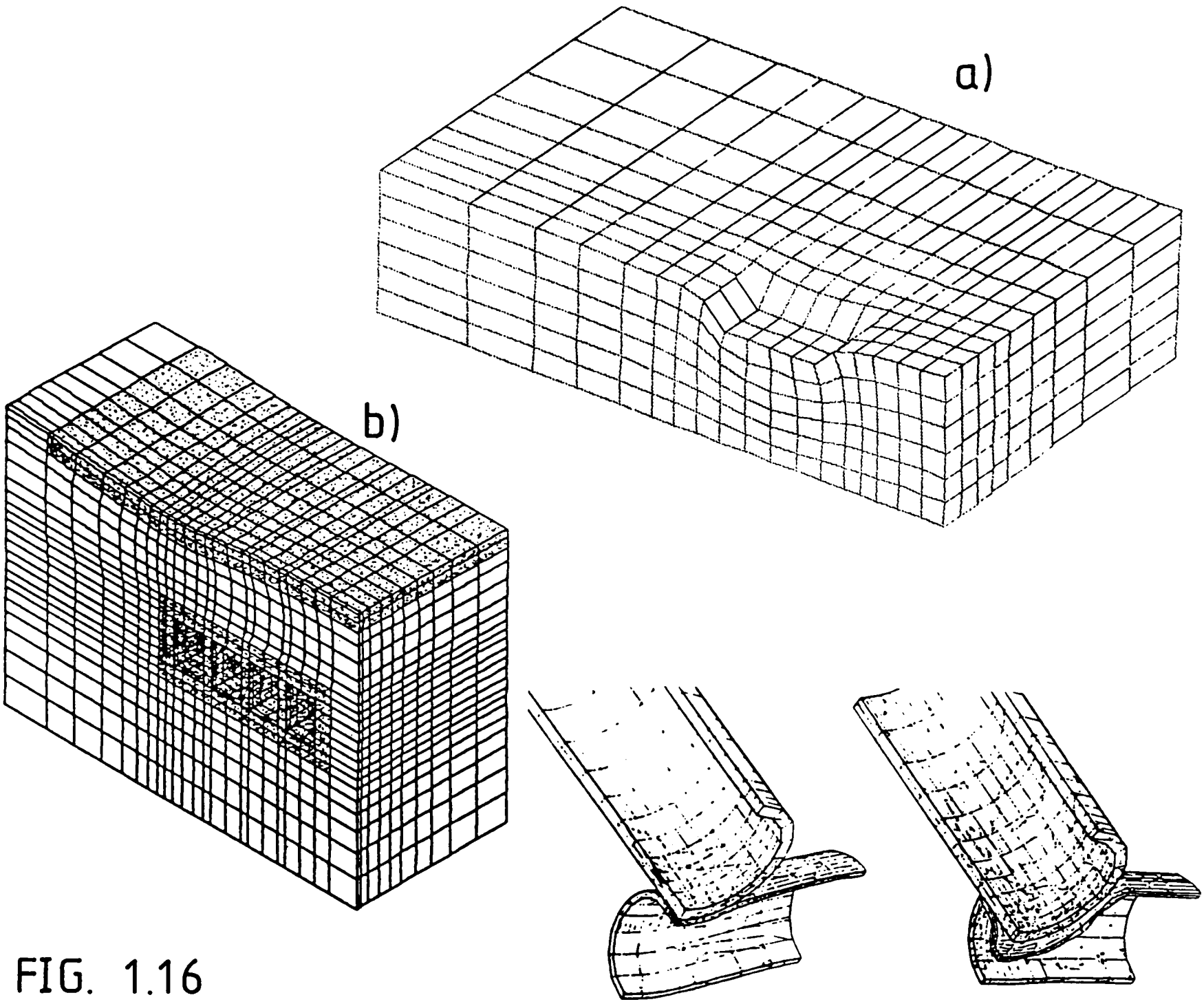

FIG. 1.16

FINITE-DIFFERENCE ANALYSES

a) INDENTATION OF METAL PLATE (REF. 25)

b) DEFORMATION OF SUB-TERRANEAN CONCRETE STRUCTURE (REF. 23)

c) IMPACT OF TWO PIPES (REF. 24)

1.2 FINITE-ELEMENT ANALYSES

In a finite-element analysis, material displacement is assumed to be a continuous function defined over a finite number of discrete regions or elements of the body. Interpolating procedures enable this quantity to be expressed in terms of its values at certain points, or nodes, usually on the boundaries between elements. By means of the familiar geometric relationship between strain increment and displacement, and a constitutive relationship between stress and strain increments, a virtual-work formulation can be constructed for the whole body which in turn determines the stiffness matrix relating nodal displacement to nodal force. For elastic deformations, the stiffness matrix is linear, but this is not generally the case for plastic flow. A fuller description of the method will be given in the next chapter.

Even simple finite-element treatments require the solution of matrix equations with a large number of degrees of freedom, and the use of an electronic computer is essential. Normally, a large main-frame or mini-computer would be used for non-linear problems, although advances have been made in adapting bulk-deformation finite-element programs to micro-computers (26).

The development of finite-element analysis and its applications to fields as diverse as civil engineering, quantum mechanics and pure mathematics are reviewed extensively elsewhere (27-29), so only a selection of the literature specifically concerned with its use in plasticity problems and metal-forming research will be mentioned here.

1.3 FINITE-ELEMENT METHODS IN PLASTICITY

A comparative study of different methods of finite-element analysis of plastic deformation has been conducted by Kudo and Matsubara (30), who collated solutions, for the upsetting of a cylindrical billet, from research groups all over the world (fig. 1.17). There was considerable variation in the predicted profiles and working loads of the deformed billets, which was attributed to differences in the type of element, their configuration in the mesh and the size of increment. A detailed comparison of individual techniques was prevented by a lack of precise computational information, but the study was of great interest in showing the range of different approaches to the problem.

Currently, finite-element treatments of metal-forming processes can be divided according to their basic assumptions about the behaviour of the material, namely the visco-plastic, the rigid-plastic and the elastic-plastic methods. There are marked similarities between the first two, since both neglect any elastic behaviour of the work-piece, and both enforce volume constancy by means of a penalty-function or similar technique. In the rigid-plastic method, sometimes called the matrix method (31), nodal displacements or velocities are the unknown quantities, and regions in which the strain is low are assumed to be rigid and are ignored. In a visco-plastic analysis, the yielded material is assumed to behave like a non-Newtonian fluid, so this method is particularly suitable for steady-state processes.

Visco-plastic analyses involve a non-linear relationship of stress to strain-rate and are usually iterative; the stress and strain-rate distributions at the end of a step being used to calculate the stiffness matrix for the next iteration. Typical applications are those by Zienkiewicz and Godbole (32) for steady-state forward extrusion, Price and Alexander (33) for die-less drawing

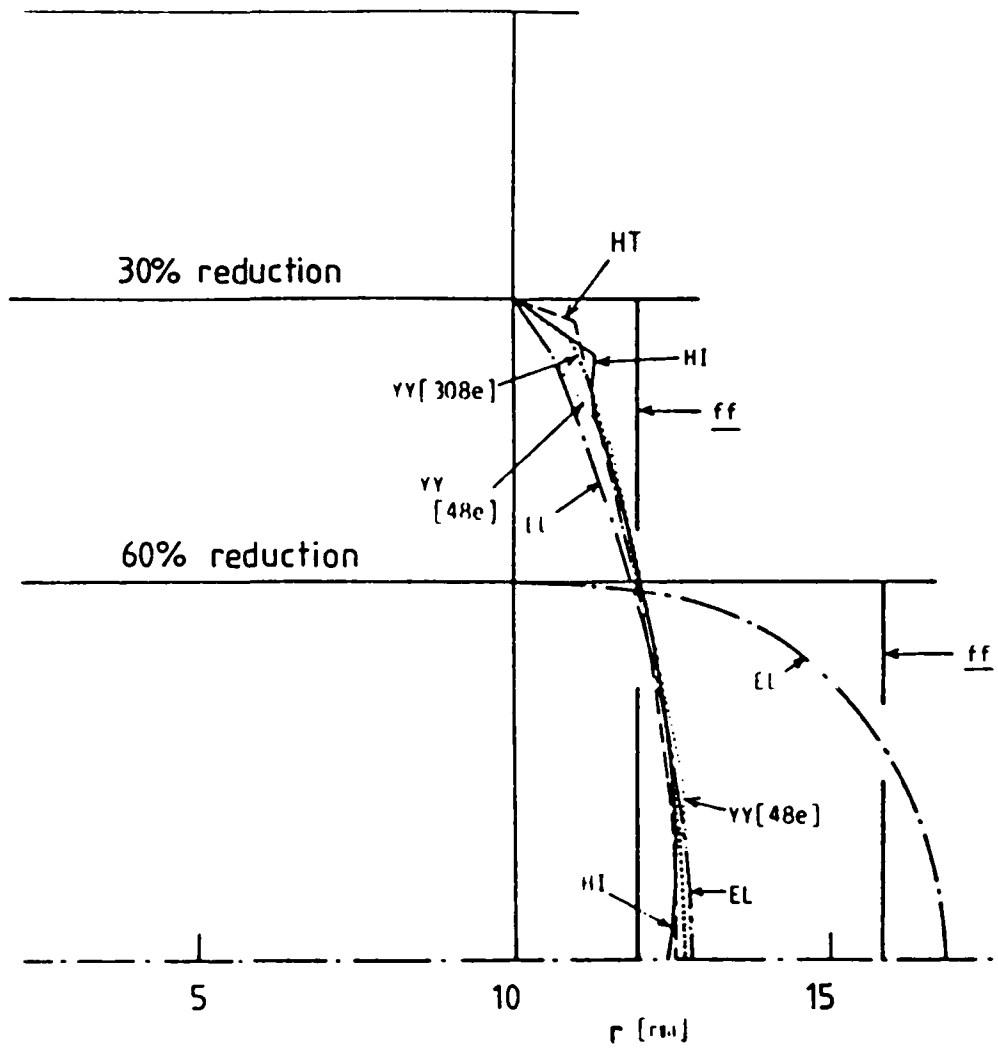

FIG. 1.17

COMPARISON OF BULGE PROFILES OF UPSET AXISYMMETRIC BILLETS PREDICTED BY VARIOUS ELASTIC-PLASTIC FINITE-ELEMENT TECHNIQUES (REF. 30)

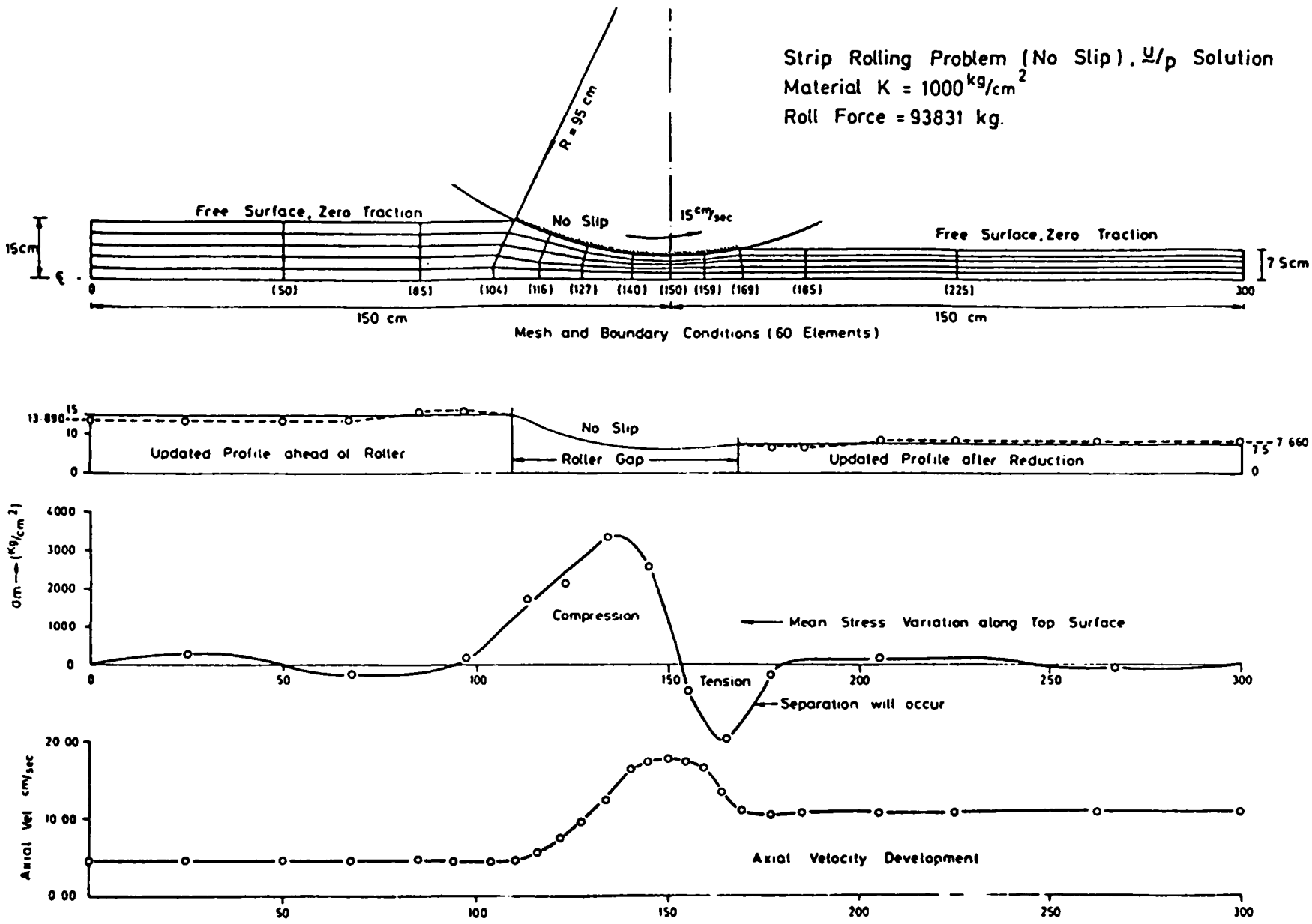

FIG. 1.18

VISCO-PLASTIC FINITE-ELEMENT ANALYSIS OF ROLLING (REF. 34)

and Zienkiewicz, Jain and Onate (34) for rolling (fig. 1.18). An incremental form was used by Oh, Rebelo and Kobayashi (35) to examine the upsetting of billets with properties dependent upon strain-rate.

The rigid-plastic approach also involves non-linearity. It has been used to analyse non-steady-state, forging-type operations, for example, Lee and Kobayashi (31) examined the expansion and contraction of a hole in a circular plate, Chen and Kobayashi (36) looked at the upsetting of a ring while Price and Alexander (37) and Dung, Klie and Mahrenholtz (38) considered the upsetting of a solid cylinder and backward extrusion. The method has also been applied to steady-state processes, such as wire drawing by Klie, Lung and Mahrenholtz (39, fig. 1.19) and hot rolling by Sharman (40,41) and Cornfield and Johnson (42).

Although efficient for steady-state processes, the rigid-plastic and visco-plastic techniques are unable to model the elastic recovery resulting from the removal of the deforming load, and so cannot predict distributions of residual stress. Since the residual stresses in a work-piece are important in determining its behaviour during use or subsequent manufacturing operations, this is a serious disadvantage of the rigid-plastic and visco-plastic approaches. In addition, since no elastic regions can be present, small-strain deformation, in which parts of the body may be unyielded, cannot be adequately modelled, although for a process such as heading (43) where the persistent elastic region is accompanied by extensive plastic deformation elsewhere, the approximation may not be so bad. For these reasons, an elastic-plastic approach is necessary for a full analysis of forging operations, and it is this technique which will be considered in detail in this thesis.

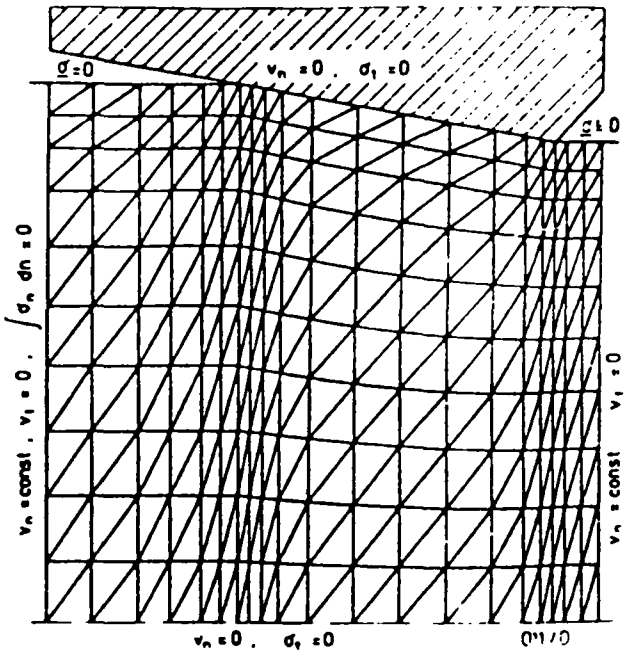

Subdivision in finite elements and boundary conditions .

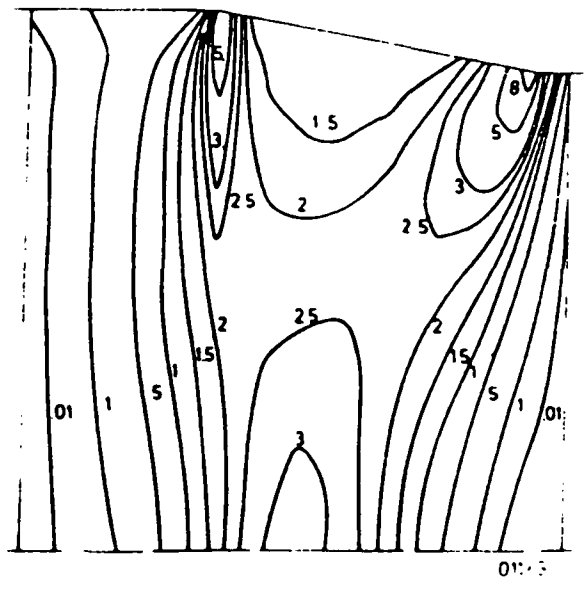

Equivalent strain rate λ/λ_N .

FIG. 1.19

RIGID-PLASTIC FINITE-ELEMENT ANALYSIS OF WIRE DRAWING (REF. 39)

1.4 ELASTIC-PLASTIC ANALYSES

These methods are based on the Prandtl-Reuss incremental stress-strain relationships, and so are performed in small steps. In their simplest form, called the tangent-modulus method, the stiffness of the body is calculated at the beginning of each increment, using the state of stress and plastic strain at the end of the previous step. Satisfactory results have been obtained by this method for such examples as tensile specimens, by Marcal and King (44) and Yamada, Yoshimura and Sakurai (45); for axisymmetric and plane-strain upsetting by Nagamatsu et al (46-48); for side pressing by Lee and Kobayashi (49, fig. 1.20); for ball indentation by Lee, Masaki and Kobayashi (50); for extrusion by Iwata, Osakado and Fujino (51) and Lee, Mallett and McMeeking (52, fig. 1.21); for plane-strain drawing by Gordon and Weinstein (53); and for backward extrusion by Hartley, Sturgess and Rowe (9). There is some evidence that computational time can be decreased, without loss of accuracy, by increasing the increment size and performing iterations within each increment, providing the inverted form of the stiffness matrix is stored from the first iteration and re-used (modified Newton-Raphson method). This is the basis of the initial-stress technique used by Zienkiewicz, Valliappan and King (54) to analyse the tension of perforated plates and notched beams, and by Barnard and Sharman (55) to examine the yielding of edge-supported plates by perpendicular loads

However, when the deformation involves large strain, it is not always possible to obtain convergence using the modified Newton-Raphson technique (56); the un-modified Newton-Raphson method usually leads to convergent solutions but takes longer to perform since the stiffness matrix must be inverted during each iteration.

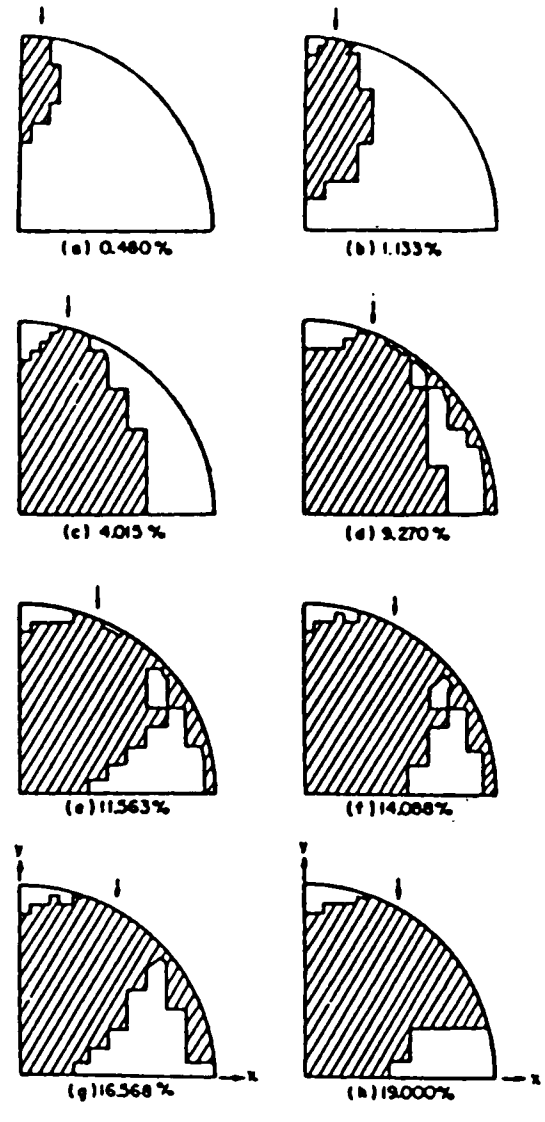

Plastic zones at various reductions in side-pressing

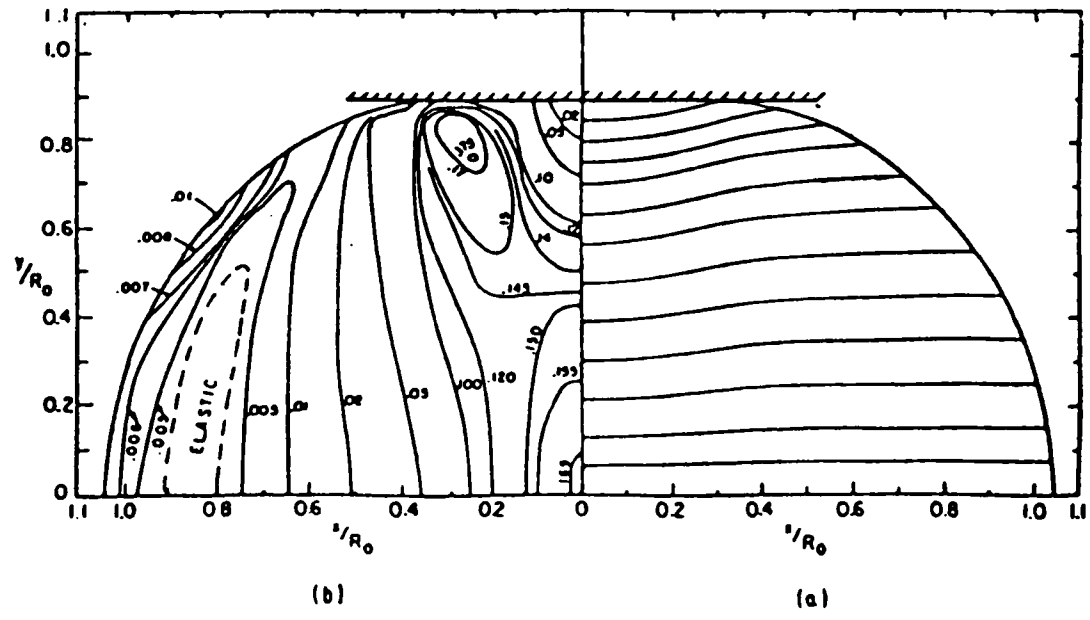

(a) Line distortions and (b) contours of constant effective strain at 10 percent reduction in height in side-pressing

FIG. 1.20

ELASTIC-PLASTIC FINITE-ELEMENT ANALYSIS OF PLANE-STRAIN SIDE-PRESSING (REF. 49)

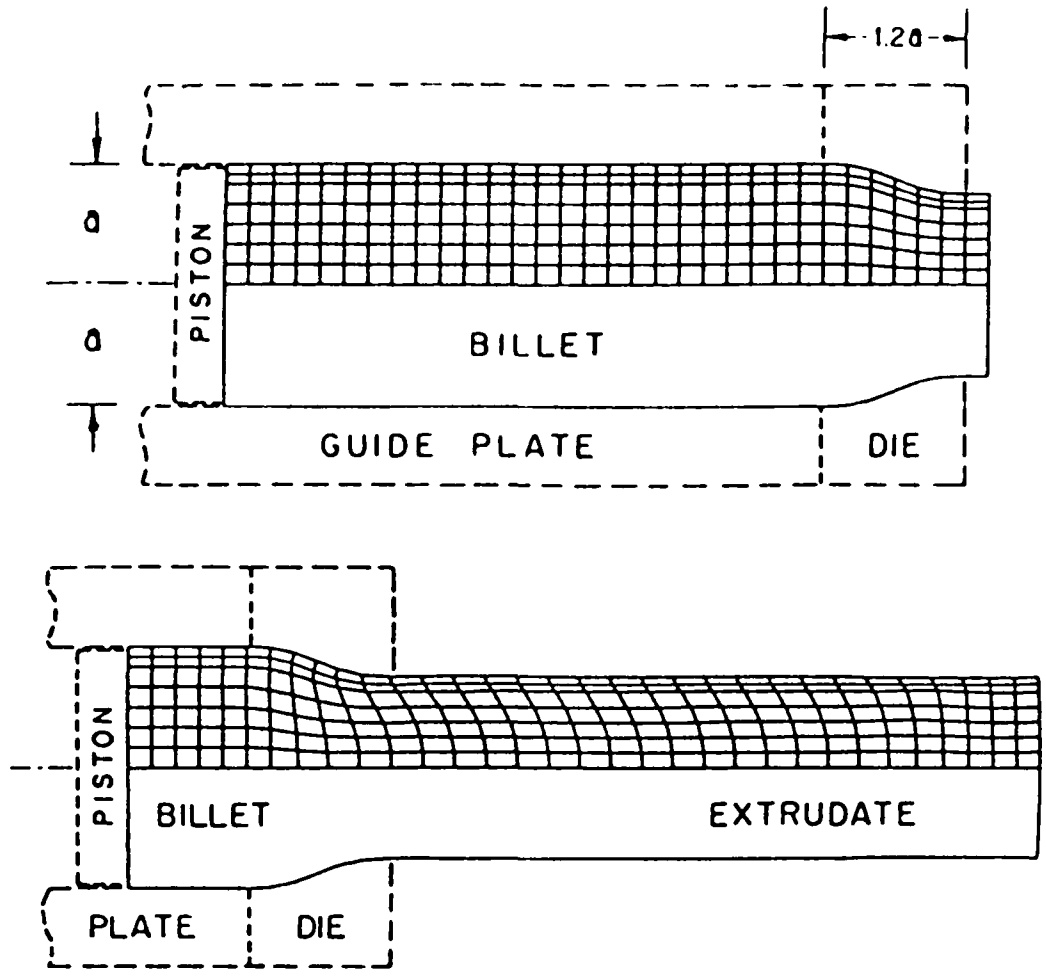

Undeformed and deformed plane-strain finite-element mesh.

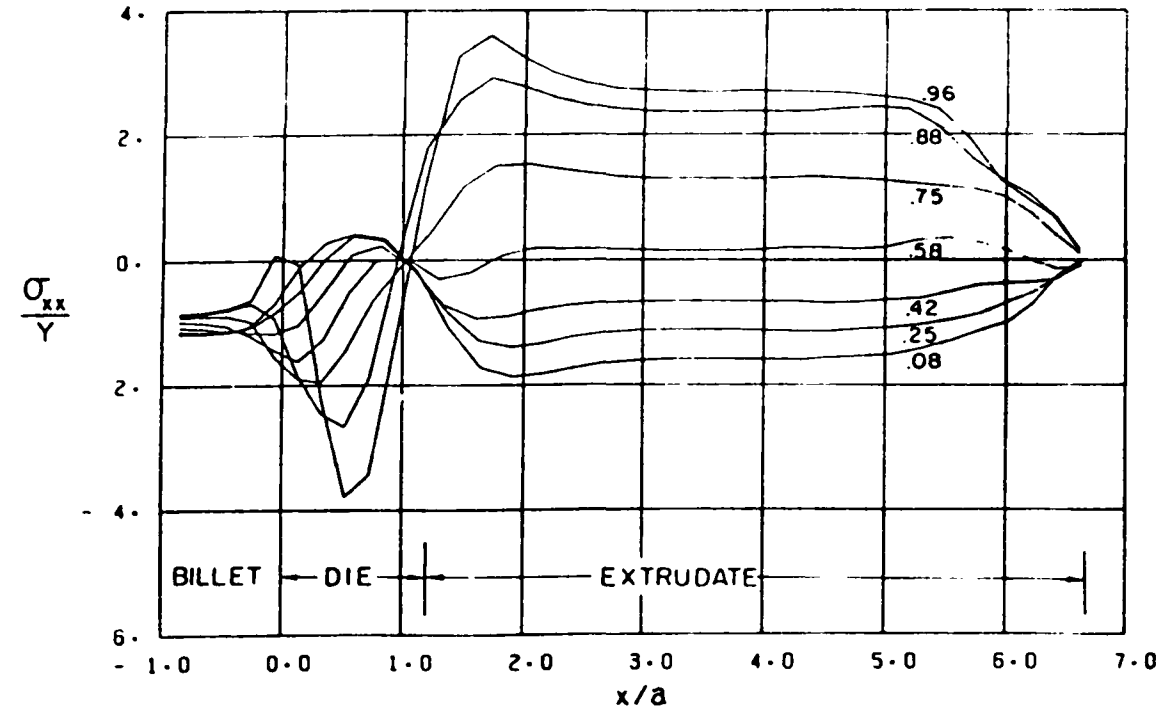

Longitudinal variation of normalized longitudinal stress at 7 lateral stations for frictionless plane strain extrusion with 25% thickness reduction.

FIG. 1.21

ELASTIC-PLASTIC FINITE-ELEMENT ANALYSIS OF PLANE-STRAIN FORWARD EXTRUSION (REF. 52)

1.4.1 Large-Strain Elastic-Plastic Formulations

The Prandtl-Reuss equations are, strictly, only defined for infinitesimal increments of deformation. When finite steps are used, the underlying assumption, that the strain increment may be decomposed into elastic and plastic parts, may no longer be valid (57-59), and any stress-strain relationship for finite increments should take into account the effect of the deforming continuum.

The latter problem has been investigated by Thomas (60-62), Prager (63), and more recently by Rice (64) and Lee (65). Various finite-element solutions based on large-strain formulations have been proposed, notably by Hibbitt, Marcal and Rice (66), Osias and Swedlow (67), Yamada, Wifi and Hirakawa (68), Mallett (69) and Nagtegaal and de Jong (70).

Although a finite-deformation technique is more complex than one using an infinitesimal definition of strain, Rice (64) has shown that use of the latter can lead to serious error during plastic deformations if the slope of the stress-strain curve is of the same order of magnitude as the current stress - a condition which is frequently met in forming operations. Consequently, a finite-deformation formulation is used in the program described in this thesis.

Lee and McMeeking (57) concluded that, although the decomposition of strain into elastic and plastic components is only an approximation for finite increments, the approximation is quite a good one providing the incremental strain is small. Since only small increments will be considered in the processes to be examined here, the formulation used in the present finite-element analysis does split strain into elastic and plastic parts.

1.5 THREE-DIMENSIONAL TREATMENTS

All the investigations mentioned so far have been of two-dimensional deformations, either plane-strain or axisymmetric. There have been few reports of three-dimensional finite-element analyses of large-scale deformation.

Webster (71) and Baynham (72) used a rigid-plastic and visco-plastic technique, respectively, to examine the forward extrusion of round stock through a square die. Sebastian, Rodriguez and Sanchez (73) also employed a visco-plastic treatment for the analysis of the extrusion of round bar through a tapered circular die. In all three cases the finite-element meshes were very coarse (fig. 1.22) and only the steady-state solutions were obtained.

A rigid-plastic analysis was also used by Mori and Osakada (74) to study three-dimensional rolling. This was not, strictly, a full three-dimensional approach since they used a modified eight-noded brick element, with fewer degrees of freedom, obtained by assuming that the axial velocity of the material was independent of position across the roll gap. A similar type of element was used by Sun, Li and Kobayashi (75) to examine the forging of a rectangular bar by flat, narrow dies which overlap the work-piece in the transverse direction.

Although the two last-mentioned analyses were able to predict the spread of the material during the deformation, the assumptions underlying the use of these simplified three-dimensional elements impose severe restrictions on the application of this technique.

Nagamatsu (76) obtained results for the simple upsetting of cubes using an elastic-plastic treatment, but only up to very small total strains.

Desai and Phan (56) developed a general three-dimensional finite-element procedure for the analysis of stress during

FIG. 1.22

THREE-DIMENSIONAL IDEALISATION OF EXTRUSION OF ROUND BILLET THROUGH A SQUARE DIE — BOUNDARY CONDITIONS (REF. 72)

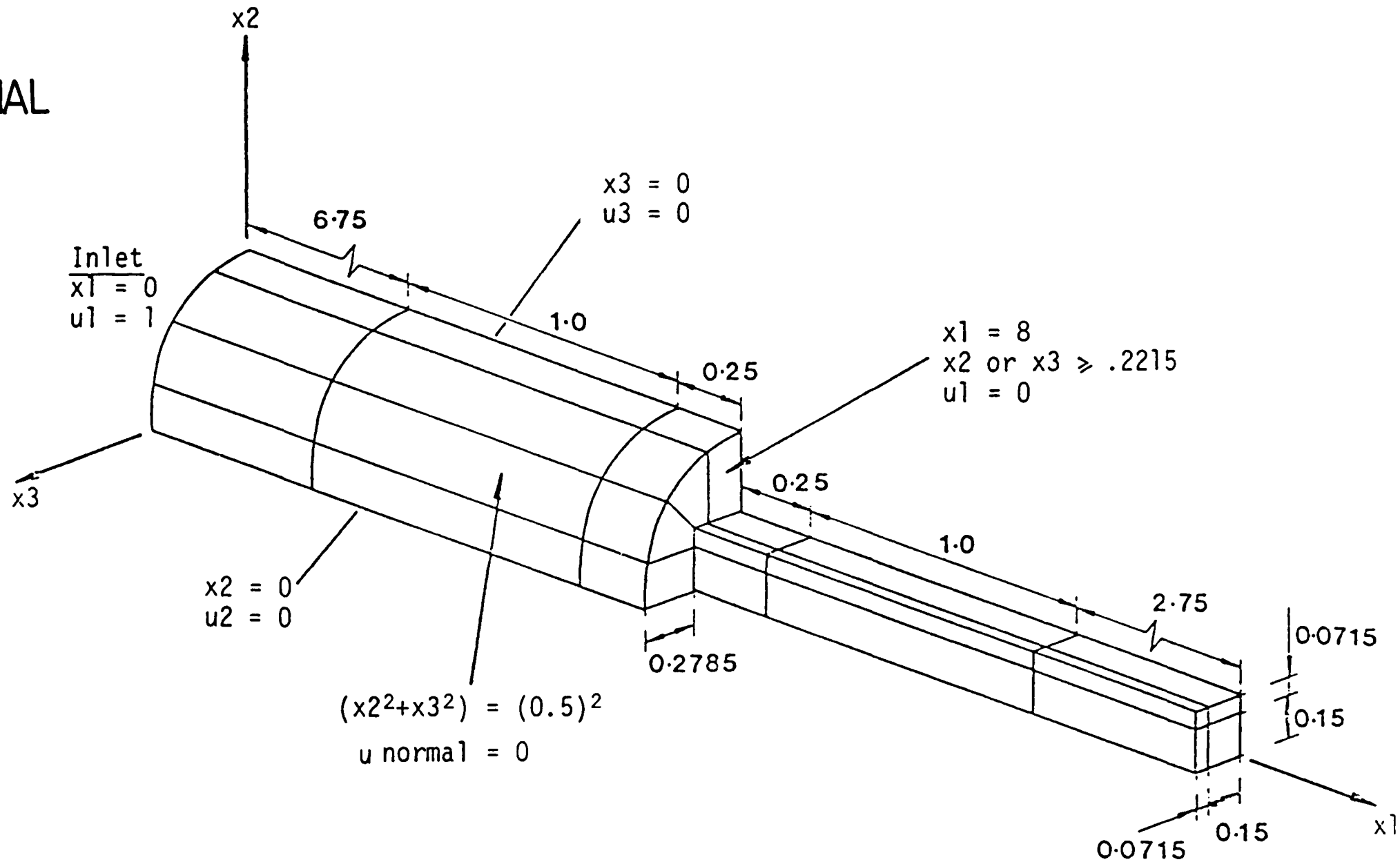

Mesh symmetric about line x2 = x3

u1, u2, and u3 = velocities in x1, x2, and x3 directions.

deformations involving large strain. Although primarily intended to study foundations and their interaction with soils, the authors state that the formulation can adopt an elastic-plastic approach for metal forming analyses.

CHAPTER TWO

THE FINITE-ELEMENT METHOD

2.0 INTRODUCTION

This chapter introduces the concepts and theory which form the basis of the finite-element formulation, developed here for the analysis of three-dimensional forging operations, and described in detail in the next chapter. It is not meant to be a comprehensive guide to the finite-element method or to its computer implementation, for which several texts are available. These cover the subject of both finite-element analysis in general (28,77,78) and its application to plasticity (79).

The fundamental matrix equations of finite-element analysis are derived in the following section, and their solution examined in section 2.2. The application of the method to plasticity is discussed in section 2.3, and, finally, consideration is given to the implications of a three-dimensional treatment.

2.1 INCREMENTAL STIFFNESS RELATIONSHIP

As its name implies, the finite-element analysis of deformation commences by dividing up the body into a finite number of discrete elements. The unknown displacements are approximated over each of these by continuous functions, interpolating between the actual values or gradients at certain points or nodes of the element. The number of nodes serves to determine the order of the interpolating function.

Elements may be of various types, such as triangles or quadrilaterals for two-dimensional analysis, tetrahedra or 'bricks' for three-dimensional treatments. The present analysis uses the three-dimensional, eight-node, linear-isoparametric element. The term

'linear-isoparametric' refers to the fact that the same, linear, order of interpolation is used both for displacements and for positional coordinates.

2.1.1 Governing Equations

2.1.1.1 Expression for Virtual Work

For the nth element of the body, the principle of virtual work (80) states that:

$$\Delta \underline{d}_n^{*T} \underline{f}_n = \int [Q^*]:[s]dvol \qquad (2.1)$$

for integration over the volume of the element, where $\Delta \underline{d}_n$ and $\underline{f}_n$ are the incremental displacement and the force vectors at the nodes of the element, [s] is the stress tensor at a point within the element and [Q] is the incremental-displacement gradient tensor defined by:

$$[Q] = \underline{\nabla}(\Delta \underline{u})^T \qquad (2.2)$$

in which $\underline{\nabla}$ is the gradient-operator vector:

$$\underline{\nabla} = \left(\frac{\delta}{\delta x} \quad \frac{\delta}{\delta y} \quad \frac{\delta}{\delta z}\right)^T \qquad (2.3)$$

and $\underline{u}$ is the vector of displacement of a point of the element with

coordinates (x,y,z) in the initial, reference state. Both displacement and coordinates are measured in the Cartesian reference frame. The operation : in eqn. 2.1 denotes the inner tensor-product (81) defined by:

$$[a]:[b] = a_{ij}b_{ij} \qquad (2.4)$$

with the usual tensor summation convention. The asterisks in eqn. 2.1 indicate that the expression must be true for any small, arbitrary nodal displacement and corresponding point displacement.

In addition to the Cartesian reference axes, another set of axes may be defined which deform with the material in the sense that a given point of the body will have the same coordinates with respect to these axes at all stages of the deformation. These axes, which in general will be curvilinear, will be referred to as the current frame.

Since the analysis is carried out incrementally, the initial, reference state is the state at the start of the increment. Assume that at this stage the distribution of stress in element n and the forces acting on its nodes satisfy eqn. 2.1. Suppose an infinitesimal increment of deformation causes a change in nodal force of $\Delta\underline{f}_n$ and a change in the distribution of stress of $[\Delta s]$, then since the values of nodal force and point stress must also satisfy eqn. 2.1 at the end of the deformation step, taking the difference between the two expressions gives:

$$\Delta\underline{d}^{*T}_n\Delta\underline{f}_n = \int [Q^*]:[\Delta s]\,dvol \qquad (2.5)$$

2.1.1.2 Use of Co-rotational Increment of Stress

In deriving eqn. 2.5, the integration in eqn. 2.1 is carried out, both for the beginning and for the end of the increment, over the geometry of the element at the start of the increment. Hence the stress [s] is defined by supposing that the forces which are actually applied to an infinitesimal element of the deformed body act on this element in its undeformed or reference state. [s] is therefore the nominal, Lagrange or Piola-Kirchhoff I stress, and is in general not symmetric (82).

In order to obtain a relationship between increments of nodal force and increments of nodal displacement, [Δs] must be expressed in terms of strain increment by means of the elastic-plastic constitutive equations. However, the appropriate stress to use in these constitutive equations is the Piola-Kirchhoff II stress (65) which is calculated by considering that the components, in the reference frame, of the force applied to an element of the body in its undeformed geometry are the same as the components, with respect to the current axes, of the force acting on the deformed element. Since the stress-strain relations are independent of rigid-body rotation, they must be expressed in terms of a co-rotational increment of this stress.

Finite-element analyses which use increments of nominal stress in the constitutive relations cannot accurately model the behaviour of stressed bodies during deformations in which the displacements of the material points are finite. This is demonstrated in appendix A where the changes in applied force calculated for the combined rotation and extension of a single element by two finite-element programs, one using the increment of nominal stress in the constitutive equations and the other using the co-rotational increment of Piola-Kirchhoff II stress, are compared with the actual changes in the components of force acting on the element.

The expressions relating increments of nominal stress and increments of Piola-Kirchhoff II stress at a point involve derivatives of the displacement at that point with respect to its current coordinates. In the following theory, the current state is chosen to be the reference state (updated Lagrangian technique) so that the derivatives of displacement in these expressions are with respect to the reference coordinates of the point.

In reference 65 it is shown that:

$$[\Delta s] = [\Delta\sigma] - [Q]^T[\sigma] \qquad (2.6)$$

where $[\sigma]$ is the true-or Cauchy-stress tensor with respect to the reference Cartesian axes and is defined in terms of the forces acting on an infinitesimal element of the body in its deformed state and the deformed geometry of that element.

Providing the reference and current axes are chosen to coincide at the start of the increment, the co-rotational increment of Piola-Kirchhoff II stress is the same as the Jaumann increment of Cauchy stress $[\Delta\sigma^J]$. This is defined (83) by:

$$[\Delta\sigma^J] = [\Delta\sigma] + \tfrac{1}{2}([Q]-[Q]^T)[\sigma] + \tfrac{1}{2}[\sigma]([Q]^T-[Q]) \qquad (2.7)$$

Substituting for $[\Delta\sigma]$ from eqn. 2.7 into eqn. 2.6 gives:

$$[\Delta s]' = [\Delta\sigma^J] - \tfrac{1}{2}([Q]-[Q]^T)[\sigma] - \tfrac{1}{2}[\sigma]([Q]^T-[Q]) - [Q]^T[\sigma]$$

$$= [\Delta\sigma^J] - \tfrac{1}{2}([Q]+[Q]^T)[\sigma] - \tfrac{1}{2}[\sigma]([Q]+[Q]^T) + [\sigma][Q] \qquad (2.8)$$

The finite-element formulation which expresses strain increment in terms of the Jaumann increment of Cauchy stress by means of the constitutive equations and which uses equation 2.8 to incorporate this stress into the virtual-work relationship, will be referred to throughout this thesis as using the Jaumann correction, to distinguish it from simple finite-element treatments which use $[\Delta s]$ directly in the stress-strain equations.

Taking the inner tensor-product of both sides of eqn. 2.8 with $[Q^*]$ and using the symmetry of the Cauchy stress tensors leads to:

$$[Q^*]:[\Delta s] = [Q^*]:[\Delta\sigma^J] - \tfrac{1}{2}[Q^*]:([Q]+[Q]^T)[\sigma] - \tfrac{1}{2}[Q^*]:[\sigma]([Q]+[Q]^T) + [Q^*]:[\sigma][Q]$$

$$= \tfrac{1}{2}([Q^*]+[Q^*]^T):[\Delta\sigma^J] - \tfrac{1}{2}[Q^*]^T:[\sigma]([Q]+[Q]^T) - \tfrac{1}{2}[Q^*]:[\sigma]([Q]+[Q]^T) + [Q^*]:[\sigma][Q]$$

$$= \tfrac{1}{2}([Q^*]+[Q^*]^T):([\Delta\sigma^J] - [\sigma]([Q]+[Q]^T)) + [Q^*]:[\sigma][Q] \qquad (2.9)$$

2.1.1.3 Finite-Strain Formulation

2.1.1.3.1 Co-rotational Increment of Strain

The theory presented so far has assumed that both the arbitrary change in the virtual displacement and the applied increment of the displacement are infinitesimally small. Under these circumstances, the expression for incremental strain (for this type of analysis the Lagrangian (83) or right Cauchy-Green (84) measure, defined by $([Q]+[Q]^T+[Q][Q]^T)/2$) may be simplified by omitting the second-order term $[Q][Q]^T/2$ to give the infinitesimal-strain increment $([Q]+[Q]^T)/2$ found in eqn 2.9.

In finite-element analyses of metal-forming problems, the material displacements, though small, are necessarily finite in magnitude. When this is the case, the infinitesimal expression is not an accurate measure of strain, particularly when the material is rotating. For example, infinitesimal strain is not zero for rigid-body rotation in which, by definition, no strain should occur. This is discussed further in appendix B.

If the finite-element formulation is to be used to examine finite increments of deformation, the terms representing infinitesimal-strain increment in eqn. 2.9 should, strictly, be replaced by the expressions for incremental Lagrangian strain. Unfortunately, it is not practicable to do this because Lagrangian strain is not a linear function of incremental-displacement gradients, and the resulting relationship between displacements and force would be very difficult to solve.

The method developed for the finite-element formulation described here effects a compromise solution to this problem by adopting a linear incremental-strain measure in eqn. 2.9 which, though not

precisely the same as the Lagrangian-strain increment, is a very good approximation to it for small, but finite, increments of deformation.

Providing the incremental strains are small, (of the order of a few percent), the error incurred in using infinitesimal strain generally derives not so much from the finite size of the strain increment itself (which causes an error of the order of the strain squared) but mostly from the presence of superimposed rotation, which may be large compared with the strain, and which introduces an erroneous volume component of strain. This is particularly significant when the deformation is plastic, since the change in the elastic hydrostatic stress calculated as a result may be orders of magnitude greater than the true, plastic increment of stress. In addition, when volume constancy is enforced, the tendency for rotation to be incorrectly interpreted as a volume change may lead to over-stiffness of the response to rotation.

The linear incremental strain mentioned above is therefore derived from a new incremental measure of strain which is independent of any superimposed rotation. This is called the <u>co-rotational increment of strain</u>.

By the definition of [Q] given earlier, the vector increment $d\underline{x}$ of reference-frame coordinates, representing an infinitesimal line segment, is transformed during an increment by:

$$d\underline{x} \rightarrow ([Q]^T+[I])d\underline{x} \qquad (2.10)$$

where [I] is the 3x3 identity matrix.

This transformation, which is clearly real, is also non-singular since we can define the inverse transformation. It may therefore be uniquely expressed as a product of a pure rotation [R] and a symmetric deformation [V] (85). [R] is shown in fig. 2.1, in which l_i, m_i, n_i are

the direction cosines of the rotated ith axis with respect to the initial, unrotated x, y and z axes.

Generally the product of rotation and deformation may be taken in either order, (leading to different values of [V]), but for a Lagrangian treatment, the deformation should be applied first because then the strain increment is calculated with respect to the reference frame. Therefore:

$$[R][V] = [Q]^T + [I] \qquad (2.11)$$

or

$$[V] = [R]^T([Q]^T + [I]) \qquad (2.12)$$

since the inverse of a rotational matrix is its transpose.

The co-rotational increment of strain $[\Delta\varepsilon^{cr}]$ is then defined to be:

$$[\Delta\varepsilon^{cr}] = [V] - [I] \qquad (2.13)$$

$[\Delta\varepsilon^{cr}]$ is clearly symmetric, and this strain measure reduces to the infinitesimal definition when there is no rotation (i.e. when [R] = [I]). It is also readily seen from eqns. 2.12 and 2.13 that when the deformation is a pure rotation, (i.e. when $[Q]^T = [R]$), the new strain increment is zero. By comparing eqn. 2.13 with the definition of incremental-Lagrangian strain given above, it can be seen that the co-rotational increment of strain differs from the Lagrangian measure by the term $([V]-[I])^2/2$ which, as mentioned previously, is of the order of the strain squared.

$$[R] = \begin{bmatrix} l_1 & l_2 & l_3 \\ m_1 & m_2 & m_3 \\ n_1 & n_2 & n_3 \end{bmatrix} \qquad [T_n] = \begin{bmatrix} 2\sigma_{xx} & 0 & 0 & \sigma_{xy} & 0 & \sigma_{zx} \\ & 2\sigma_{yy} & 0 & \sigma_{xy} & \sigma_{yz} & 0 \\ & & 2\sigma_{zz} & 0 & \sigma_{yz} & \sigma_{zx} \\ & & & \frac{1}{2}(\sigma_{xx}+\sigma_{yy}) & \frac{1}{2}\sigma_{zx} & \frac{1}{2}\sigma_{yz} \\ & \text{SYM} & & & \frac{1}{2}(\sigma_{yy}+\sigma_{zz}) & \frac{1}{2}\sigma_{xy} \\ & & & & & \frac{1}{2}(\sigma_{zz}+\sigma_{xx}) \end{bmatrix}$$

$$[U_n] = \begin{bmatrix} \sigma_{xx} & \sigma_{xy} & \sigma_{zx} & 0 & 0 & 0 & 0 & 0 & 0 \\ & \sigma_{yy} & \sigma_{yz} & 0 & 0 & 0 & 0 & 0 & 0 \\ & & \sigma_{zz} & 0 & 0 & 0 & 0 & 0 & 0 \\ & & & \sigma_{xx} & \sigma_{xy} & \sigma_{zx} & 0 & 0 & 0 \\ & & & & \sigma_{yy} & \sigma_{yz} & 0 & 0 & 0 \\ & & & & & \sigma_{zz} & 0 & 0 & 0 \\ & \text{SYM} & & & & & \sigma_{xx} & \sigma_{xy} & \sigma_{zx} \\ & & & & & & & \sigma_{yy} & \sigma_{yz} \\ & & & & & & & & \sigma_{zz} \end{bmatrix} \qquad \Delta\underline{q} = \begin{bmatrix} \frac{\delta \Delta u_x}{\delta x} \\ \frac{\delta \Delta u_x}{\delta y} \\ \frac{\delta \Delta u_x}{\delta z} \\ \frac{\delta \Delta u_y}{\delta x} \\ \frac{\delta \Delta u_y}{\delta y} \\ \frac{\delta \Delta u_y}{\delta z} \\ \frac{\delta \Delta u_z}{\delta x} \\ \frac{\delta \Delta u_z}{\delta y} \\ \frac{\delta \Delta u_z}{\delta z} \end{bmatrix}$$

FIG. 2.1

VECTORS AND MATRICES USED IN VIRTUAL-WORK FORMULATION

2.1.1.3.2 Linearised Co-rotational Strain

Since the rotational matrix [R] is a function of [Q], the co-rotational increment of strain defined by eqns. 2.12 and 2.13 is a non-linear function of incremental-displacement gradients and so cannot be used directly in the expression for virtual-work.

However, a linearised form of this strain can be easily derived providing the incremental rotation of the material is of the order of ten degrees or less and the incremental strain is of the order of one or two percent. Since the finite-element analyses are carried out in small steps, these are reasonable assumptions to make. Note, these assumptions do not make the use of co-rotational strain unnecessary since the rotational component of the deformation may still be an order of magnitude larger than the strain.

Since the co-rotational increment of strain is symmetric, no loss of generality is involved in taking, for convenience, the symmetric part of eqn. 2.13 as the starting point for the process of linearisation.

Substituting eqn. 2.12 into this expression and multiplying out leads to:

$$[\Delta\varepsilon^{cr}] = 0.5([R]^T[Q]^T + [Q][R] + [R]^T + [R] - 2[I])$$
$$= 0.5([R]^T[Q]^T + [Q][R] - ([R]-[I])([R]^T-[I]) \qquad (2.14)$$

For the limit of the incremental angles of rotation stated above, [R]-[I] is approximately skew-symmetric to within a few percent and may be replaced in eqn. 2.14 by $0.5([R]-[R]^T)$. Hence:

$$[\Delta\varepsilon^{cr}] \simeq 0.5([R]^T[Q]^T + [Q][R] - 0.25([R]-[R]^T)([R]^T-[R]) \qquad (2.15)$$

For incremental strains of the order of 0.01 or less $[R]-[R]^T \simeq [Q]^T-[Q]$, so:

$$[\Delta\varepsilon] = 0.5([R]^T[Q]^T + [Q][R] - 0.125(([R]-[R]^T)([Q]-[Q]^T)+([Q]^T-[Q])([R]^T-[R]))) \quad (2.16)$$

In which the last product term of eqn. 2.15 has been averaged with its transpose to preserve the symmetry of the expression after this last substitution.

The quantity $[\Delta\varepsilon]$ defined by eqn. 2.16 is called the linearised co-rotational (LCR) increment of strain because, once the coefficients of [R] have been evaluated, it is a linear function of the incremental-displacement gradients. It can therefore be used to replace the expressions for infinitesimal increment of strain in eqn. 2.9.

The matrix [R] is a function of position but for the present analysis it is assumed that an average rotational matrix can be applied to all points of a given element.

2.1.1.3.3 Estimation of Rotational Values

Before eqn. 2.16 can be used in the virtual-work expression, the coefficients of the matrix [R] must be evaluated. The correct values for a given increment are not known until that increment is actually performed and the nodal displacements calculated. However, it is possible to estimate the rotational coefficients if it is assumed that the matrix [R] for a given element does not change greatly from one

increment to the next. The rotational coefficients may then be calculated from the incremental-displacement gradients for the previous increment (section 3.2.4.1). For the first increment of the deformation, [R] is assumed to be equal to the identity matrix. When the secant-modulus technique is used (see section 3.2.3.2), then during the second or corrector part of the solution, [R] is evaluated from the incremental-displacement gradients for the first or predictor part.

Although this method will not in general predict the exact rotational component of the current deformation, it is shown in appendix B that even so, the use of the LCR incremental strain measure with estimated rotational coefficients leads to better results than if the rotation is ignored altogether.

2.1.1.4 Vector Expression

Replacing the expression for infinitesimal increment of strain in eqn. 2.9 by the linearised co-rotational increment of strain gives:

$$[Q^*]:[\Delta s] = [\Delta\varepsilon^*]:([\Delta\sigma^J]-2[\sigma][\Delta\varepsilon]) + [Q^*]:[\sigma][Q] \qquad (2.17)$$

It is convenient to express the right-hand side of eqn. 2.17 in its vector form, in which the symmetric tensors of incremental strain and stress are replaced by six-dimensional column vectors and the incremental-displacement gradient tensors are replaced by nine-dimensional vectors. Eqn. 2.17 then becomes:

$$[Q^*]:[\Delta s] = \Delta\underline{\varepsilon}^{*T}(\Delta\underline{\sigma}^J-[T_n]\Delta\underline{\varepsilon}) + \Delta\underline{q}^{*T}[U_n]\Delta\underline{q} \qquad (2.18)$$

where $\Delta\underline{\varepsilon}$ is the vector of the LCR increment of strain, $\Delta\underline{\sigma}^J$ is the corresponding Cartesian vector of the Jaumann increment of Cauchy stress and $\Delta\underline{q}$ is the vector gradient of incremental displacement. $\Delta\underline{q}$ and the matrices $[T_n]$ and $[U_n]$ are shown in fig. 2.1. As before, the asterisks in eqn. 2.18 refer to corresponding, small, arbitrary increments of displacement or strain. The expression for $\Delta\underline{\varepsilon}$, derived from eqn. 2.16, is given in fig. 2.2.

If $[D_n]$ is the appropriate incremental 6x6 stress-strain matrix for this element then eqn. 2.15 may be written as:

$$[Q^*]:[\Delta s] = \Delta\underline{\varepsilon}^{*T}([D_n]-[T_n])\Delta\underline{\varepsilon} + \Delta\underline{q}^{*T}[U_n]\Delta\underline{q} \qquad (2.19)$$

$$\Delta\underline{\varepsilon} = \begin{bmatrix}
l_1\frac{\delta\Delta u_x}{\delta x} + (\frac{m_1-l_2}{8})\frac{\delta\Delta u_x}{\delta y} + (\frac{n_1-l_3}{8})\frac{\delta\Delta u_x}{\delta z} + (\frac{7m_1+l_2}{8})\frac{\delta\Delta u_y}{\delta x} + (\frac{7n_1+l_3}{8})\frac{\delta\Delta u_z}{\delta x} \\
(\frac{7l_2+m_1}{8})\frac{\delta\Delta u_x}{\delta y} + (\frac{l_2-m_1}{8})\frac{\delta\Delta u_y}{\delta x} + m_2\frac{\delta\Delta u_y}{\delta y} + (\frac{n_2-m_3}{8})\frac{\delta\Delta u_y}{\delta z} + (\frac{7n_2+m_3}{8})\frac{\delta\Delta u_z}{\delta y} \\
(\frac{7l_3+n_1}{8})\frac{\delta\Delta u_x}{\delta z} + (\frac{7m_3+n_2}{8})\frac{\delta\Delta u_y}{\delta z} + (\frac{l_3-n_1}{8})\frac{\delta\Delta u_z}{\delta x} + (\frac{m_3-n_2}{8})\frac{\delta\Delta u_z}{\delta y} + n_3\frac{\delta\Delta u_z}{\delta z} \\
l_2\frac{\delta\Delta u_x}{\delta x} + l_1\frac{\delta\Delta u_x}{\delta y} + (\frac{n_2-m_3}{8})\frac{\delta\Delta u_x}{\delta z} + m_2\frac{\delta\Delta u_y}{\delta x} + m_1\frac{\delta\Delta u_y}{\delta y} + (\frac{n_1-l_3}{8})\frac{\delta\Delta u_y}{\delta z} + (\frac{7n_2+m_3}{8})\frac{\delta\Delta u_z}{\delta x} + (\frac{7n_1+l_3}{8})\frac{\delta\Delta u_z}{\delta y} \\
(\frac{7l_3+n_1}{8})\frac{\delta\Delta u_x}{\delta y} + (\frac{7l_2+m_1}{8})\frac{\delta\Delta u_x}{\delta z} + (\frac{l_3-n_1}{8})\frac{\delta\Delta u_y}{\delta x} + m_3\frac{\delta\Delta u_y}{\delta y} + m_2\frac{\delta\Delta u_y}{\delta z} + (\frac{l_2-m_1}{8})\frac{\delta\Delta u_z}{\delta x} + n_3\frac{\delta\Delta u_z}{\delta y} + n_2\frac{\delta\Delta u_z}{\delta z} \\
l_3\frac{\delta\Delta u_x}{\delta x} + (\frac{m_3-n_2}{8})\frac{\delta\Delta u_x}{\delta y} + l_1\frac{\delta\Delta u_x}{\delta z} + (\frac{7m_3+n_2}{8})\frac{\delta\Delta u_y}{\delta x} + (\frac{7m_1+l_2}{8})\frac{\delta\Delta u_y}{\delta z} + n_3\frac{\delta\Delta u_z}{\delta x} + (\frac{m_1-l_2}{8})\frac{\delta\Delta u_z}{\delta y} + n_1\frac{\delta\Delta u_z}{\delta z}
\end{bmatrix}$$

FIG. 2.2

VECTOR OF LINEAR FORM OF CO-ROTATIONAL INCREMENT OF STRAIN

2.1.1.5 Constant-Dilatation Technique

As mentioned later in section 3.2.5, the volume of the yielded finite-element mesh must be explicitly constrained to be approximately constant. A convenient way of doing this is to increase the contribution of the bulk-strain changes of yielded elements to the virtual-work expression (34), the effect of which is to tend to enforce incompressibility at every point of the body. Nagtegaal, Parks and Rice (86) demonstrate that, for most types of element, this results in far too many constraints being applied to the nodal displacements, leading to excessive predicted loads and general over-stiffness of behaviour (70).

For example, for the eight-node brick element used here, the requirement that the bulk strain is zero throughout an element means that the nodal displacements associated with that element have to satisfy seven constraining equations. In the limit, as discretisation is refined, the number of nodes in the mesh equals the number of elements. Since there are three degrees of freedom per node this gives a ratio of no. of degrees of freedom/no. of constraints equal to 3/7. However, for a continuum, there are three degrees of freedom and one incompressibility constraint at every point of the material, so with a large number of elements, the finite-element model is clearly over-constrained. (This is not the case with a small number of elements; a single element has 24 degrees of freedom and only 7 incompressibility constraints.)

The solution to this problem proposed by Nagtegaal et al for the eight-node brick element, and the one adopted here, is to relax the requirement that the bulk strain is zero at every point of an element and only require that the total volume of an element is (approximately) constant. The seven incompressiblity constraints per

element are then replaced by just one, and the ratio of no. of degrees of freedom/no. of constraints for progressively refined meshes tends to the continuum value of three.

This technique is referred to as the constant-dilatation method since the dilatation (or average value of bulk strain for an element) is the same for all points of an element.

Consider the contribution of deformation of the material to the virtual-work expression and split this into deviatoric and bulk parts:

$$\Delta\underline{\varepsilon}^{*T}[D_n]\Delta\underline{\varepsilon} = \Delta\underline{\varepsilon}'^{*T}[D_n]\Delta\underline{\varepsilon}' + \tfrac{1}{3}\Delta\hat{\underline{\varepsilon}}^{*T}[D_n]\Delta\underline{\varepsilon}' + \tfrac{1}{3}\Delta\underline{\varepsilon}'^{*T}[D_n]\Delta\hat{\underline{\varepsilon}} + \tfrac{1}{9}\Delta\hat{\underline{\varepsilon}}^{*T}[D_n]\Delta\hat{\underline{\varepsilon}} \qquad (2.20)$$

where: $$\Delta\underline{\varepsilon}' = \Delta\underline{\varepsilon} - \tfrac{1}{3}\Delta\hat{\underline{\varepsilon}} \qquad (2.21A)$$

$$\Delta\hat{\underline{\varepsilon}} = (\Delta\varepsilon_b \; \Delta\varepsilon_b \; \Delta\varepsilon_b \; 0 \; 0 \; 0)^T \qquad (2.21B)$$

$$\Delta\varepsilon_b = \Delta\varepsilon_{xx} + \Delta\varepsilon_{yy} + \Delta\varepsilon_{zz} \qquad (2.21C)$$

The elastic-plastic stress-strain matrix $[D_n]$ will be defined later, but it is sufficient here to note the following properties of this matrix:

(1) it is symmetric (because the material is assumed to be isotropic),

(2) the sum of the first three entries in any of rows 1 to 3 is constant and equal to 3κ, where κ, the bulk modulus = $E/3(1-2\nu)$ for Young's modulus E and Poisson's ratio ν (because any bulk-strain change causes the same purely elastic response in all three normal components of stress),

(3) the sum of the first three entries in any of rows 4 to 6 is zero

(because bulk strain cannot influence shear components of stress).

Thus the second and third terms on the right-hand side of eqn. 2.20 disappear leaving:

$$\Delta\underline{\varepsilon}^{*T}[D_n]\Delta\underline{\varepsilon} = \Delta\underline{\varepsilon}'^{*T}[D_n]\Delta\underline{\varepsilon}' + \kappa\Delta\varepsilon_b^*\Delta\varepsilon_b \qquad (2.22)$$

in which the work contribution is separated into purely deviatoric and purely bulk parts. If the second of these is expressed in terms of the average bulk-strain increment for element n, the dilatation increment $\Delta\phi_n$ where:

$$\Delta\phi_n = \frac{1}{V_n}\int \Delta\varepsilon_b \, dvol \qquad (2.23)$$

and V_n is the volume of element n, then the contribution of deformation to the work expression in terms of the modified strain increment $\Delta\underline{\varepsilon}^{cd}$ is:

$$\Delta\underline{\varepsilon}^{cd*T}[D_n]\Delta\underline{\varepsilon} = \Delta\underline{\varepsilon}'^{*T}[D_n]\Delta\underline{\varepsilon}' + \kappa\Delta\phi_n^*\Delta\phi_n$$

$$= \Delta\underline{\varepsilon}^{*T}[D_n]\Delta\underline{\varepsilon} + \kappa(\Delta\phi_n^*\Delta\phi_n - \Delta\varepsilon_b^*\Delta\varepsilon_b) \qquad (2.24)$$

Using this modified contribution in eqn. 2.16 then gives:

$$[Q^*]:[\Delta s] = \Delta\underline{\varepsilon}^{*T}([D_n]-[T_n])\Delta\underline{\varepsilon} + \Delta\underline{q}^T[U_n]\Delta\underline{q}$$
$$+ \kappa(\Delta\phi_n^*\Delta\phi_n - \Delta\varepsilon_b^*\Delta\varepsilon_b) \qquad (2.25)$$

2.1.1.6 Virtual Work in Terms of Generalised Displacement

The expression in eqn. 2.25 represents the infinitesimal contribution to virtual work from an arbitrary point of element n. In order to use the interpolation functions for the element, this must be re-written in terms of the generalised displacement of a point $\Delta\underline{u}$.

From the expression for $\Delta\underline{\varepsilon}$ given in fig. 2.2, we may write:

$$\Delta\underline{\varepsilon} = [L_n^{\varepsilon}]\Delta\underline{u} \qquad (2.26)$$

where the operator matrix $[L_n^{\varepsilon}]$ is illustrated in fig. 2.3. This operator is a function of the previously determined values of l_i, m_i and n_i which will be different for each element - hence the subscript n. Similarly, the expression for $\Delta\underline{q}$ in fig. 2.1 gives:

$$\Delta\underline{q} = [L^q]\Delta\underline{u} \qquad (2.27)$$

where the operator matrix $[L^q]$ is shown in fig. 2.3.

Combination of eqn. 2.21C and the definition of $[L_n^{\varepsilon}]$ leads to:

$$\Delta\varepsilon_b = [L_n^b]\Delta\underline{u} \qquad (2.28)$$

The operator matrix $[L_n^b]$ for element n is also illustrated in fig. 2.3. Finally, eqns. 2.23 and 2.28 give:

$$\Delta\phi_n = [L_n^{\phi}]\Delta\underline{u} \qquad (2.29)$$

where the operator matrix $[L_n^{\phi}]$ is defined to be:

$$[L_n^{\phi}] = \frac{1}{V_n}\int [L_n^b]\mathrm{dvol} \qquad (2.30)$$

$$[L_n^{\varepsilon}] = \begin{bmatrix}
(l_1\frac{\delta}{\delta x} + (\frac{m_1-l_2}{8})\frac{\delta}{\delta y} + (\frac{n_1-l_3}{8})\frac{\delta}{\delta z}) & (\frac{7m_1+l_2}{8})\frac{\delta}{\delta x} & (\frac{7n_1+l_3}{8})\frac{\delta}{\delta x} \\
(\frac{7l_2+m_1}{8})\frac{\delta}{\delta y} & ((\frac{l_2-m_1}{8})\frac{\delta}{\delta x} + m_2\frac{\delta}{\delta y} + (\frac{n_2-m_3}{8})\frac{\delta}{\delta z}) & (\frac{7n_2+m_3}{8})\frac{\delta}{\delta y} \\
(\frac{7l_3+n_1}{8})\frac{\delta}{\delta z} & (\frac{7m_3+n_2}{8})\frac{\delta}{\delta z} & ((\frac{l_3-n_1}{8})\frac{\delta}{\delta x} + (\frac{m_3-n_2}{8})\frac{\delta}{\delta y} + n_3\frac{\delta}{\delta z}) \\
(l_2\frac{\delta}{\delta x} + l_1\frac{\delta}{\delta y} + (\frac{n_2-m_3}{8})\frac{\delta}{\delta z}) & (m_2\frac{\delta}{\delta x} + m_1\frac{\delta}{\delta y} + (\frac{n_1-l_3}{8})\frac{\delta}{\delta z}) & ((\frac{7n_2+m_3}{8})\frac{\delta}{\delta x} + (\frac{7n_1+l_3}{8})\frac{\delta}{\delta y}) \\
((\frac{7l_3+n_1}{8})\frac{\delta}{\delta y} + (\frac{7l_2+m_1}{8})\frac{\delta}{\delta z}) & ((\frac{l_3-n_1}{8})\frac{\delta}{\delta x} + m_3\frac{\delta}{\delta y} + m_2\frac{\delta}{\delta z}) & ((\frac{l_2-m_1}{8})\frac{\delta}{\delta x} + n_3\frac{\delta}{\delta y} + n_2\frac{\delta}{\delta z}) \\
(l_3\frac{\delta}{\delta x} + (\frac{m_3-n_2}{8})\frac{\delta}{\delta y} + l_1\frac{\delta}{\delta z}) & ((\frac{7m_3+n_2}{8})\frac{\delta}{\delta x} + (\frac{7m_1+l_2}{8})\frac{\delta}{\delta z}) & (n_3\frac{\delta}{\delta x} + (\frac{m_1-l_2}{8})\frac{\delta}{\delta y} + n_1\frac{\delta}{\delta z})
\end{bmatrix}$$

$$[L^q] = \begin{bmatrix}
\frac{\delta}{\delta x} & 0 & 0 \\
\frac{\delta}{\delta y} & 0 & 0 \\
\frac{\delta}{\delta z} & 0 & 0 \\
0 & \frac{\delta}{\delta x} & 0 \\
0 & \frac{\delta}{\delta y} & 0 \\
0 & \frac{\delta}{\delta z} & 0 \\
0 & 0 & \frac{\delta}{\delta x} \\
0 & 0 & \frac{\delta}{\delta y} \\
0 & 0 & \frac{\delta}{\delta z}
\end{bmatrix}$$

$$[L_n^b]^T = \begin{bmatrix}
l_1\frac{\delta}{\delta x} + (\frac{3l_2+m_1}{4})\frac{\delta}{\delta y} + (\frac{3l_3+n_1}{4})\frac{\delta}{\delta z} \\
(\frac{3m_1+l_2}{4})\frac{\delta}{\delta x} + m_2\frac{\delta}{\delta y} + (\frac{3m_3+n_2}{4})\frac{\delta}{\delta z} \\
(\frac{3n_1+l_3}{4})\frac{\delta}{\delta x} + (\frac{3n_2+m_3}{4})\frac{\delta}{\delta y} + n_3\frac{\delta}{\delta z}
\end{bmatrix}$$

FIG. 2.3

DIFFERENTIAL – OPERATOR MATRICES

2.1.2 Finite-Element Interpolation

Let a local axis system, X, Y and Z be defined for each element so that the local coordinates of the nodes of the element are $(\pm 1, \pm 1, \pm 1)$. A typical element is shown in fig. 2.4 with its associated local axes and the local coordinates of the nodes.

Consider the nth element in the assembly or mesh. Let $\underline{x}_n$ be the vector of global coordinates at all the nodes of the element and let $\underline{x}$ be the coordinate vector of a point within the element with respect to the Cartesian axes.

Define for each node I of the element, an interpolating or shape function of local coordinates:

$$N_I = \tfrac{1}{8}ijk(X+i)(Y+j)(Z+k), \quad I = 4+2i+j+(k+1)/2 \qquad (2.31)$$

for $i,j,k = \pm 1$.

This has the property of attaining the value one at node I, zero at all the other nodes, and varying linearly (with respect to local coordinates) between any two adjacent nodes.

Therefore, the assumed function for displacement takes the form:

$$\underline{u} = [N_n]\underline{d}_n \qquad (2.32)$$

where $[N_n] = (N_1[I] \quad N_2[I] \quad \ldots \quad N_8[I])$. Substituting from eqn. 2.32 into eqns. 2.26 to 2.29 gives:

$$\Delta\underline{\varepsilon} = [B_n^{\varepsilon}]\,\underline{d}_n \qquad (2.33)$$

$$\Delta\underline{q} = [B_n^{q}]\,\underline{d}_n \qquad (2.34)$$

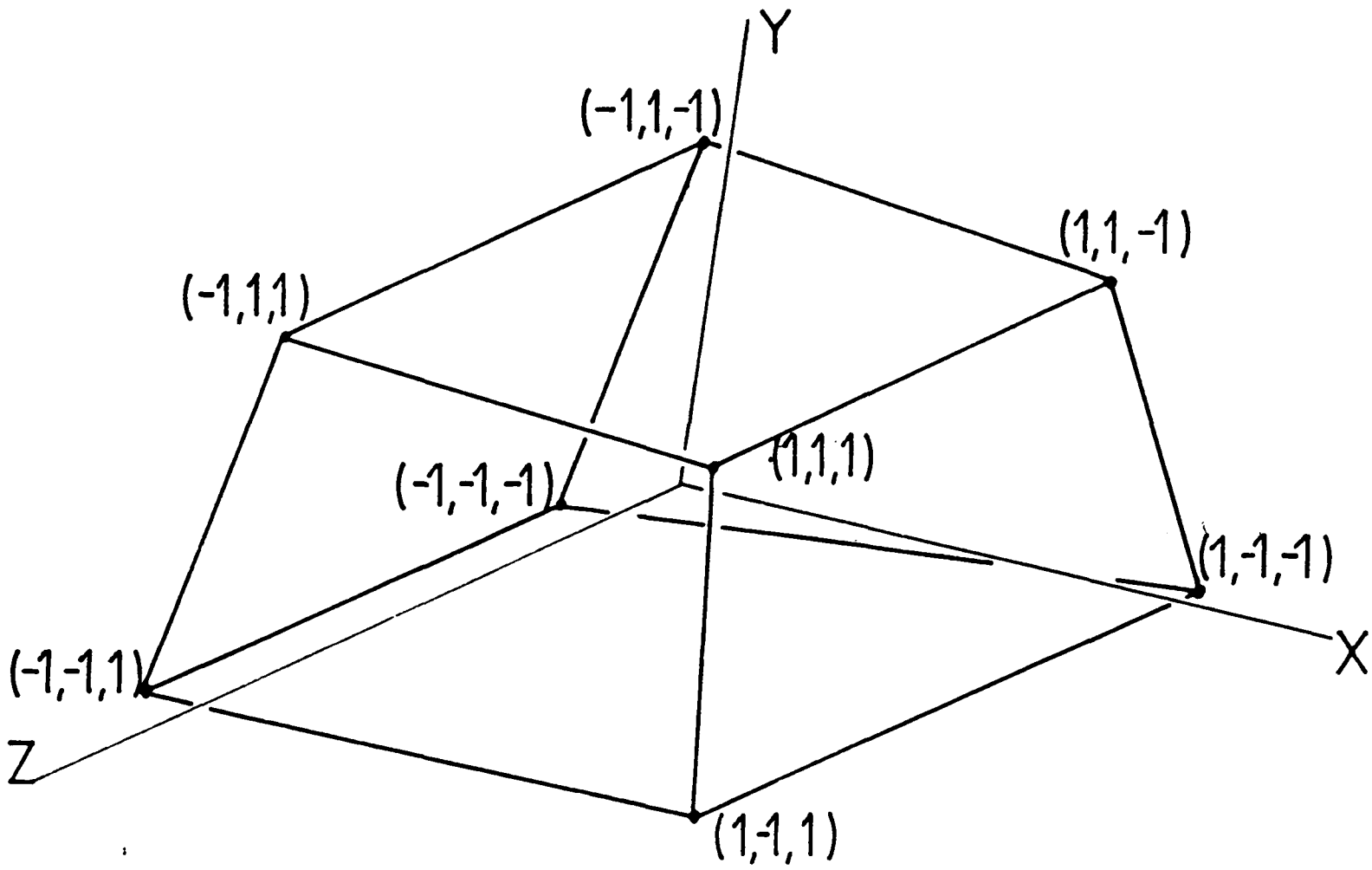

FIG. 2.4

THREE-DIMENSIONAL, EIGHT-NODE ELEMENT WITH LOCAL AXES

$$\Delta\varepsilon_b = [B_n^b]\Delta\underline{d}_n \tag{2.35}$$

$$\Delta\phi_n = [B_n^\phi]\Delta\underline{d}_n \tag{2.36}$$

where:

$[B_n^\varepsilon] = [L_n^\varepsilon][N_n]$ is the strain-nodal displacement matrix

$[B_n^q] = [L^q][N_n]$ is the displacement gradient-nodal displacement matrix

$[B_n^b] = [L_n^b][N_n]$ is the bulk strain-nodal displacement matrix and

$[B_n^\phi] = [L_n^\phi][N_n]$ is the dilatation-nodal displacement matrix.

All four of these matrices depend on the geometry of element n; all except $[B_n^q]$ also depend on the current value of [R] for this element and all except $[B_n^\phi]$ are functions of position within the element.

In order to evaluate $[B_n^\varepsilon]$, $[B_n^q]$, $[B_n^b]$ and $[B_n^\phi]$ the derivatives with respect to the global coordinates must be expressed in terms of derivatives in the local axis system by means of the inverse of the Jacobian transformation matrix $[J_n]$, where:

$$[J_n] = \begin{bmatrix} \frac{\delta}{\delta X} \\ \frac{\delta}{\delta Y} \\ \frac{\delta}{\delta Z} \end{bmatrix} . \underline{x}^T \quad \text{and} \quad \begin{bmatrix} \frac{\delta}{\delta x} \\ \frac{\delta}{\delta y} \\ \frac{\delta}{\delta z} \end{bmatrix} = [J_n]^{-1} \begin{bmatrix} \frac{\delta}{\delta X} \\ \frac{\delta}{\delta Y} \\ \frac{\delta}{\delta Z} \end{bmatrix} \tag{2.37}$$

Using the shape functions, once again, to determine the global

coordinates of a point as a function of the local coordinates of that point, and the known, global coordinates of the nodes:

$$[J_n] = \begin{bmatrix} \underline{x}_n^T \dfrac{\delta[N_n]^T}{\delta X} \\ \underline{x}_n^T \dfrac{\delta[N_n]^T}{\delta Y} \\ \underline{x}_n^T \dfrac{\delta[N_n]^T}{\delta Z} \end{bmatrix} \qquad (2.38)$$

The local derivatives of the shape functions may be obtained easily from eqn. 2.31.

Substituting from eqns. 2.33 to 2.36 into eqn. 2.25:

$$[Q^*]:[\Delta s] = \underline{\Delta d}_n^{*T}([B_n^{\varepsilon}]^T([D_n]-[T_n])[B_n^{\varepsilon}] + [B_n^q]^T[U_n][B_n^q] + \kappa([B_n^{\phi}]^T[B_n^{\phi}]-[B_n^b]^T[B_n^b]))\,\underline{\Delta d}_n \qquad (2.39)$$

Inserting this into eqn. 2.5, removing the nodal displacement vectors outside the volume integral and cancelling $\underline{\Delta d}^*$ produces:

$$\underline{\Delta f}_n = (\int[B_n^{\varepsilon}]^T([D_n]-[T_n])[B_n^{\varepsilon}] + [B_n^q]^T[U_n][B_n^q] + \kappa([B_n^{\phi}]^T[B_n^{\phi}]-[B_n^b]^T[B_n^b])\,dvol)\,\underline{\Delta d}_n \qquad (2.40)$$

This integral does not, in general, permit an analytical solution. Multiplying the integrand of the above by the determinant of the Jacobian matrix means the integration is carried out over the volume of the element in the local axis system. This allows Gaussian quadrature (108) to be used to evaluate this integral. Since $[B_n^{\phi}]$ is independent of position, it may be taken outside the integral and also evaluated by means of Gaussian quadrature and eqn. 2.30. Hence:

$$\Delta \underline{f}_n = [K_n]\Delta \underline{d}_n \qquad (2.41)$$

where:

$$[K_n] = \Sigma w_i \{([B_n^\varepsilon]^T([D_n]-[T_n])[B_n^\varepsilon]+[B_n^q]^T[U_n][B_n^q]- \kappa[B_n^b]^T[B_n^b])|J_n|\}$$
$$+ \frac{\kappa}{V_n} \Sigma w_i \{[B_n^b]^T|J_n|\} \Sigma w_i \{[B_n^b]|J_n|\} \qquad (2.42)$$

in which the expressions inside the braces are evaluated for the local coordinates of sample point i, and w_i is the corresponding Gaussian weighting factor.

Since the integrands of $[K_n]$ are generally rational functions, the numerical integration can never be exact, but will approach the true value as the number of sample points is increased. This is at the expense of increased computational time, and in practice only a small number of sample points are required to obtain sufficient accuracy.

Eqns. 2.41 and 2.42 are valid for an isolated element. To find the stiffness matrix relating the nodal displacement increments to the nodal force increments for a collection of elements, the individual element matrices are simply superposed or <u>assembled</u>. By this method, a coefficient in the final matrix relating displacement component j to force component i, is the sum of all such coefficients in the constituent element matrices.

The assembled stiffness relationship takes the form:

$$\Delta \underline{f} = [K]\Delta \underline{d} \qquad (2.43)$$

where $\Delta \underline{f}$ and $\Delta \underline{d}$ are the vectors of nodal increments in force and displacement, [K] is the <u>(global) stiffness matrix</u>.

2.2 SOLUTION OF INCREMENTAL STIFFNESS EQUATIONS

The type of finite-element analysis presented here is known as the displacement formulation because, for the most part, the increments in displacement are the unknown quantities in the problem. (The values of nodal displacement may of course be specified for certain boundaries.)

Therefore, eqn. 2.43 must be solved in order to determine $\Delta\underline{d}$ for an increment of deformation. Before considering the method adopted for this purpose, certain properties of the matrix [K] should be mentioned.

Firstly, [K] is symmetric. This is a consequence of the symmetry of the D, T and U matrices used in the formulation. As a result, and if care is taken in its manipulation, only the half of the matrix above (or below) the leading diagonal need be computed or stored.

The second property, which leads to even greater economies of storage, is that providing the nodes of the mesh are ordered in a particular way in the displacement and force vectors, then the coefficients of the stiffness matrix are zero everywhere except within a band lying about the leading diagonal. These zero values need not be stored. The number of coefficients lying within this band, for any given row, is known as the bandwidth of the matrix.

The property of bandedness derives from the fact that the force at a given node depends upon the displacements at another node only if these two nodes belong to the same element. The optimum ordering of nodes therefore minimises the separation, in the ordering sequence, of any two nodes which affect each other in this way.

The solution of eqn. 2.43 is obtained by a modification of the method of Gaussian elimination and back-substitution. Firstly, consider the Gaussian method in its usual form.

During the elimination stage, the matrix is converted into upper-

triangular form (zeros everywhere below the leading diagonal) in a way which preserves the relationships expressed by the original equations. The transformed or reduced set of equations can be solved quite simply during the back-substitution phase by considering each equation in turn, from the bottom of the matrix up, substituting in all the displacement increments calculated so far, and hence evaluating the displacement component on the diagonal from the remaining load term on the right-hand side of the equation.

Fig. 2.5 is a diagrammatic representation of the elimination process, when only the upper band of the matrix is stored (shaded portion). Fig. 2.5a shows the stiffness equations at a stage in the elimination when all the columns in the lower triangle up to but not including column i have been made zero. By symmetry, the coefficient k_{ij} in row i of the matrix indicates that there is the same coefficient in column i of row j. This is eliminated by subtracting from the whole of the equation of row j (coefficients and load term) k_{ij}/k_{ii} times the equation of row i. Coefficients of row j lying below the diagonal need not be dealt with explicitly since their symmetric counterparts are automatically adjusted by the same amount when the elimination is carried out on the rows higher up.

Fig. 2.5b shows the stiffness equations after this manipulation has been carried out. The process is repeated for all the other rows containing a coefficient in column i. The elimination is complete when all the columns have been dealt with in this manner.

The method actually adopted is a modification of the above, called the frontal solution (78), in which only a part of the upper band and the corresponding load terms are stored in the main computer memory at any one time. During the frontal solution, the assembly of the stiffness matrix from the element contributions and the elimination of coefficients in the lower triangle are performed concurrently.

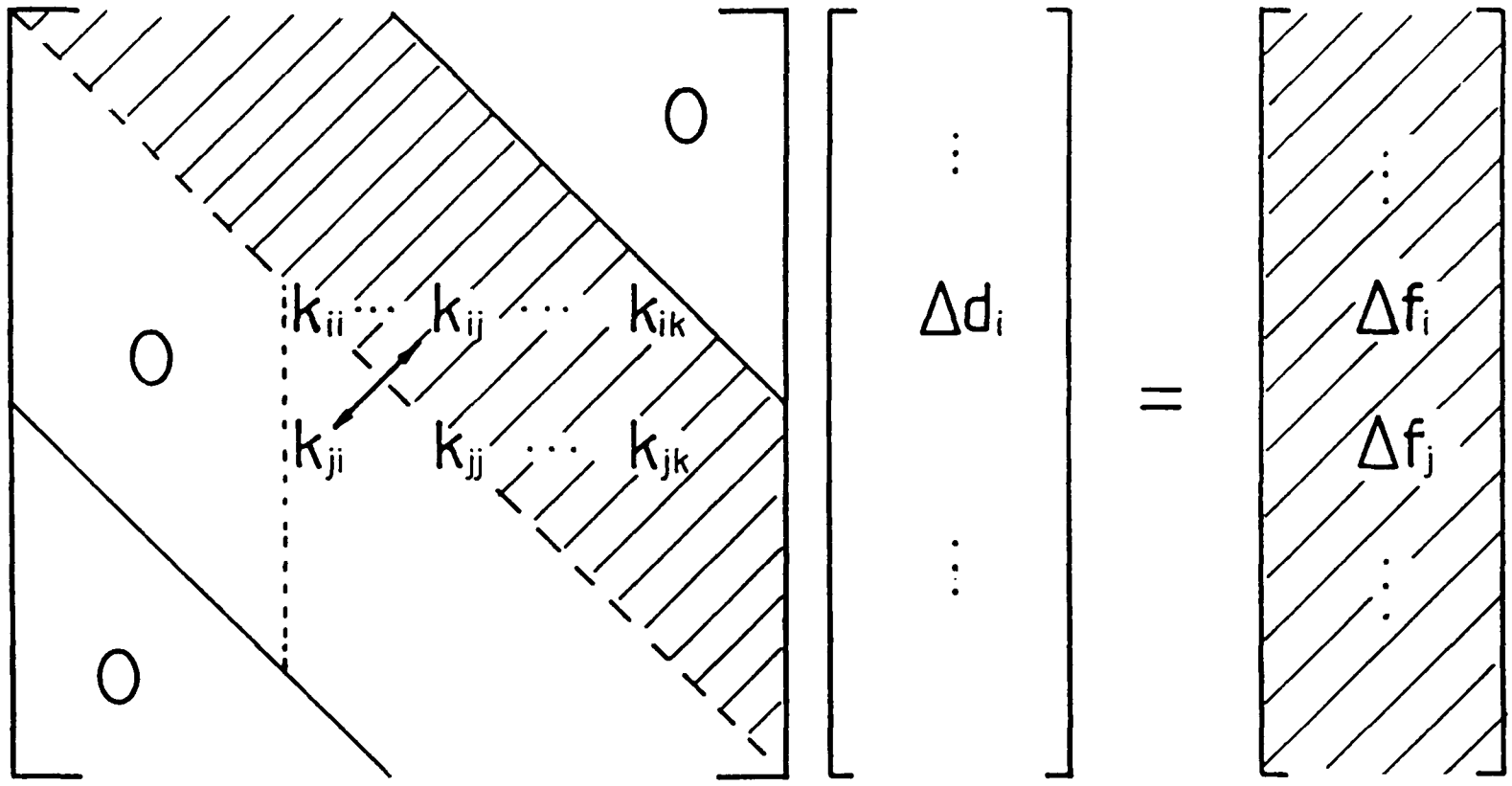

FIG. 2.5

DIAGRAMMATIC REPRESENTATION OF STIFFNESS EQUATIONS - a) BEFORE, b) AFTER ELIMINATION OF DISPLACEMENT Δd_i FROM LOWER TRIANGLE OF MATRIX

Fig. 2.6 represents the stiffness equations, with the hatching indicating the part stored at a given moment. This time the nodes are considered in the order in which they last appear in the elements, when these are examined in numerical order.

As the element stiffness matrices are assembled, in order of element number, into the stored portion of the global matrix, eventually an element will be considered which will be the last one to contain the node associated with row i of the matrix. This row will not be altered by any subsequent assembly and is called <u>fully-assembled</u>. As a result, the coefficients in this row can be used, in the manner described above, to eliminate all coefficients below the diagonal in column i. Once this is accomplished, this row has no further effect upon the matrix, and so may be removed, along with its load term, to disc storage. (In practice, the three equations corresponding to the force at a given node are dealt with and transferred together.)

When the transfer is complete, the storage used by these rows is freed for use by other parts of the band, i.e. the frontal area has moved as shown by the dashed lines in fig. 2.6b.

When the assembly and elimination are finished, the back-substitution can be performed, as before, by recalling the equations, in reverse order, from disc storage.

It is clear from the above that the bandwidth, and the size of the frontal area in store, are not affected at all by the numbering of the nodes, but only by the order of assembly of the elements, i.e. element numbering, and care must be taken to ensure that the elements are numbered most efficiently (see appendix C).

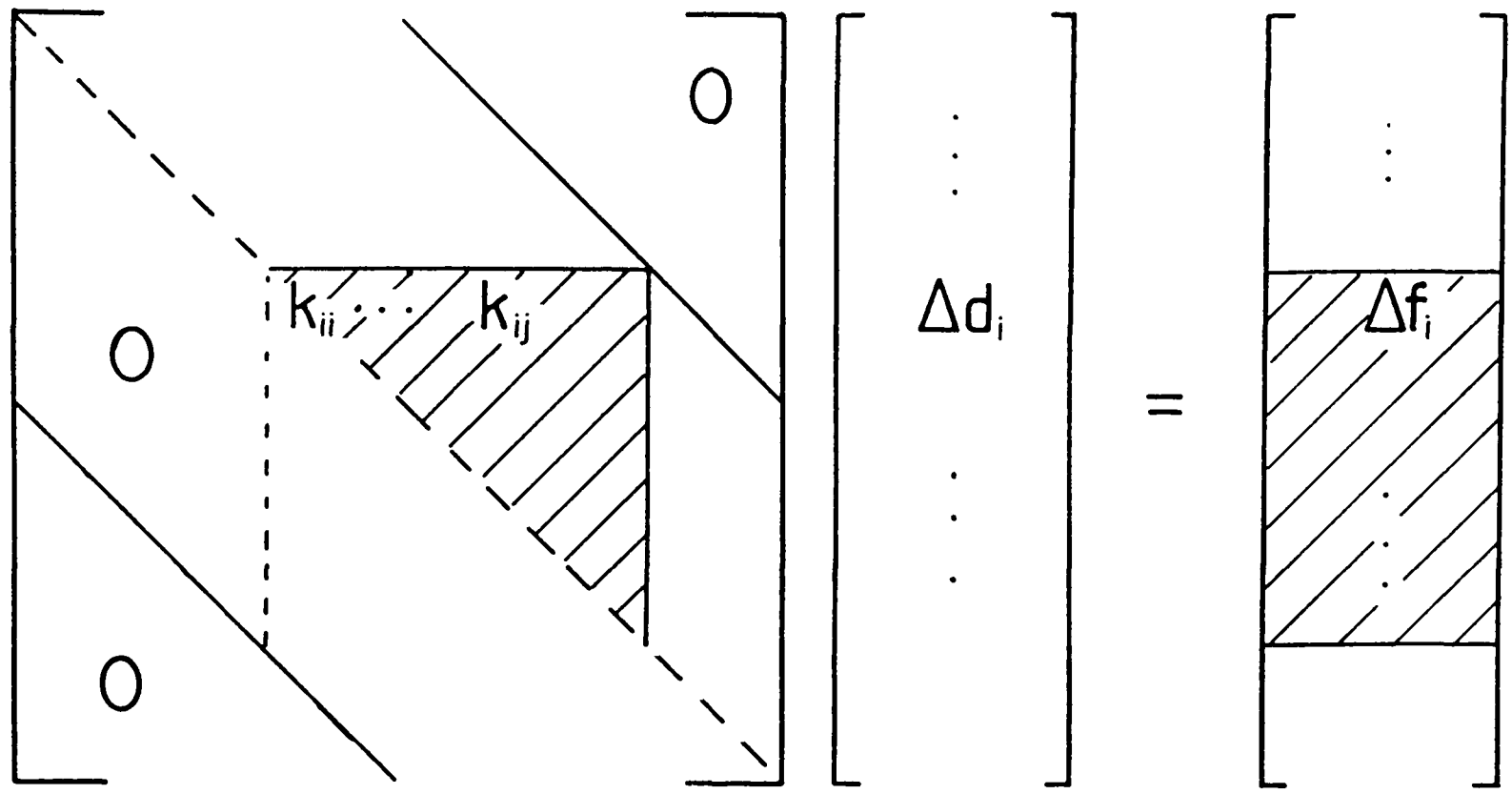

a)

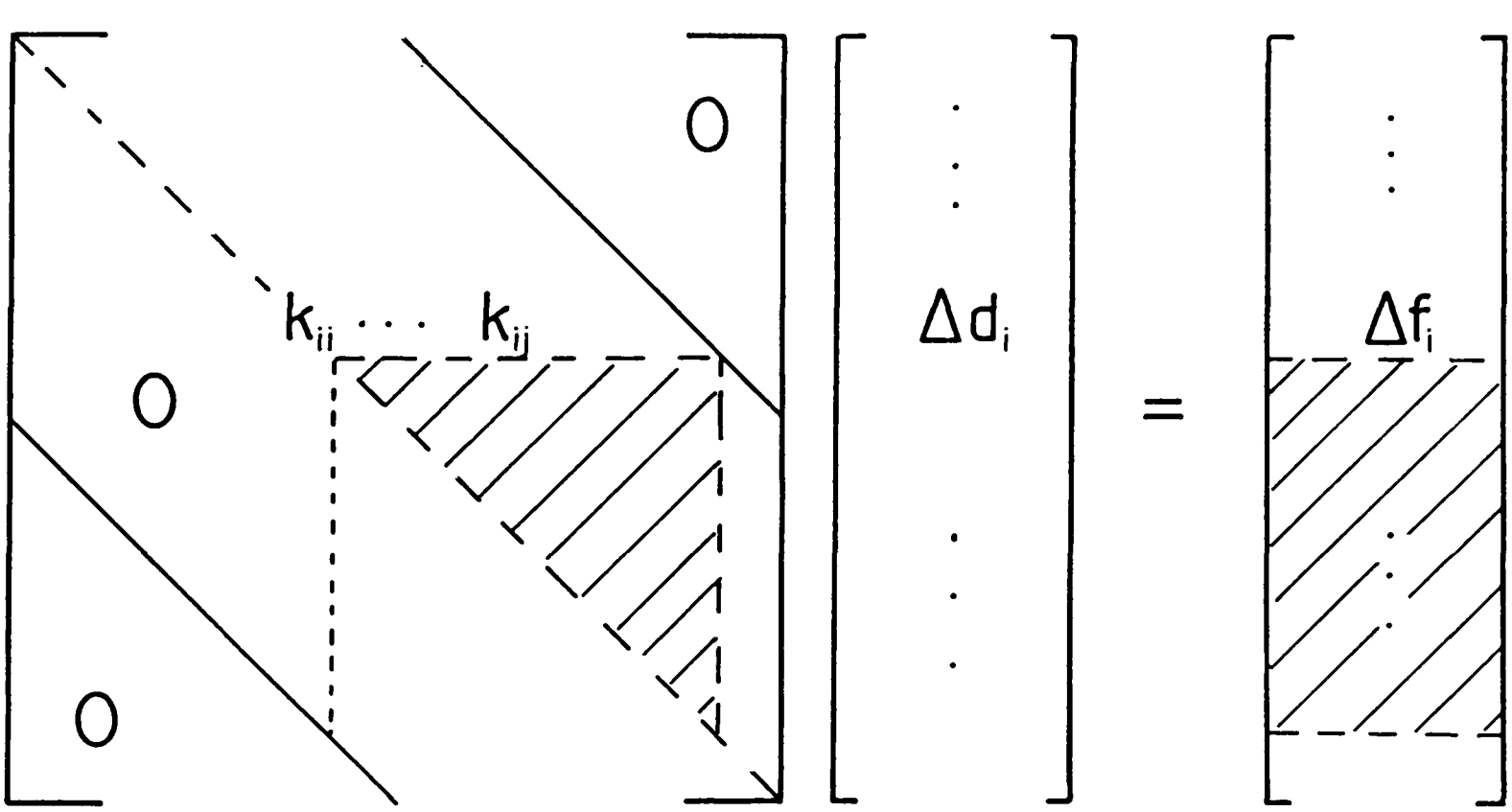

b)

FIG. 2.6

DIAGRAMMATIC REPRESENTATION OF STIFFNESS EQUATIONS – FRONTAL SOLUTION.

a) ROW i FULLY-ASSEMBLED

b) ROW i REMOVED TO DISC

2.3 APPLICATIONS TO PLASTICITY - NON-LINEARITY

Eqn. 2.43 is quite generally applicable to a range of different types of deformation, providing the appropriate constitutive, incremental stress-strain relationships are used in the evaluation of the element stiffness matrices.

When applied to problems in plasticity, there is a choice of constitutive relationship, dependent upon the assumptions made about the nature of the plastic flow.

The yield criterion of Von Mises (section 3.2.3) is generally agreed to be the most satisfactory means of assessing whether the strain at a point is completely elastic (i.e. recoverable) or contains a plastic (permanently strained) component (20). Drucker (88) has shown that an increment of plastic strain, when represented as a vector in stress/strain space, is normal to the surface representing the yield condition in that space. This behaviour is referred to as associated flow. The plastic flow associated with Von Mises' criterion can be shown to be such that the components of the incremental, plastic, strain tensor are proportional to the corresponding components of the deviatoric-stress tensor.

Where the constitutive relations, which are used in the finite-element analysis of plastic deformation, differ, is in their assumptions about the elastic component of the strain occurring after yield. The rigid-plastic, finite-element analysis assumes that no straining occurs in the material before yield and that there is no elastic component to the strain occurring afterwards. The rigid-plastic treatment is therefore based upon the Lévy-Mises flow equations. The visco-plastic approach is similar, but is concerned with strain rates rather than strain increments.

Since the increment in the component of elastic strain after

yield, is usually much smaller than the plastic part, (typically by an order of .001), this assumption is valid for fully-plastic deformations. But just after yield, the total strain in a body is dominated by the elastic strain which occurred before yield, and the rigid-plastic assumption is no longer justified.

In addition, the rigid-plastic approach can give no information about the deformation occurring before yield, or of the effects of removing from the body the forces causing the plastic deformation, (elastic unloading).

The elastic-plastic method, used in the program developed here, does not suffer from these disadvantages because it takes into account elastic strain both before and after yield. The corresponding constitutive relationship is derived from the Prandtl-Reuss, incremental stress-strain equations described in a later section.

Whichever relationship is used, the matrix [K] will depend, in general, upon the current state of deformation. Thus eqn. 2.43 is non-linear and cannot be solved directly for $\Delta\underline{d}$. However, an estimate of $\Delta\underline{d}$, which is close to the correct value, may be obtained if the increment $\Delta\underline{f}$ is chosen to be small, and the matrix [K] assumed to be constant over the increment. [K] may either be evaluated at the start of the increment (tangent-modulus or Euler method), or half-way through (mid-increment, secant-modulus or second order Runge-Kutta method). The second approach is more accurate, but requires two solutions - predictor and corrector - per increment. The finite-element program developed here is designed so that either of these solution techniques may be used.

Another way of tackling the problem of non-linearity, and one which is a further option offered by the program, is to calculate $\Delta\underline{d}$ from $\Delta\underline{f}$ as in the Euler method, and then to estimate the true value of force increment causing the increment in displacement. The

difference between this 'true' force increment and the applied one may then be inserted into eqn. 2.43 to calculate a correction displacement, and the process repeated. This iterative procedure is of the initial stress type, because the corrections are made to displacements, the stress increment being unchanged.

The matrix [K] for each step of the iteration can either be calculated from the most up-to-date information about the state of deformation (Newton-Raphson method), or be the same one which was used for the first solution of the increment (modified Newton-Raphson approach).

The second of these alternatives, which is the one adopted for the present finite-element program, offers the greatest saving in computational time, since the lengthy inversion of the [K] matrix need only be done once for each increment. As a result, and despite the fact that more iterations may be required in the modified than the unmodified Newton-Raphson solution, the former method is usually quicker.

In theory, the advantage of the iterative method over the tangent-modulus approach is again one of reduction in the time of computation, since the former analysis can use fewer, larger increments of deformation to give the same or better degree of accuracy of solution. However, for certain types of deformation, the initial-stress method of iteration may converge only very slowly to a solution. In these cases the tangent- or secant-modulus approaches give reasonable results providing the increments of deformation are not too large.

2.4 APPLICATIONS TO THREE-DIMENSIONAL ANALYSIS

The formulation of a finite-element analysis for three-dimensional deformations presents no theoretical difficulties. However, from a practical point of view, three-dimensional analyses pose special computational problems due to the large number of variables in the calculation.

Compared with two-dimensional finite-element solutions, for example, three-dimensional applications require many more nodes and elements in the mesh used to model the deforming body, in order to produce the same fineness of discretisation, because the mesh extends in a third direction. Also, the number of degrees of freedom possessed by each node is increased from two to three, thus more than doubling, for each node, the number of coefficients in the stiffness matrix (square of number of degrees of freedom).

It is apparent that the computer storage requirements of three-dimensional analyses are considerable. Compared to two-dimensional treatments, the finest mesh which the present program can accommodate is very coarse, and yet even this requires the use of out-of-core storage, at the expense of greatly increased time of computation.

It should be noted though, that this is a problem relating to the current state of computer technology. As faster machines, with larger main memories, come onto the market, it will largely disappear.

Since a large part of the computational time is devoted to large-scale matrix manipulations, three-dimensional finite-element programs are ideally suited to the next generation of vector-processing computers.

CHAPTER THREE

FINITE-ELEMENT PROGRAM

3.0 INTRODUCTION

The finite-element program, which has been developed to predict material flow and properties in three-dimensional forgings, is considered in detail in this chapter. The next section gives a brief outline of the method of analysis, the important aspects of which are discussed more fully in section 3.2. The structure of the program is described, with the aid of flow charts, in section 3.3.

3.1 GENERAL DESCRIPTION OF PROGRAM

Type of Analysis:

The program uses an elastic-plastic formulation based on Von Mises' criterion of plastic yield and the Prandtl-Reuss equations of plastic flow. The treatment can optionally use the Jaumann correction to stress increments (section 2.1.1.2) and co-rotational increments of strain (section 2.1.1.3) for accurate analysis of deformation in which the steps involve finite strain or finite rotation. Strain-hardening materials can be modelled by supplying the appropriate constants to a combined logarithmic and exponential strain-hardening function. The incompressibility of yielded regions can be enforced by specifying a value close to 0.5 for Poisson's ratio used in the formulation for fully-yielded elements; the constant-dilatation technique (section 2.1.1.5) can be used to prevent the nodal displacements being over-constrained.

Type of Element, Size of Mesh:

Three-dimensional, eight-node, linear-isoparametric elements are

used, the stiffness matrices of which are evaluated by a Gaussian numerical-integration scheme of variable order. The mesh may contain up to 1000 elements and 1331 nodes, providing the nodal semi-bandwidth does not exceed 92. The definition of bandwidth for the frontal-solution procedure and the method of calculating its value are discussed in appendix C.

Specification of Deformation:

Any combination of incremental components of nodal force, nodal constraining conditions and boundary surfaces may be specified. A constraining condition is a set of prescribed values for the incremental components of displacement and may be applied to more than one node. These components of displacement may be referred to any orthogonal axis system and any of the components may be left unspecified in order to constrain nodes within straight lines or planes.

A boundary surface may consist of any one of five simple geometric shapes. Nodes are prevented from passing through these surfaces throughout the deformation and nodes making contact with a surface may either be fixed in position on the surface or constrained to move tangentially to it. In the latter case, the movement can be subject to the frictional restraint applying to that surface.

Type of Solution:

A mixed incremental/iterative approach is used, the iteration being a modified-Newton-Raphson, initial-stress procedure. The solution of the stiffness equations is by a frontal technique. The residual forces in the iteration may be derived, for fully-yielded elements, either from the deviatoric or from the total changes in stress throughout the element. By altering the criterion for convergence, the solution can be performed without iteration as a

tangent-modulus or secant-modulus technique.

Output:

The program prints the values of the coordinates of the displaced nodes, the average components of element stress (for which the hydrostatic components may be calculated either directly from bulk-strain changes or indirectly from deviatoric stress), and the forces on external faces of the mesh at the end of the analysis or at any specified interval during the calculation. The volume of the mesh and the average work of deformation are printed for each increment. Both projected and sectional views of the deformed mesh may be drawn at the end of the analysis and during the calculation. Hidden lines are removed in the projected views by means of an algorithm developed for the current work. Generalised stress, generalised plastic strain and incremental displacement vectors can be shown on any of the sectional views.

Continuation Facility:

Lengthy analyses may be spread over several runs of the program by the use of the automatic dump-and-retrieval facility.

3.2 DETAILS OF ANALYSIS

3.2.1 Boundary Conditions

Eqn. 2.43 represents a set of n simultaneous equations in n unknowns - the three components of displacement increment at every node of the finite-element mesh. Each equation gives a component of the force increment at a node. The physical basis of the stiffness matrix [K] ensures that it is non-singular, so if the incremental components of force are given at each node, eqn. 2.43 may be inverted to give the corresponding incremental components of displacement.

In metal-forming problems though, the increments of force are not generally known at every node of the mesh. Certainly, for those nodes lying inside the body or on a free surface, the principle of equilibrium requires that the net force is zero, but the distribution of force on a constrained surface, e.g. a surface in contact with a platen or a container wall or a surface of symmetry, is not known before the analysis is performed, unless it is measured experimentally.

However, the incremental displacement of points on constrained surfaces is determined, to some extent, by the geometry of the forming process. Thus the solution of eqn. 2.43 must be carried out subject to specified boundary conditions whereby certain incremental nodal displacements have prescribed values.

Section 3.2.1.1 describes how prescribed values of displacement are incorporated into the solution of the stiffness equations in the present finite-element program.

Although the displacement of nodes on constrained surfaces depends on the geometry of the process, it may not always be possible

to predict the actual values of the components of the displacement for any given increment before the start of the calculation. For these cases, geometric boundary surfaces may be defined which limit the deformation of the finite-element mesh and from which the program can determine the prescribed displacement of nodes, where appropriate, at each increment. This procedure is discussed in detail in section 3.2.1.2.

3.2.1.1 Prescribed Displacements

3.2.1.1.1 Prescribed Displacements in Coordinate Axes

The components of incremental displacement, measured in the coordinate axis system, may be specified at any of the nodes in order to define the deformation. These prescribed values may be zero, as for the out-of-plane displacement of nodes on a plane of symmetry, or finite, as for the nodes on a surface in contact with a moving die.

There are several ways in which prescribed values of displacement may be incorporated into the solution of the stiffness equations. For example, Cheung and Yeo (78) describe methods which modify the stiffness matrix before the solution begins, so that the prescribed values are automatically taken into account by the usual Gaussian elimination and back-substitution.

The approach adopted here, which may be termed direct insertion, is essentially the same as that presented by Irons and Ahmad (89). It is simpler in concept than those methods which modify the stiffness

matrix, though it does require the use of a slightly different method of elimination and back-substitution for the components of displacement change which have prescribed values. In practice, this is not a great disadvantage since it is arranged that the elimination process for prescribed components of displacement change simply omits certain stages of the usual procedure.

As mentioned in the previous chapter, the solution of the stiffness equations by the Gaussian method, whether or not this is implemented as a frontal technique, consists of transforming the augmented matrix of coefficients and load terms into upper-triangular form which then permits successive evaluation of the unknowns in terms of those already determined. The upper-triangular matrix is formed by considering each equation in turn (in the frontal solution, the sequence being determined by the order in which nodes become fully-assembled), and eliminating all the coefficients below, and in the same column as, the current diagonal coefficient.

This is usually accomplished by subtracting appropriate multiples of the equation under consideration from all the others which have a coefficient in this column. If, however, the value of the change in the corresponding component of displacement is known, the elimination can be carried out by subtracting, from both sides of these equations, the value of the displacement change times the relevant coefficient.

This process is illustrated, for a frontal solution, in fig. 3.1, which uses the same diagrammatic conventions as figs. 2.5 and 2.6. The first diagram shows the situation when the equation for the ith component of force is fully-assembled. This equation has a coefficient in column j and so, by symmetry, the fully-assembled equation for the jth component of force will have the same coefficient in column i. The second diagram shows the stiffness equations after the elimination of this coefficient from its equation.

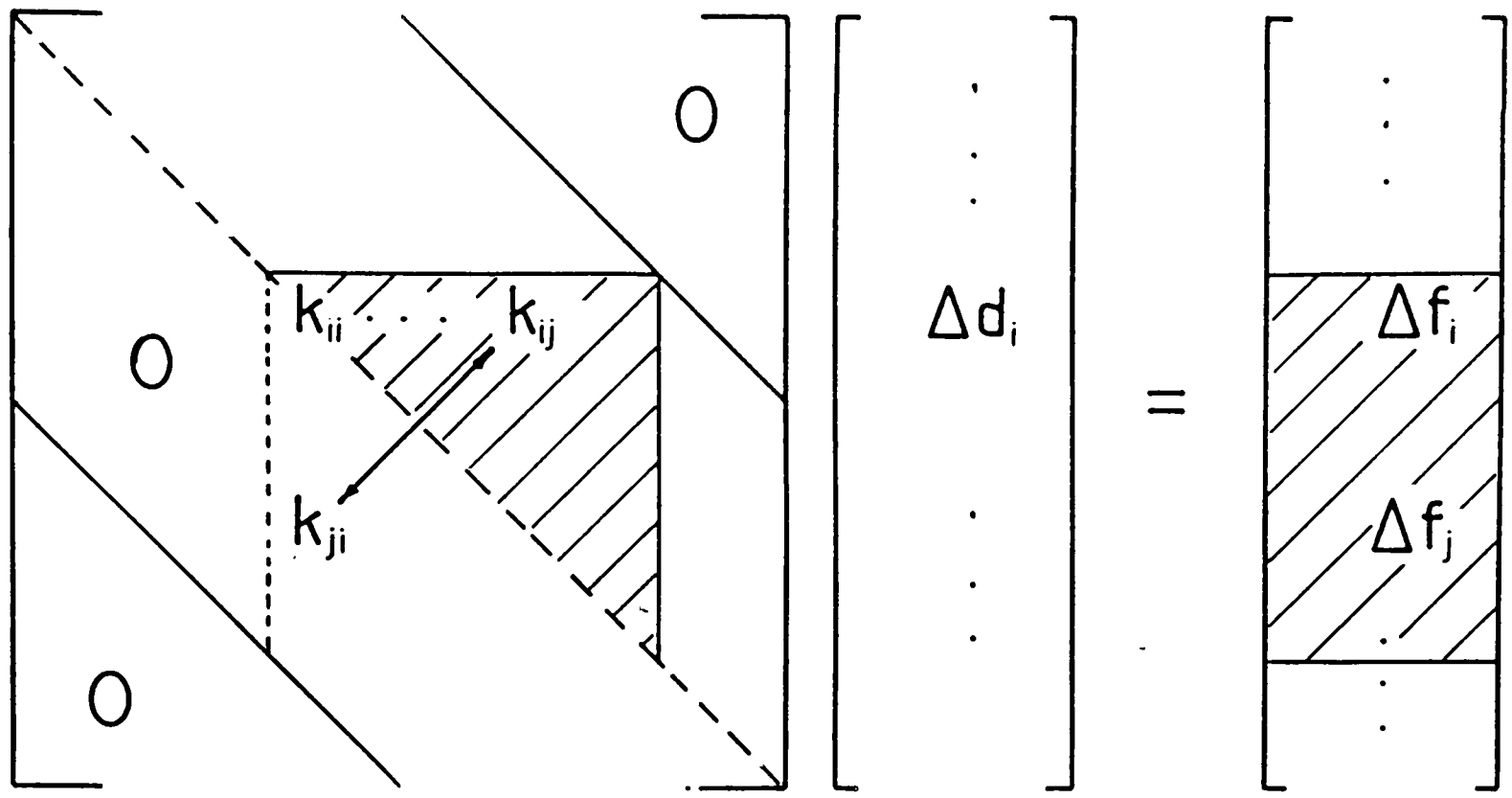

a)

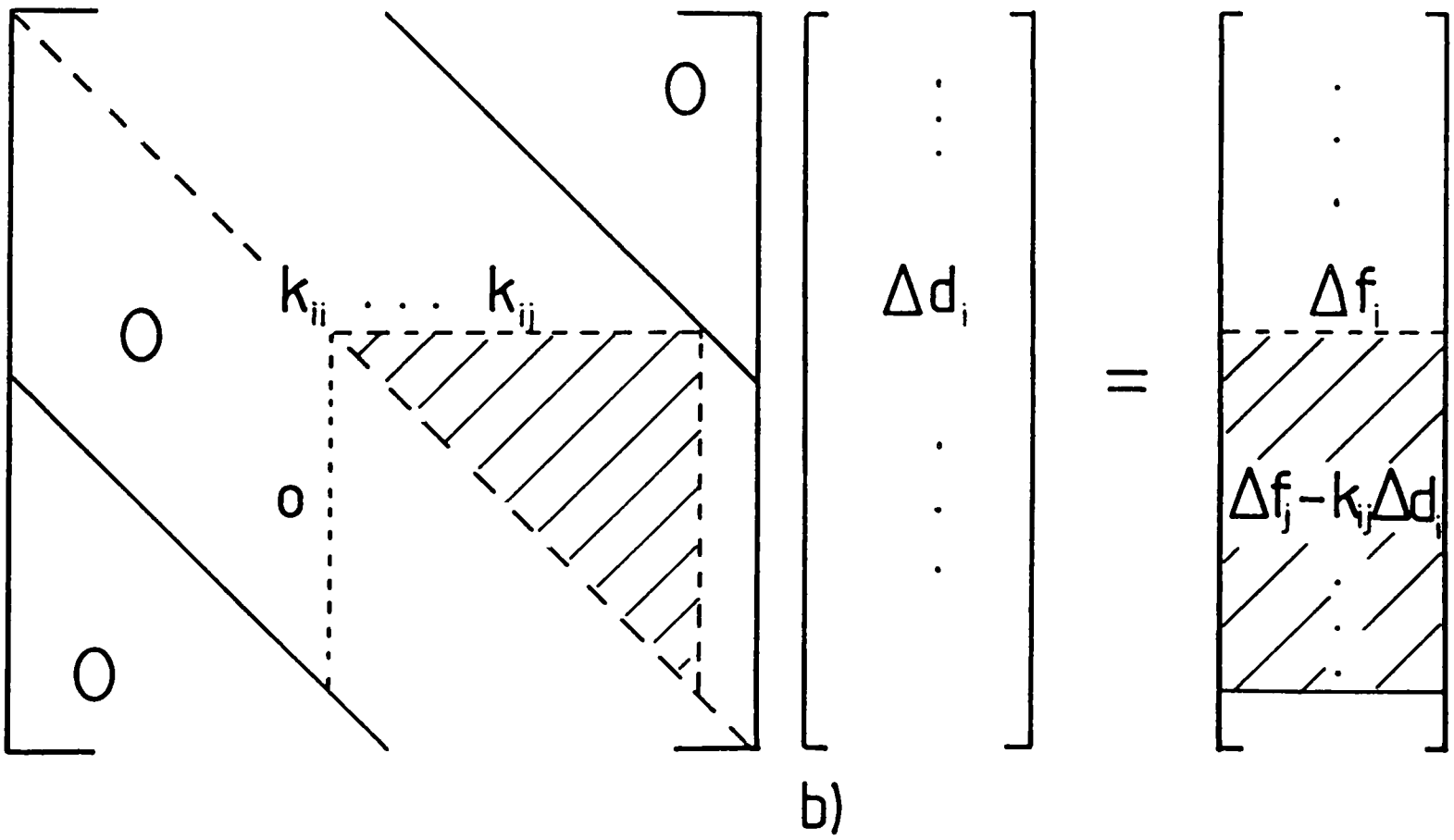

b)

FIG. 3.1

DIAGRAMMATIC REPRESENTATION OF STIFFNESS EQUATIONS.

a) ROW i FULLY-ASSEMBLED

b) EFFECT OF PRESCRIBED DISPLACEMENT Δd_i TRANSFERRED TO LOAD OF ROW j

When the process has been repeated for all the other non-zero coefficients in the ith equation, the fully-assembled equation may be transferred to disc storage as before (along with the other equations relating to the same node), and the front moved, as indicated by the dashed lines.

Back-substitution is unchanged except that when an equation is encountered which corresponds to a node with a prescribed displacement change, all the incremental displacements in the reduced equation are known, and can all be substituted into it. Subtraction of the load term from the resulting value on the left-hand side, gives the component of reaction of the external system to the mesh, at the node in question.

3.2.1.1.2 Prescribed Displacements in Rotated Axes

It is convenient to be able to specify the incremental displacement of a node relative to axes which are rotated with respect to the coordinate system. For example, the effect of a stationary and frictionless die surface is simulated in the finite-element model by prescribing zero displacement, to nodes imagined to be in contact with the die, in a direction perpendicular to this surface, the displacement in other directions being unspecified. This, therefore, requires that, for each of these nodes, one of the axes of the system in which the displacement is prescribed be perpendicular to the die surface. It may be necessary to use a die surface which is not normal to any of the coordinate axes.

The program developed here follows the technique suggested by

Cheung and Yeo (78) and allows any of the prescribed displacement conditions to be referred to a local set of Cartesian axes, by specifying the direction ratios of the local axes with respect to the coordinate system. (At most, the direction ratios of just two of these axes need be given.)

Suppose such a condition applies to node I. If l, m and n refer to direction cosines with respect to coordinate axes x, y and z respectively, and a subscript refers to one of the rotated axes X, Y or Z for node I, then the rotational transformation matrix [R] may be defined according to fig. 3.2a. (Note that the matrix [R] is used in a different context to that in section 2.1.1.3.) The vectors for change in displacement and force in the two systems are then related by:

$$\Delta \underline{d}_I = [R]\Delta \underline{d}'_I \quad \text{and} \quad \Delta \underline{f}_I = [R]\Delta \underline{f}'_I \qquad (3.1)$$

where a prime indicates a vector in the local axis system.

Fig. 3.2b is the usual diagrammatic representation of the stiffness relationships at a stage when the three equations for the force at node I are fully-assembled, except that the three components at a node are grouped together, and that the terms in the brackets refer to 3x3 sub-matrices of the stiffness matrix.

Substituting for the incremental displacement vector from eqn. 3.1, results in the situation shown in fig. 3.2c. By the usual matrix property, [R] may be removed from the displacement change array and, instead, used to post-multiply all the stiffness sub-matrices corresponding to the change in displacement at node I, (i.e column I). The force at node I may be expressed in the same rotated axes as the displacement by pre-multiplying all the sub-matrices, and the load vector, of the equations for this node by the inverse of [R]. This inverse can be shown to be equal to the transpose of [R].

$$[R] = \begin{bmatrix} l_X & l_Y & l_Z \\ m_X & m_Y & m_Z \\ n_X & n_Y & n_Z \end{bmatrix}$$

a)

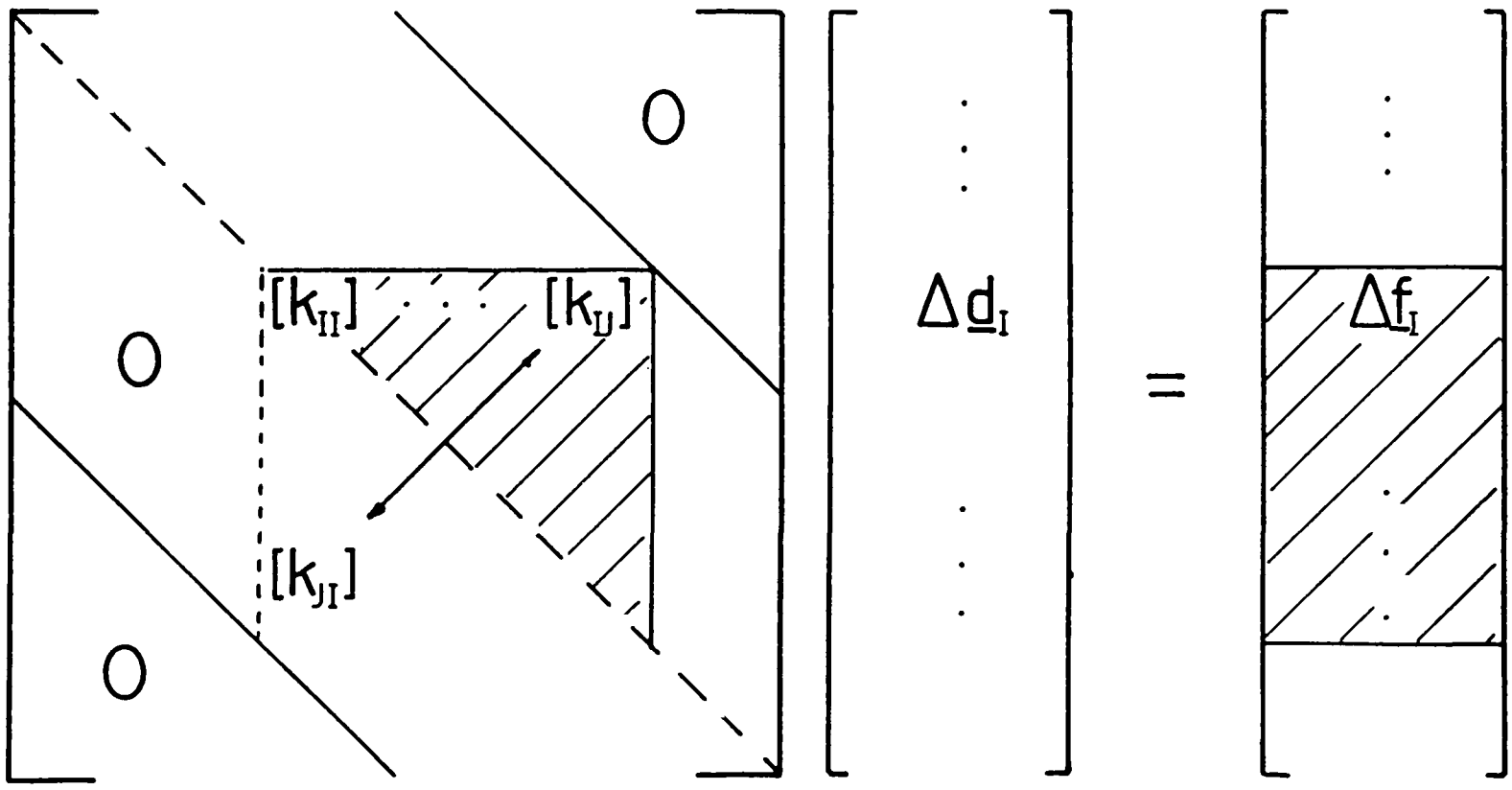

b)

FIG. 3.2

a) ROTATIONAL TRANSFORMATION MATRIX

b) DIAGRAMMATIC REPRESENTATION OF STIFFNESS EQUATIONS USING NODAL SUB-MATRICES

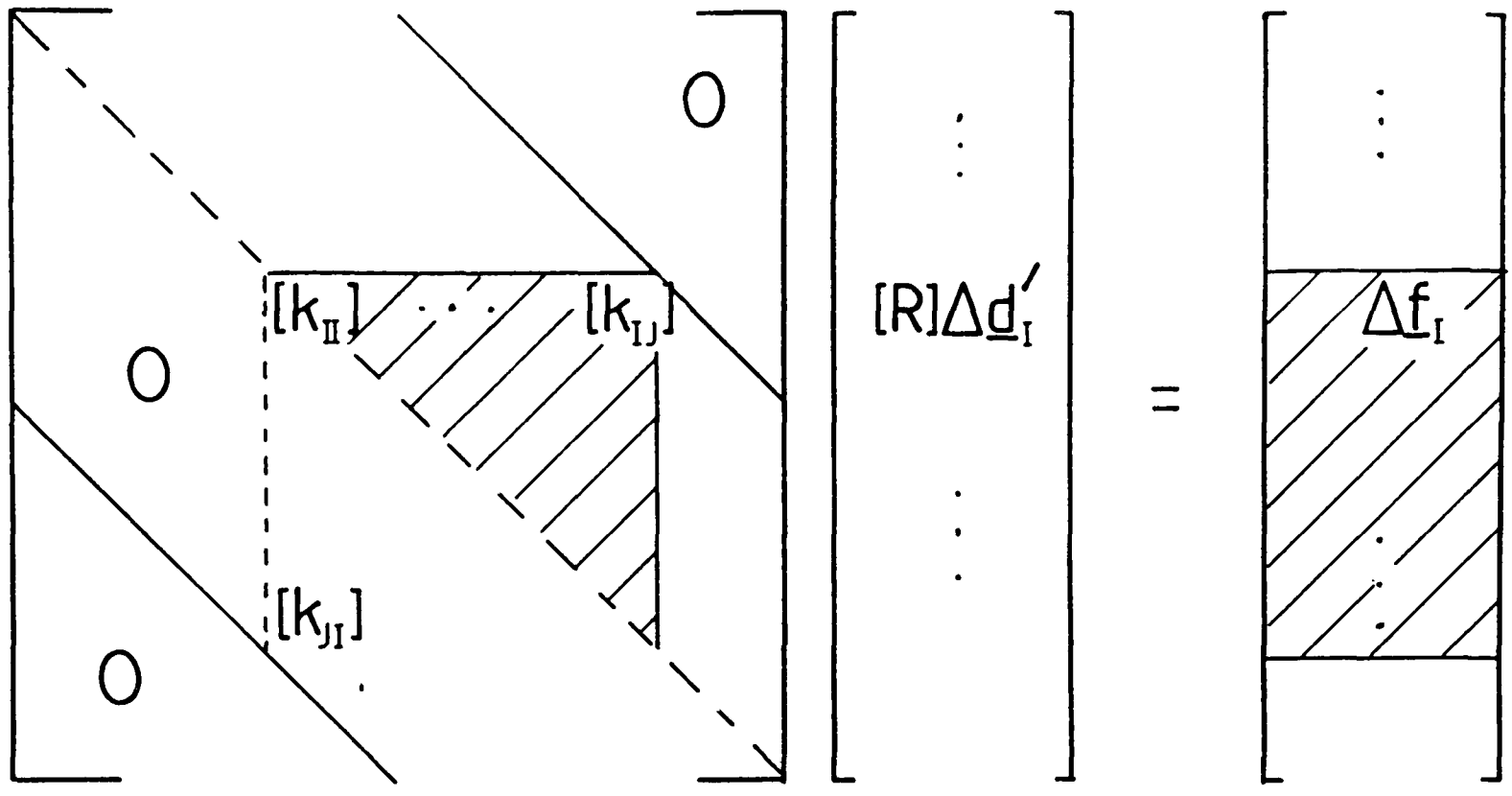

c)

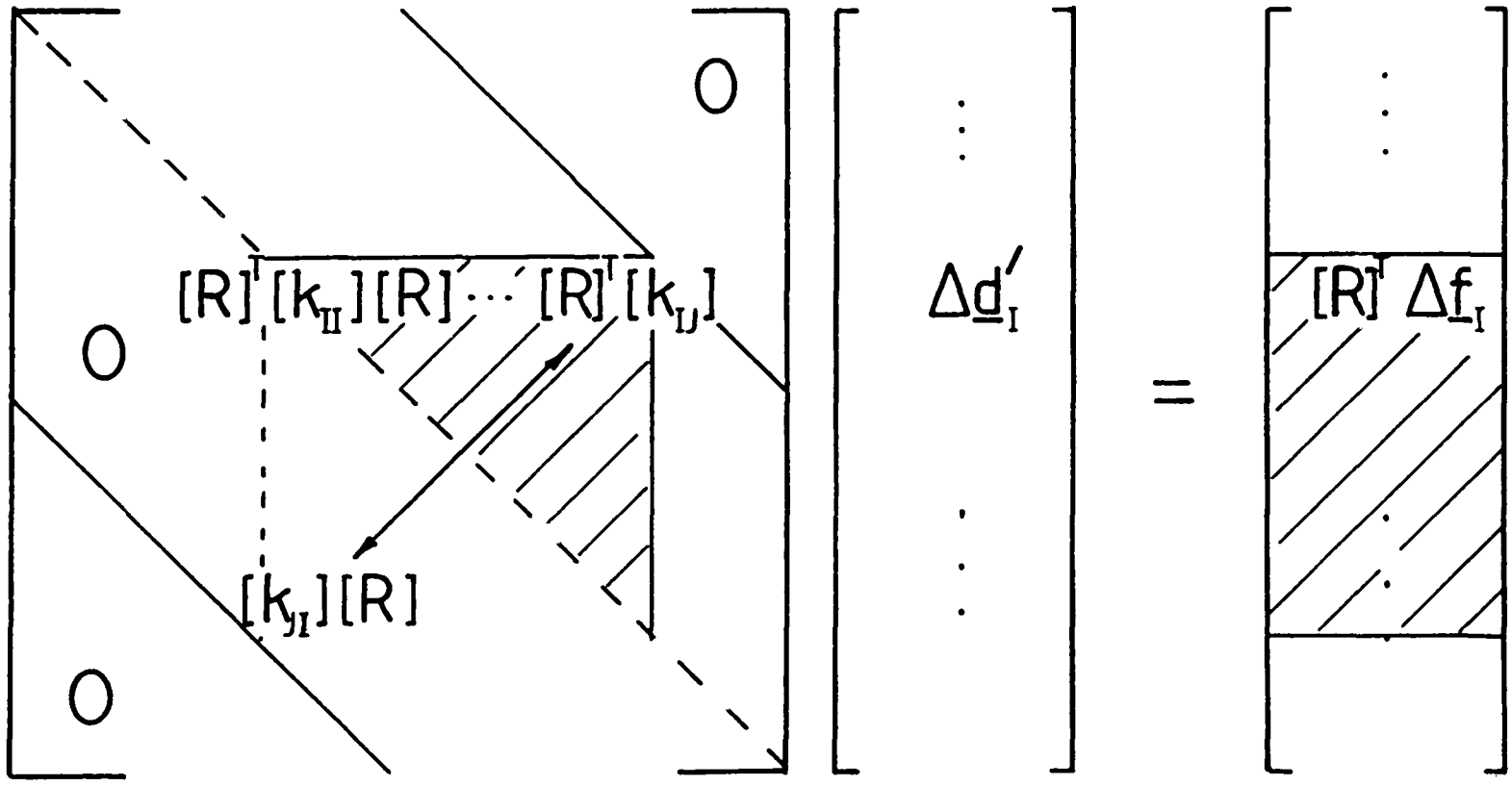

d)

FIG. 3.2

c),d) TRANSFORMATION OF DISPLACEMENT AND LOAD AT NODE I TO ROTATED AXES

Fig. 3.2d shows the transformed stiffness equations, in which it is to be noted that:

$$([k_{JI}][R])^T = [R]^T[k_{IJ}] \qquad (3.2)$$

so that symmetry has been preserved, and the operations need only be carried out on row I in the frontal area. The components of $\Delta\underline{d}'_I$, including any prescribed ones may now be eliminated in the usual way.

During the back-substitution, the vectors of the increments in displacement and force for node I are pre-multiplied by [R] to give the corresponding vectors in the coordinate frame.

3.2.1.2 Prescribed Boundary Surfaces

Section 3.2.1.1 describes how the solution procedure can be modified to take into account pre-determined values of displacement increment at certain boundary nodes. By this means, a node can be assigned a constant displacement vector for each increment, or it can be constrained to move in a straight line throughout the deformation without requiring it to be at any particular position on that line, or it can be constrained to move in a plane, again its actual position in that plane being unspecified.

However, this procedure requires that the constraint applied to a node is the same for each increment and is known beforehand. Thus it cannot model boundaries which are not planes, since the constraint needed for nodes on non-planar boundaries changes at each increment, and it cannot deal with nodes which come into contact with a die during the course of a deformation, e.g. when a surface rolls onto the platen in simple upsetting with high interfacial friction.

Consequently, a second method of specifying boundary conditions, by means of prescribed boundary surfaces, has been developed for the present finite-element program. This method allows the solid surfaces (die, container etc.) with which the work-piece interacts during a forging operation to be modelled as part of the finite-element analysis.

3.2.1.2.1 Boundary Surfaces with Zero or Sticking Friction

A prescribed boundary surface may be, at present, any one of five types of finite geometric surface, i.e. a portion of a plane (rectangle or annulus), a portion of the curved surface of a cylinder, the surface of a sphere or the surface of a torus. These simple shapes have proved to be sufficient for the present work, but the implementation of the boundary-surface procedures has been carried out so that additional primitive surfaces, such as the curved surface of a cone or the surface of an ellipsoid, may be included easily in the finite-element program.

Up to 98 distinct boundary surfaces may be specified. They are defined by a code number determining the type of surface (cylinder, disc etc.) and the coordinates of two or three points, related to the surface in a natural way (fig. 3.3). For example, a rectangular region of a plane is defined by two points which lie at the ends of one of its four sides and a third point which lies anywhere on the opposite side (produced if required). The cylindrical and toroidal surfaces need an auxiliary parameter, the angle subtended by the required part of the curved surface for the former, and the radius of the curved surface for the latter.

Associated with each defined surface (primary surface) is a secondary surface which is parallel to it and lies a small distance d away from it. The value of d can be different for different surfaces and may be positive or negative, depending upon which side of the primary surface the secondary surface is meant to be. The sign conventions are shown in fig. 3.3.

At the beginning of each increment of deformation, the current positions of the nodes are determined relative to each of the boundary surfaces. If a node is found to have passed through a boundary

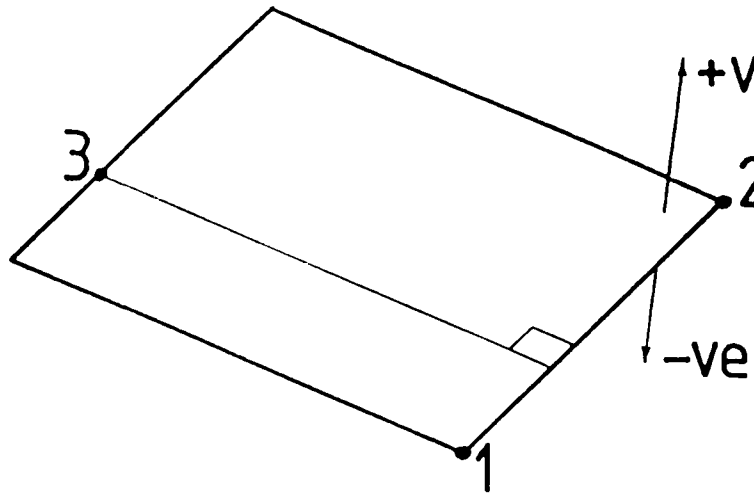

rectangle: t = -1

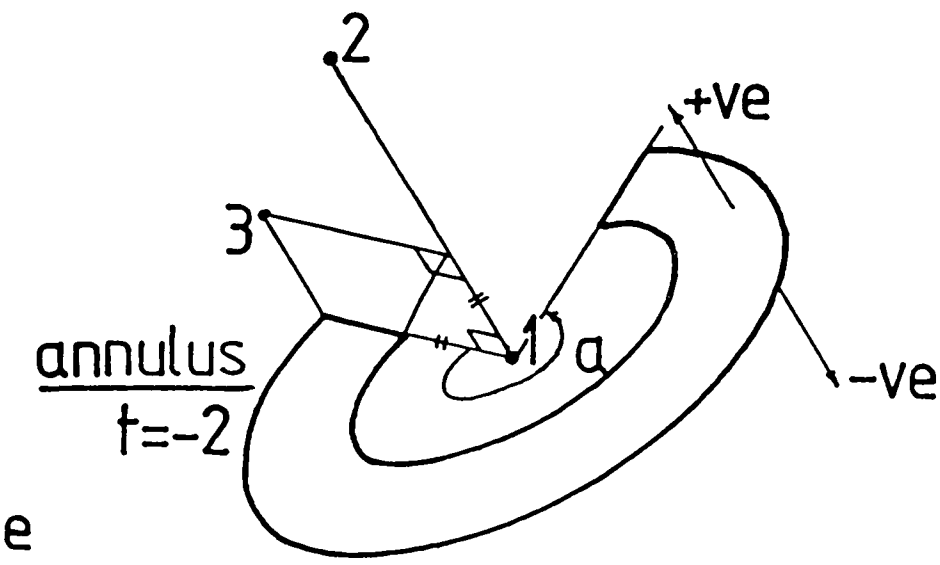

annulus
t=-2

cylinder:
t=-3

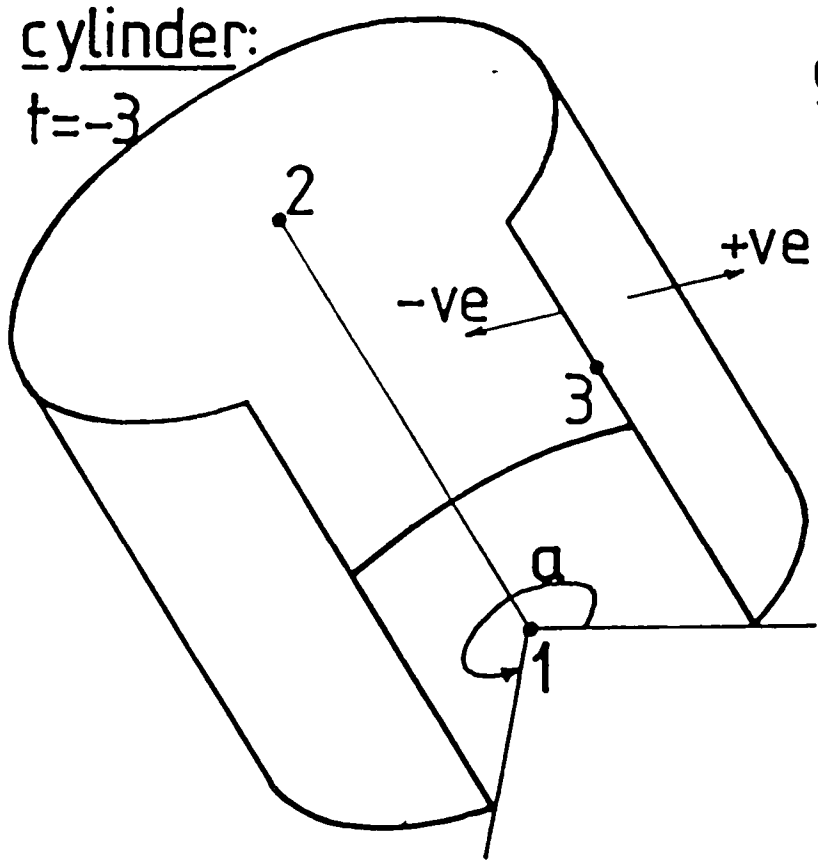

torus: t=-4

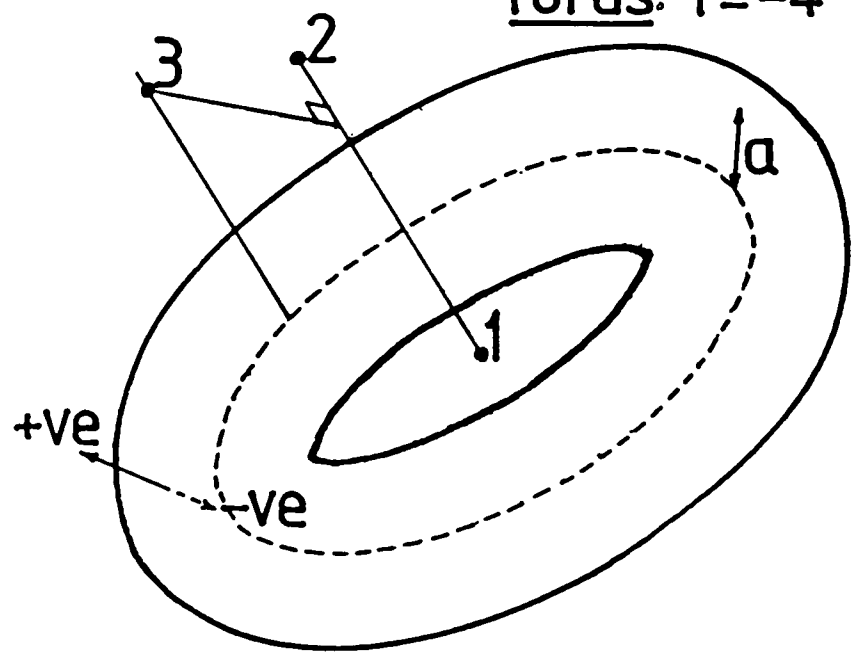

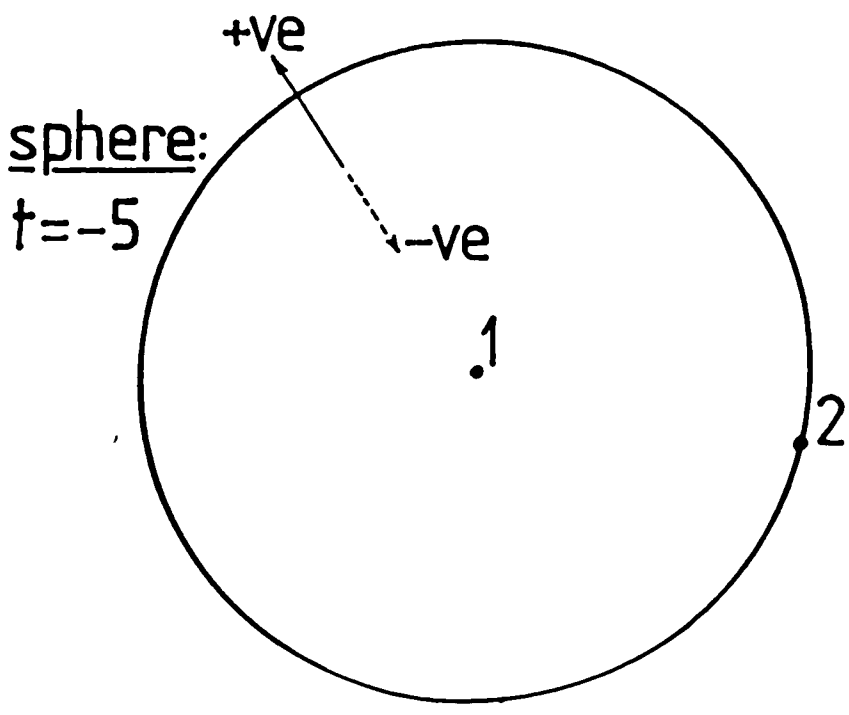

sphere:
t=-5

Figure 3.3

Types of Boundary Surface

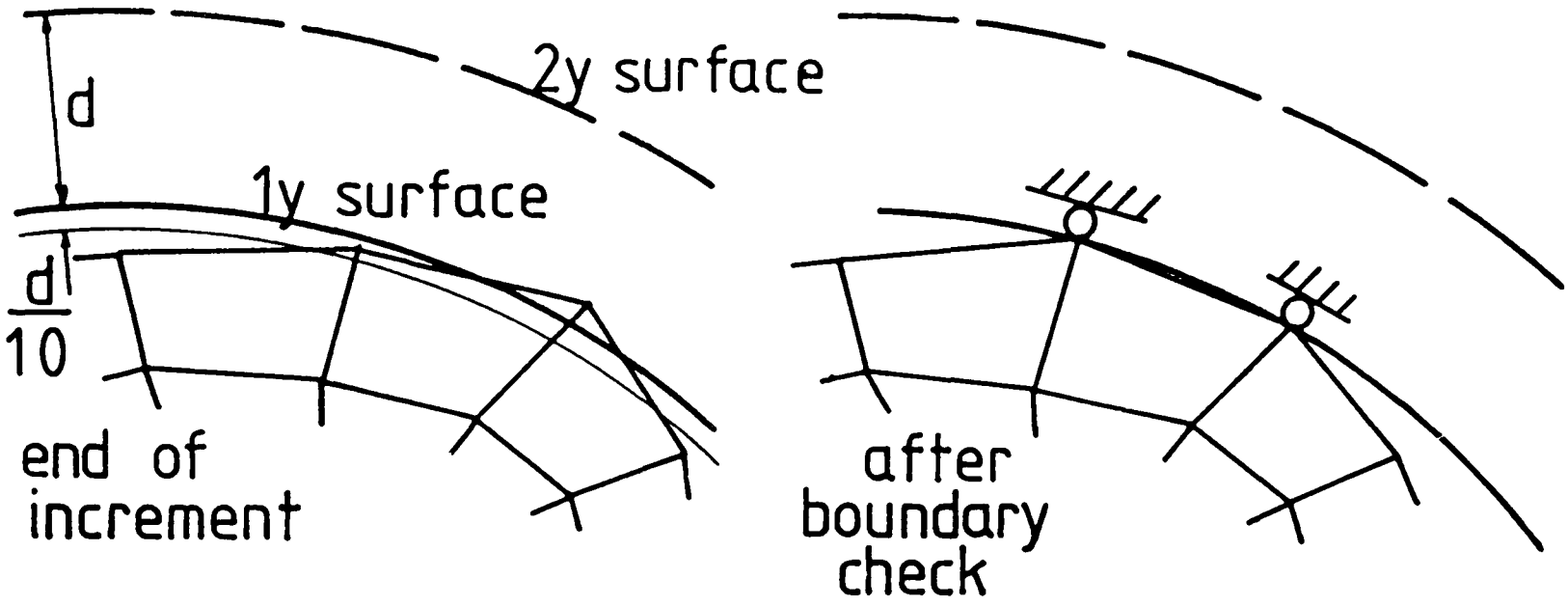

FIG. 3.4 CHECKING FOR VIOLATION OF BOUNDARY SURFACE

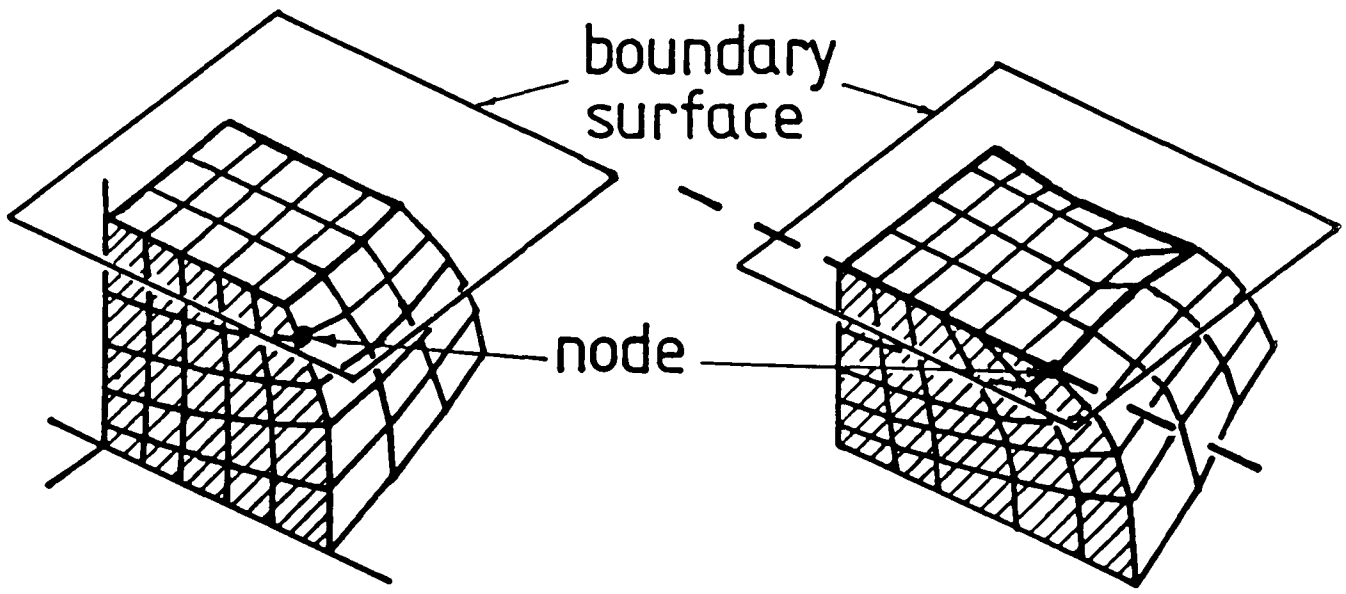

FIG. 3.5 ROLL-ROUND OF PREVIOUSLY-CONSTRAINED NODE

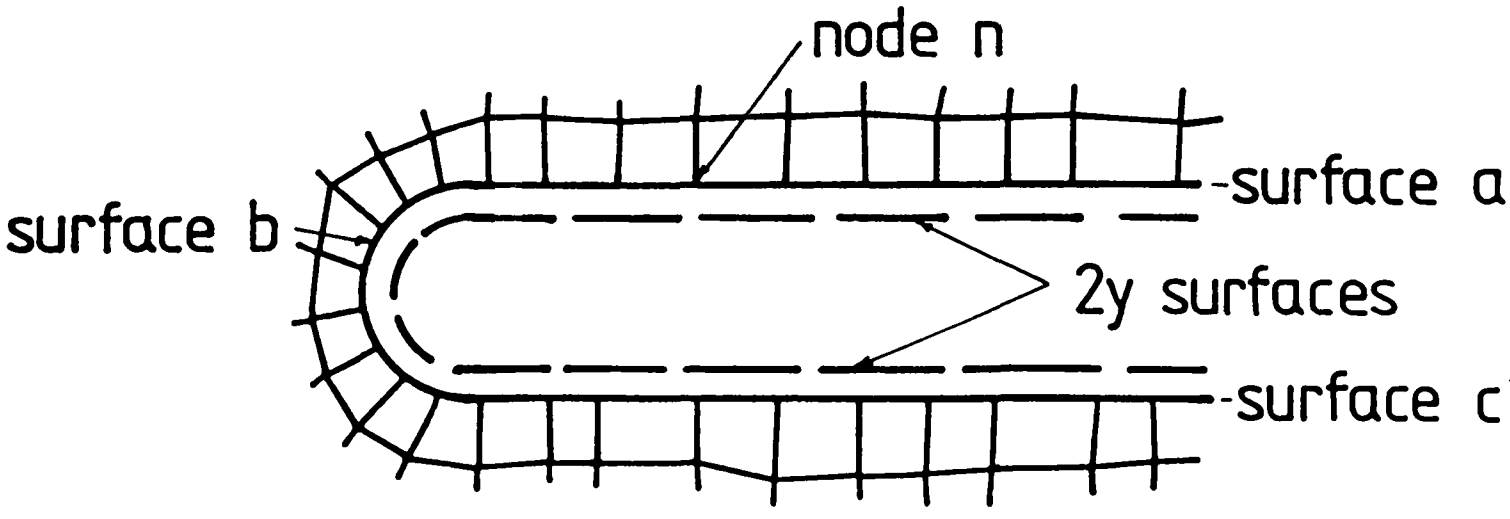

FIG. 3.6 INDENTATION OF SURFACE

surface, so that it lies on the same side as the associated secondary surface, then the node is moved by the shortest path back to the primary surface. In practice, it is more convenient to re-position a node if it approaches within a distance of d/10 of a boundary surface (fig. 3.4).

Once a node has been moved onto a boundary surface, it may be either fixed in position for the rest of the deformation, if the surface has been designated as a sticking-friction boundary, or constrained to move tangentially to it if zero friction has been specified for the surface.

In the latter case, the actual constraint applied to a node takes into account any incremental displacement which was originally specified for that node. For example, in fig. 3.5, the marked node, which in the first diagram lies on the free surface of a cylindrical billet (one quarter of the billet modelled here), also lies on a plane of symmetry of the billet (hatched in diagram). Thus originally it would have been constrained to move only within that plane. If, after upsetting, the node has rolled onto a prescribed boundary plane (second diagram), then the node must be constrained to move within that plane whilst still remaining on the plane of symmetry. The boundary surface procedures in the program would therefore constrain the node to move in the dashed line of intersection of these two planes, as shown in the diagram.

If movement within the plane which is a tangent to the boundary surface is not consistent with the originally specified displacement, then the latter constraint is ignored.

When there are folds or indentations in the surface of the deformed body, it is quite likely that certain nodes appear to pass through boundary surfaces with which they actually have no contact. For example, in the simple situation illustrated in fig. 3.6, any node

in contact with boundary surface a, is also on the 'wrong' side of surface c, and would normally be transferred onto the latter surface during the check for violation of boundary surfaces.

To prevent this sort of thing happening, a node which appears to have passed through a boundary surface (i.e. so that it is on the same side as the secondary surface), is only re-positioned if it lies between the primary and the secondary surfaces. Thus in fig. 3.6, the nodes on surface a are well beyond the secondary surface for boundary c and are not re-positioned.

3.2.1.2.2 Boundary Surfaces with Intermediate Friction

The conditions of sticking and zero friction assumed in the previous section are very convenient to implement in finite-element programs. Unfortunately, both these conditions are idealisations and any finite-element analysis which attempts to model actual forming processes must be capable of incorporating intermediate conditions of friction on the boundary surfaces.

Since the aim of the present work is to develop a fully-predictive analytical technique, the information required to specify the frictional constraint should, if possible, be independent of billet geometry and forming process and depend only on the nature of the work-piece, die and any lubricant associated with each surface of contact.

3.2.1.2.2.1 Friction in Finite-Element Analyses - Previous Work

Nagamatsu et al (46-48,76) specified the tangential displacement of the material in contact with the die during simple upsetting. The distribution of this displacement was obtained experimentally and approximated by a linear function of position in the finite-element program. More recently, Brouha et al (6) used a similar technique but were able to specify the tangential displacement more accurately. Although this approach is useful for checking finite-element results, an experiment must be performed for every process, geometry and frictional condition investigated analytically and it is not, therefore, a predictive technique.

As an alternative to specifying the tangential displacement on the frictional boundary, the frictional force can be specified. The force may be proportional to the pressure acting on the boundary (Coulomb friction) as in the analyses by Iwata et al (51), Gordon and Weinstein (53), Klie et al (39) and Mori et al (90), or may be obtained from a value of shear stress which is assumed to be proportional to the actual shear yield stress. The latter approach, usually called the shear-stress method, has been adopted by, among others, Kobayashi and his co-workers (31,91,43) and Dung et al (38).

In either case, The values of the forces applied to the boundary nodes do not have to be specified beforehand since they may be calculated from information supplied by the computer program, such as normal stress at the boundary or current yield stress. Unfortunately, the direction of application of the forces must be known in advance. This presents no problems for simple deformations such as upsetting, but the direction may not be obvious in more complicated examples where there is a flow divide, such as the ring test. The technique therefore requires some assumption to be made about the flow and is

not fully predictive.

Lee, Mallet and McMeeking (52) avoided this problem by including friction in the virtual-work formulation. However, this leads to an unsymmetric stiffness matrix and doubles the computer storage requirements.

Another approach was proposed by Chen and Kobayashi (36) and later generalised to arbitrarily-shaped boundary surfaces by Oh (92). In this technique, the relationship between frictional force f and relative interfacial velocity v:

$$f = -mkv/|v| \qquad (3.3)$$

(i.e. frictional force always has magnitude equal to the friction factor m times the shear yield stress k, but acts in the opposite direction to the relative interfacial velocity) which is not continuous at v = 0, is replaced by the continuous approximation:

$$f = -2mk\{\tan^{-1}(v/u)\}/\pi \qquad (3.4)$$

where u is small compared with the usual values of v. The frictional force can then be introduced into the variational principle as a function of nodal velocity.

This method is fully predictive, but the results do not compare well with experimental data for the upsetting of a ring with low friction (36).

Various attempts have been made to model the frictional boundary constraint by an extra layer of finite elements. Zienkiewicz et al (34) and Sharman (41) used layers in which the yield stress was reduced by multiplying it by the friction factor. In the latter reference, the layer of elements physically represented the layer of

glass used as a lubricant in hot extrusion.

Webster (93) introduced a plate-type friction element into his three-dimensional rigid-plastic analysis. The shear stresses acting on these friction elements were calculated from the strain-rate components and the technique required an initial, zero-friction, iteration to estimate these before the frictional boundary restraint could be applied. The velocity field calculated without friction was not always consistent with the velocity field to be expected when the frictional forces acted, and the process sometimes failed to converge.

The friction layer used by Hartley, Sturgess and Rowe (14) did not physically represent any layer of lubricant, but instead was a mechanism to model the effects of such a layer. In this technique, the stiffnesses of the elements in the friction layer were multiplied by the factor $m/(1-m)$, where m is the friction factor of the surface. The finite-element results obtained using this friction technique were in good agreement with experimental findings for the upsetting of solid cylinders (14) and rings (1).

The last method mentioned above would appear to be the most promising technique for the present analysis because it is fully predictive, it has proved to work well in axi-symmetric treatments and may be incorporated into finite-element programs with little difficulty. This technique has been modified for use in the current three-dimensional analysis as described in the next section.

3.2.1.2.2.2 'Beta-Stiffness' Friction Mechanism

When there is relative movement between a work-piece and the die surface during a forging operation, a frictional force is developed which tends to oppose the relative motion. Friction-layer techniques model this behaviour by means of an extra layer of finite elements placed on surfaces of the mesh on which friction is meant to act.

The general principle is illustrated in fig. 3.7a (a two-dimensional mesh is shown for clarity), in which the friction layer is drawn with dashed lines. The friction-layer nodes (i.e. those which only belong to the additional, friction layer of elements) are constrained so that they may only move perpendicularly to the interface between the die and the billet. The nodes of the billet which are meant to be in contact with the die are constrained to move tangentially to it.

Thus any movement of the surface nodes of the billet will introduce shear strain into the friction-layer elements which will generate opposing, stiffness forces. By adjusting the stiffness of the friction layer, these forces can be made to simulate the required frictional restraint.

In order to preserve the integrity of the friction layer, and to avoid excessively deformed friction-layer elements, the friction layer should be re-formed at the start of each increment.

Hartley (1) demonstrated that, for axisymmetric analyses, the adjustment could be carried out by multiplying the whole stiffness matrix of any friction-layer element by what he called the beta factor $= m/(1-m)$, where m is the friction factor of the billet-die surface defined by eqn. 3.3. As m approaches one, this factor tends to infinity, the friction layer becomes very stiff and prevents the surface billet nodes from moving (sticking-friction condition).

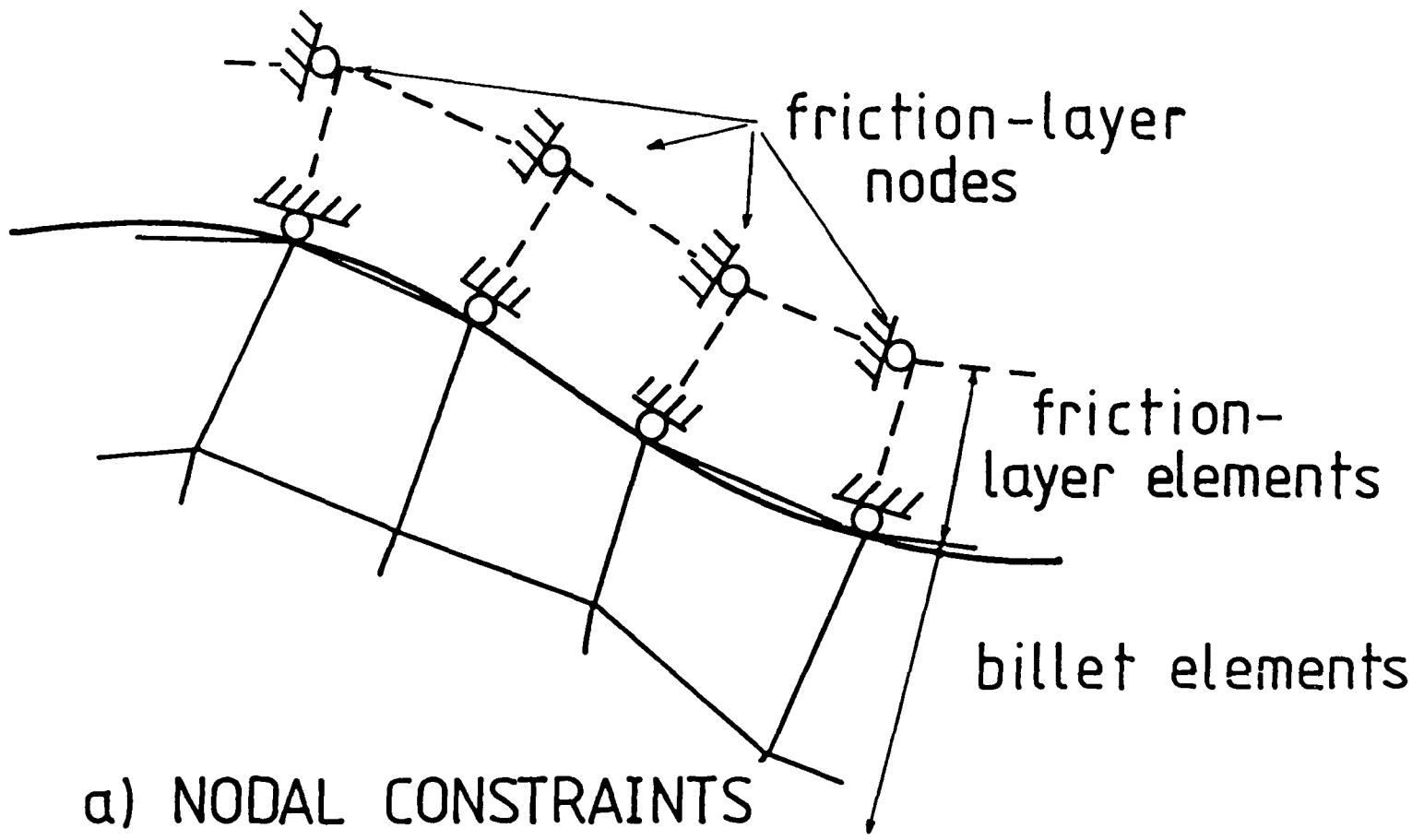

a) NODAL CONSTRAINTS

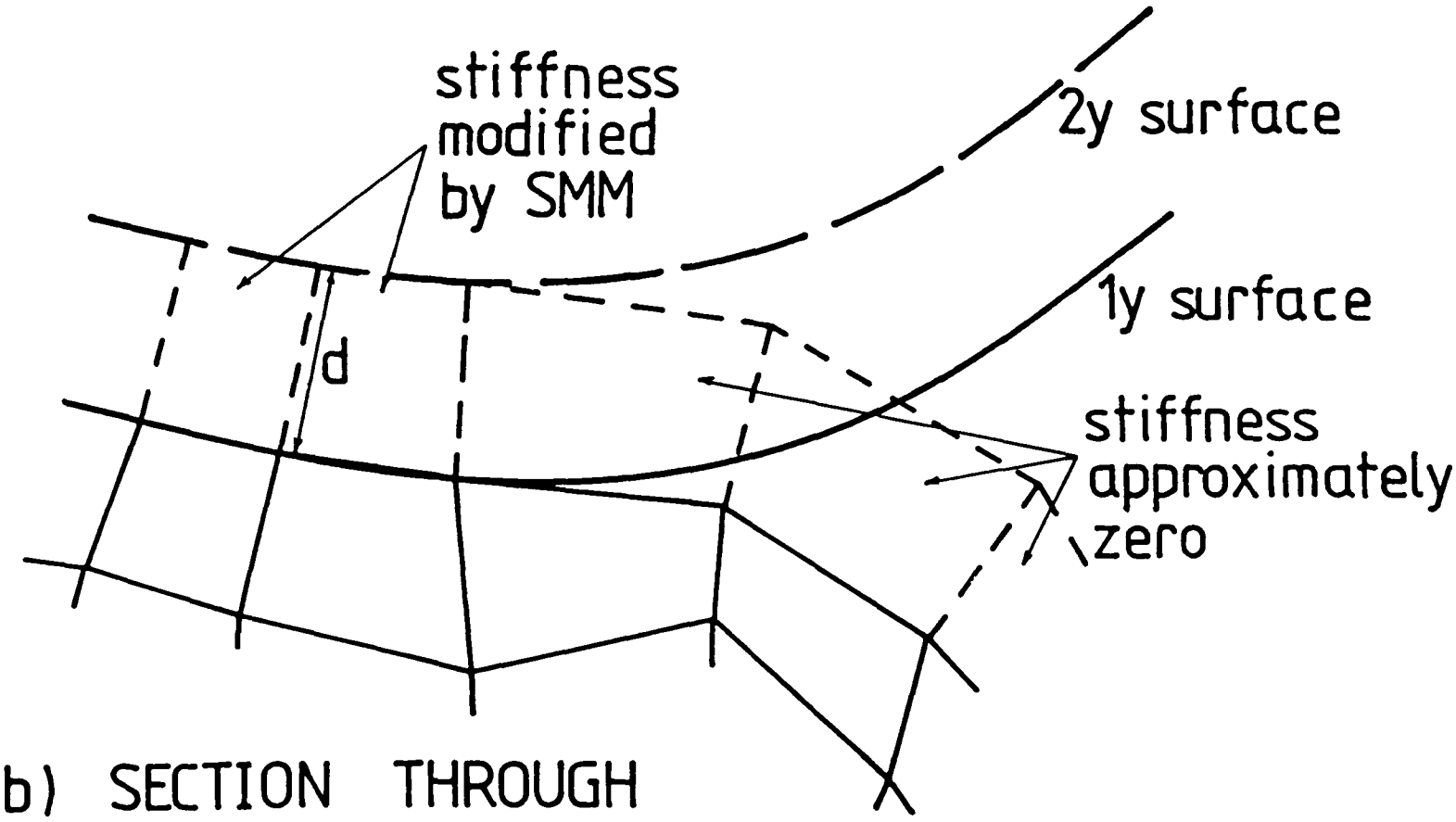

b) SECTION THROUGH
MESH IN PARTIAL CONTACT WITH
FRICTIONAL BOUNDARY SURFACE

FIG. 3.7

FRICTION-LAYER TECHNIQUE

When m is small, the beta factor is approximately equal to m, and as m tends to zero so does the stiffness of the friction layer (zero-friction condition).

In Hartley's work, the stiffness matrices of the friction-layer elements were based upon the current state of strain and stress in those elements. The frictional restraint generated by this mechanism therefore depended upon the strain history of the friction layer. Since this technique is not meant to model any physical interface layer, there is little justification for including this dependence.

Thus for the present work, the friction-layer elements are assumed to be stress- and strain-free at the start of each increment. As a consequence, these elements always deform elastically, with a stiffness which is much larger than that of the plastically-deforming billet, and it is necessary to use a modified multiplier for the stiffness matrices of the friction-layer elements. For a given element this is the product of the beta factor and the ratio H'/E, where E is Young's modulus and H' is the slope of the generalised stress vs plastic strain curve of the material for the value of plastic strain in the billet element adjoining the friction-layer element under consideration. This product is called the stiffness-matrix multiplier (SMM).

3.2.1.2.2.3 Implementation of Friction Mechanism

Friction is incorporated into the current finite-element analysis as a natural extension of the method used to model zero- and sticking-friction surfaces (section 3.2.1.2.1).

When the finite-element mesh is defined, an additional layer of elements is modelled on every surface of the billet which can come into contact with a die surface during the deformation. The extra nodes thus introduced are called friction-layer nodes. Friction-layer nodes and elements are recognised by the finite-element program and are treated differently to billet nodes and elements. For example, change of stress is not calculated for friction-layer elements.

The only additional information which has to be supplied is a friction factor for each boundary surface, from which the program determines whether the surface has a zero-, a sticking- or an intermediate-friction restraint, and in the last case calculates the SMM, as above.

Any billet node passing through, or close to, an intermediate-friction boundary surface is re-positioned and constrained as for a zero-friction surface. When a friction-layer element has four of its billet nodes in contact with the same frictional-boundary surface, any friction-layer node belonging to the element is re-positioned so that it lies on the corresponding secondary surface, directly opposite the billet node which is adjacent to it (i.e. shares an edge of the element with it), and is constrained so that it may only move normally to the boundary surface during the following increment of deformation. Also, the stiffness matrix of such an element is multiplied by the appropriate SMM for that element and boundary surface before assembly into the global matrix for this step.

If a friction-layer element does not have four of its billet

nodes in contact with the same boundary surface, its stiffness matrix is multiplied by a very small number, effectively de-coupling the relevant friction-layer nodes from the rest of the mesh. Thus the friction-layer elements have no effect upon the deformation of the mesh until they are completely in contact with a frictional-boundary surface, whereupon they exert the required frictional restraint (fig. 3.7b).

If at any stage a friction-layer node does not belong to a friction-layer element which has four of its billet nodes in contact with a boundary surface, it is not re-positioned and is subject to any originally-prescribed displacement during the following increment.

3.2.2 Frontal Technique

The frontal technique reduces the computer core storage required to solve banded simultaneous equations at the cost of greater computational complexity and effort, and increased solution time. The latter is mainly due to the dependence upon slow, disc transfers to bring the reduced equations in and out of core.

The reductions in main-memory storage are considerable. For example, the finite-element program described here can cope with meshes containing up to 1331 nodes, each with three degrees of freedom, and a maximum, nodal semi-bandwidth of 92. It requires about 64K words of the core to be devoted to storing the frontal area and other arrays used in the solution. This compares with a core space of just over 1.1M words to store the entire upper band of the stiffness matrix, or almost 16M words for the whole matrix.

The CDC 7600 used for the finite-element analysis has, technically, an available core of about 180K words. In practice, this figure is much less because of system overheads. In any case, there would not be enough room to store the whole, upper band of the stiffness matrix, for the size of mesh it is necessary to consider in three-dimensional problems.

3.2.2.1 Implementation

The area of core used to store the frontal part of the stiffness matrix, called the processing area, is divided up into blocks of nine consecutive words, each of which can contain a 3x3 submatrix. Associated with each block is an entry in an indexing array,

indicating by a simple 0-1 switch whether that block is currently occupied. To reduce search times, the index is itself divided into sections, each of which corresponds to an entry of a sub-index. These entries are switched to show a vacancy if and only if at least one of the entries of the associated section of the indexing array indicates a vacant block.

A destination array shows which block of the processing area is used to store a given sub-matrix. The destination array is divided into sections, one for each of the 92 equations which can be accommodated, in upper-triangular form, in the processing area at any one time. Each section consists of an entry for each of the nodal displacements which can occur in the associated equation, in the order of elimination of these nodes from the processing area.

A separate array lists all the node numbers in the mesh in this same order, and another gives the order of elimination of each node. A directory array, with one entry for each node in the mesh, gives the section of the destination array referring to the equations at that node, when they are in the processing area.

3.2.2.1.1 Assembly

Each element is considered in turn, in numerical order, and its element stiffness matrix formed by numerical integration over the specified number of sample points, according to equation 2.42. Each of its sub-matrices are then considered, and the orders of elimination of the two nodes, with which it is associated, are compared to see whether this sub-matrix occurs in the upper triangle of the global

matrix. If this is so, the section of the destination array, referring to the equations of which this sub-matrix forms a part, is found from the directory array, and the appropriate entry of the destination array examined.

If this is non-zero, the number refers to a block of the processing area, and so the sub-matrix can be added to the current occupant of the block. If it is zero, the sub-index and index are searched to find the first vacant block of the processing area. The sub-matrix is then entered into this block, and the corresponding entries of the index, and if necessary, the sub-index, re-set. The number of the block replaces the zero entry just found in the destination array.

3.2.2.1.2 Elimination

After each element has been assembled into the processing area, any node which occurs in none of the subsequent elements is identified, (this information is encoded into the element definition array). The three equations for the force at such a node are therefore fully-assembled, and may be transferred to disc storage, after they have been used to eliminate the displacement at their node from the other equations in the processing area.

Each set of three fully-assembled and reduced equations is transferred to a holding array from the various blocks of the processing area. The latter can then be cleared, and the appropriate entries in the index and the destination arrays re-set, after the production of a list of the node numbers associated with the

displacements of the three reduced equations. These numbers help to identify the equations affected by the elimination, and are also used later during the back-substitution.

The elimination of the displacement from the other equations is carried out in the usual way, with the appropriate section and entry of the destination array again being used to find the blocks containing the sub-matrices to be modified. As before, a vacant block is used if the sub-matrix has not yet been inserted into the processing area.

The three fully-assembled equations, along with the list of associated nodes and the modified load terms can then be transferred to disc storage.

3.2.2.2 Disadvantages

The main problem with the frontal technique, apart from the initial complexity of the computer coding, is that, compared with a direct elimination method, it is very slow. This is largely because of the disc transfers. Currently, a transfer is carried out for every node, as its equations become fully-assembled. The situation could be improved by buffering, and this should be considered for the next stage of development of the program.

3.2.3 Methods of Non-Linear Analysis

In the previous chapter, the relationship between increments of nodal displacement and force was expressed in terms of the global stiffness matrix [K], this being the superposition of the element stiffness matrices $[K_n]$ where:

$$[K_n] = \Sigma w_i\{([B_n^{\varepsilon}]^T([D_n]-[T_n])[B_n^{\varepsilon}]+[B_n^{q}]^T[U_n][B_n^{q}]- \kappa[B_n^{b}]^T[B_n^{b}])|J_n|\} + \frac{\kappa}{V_n}\Sigma w_i\{[B_n^{b}]^T|J_n|\}\,\Sigma w_i\{[B_n^{b}]|J_n|\} \qquad (3.5)$$

The numerical integration is carried out over the volume of the nth element, and all the matrices have been defined earlier.

The nature of the matrix $[D_n]$ depends upon the assumptions made about the elastic and plastic behaviour of the material. In the elastic-plastic analysis considered here, $[D_n]$ is based upon Von Mises' yield criterion and the Prandtl-Reuss equations of flow.

The latter express increments of strain in terms of their elastic and plastic parts (20). In vector form, the equations may be written as:

$$\Delta\underline{\varepsilon} = [D]^{-1}\Delta\underline{\sigma}^J + [M]\underline{\sigma}'\Delta\lambda \qquad (3.6)$$

where $\Delta\underline{\varepsilon}$ and $\Delta\underline{\sigma}^J$ are the increments in the linearised co-rotational strain and Jaumann stress vectors. [D] is the elastic stress-strain matrix derived from Hooke's law (94) and defined in fig. 3.8, in which E is Young's modulus and ν is Poisson's ratio, and [M], which is also defined in fig. 3.8, is used to simplify the vector expression. Its form results from the fact that the shear components of $\Delta\underline{\varepsilon}$ are twice the values of the corresponding shear components in the incremental-strain tensor.

$$[D] = \frac{E}{1+\nu}\begin{bmatrix} \frac{1-\nu}{1-2\nu} & \frac{\nu}{1-2\nu} & \frac{\nu}{1-2\nu} & 0 & 0 & 0 \\ & \frac{1-\nu}{1-2\nu} & \frac{\nu}{1-2\nu} & 0 & 0 & 0 \\ & & \frac{1-\nu}{1-2\nu} & 0 & 0 & 0 \\ & & & \frac{1}{2} & 0 & 0 \\ & \text{SYM} & & & \frac{1}{2} & 0 \\ & & & & & \frac{1}{2} \end{bmatrix}$$

$$[M] = \begin{bmatrix} 1 & 0 & 0 & 0 & 0 & 0 \\ & 1 & 0 & 0 & 0 & 0 \\ & & 1 & 0 & 0 & 0 \\ & & & 2 & 0 & 0 \\ & & & & 2 & 0 \\ & \text{SYM} & & & & 2 \end{bmatrix}$$

FIG. 3.8
MATRICES USED IN CALCULATION OF STRESS

The deviatoric stress, $\underline{\sigma}'$ in eqn. 3.6, is defined by:

$$\underline{\sigma}' = \underline{\sigma} - (1\ 1\ 1\ 0\ 0\ 0)^T \sigma_h \qquad (3.7)$$

where

$$\sigma_h = \frac{1}{3}(\sigma_{xx} + \sigma_{yy} + \sigma_{zz}) \qquad (3.8)$$

The quantity $\Delta\lambda$, in eqn. 3.6, is a proportionality factor dependent upon the state of deformation and the size of the increment. It may be taken to be zero if Von Mises's yield criterion is not satisfied, i.e.:

$$\Delta\lambda = 0 \quad \text{if} \quad \bar{\sigma} < Y \qquad (3.9)$$

where $\bar{\sigma}$ is the generalised stress, a function g of $\underline{\sigma}'$ such that:

$$\bar{\sigma} = g(\underline{\sigma}') = \left(\frac{3}{2} \underline{\sigma}'^T [M] \underline{\sigma}' \right)^{\frac{1}{2}} \qquad (3.10)$$

and Y is the axial yield stress in a tensile test. In general, Y is a function of the accumulated, generalised, plastic strain $\bar{\varepsilon}^p$ where:

$$\bar{\varepsilon}^p = \int d\bar{\varepsilon}^p \qquad (3.11)$$

and

$$\Delta\bar{\varepsilon}^p = \left(\frac{2}{3} \Delta\underline{\varepsilon}^{pT} [\bar{M}]^1 \Delta\underline{\varepsilon}^p\right)^{\frac{1}{2}} \qquad (3.12)$$

The vector $\Delta\underline{\varepsilon}^p$ is the increment in plastic strain and the integration above is performed over the strain path.

$\Delta\lambda$ may be expressesd in terms of H', the slope of the curve of Y against $\bar{\varepsilon}^p$, generalised stress and vector increment of stress, allowing eqn. 3.6 to be inverted to give (95):

$$\Delta\underline{\sigma}^J = [D^p]\Delta\underline{\epsilon} \qquad (3.13)$$

for $\bar{\sigma} = Y$, where:

$$[D^p] = [D] - [E/(1+\nu)s]\ \underline{\sigma}'.\ \underline{\sigma}'^T \qquad (3.14)$$

and

$$s = 2\bar{\sigma}^2[1 + 2(1+\nu)H'/3E]/3 \qquad (3.15)$$

Thus, in eqn. 3.5, $[D_n] = [D^p]$ if $\bar{\sigma} = Y$, and $[D_n] = [D]$ if $\bar{\sigma} < Y$.

In general, the stiffness relationship involves both material and geometric non-linearity since [K] is a function both of the current state of strain and stress in the body (via $[D_n]$, $[T_n]$ and $[U_n]$) and of the current coordinates of the nodes (via the B matrices). Only when the whole mesh is elastic will the stiffness relationship be linear since in this case, $[D_n]$ is put equal to the constant matrix [D] in all elements, in comparison with which, $[T_n]$ and $[U_n]$ may be neglected, and the nodal displacements are small enough for the B matrices to be taken as constant throughout the deformation.

In all other cases, if [K] is calculated at the start of an increment, (tangent-modulus approach) the displacement change obtained by solving the stiffness equations will not be correct.

Iteration provides one means of improving the accuracy of the increments in displacement. The iterative technique which may be used in the program is called, variously, modified-Newton-Raphson (28), or initial-stiffness (77). This procedure is described in section 3.2.3.1.

Another method which the current finite-element program can adopt in order to correct for non-linearity is the secant (predictor-corrector) technique. This is considered in section 3.2.3.2.

3.2.3.1 Method of Iteration

Suppose the applied nodal force array for a certain increment is $\Delta\underline{f}^{(1)}$, then by the inverse of eqn. 2.43, the resulting change in displacement is given by:

$$\Delta\underline{d}^{(1)} = [K]^{-1}\Delta\underline{f}^{(1)} \qquad (3.16)$$

The corresponding change in the co-rotational strain vector and the Cauchy stress vector $\Delta\underline{\sigma}^{(1)}$ may be calculated as explained in section 3.2.4. The change in nodal force $\Delta\underline{f}^{(1)}$ which is in equilibrium with the stress change calculated for element n may then be found from eqn. 2.5 to be:

$$\Delta\underline{f}_n^{(1)} = \int [B_n]^T \Delta\underline{\sigma}^{(1)} dvol \qquad (3.17)$$

where the integration is carried out over the volume of the nth element by Gaussian quadrature, as for the element stiffness matrices, and $[B_n]$ is obtained from $[B_n^{\epsilon}]$ by putting [R] = [I]. Cauchy stress is used in this expression in preference to the nominal stress used in eqn. 2.5 because the former is symmetric and may be represented by a six-dimensional vector. The error thus introduced into the equilibrating force will be small providing the increments of deformation are not too large.

Summation of the equilibrating force changes for all the elements, allows the formation of a global array $\Delta\underline{f}^{(1)}$, which is in equilibrium with the calculated change in stress throughout the mesh.

In general, because of the non-linearity of the stiffness relationships, this force vector will not be the same as the applied force $\Delta\underline{f}^{(1)}$. A correction to the displacement may be evaluated using

the same incremental stiffness matrix, but with the residual force:

$$\Delta\underline{f}^{(2)} = \Delta\underline{f}^{(1)} - \Delta\underline{f}^{(1)=} \tag{3.18}$$

Hence:
$$\Delta\underline{d}^{(2)} = [K]^{-1}\Delta\underline{f}^{(2)} \tag{3.19}$$

This iterative process may be repeated. Generally, for the ith iteration:

$$\Delta\underline{d}^{(i)} = [K]^{-1}\Delta\underline{f}^{(i)} \tag{3.20}$$

where:
$$\Delta\underline{f}^{(i)} = \Delta\underline{f}^{(i-1)} - \Delta\underline{f}^{(i-1)=} \quad \text{for } i>1$$

$$= \text{applied nodal force, for } i=1 \tag{3.21}$$

and $\Delta\underline{f}^{(i-1)=}$ is the change in nodal force in equilibrium with the distribution of incremental stress calculated from $\Delta\underline{d}^{(i-1)}$. This process is illustrated for a single-variable problem in fig. 3.9.

The nodal displacement for an increment is, finally, the sum of the displacement changes calculated for all the iterations within that increment.

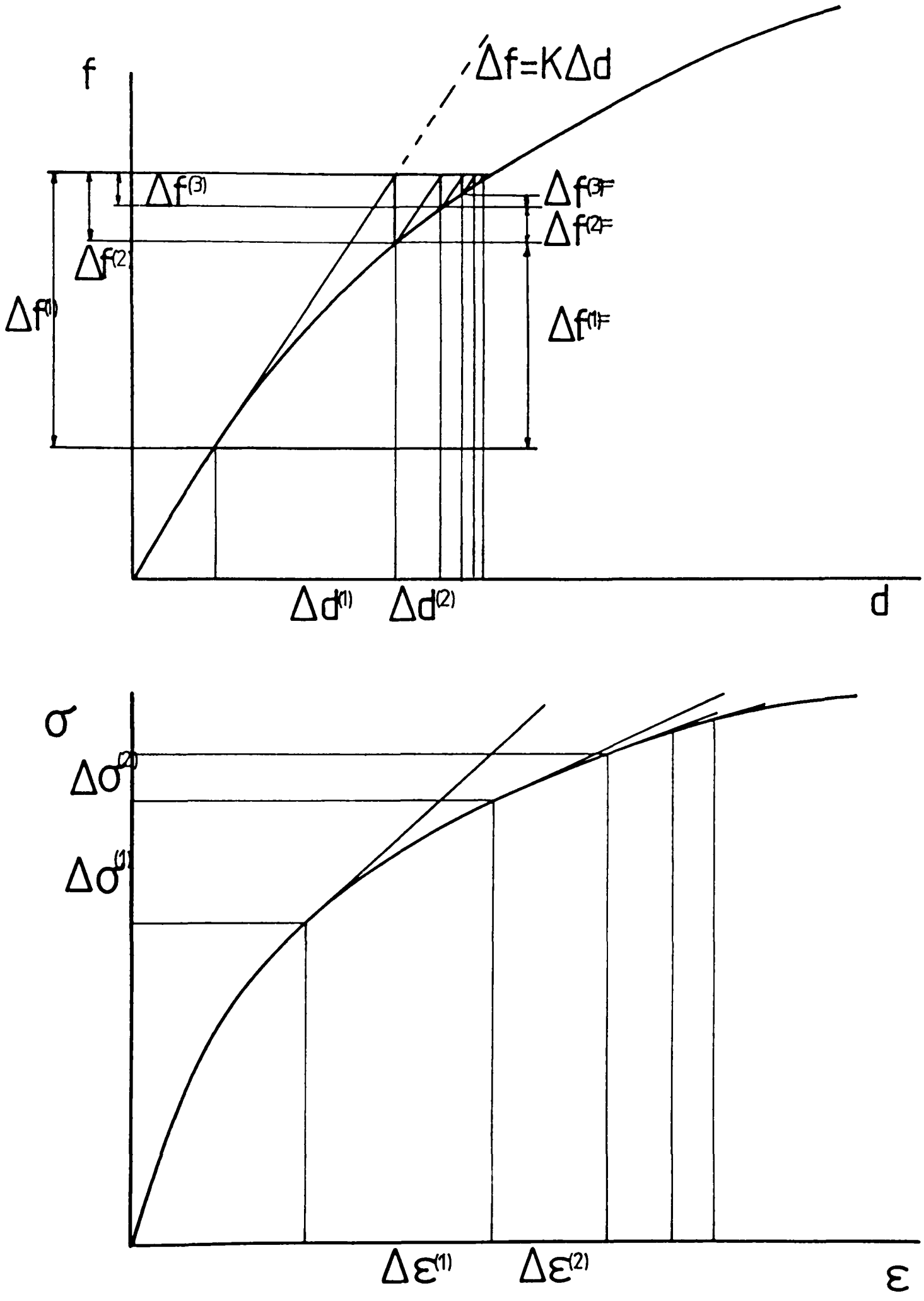

FIG. 3.9

SINGLE VARIABLE DEMONSTRATION OF METHOD OF ITERATION

3.2.3.1.1 Prescribed Displacement Changes During Iteration

The previous section described the method of iterating the incremental solution when the deformation step was defined by an applied nodal force increment. The description is equally valid if certain components of the nodal displacement also have prescribed, incremental values, except that, at the end of the first iteration, $\Delta\underline{d}^{(1)}$ contains the correct values of the specified components of displacement, and the changes brought about by subsequent iterations must not alter these quantities. To this end, during the solution of the stiffness equations, for all iterations after the first, any component of displacement which hasal value is assumed to have a prescribed value of zero.

3.2.3.1.2 Convergence Criterion

The iteration of the incremental solution may be terminated when either $\Delta\underline{d}^{(i)}$ or $\Delta\underline{f}^{(i)}$ becomes sufficiently small. In the treatment described here, the former array is used because nodal displacement values are required as output to the program. This is in contrast to the values of nodal force, which are only used internally.

It is convenient to work with a scalar measure of the displacement array, and the modulus (or vector norm) operator is suitable for this purpose.

A convergence factor CONF is specified for each analysis, and a reference value, REF, calculated from the displacement change for the first iteration of each increment as:

$$REF = CONF|\Delta \underline{d}^{(1)}| \qquad (3.22)$$

The iteration of the solution for that increment is then continued until iteration i, such that:

$$|\Delta \underline{d}^{(i)}| \leq REF \qquad (3.23)$$

If this condition is not satisfied by the time i=20, the process is stopped, and a warning printed.

The best value of CONF for a given situation can only be found by experience, bearing in mind the trade-off between accuracy of solution and speed of computation. A value of 0.001 has been used successfully in many analyses, with 0.01 being used when the rate of convergence was slow.

Since, in the current version of the finite-element program, the test for convergence is carried out for the first iteration as well as the rest, a value of CONF greater than or equal to one will cause precisely one iteration to be performed for each increment, giving a tangent- or secant-modulus analysis.

3.2.3.1.3 Re-Solution of Stiffness Equations

A large part of the computing time spent upon a finite-element analysis is devoted to assembling and solving the stiffness equations. The advantage of the modified, as opposed to the unmodified, Newton-Raphson method of iteration, is that with the former, the same stiffness matrix is used throughout an increment, so much of the

computation involved in producing a solution need be done only for the first iteration. Subsequent iterations can perform a re-solution, using different load arrays, in a much shorter time. The unmodified method requires that a different stiffness matrix be assembled and solved for each iteration, so that although the number of iterations may be smaller, the overall time of computation is usually much longer, compared with the modified approach.

Examination of the technique of Gaussian elimination, both in its usual form, as described in section 2.2, or adapted for prescribed displacements, as in section 3.2.1.1, shows that:

a) any modification made to the coefficients of the stiffness matrix is independent of the loading array, or the value of any prescribed displacement,

b) any modification made to the load terms depends only upon other load terms, values of prescribed displacements, and the values of coefficients in a row of the stiffness matrix, when that row is about to be transferred to disc storage.

These facts mean that the re-solution of the stiffness equations with different load arrays, (and different values of prescribed displacement), can use the reduced coefficients of the stiffness matrix stored on disc, without modification, to duplicate the effect of the elimination procedure upon the new load array.

The process of back-substitution is the same for a re-solution as for the first solution, except for the values used for the prescribed components of displacements.

The saving in computational time resulting from the above procedure varies widely with the number of elements in the mesh. For very small numbers of elements, the reduction in time of solution is not great, while the second or subsequent iteration of the incremental solution, for a mesh with the maximum number of elements allowed by

the program, can be accomplished in about 4% of the time for a first iteration.

3.2.3.1.4 Use of Deviatoric Stress Changes in Iteration

The option is provided in the finite-element program of calculating the residual force at the start of each iteration from the change in nodal force which is in equilibrium with the change in the deviatoric components of stress, for fully-plastic elements; total components of stress being used for all other elements. The provision of this alternative method of iterating was a response to convergence problems experienced during the development of the program.

These problems appeared to stem from excessive volume changes calculated for yielded elements. Although these volume strains were small compared with the plastic strain occurring, they gave rise to significant changes in hydrostatic stress. On iteration, the resulting residual forces seemed to over-compensate for the initial volume change, leading, eventually, to an oscillating, divergent solution.

It was hoped to avoid this behaviour by ignoring the hydrostatic stress, for the purpose of equilibrating the nodal forces, and enforcing volume constancy in yielded elements. The justification for using this technique is that:

a) the iteration should produce a solution in which the displacements are compatible with the deviatoric stresses,

b) this solution differs from the correct one by an amount of bulk strain which is small compared with the rest of the strain.

If the alternative method of evaluating residual forces is adopted,

the changes in deviatoric stress are only used to find the equilibrating nodal forces for elements which were already yielded at the start of the increment of deformation. For other elements, the change in total stress is used instead because:

a) bulk strain is not small compared with the total strain for elastic deformations,

b) erroneous values of the change in hydrostatic stress are only calculated for plastic deformations - both the deviatoric and the hydrostatic components of stress may be calculated accurately before yield.

3.2.3.2 Secant-Modulus Method

This method is an example of a predictor-corrector solution of the difference equations relating force and displacement. In particular, it is based on the second-order Runge-Kutta or modified-Euler technique (96). The latter corrects for non-linearity by calculating the slope of a function, not at the start of a given interval, but halfway through (i.e. as a secant to the curve). Since the gradient will generally depend upon the value of the function as well as the independent variable, the evaluation of the slope at the mid-point of the interval requires that a trial value of the function is first estimated or predicted there by using the gradient at the start. The mid-point slope can then be used to correct the estimated change in the value of the function.

In the finite-element program developed here, the secant-modulus

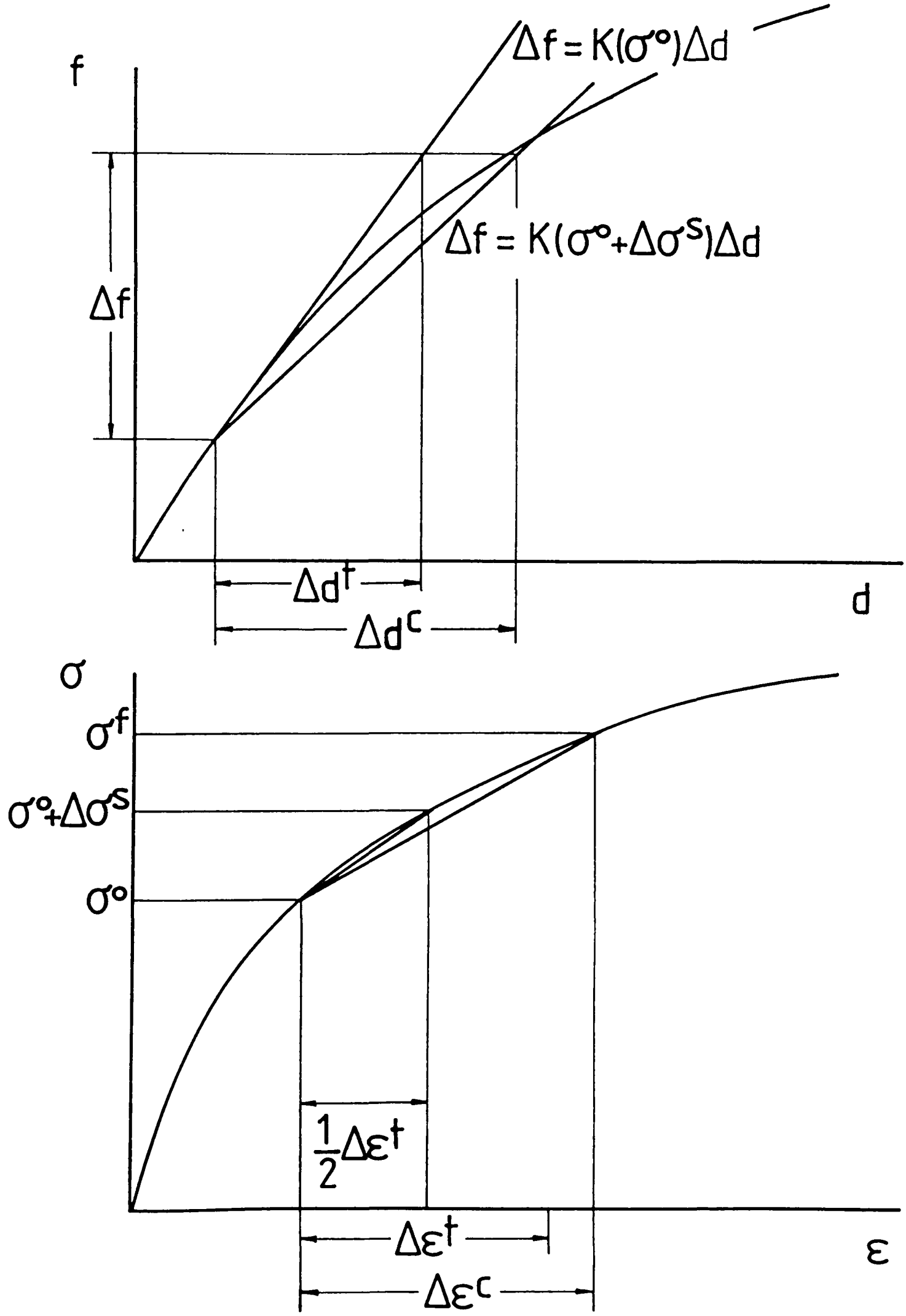

FIG. 3.10

SINGLE VARIABLE DEMONSTRATION OF SECANT-MODULUS METHOD OF SOLUTION

method is implemented by first performing a tangent-modulus solution of the stiffness equations (i.e. with [K] evaluated at the start of the increment) and obtaining the change in stress, as described in section 3.2.4, which corresponds to an application of half of the calculated strain increment. The stiffness matrix is then re-calculated using the resulting mid-increment stress (and the [R] matrices evaluated for the whole of the tangent-modulus step) and the stiffness equations re-solved with the same boundary conditions as before, to obtain the corrected, incremental-displacement array. This procedure is illustrated for a one-variable problem in fig. 3.10.

Although the secant-modulus method requires two solutions of the stiffness equations for each increment, it is generally more efficient than the tangent-modulus approach since the size of the increment can usually be made at least twice as big without decreasing the accuracy of the solution.

3.2.3.3 Elastic-Plastic Transition

One aspect of the non-linearity of the stiffness relationship which has not yet been mentioned is that concerned with the discontinuity in the slope of the stress-strain curve at the yield point. The problems in this case are more severe than those associated with the variation of $[D_n]$ with strain and stress after yield, since the slope of the stress-strain relationship can change by several orders of magnitude between the elastic and the plastic regions.

Consider an element which reaches the plastic-yield point during some increment. In order to calculate the correct displacement field

for this element, the incremental deformation ought to be divided into elastic and plastic stages, and the stiffness matrix re-calculated for the latter using the elastic-plastic stress-strain matrix. In practice, it is not feasible to split up the increments so that the deformation in each element is correctly dealt with in this way, and the deformation is calculated assuming that the element behaves elastically throughout a transition increment. Iteration is of little help in correcting the inaccurate displacements which result, and though the secant method may predict that the element has yielded during the first half of the increment, the corrector solution would then be based on the assumption that the whole increment is plastic.

However, it is possible to minimise the error caused by elastic-plastic transition by reducing the size of the increments while the mesh is still partially plastic. In the present finite-element program this procedure is carried out automatically using a technique first suggested by Yamada, Yoshimura and Sakurai (45).

Firstly, define the hypothetical-elastic increment of stress to be the change in stress calculated by assuming that the deformation is completely elastic, irrespective of whether the generalised stress exceeds the yield value. During each increment, for as long as the mesh contains unyielded elements, the calculated increment of global displacement is scaled by a factor p so that, for the reduced step, the initially-elastic element with the largest value of generalised stress has a hypothetical-elastic increment of stress which would make its final generalised stress 20% larger than the current value of yield stress.

The value of 20% is chosen as a compromise, i.e. so that only a small amount of plastic deformation occurs in an element during its transition increment, but also so that a significant number of elements yield during the same increment, to avoid excessively

lengthening the computation.

The factor p is calculated as follows. After the determination of the change in displacement for an increment, each unyielded element is considered in turn and its initial deviatoric stress, $\underline{\sigma}'$ and hypothetical-elastic, Jaumann increment of deviatoric stress $\Delta\underline{\sigma}^{eJ}{}'$ found. If Y^o is the current value of yield stress for that element, a value of p is obtained for that element such that:

$$g(\underline{\sigma}'+p\Delta\underline{\sigma}^{eJ}{}') = 1.2Y^o \qquad (3.24)$$

Using the definition of g given in eqn. 3.10, eqn. 3.24 may be expanded to give a quadratic equation in p which can be solved to produce:

$$p = ((b^2 - 4g(\Delta\underline{\sigma}^{eJ}{}')^2(g(\underline{\sigma}')^2 - 1.44Y^{o2}))^{\frac{1}{2}} - b)/2g(\Delta\underline{\sigma}^{eJ}{}')^2 \qquad (3.25)$$

where: $b = 3\underline{\sigma}'^T[M]\Delta\underline{\sigma}^{eJ}{}'$ and $\Delta\underline{\sigma}^{eJ}{}' = 2G[M]^{-1}\Delta\underline{\varepsilon}'$ (3.26)

in which $\Delta\underline{\varepsilon}'$ is the deviatoric-strain increment defined by eqns. 2.21 and G is the rigidity modulus.

The positive square root is taken in this case because $p \geq 0$. If the value of p is greater than one, the element does not yield during the increment.

The required value of p for the scaling procedure is then the minimum value of p obtained by this means for all elements which were elastic at the start of the increment.

3.2.4 Calculation Of Stress

After each evaluation of the incremental nodal-displacement array, the corresponding change in strain and stress is found at each Gaussian sample point of each element (eight sample points per element). The only exception to this is that no stress change is calculated for a friction-layer element until all four of its billet nodes are in contact with the same frictional-boundary surface.

The changes in generalised plastic strain and components of stress at the sample points are then used to update the current values of these quantities. At the end of each increment, the values of strain and stress at the eight sample points of each element are averaged to give the corresponding element values. Only these element values are printed; the sample-point values are stored for use in the calculation of hydrostatic stress by the indirect method, while the changes in the sample-point stresses are used in the calculation of residual force.

3.2.4.1 Calculation of Lagrangian Strain at Sample Points

At each sample point, The incremental-displacement gradient tensor [Q] is evaluated from the incremental displacement of the nodes of the element using eqns. 2.2 and 2.32, i.e.:

$$[Q] = \underline{\nabla}\, \underline{d}_n^T [N_n]^T \qquad (3.27)$$

As mentioned in section 2.1.1.3.1, the correct strain to use for the

present analysis is the Lagrangian measure. Although this is non-linear and cannot be incorporated into the stiffness formulation, once the incremental-displacements have been calculated according to eqn. 3.27, the increment of Lagrangian strain $[\Delta\varepsilon^L]$ may be easily evaluated using the relationship:

$$[\Delta\varepsilon^L] = 0.5([Q] + [Q]^T + [Q][Q]^T) \qquad (3.28)$$

quoted earlier.

The rotational matrix [R], required to calculate the stiffness matrix for the next increment (section 2.1.1.3.3), is found from eqn. 2.11:

$$[R] = ([Q]^T + [I])[V]^{-1} \qquad (3.29)$$

where the symmetric deformation matrix [V] is evaluated according to:

$$[V]^2 = 2[\Delta\varepsilon^L] + [I] \qquad (3.30)$$

which is derived by comparing eqns. 2.12 and 3.28.

The square root of the right-hand side of eqn. 3.30 is obtained by Newton's method, starting with an initial guess for [V] of $[\Delta\varepsilon^L]$ + [I]. Since the components of $[\Delta\varepsilon^L]$ generally have a magnitude much less than one, this procedure is rapidly convergent, typically to within 0.0001% after four or five iterations.

The existence of an inverse of [V], and hence of each of the sequence of approximations to [V], is guaranteed by the physical non-singularity of the transformation $[Q]^T$ + [I].

3.2.4.2 Calculation of Jaumann Increment of Deviatoric Stress

Suppose that at the start of the increment, the stress vector at the sample point is $\underline{\sigma}$ and the accumulated plastic strain is $\overline{\varepsilon}^p$ (defined by eqns. 3.11 and 3.12). The initial deviatoric-stress vector, from eqns. 3.7 and 3.8, is therefore $\underline{\sigma}'$. Suppose the co-rotational change in strain, in vector form, calculated for this increment from eqn. 3.28 is $\Delta\underline{\varepsilon}$. Let $\Delta\underline{\varepsilon}'$ and $\Delta\varepsilon_b$ be the corresponding deviatoric and bulk components of this strain, as described by eqns. 2.21.

In general, let a fraction r of the increment of deformation occur while the material is still elastic at the sample point, and fraction 1-r occur after the yield point has been reached, where $0 \leq r \leq 1$. The situations where the whole increment occurs elastically or plastically are special cases of the above, obtained by putting r=1 or r=0 respectively.

3.2.4.2.1 Calculation of r and Elastic Increment of Stress

Consider the situation at a stage during the increment when proportion r of the change in strain has been applied. By definition of r, and according to Von Mises' criterion mentioned in section 3.2.3, the generalised stress at this moment equals the yield stress Y at the start of the increment. For real materials, yield is a function h of plastic strain. In the finite-element program developed here the following function is used:

$$Y = h(\overline{\varepsilon}^p) = h_0 + h_1 \ln(h_2+\overline{\varepsilon}^p/h_2) + h_3 \exp(h_4(\overline{\varepsilon}^p-h_5)) \quad \text{for } \overline{\varepsilon}^p \leq e$$

$$= h(e) + h'(e)(\overline{\varepsilon}^p-e) \quad \text{for } \overline{\varepsilon}^p > e \qquad (3.31)$$

where $h_0 \ldots h_5$, e are empirically-determined constants.

Since the material at the sample point has deformed elastically so far during this increment, the current Jaumann change in deviatoric stress, $\Delta\underline{\sigma}^{IJ}{}'$ is given by Hooke's law:

$$\begin{aligned} \Delta\underline{\sigma}^{IJ}{}' &= 2G[M]^{-1}r\Delta\underline{\varepsilon}' \\ &= r\Delta\underline{\sigma}^{eJ}{}' \end{aligned} \qquad (3.32)$$

where $\Delta\underline{\sigma}^{eJ}{}'$ is the hypothetical-elastic Jaumann increment of deviatoric stress introduced in section 3.2.3.3, defined to be the change in stress which would result if the whole of the incremental deformation occurred elastically. G is the rigidity modulus for the material, = $E/2(1+\nu)$. For yield:

$$g(\underline{\sigma}'+r\Delta\underline{\sigma}^{eJ}{}') = Y^{o} \qquad (3.33)$$

where the generalised-stress function g has been defined previously. Squaring and expanding the left-hand side of eqn. 3.33 gives a quadratic equation in r:

$$g(\Delta\underline{\sigma}^{eJ}{}')^2r^2 + 3\underline{\sigma}'^{T}[M]\Delta\underline{\sigma}^{eJ}{}'r + g(\underline{\sigma}')^2 = Y^{o2}$$

or:

$$ar^2 + br + c = Y^{o2} \qquad (3.34)$$

Since $a \geq 0$ and $c \leq Y$ (i.e. initial generalised stress cannot exceed initial yield stress) it follows that $b^2 - 4a(c-Y^{o2}) \geq 0$ and eqn. 3.34 has at least one real root. Moreover, it can be seen from fig. 3.11 that eqn. 3.34 always has precisely one root greater than or equal to zero, this value being obtained by taking the positive square root in the solution for the quadratic equation.

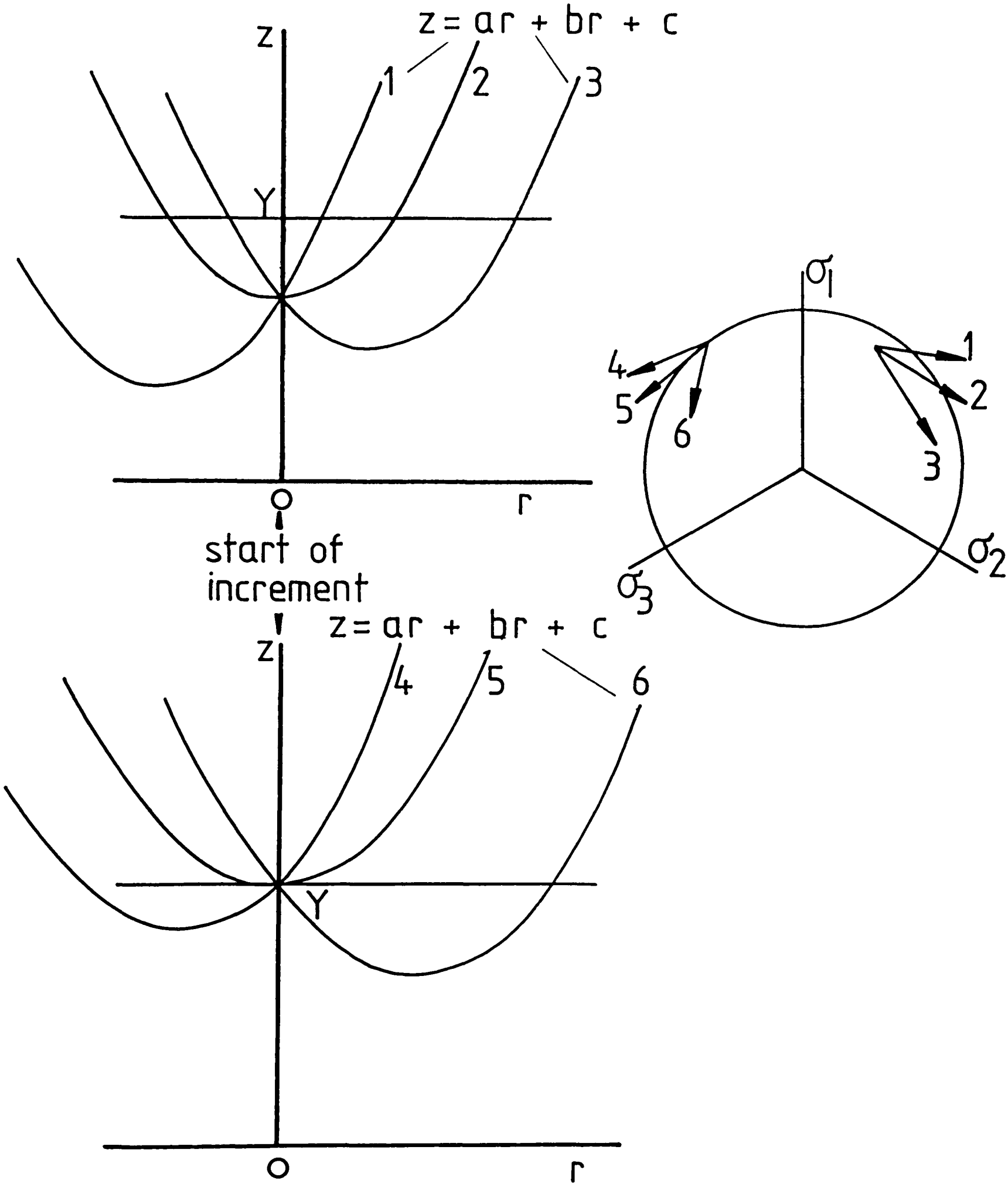

FIG. 3.11

POSSIBLE INTERPRETATIONS OF EQN. 3.34 AND CORRESPONDING STRESS VECTORS IN THE OCTAHEDRAL-STRESS PLANE

Thus:

$$r = ((b^2-4a(c-Y^{O2}))^{\frac{1}{2}} - b)/2a \qquad (3.35)$$

a, b and c are readily calculated from the initial deviatoric stress vector and the hypothetical-elastic increment of stress.

If r equals zero, the whole increment is plastic. If r is greater than or equal to one, it is elastic. In the latter case, r is put equal to one. In all situations, the Jaumann increment of stress occurring during the unyielded part of the increment is given by eqn. 3.32. The deviatoric stress at the end of the elastic part of the increment, $\underline{\sigma}^{IJ'}$ is:

$$\underline{\sigma}^{IJ'} = \underline{\sigma}' + \Delta\underline{\sigma}^{IJ'} \qquad (3.36)$$

3.2.4.2.2 Calculation of Plastic Increment of Stress

The strain applied during the part of the increment after yield has occurred is $\Delta\underline{\varepsilon}^{II} = (1-r)\,\Delta\underline{\varepsilon}$. The corresponding Jaumann increment of stress could be calculated from eqn. 3.13, but this relationship is not linear since $[D_n]$ depends on the current stress and strain, which vary throughout the increment. Thus, if this matrix is calculated at the start of the plastic part of the increment, the resulting change in stress will be incorrect. Although an adjustment can be made to give the correct yield stress at the end of the increment (97), this does not fully correct the error in the direction of the stress-increment vector.

A more serious problem associated with this method of calculating

stress is that of instability. If, in the Prandtl-Reuss equations, the plastic component of the incremental-strain vector is assumed to be proportional to the deviatoric stress at the start of the increment, then any small error in the calculated increment of strain, such as may be caused by numerical round-off in a computer, will tend to induce increasingly larger errors in subsequent increments. There is usually a stability limit - a value of incremental strain below which the errors do not grow uncontrollably - but this limit is of the order of the yield strain. It is generally impractical to perform analyses of large-deformation processes with such small increments.

This problem has been studied analytically by Nagtegaal and de Jong (70), who demonstrated the instability for the special case of a non-hardening, proportionally-loaded deformation. In this situation, the error not only grows, but also changes in sign between increments. An example of instability in a finite-element treatment is also given in appendix D.

Nagtegaal and de Jong showed that the instability could be avoided if the plastic incremental-strain vector is taken to be proportional to the deviatoric stress at the middle of the increment, the so-called mean-normal method, which was first suggested by Rice and Tracey (98). The technique has the additional advantage that the stress state predicted at the end of an increment automatically satisfies the yield criterion (99). In contrast with the usual (tangent) estimation of the increment of stress, which is essentially an Euler solution of the stress-strain difference equations, the mean-normal method corresponds to the more accurate modified-Euler or second-order Runge-Kutta technique.

The previous applications of the mean-normal method have been for non-hardening finite-element treatments. For the present work, the technique has been generalised to include strain hardening.

3.2.4.2.2.1 Mean-Normal Method

By the Prandtl-Reuss flow rule, the deviatoric increment of strain occurring after yield may be divided into elastic and plastic parts:

$$\overset{II}{\Delta\underline{\varepsilon}}' = (1-r)\Delta\underline{\varepsilon}' = \overset{IIe}{\Delta\underline{\varepsilon}}' + \overset{IIp}{\Delta\underline{\varepsilon}}' \qquad (3.37)$$

or:

$$\overset{II}{\Delta\underline{\varepsilon}}' = [M]\overset{IIJ}{\Delta\underline{\sigma}}'/2G + \Delta\lambda[M]\tilde{\underline{\sigma}}' \qquad (3.38)$$

where $\overset{IIJ}{\Delta\underline{\sigma}}'$ is the deviatoric stress change for the plastic part of the increment and G is the rigidity modulus defined in section 3.2.4.2.1. For strictly infinitesimal increments, $\tilde{\underline{\sigma}}'$ would be the deviatoric stress at the start of the plastic stage of the deformation ($= \overset{IJ}{\underline{\sigma}}'$). However, when increments are finite, this is no longer the case and, as mentioned before, it is more appropriate to use the state of deviatoric stress halfway through the plastic part of the interval, i.e.:

$$\tilde{\underline{\sigma}}' = \overset{IJ}{\underline{\sigma}}' + 0.5\overset{IIJ}{\Delta\underline{\sigma}}' \qquad (3.39)$$

Now eqn. 3.38 may be arranged to give:

$$\begin{aligned}\overset{IIJ}{\Delta\underline{\sigma}}' &= 2G[M]^{-1}\overset{II}{\Delta\underline{\varepsilon}}' - 2G\Delta\lambda\tilde{\underline{\sigma}}' \\ &= (1-r)\overset{eJ}{\Delta\underline{\sigma}}' - 2G\Delta\lambda\tilde{\underline{\sigma}}' \qquad (3.40)\end{aligned}$$

where $\overset{eJ}{\Delta\underline{\sigma}}'$ is the hypothetical-elastic Jaumann increment of deviatoric stress defined earlier. The relationship described by eqn. 3.40 is represented in fig. 3.12 which depicts these vectors in the octahedral-stress plane.

Point A on the initial-yield locus (solid curve), represents the

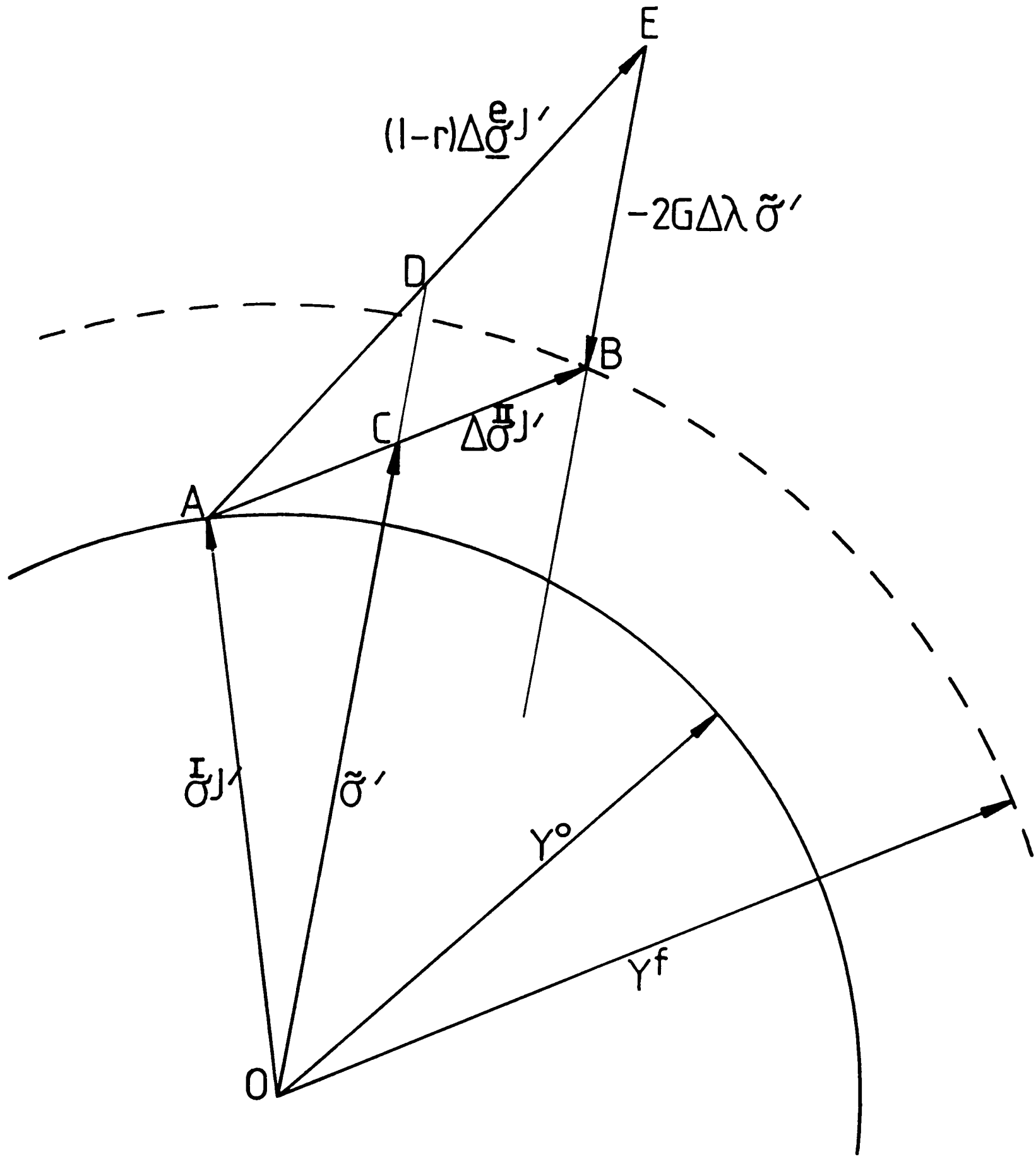

FIG. 3.12

CALCULATION OF STRESS INCREMENT BY MEAN-NORMAL METHOD

state at the start of the plastic part of the increment, while point B represents the final state, for which the yield stress is Y^f. C is the mid-point of AB so that by eqn. 3.39, $\underline{OC}$ represents the vector $\underset{\sim}{\sigma}'$.

$\Delta\lambda$ in eqn. 3.40 is simply a scalar which must be evaluated in terms of strain increment and strain-hardening parameters. Thus $\underset{\sim}{\sigma}'$ in this equation may be replaced by any parallel vector, for example that represented by $\underline{OD}$, providing the appropriate scalar multiplier is chosen.

But by the geometry of the triangle ABE, D is also the midpoint of AE, so that $\underline{OD}$ represents the vector $\underline{\hat{\sigma}}'$ where:

$$\underline{\hat{\sigma}}' = \underline{\sigma}^{IJ}{}' + 0.5(1-r)\Delta\underline{\sigma}^{eJ}{}' \qquad (3.41)$$

Hence, from eqn. 3.40:

$$\Delta\underline{\sigma}^{IIJ}{}' = (1-r)\Delta\underline{\sigma}^{eJ}{}' - \Delta m\underline{\hat{\sigma}}' \qquad (3.42)$$

where Δm is some scalar multiplier.

Applying Von Mises' yield criterion to the initial and final states of stress produces:

$$g(\underline{\sigma}^{IJ}{}'+\Delta\underline{\sigma}^{IIJ}{}') - g(\underline{\sigma}^{IJ}{}') = Y^{f2} - Y^{o2} \qquad (3.43)$$

which may be expanded, using the definition of g in eqn. 3.10 to give:

$$3\Delta\underline{\sigma}^{IIJ}{}^{,T}[M](\underline{\sigma}^{IJ}{}'+0.5\Delta\underline{\sigma}^{IIJ}{}') = Y^{f2} - Y^{o2} \qquad (3.44)$$

This may be expressed in terms of $\underline{\hat{\sigma}}'$ and Δm using eqns. 3.41 and 3.42:

$$3\Delta\underline{\sigma}^{IIJ}{}^{,T}[M](\underline{\hat{\sigma}}' - 0.5\Delta m\underline{\hat{\sigma}}') = Y^{f2} - Y^{o2} \qquad (3.45)$$

Substituting from eqn. 3.42 again gives:

$$1.5(2-\Delta m)((1-r)\Delta\underline{\sigma}^{eJ\prime} - \Delta m\hat{\underline{\sigma}}')^T[M]\hat{\underline{\sigma}}' = Y^{f2} - Y^{o2} \qquad (3.46)$$

which on multiplying out leaves:

$$g(\hat{\underline{\sigma}}')^2\Delta m^2 - 3\hat{\underline{\sigma}}'^T[M](\underline{\sigma}'+\Delta\underline{\sigma}^{eJ\prime})\Delta m + 3(1-r)\hat{\underline{\sigma}}'^T[M]\Delta\underline{\sigma}^{eJ\prime} + Y^{o2} = Y^{f2} \qquad (3.47)$$

All the coefficients on the right-hand side of this quadratic equation in Δm can be calculated immediately from the previously evaluated $\Delta\underline{\varepsilon}^{II\prime}$. Y^f will, in general, be some function h of the accumulated plastic strain, the increment $\Delta\bar{\varepsilon}^p$ of which may be easily found by comparing eqns. 3.37 and 3.42:

$$2G\Delta\underline{\varepsilon}^{IIp\prime} = \Delta m[M]\hat{\underline{\sigma}}' \qquad (3.48)$$

and from eqns. 3.10 and 3.12:

$$3G\Delta\bar{\varepsilon}^p = \Delta m g(\hat{\underline{\sigma}}') \qquad (3.49)$$

so that:

$$Y^f = h(\bar{\varepsilon}^p + \Delta\bar{\varepsilon}^p) = f(\Delta m) \qquad (3.50)$$

where the functional relationship f is obtained by substituting eqn. 3.49 into the hardening function h.

Eqns. 3.47 and 3.50 are solved alternately, starting with some convenient guess for Y^f (e.g. Y^o), always taking the smaller value for Δm when solving eqn. 3.47.

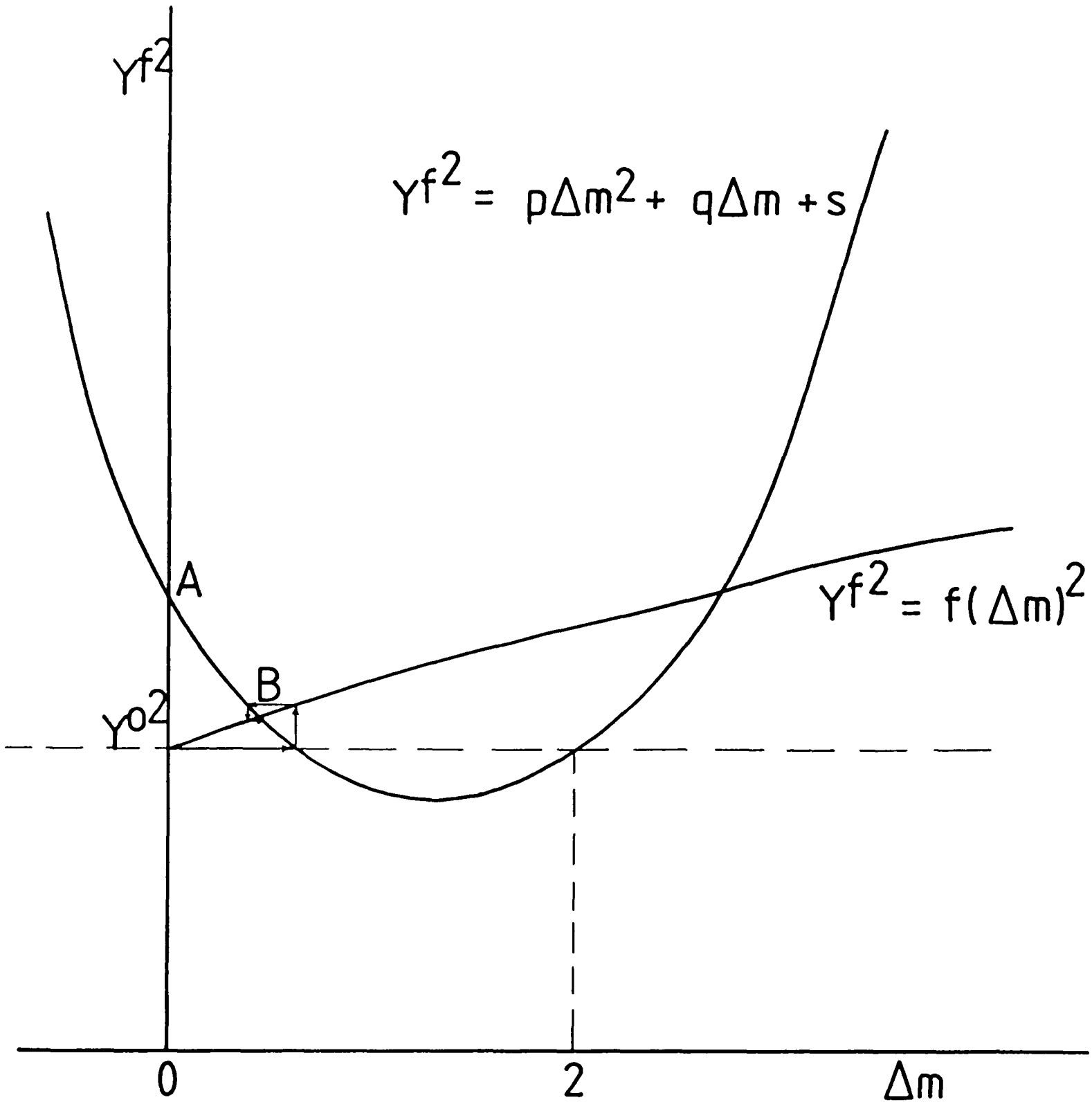

FIG. 3.13

ITERATIVE SOLUTION FOR CONSTANT OF PROPORTIONALITY Δm IN MEAN-NORMAL METHOD

This procedure is illustrated in fig. 3.13. By substituting $\Delta m = 0$ into eqn. 3.47, it can readily be proved that the corresponding value of Y^{f_2} is greater than or equal to Y^{o_2}, thus determining point A on the parabolic curve in the figure. (This is another way of saying that the hypothetical-elastic stress-increment vector extends outside the initial yield locus.)

Examination of the coefficients of eqn. 3.47 shows that the slope of the parabola is negative at point A, that this curve has a local minimum, and that it cuts the horizontal line $Y^{f_2} = Y^{o_2}$ at least once. (The value of Δm for this root, or the larger value when there are two roots, is always 2. This can be proved quite easily by substitution into eqn. 3.47 or by a geometric argument based on fig. 3.12.)

The hardening function represented by eqn. 3.50 is, in general, monotonically increasing for quasi-static, isothermal cold-forging operations. When $\Delta m = 0$, i.e. plastic increment of strain is zero, the yield stress equals the initial value Y^o.

Thus the curves defined by eqns. 3.47 and 3.50 will always have the general forms shown in fig. 3.13. The relationship between the two curves ensures that the iterative solution for their point of intersection B is rapidly convergent. For example, the correct value of Y^f is usually obtained to within 0.1% after three or four steps. The procedure is particularly efficient since the coefficients of eqn. 3.47 need only be computed once for each set of iterations. A typical solution route is shown in fig. 3.13. An example of the improvement of the finite-element solution obtained by using the mean-normal method is given in appendix D.

When the correct value of Δm has been obtained, $\Delta \underline{\sigma}^{II_J}{}'$ may be calculated from eqn. 3.42 and the increment of generalised plastic strain $\Delta \bar{\varepsilon}^p$ calculated from eqn. 3.49.

3.2.4.3 Final Values of Strain and Deviatoric Stress

The accumulated generalised plastic strain at the end of the increment is given by:

$$\bar{\varepsilon}^{pf} = \bar{\varepsilon}^{p} + \Delta\bar{\varepsilon}^{p} \qquad (3.51)$$

since the increment of plastic strain is generally small.

The Jaumann increment of Cauchy stress occurring during this stage of the deformation is the sum of the changes obtained for the parts of the increment before and after yield, i.e.:

$$\Delta\underline{\sigma}^{J'} = \Delta\underline{\sigma}^{IJ'} + \Delta\underline{\sigma}^{IIJ'} \qquad (3.52)$$

This equation gives the change in stress measured in the current frame of reference. Thus the final deviatoric stress in this frame is given by:

$$\underline{\sigma}^{R'} = \underline{\sigma}' + \Delta\underline{\sigma}^{J'} \qquad (3.53)$$

Since the transformation between the reference and the current states is determined by the rotational matrix [R] obtained from eqn. 3.29, the usual axis transformation expressions give that the final deviatoric stress in the reference frame, $\underline{\sigma}^{f'}$ and the change in deviatoric Cauchy stress are:

$$\underline{\sigma}^{f'} = [W]\underline{\sigma}^{R'} \quad \text{and} \quad \Delta\underline{\sigma}' = \underline{\sigma}^{f'} - \underline{\sigma}' \qquad (3.54)$$

where the matrix [W] is defined in fig. 3.14 in terms of the coefficients of [R].

FIG. 3.14

MATRIX [W] FOR TRANSFORMATION OF COMPONENTS OF STRESS DURING ROTATION OF AXES

$$
\begin{bmatrix}
l_1^2 & l_2^2 & l_3^2 & 2l_1l_2 & 2l_2l_3 & 2l_1l_3 \\
m_1^2 & m_2^2 & m_3^2 & 2m_1m_2 & 2m_2m_3 & 2m_1m_3 \\
n_1^2 & n_2^2 & n_3^2 & 2n_1n_2 & 2n_2n_3 & 2n_1n_3 \\
l_1m_1 & l_2m_2 & l_3m_3 & l_1m_2+l_2m_1 & l_2m_3+l_3m_2 & l_1m_3+l_3m_1 \\
m_1n_1 & m_2n_2 & m_3n_3 & m_1n_2+m_2n_1 & m_2n_3+m_3n_2 & m_1n_3+m_3n_1 \\
l_1n_1 & l_2n_2 & l_3n_3 & l_1n_2+l_2n_1 & l_2n_3+l_3n_2 & l_1n_3+l_3n_1
\end{bmatrix}
$$

Since the change in the hydrostatic component of stress depends only upon the change in the purely-elastic bulk strain, the increment in hydrostatic stress may be written as:

$$\Delta\sigma_h = \kappa\Delta\varepsilon_b \qquad (3.56)$$

where κ has been defined in section 2.1.1.6.

However, as explained in section 3.2.4.4, in the fully-plastic range, small errors in the bulk strain can lead to large errors in hydrostatic stress. To remedy this situation, the total hydrostatic stress may be calculated throughout the body, when required, by the indirect method. This technique is described next.

3.2.4.4 Indirect Calculation of Hydrostatic Stress

3.2.4.4.1 Theory

The indirect calculation of hydrostatic stress is based on a method suggested by Alexander and Price (95).

The condition for equilibrium of stress at a point is expressed by the three equations (21):

$$\frac{\delta\sigma_{xx}}{\delta x} + \frac{\delta\sigma_{xy}}{\delta y} + \frac{\delta\sigma_{zx}}{\delta z} = 0 \qquad (3.57A)$$

$$\frac{\delta\sigma_{xy}}{\delta x} + \frac{\delta\sigma_{yy}}{\delta y} + \frac{\delta\sigma_{yz}}{\delta z} = 0 \qquad (3.57B)$$

$$\frac{\delta\sigma_{zx}}{\delta x} + \frac{\delta\sigma_{yz}}{\delta y} + \frac{\delta\sigma_{zz}}{\delta z} = 0 \qquad (3.57C)$$

where body forces are assumed to be zero for the quasi-static processes under consideration.

The derivatives of the three normal components of stress can be divided into deviatoric and hydrostatic terms to give:

$$S_x = \frac{\delta\sigma_h}{\delta x} = -\left(\frac{\delta\sigma'_{xx}}{\delta x} + \frac{\delta\sigma_{xy}}{\delta y} + \frac{\delta\sigma_{zx}}{\delta z}\right) \qquad (3.58A)$$

$$S_y = \frac{\delta\sigma_h}{\delta y} = -\left(\frac{\delta\sigma_{xy}}{\delta x} + \frac{\delta\sigma'_{yy}}{\delta y} + \frac{\delta\sigma_{yz}}{\delta z}\right) \qquad (3.58B)$$

$$S_z = \frac{\delta\sigma_h}{\delta z} = -\left(\frac{\delta\sigma_{zx}}{\delta x} + \frac{\delta\sigma_{yz}}{\delta y} + \frac{\delta\sigma'_{zz}}{\delta z}\right) \qquad (3.58C)$$

Hence the difference in hydrostatic stress between two points $A(x^A, y^A, z^A)$ and $B(x^B, y^B, z^B)$ is given by:

$$\sigma_h^B - \sigma_h^A = \int_{x^A}^{x^B} S_x dx + \int_{y^A}^{y^B} S_y dy + \int_{z^A}^{z^B} S_z dz \qquad (3.59)$$

Since S_x, S_y and S_z depend only upon spatial derivatives of deviatoric stress, if the distribution of the latter is known throughout the body, and the value of hydrostatic stress is known at one point, then eqn. 3.59 provides a means of evaluating the hydrostatic stress at any other point in the body.

3.2.4.4.2 Implementation

As explained earlier, the components of deviatoric stress are calculated at the sample points of each element, at the end of each

increment of deformation, and averaged to give the components of deviatoric stress at the centroid of the element. Since only the latter values of stress are printed, it is only necessary to calculate, by the indirect method, the components of hydrostatic stress at the element centroids. Friction-layer elements are ignored completely during the indirect calculation of hydrostatic stress.

The process is started by calculating the hydrostatic stress at the mid-point of a specified element face, chosen to remain on the free surface of the billet throughout the deformation. Since the component of total stress perpendicular to a free surface is, by definition, zero, the hydrostatic stress at this mid-point equals the negative of the component of deviatoric stress normal to the specified face at this point. The latter can easily be found by extrapolating from the sample-point values of stress, with the appropriate rotation of axes.

The hydrostatic stress at the centroid of any billet element may then be found from eqn. 3.59 by choosing the integration path to be a set of straight-line segments, each of which passes between the centroid of an element and the mid-point of one of its faces. Therefore, eqn. 3.59 need only be defined for the situation where A and B are the end-points of one such line segment.

Care has to be taken in the evaluation of the functions defined by eqns. 3.58, because these involve spatial derivatives of stress, and small errors in stress can lead to large errors in the gradients.

Firstly, the average values of the components of deviatoric stress at each billet node of the mesh are calculated by extrapolation from the values at the sample points of all the elements to which the node belongs.

The deviatoric stress, $\underline{\sigma}'$, at any point within an element can be expressed in terms of the deviatoric stress at the nodes of the

element, $\underline{\sigma}'_I$, I = 1,8 by:

$$\underline{\sigma}' = \sum_{I=1}^{8} N_I \underline{\sigma}'_I \qquad (3.60)$$

where N_I is the shape function for node I defined in the previous chapter. Thus, for this element:

$$\frac{\delta \underline{\underline{\sigma}}'}{\delta x_i} = \sum_{I=1}^{8} \frac{\delta N_I}{\delta x_i} \underline{\sigma}'_I \qquad \text{for } i=1,3 \quad (3.61)$$

where x_i , i=1,3 are the global coordinate axes. The Cartesian derivatives of shape functions in eqn. 3.61 can be expressed in terms of local, element coordinates by means of the Jacobian matrix. This allows the required spatial derivatives of deviatoric stress to be evaluated at the nodes of each element. Since, in general, a node may belong to more than one element, several estimates of these spatial derivatives may be obtained for each node, and the weighted averages of the derivatives are calculated.

The weighting factor, for an element contribution to the average value of the nodal derivative of stress is the inverse of the volume of the element. This particular weighting factor is used because it degenerates, in the case where a local and global axis are parallel, to the familiar three-point (quadratic) approximation to the derivative of a single variable function. Also, intuitively, the estimates of the derivatives of stress obtained from a large element ought to be less significant than those calculated for an element which has its centroid closer to the node under consideration.

The average, nodal derivatives of deviatoric stress are then used to calculate nodal values of the three functions S_x , S_y and S_z according to eqns. 3.58. These functions are assumed to vary linearly over each element of the mesh.

For any integration path between an element centroid and the mid-point of the element face, eqn. 3.59 may be evaluated as follows. Without loss of generality, assume A is the element centroid and B is the mid-point of the face. The coordinates (x^A,y^A,z^A) and the values of the S functions (S_x^A,S_y^A,S_z^A) are evaluated at point A by averaging the values at the eight nodes. Similarly, (x^B,y^B,z^B) and (S_x^B,S_y^B,S_z^B) are found at B by averaging the values at the four nodes of the face containing this point.

By definition, the straight line AB joining the element centroid to the mid-point of a face, is one of the local, coordinate axes. Thus, by the assumption of linearity made earlier, at a point on this line with global coordinates (x,y,z):

$$S_x = ((x^B-x)S_x^A + (x-x^A)S_x^B)/(x^B-x^A) \qquad (3.62A)$$

$$S_y = ((y^B-y)S_y^A + (y-y^A)S_y^B)/(y^B-y^A) \qquad (3.62B)$$

$$S_z = ((z^B-z)S_z^A + (z-z^A)S_z^B)/(z^B-z^A) \qquad (3.62C)$$

Substituting into eqn. 3.59, and integrating:

$$\sigma_h^B - \sigma_h^A = \tfrac{1}{2}[(x^B-x^A)(S_x^A+S_x^B)+(y^B-y^A)(S_y^A+S_y^B)+(z^B-z^A)(S_z^A+S_z^B)] \qquad (3.63)$$

3.2.5 Enforcement of Volume Constancy

Plastic flow is, for practical purposes, volume constant (32), and any change in volume occurring in a yielded element is elastically recoverable. It follows that any level of hydrostatic stress could be superimposed upon a plastically deformed body, and a corresponding change in volume brought about, without altering the initial plastic state. It is for this reason that an elastic-plastic, finite-element formulation produces displacement fields which lead to, essentially, the correct plastic flow, but which may or may not correspond to correct values of infinitesimal volume change. The distribution of bulk strain is certainly not arbitrary - the bulk components occur explicitly in the Prandtl-Reuss equations used to derive $[D_p]$ - but it does seem to depend, in some complicated way, upon the accompanying plastic deformation.

For instance, preliminary investigations, during the development of the finite-element program described here, have shown that for a finite-element analysis of the homogeneous upsetting of a billet, (zero interfacial friction), the volume loss is very small, and predictable, for this simple mode of deformation, by alternative elastic-plastic theory. However, much larger volume losses occur during inhomogeneous upsetting (sticking interfacial friction).

Although, in general, the correct elastic-plastic volume change cannot be predicted, it is known that, for fully-yielded bodies, all elastic strain is much smaller than the plastic strain. It seems reasonable, therefore, to artificially constrain the deformation so that volume change in yielded elements is very small.

This can be brought about by increasing the contribution of the bulk strain, in plastic elements, to the finite-element work formulation, the basis of the penalty-function technique often used in

rigid-plastic and visco-plastic analyses (37,72). A simple way to introduce the modification into elastic-plastic formulations, is by specifying a value, close to 0.5, for Poisson's ratio in the $[D_n]$ matrices used in the stiffness relationship for yielded elements.

Throughout the remainder of this thesis, ν_e will refer to the usual, elastic value of Poisson's ratio, and ν_p will denote the value used for yielded elements.

It should be noted that even when the volume constancy of yielded elements is enforced, the present finite-element technique is still elastic-plastic, as opposed to rigid- or visco-plastic, because:

a) only the elastic bulk strain is forced to be negligibly small - elastic deformation strain can still occur,

b) the enforcement is only applied to yielded elements - the mesh may still contain elastic regions which deform according to the usual elasticity theory.

3.2.6 Calculation of Deforming Load

To provide a comparison, the program allows the deforming load to be calculated by two different methods,

a) from the incremental work of deformation,

b) from the current values of force applied to the the external faces.

3.2.6.1 Work of Deformation

For zero or sticking friction conditions, no work can be done against surface traction forces and so the energy supplied by the applied deforming force must equal the total work of deformation throughout the body. Since the incremental displacement of the applied force is generally known, this force can be easily calculated once the total work of deformation is known. The latter quantity is evaluated by the program as follows.

If, during an increment, the accumulated generalised strain at the centroid of an element changes from $\bar{\varepsilon}$ to $\bar{\varepsilon}^f$, and the generalised stress at this point changes from $\bar{\sigma}$ to $\bar{\sigma}^f$, then the increment of work done in deforming that element plastically is approximately:

$$0.5(\bar{\sigma} + \bar{\sigma}^f)(\bar{\varepsilon}^f - \bar{\varepsilon}) \times \text{element volume} \qquad (3.63)$$

and summation over all the elements gives the required value.

The calculation is performed at the end of each increment; the value of work referring to the increment just completed and $\bar{\sigma}^f$ being the current value of generalised stress for the element. $\bar{\sigma}$, $\bar{\varepsilon}$ and $\bar{\varepsilon}^f$ are stored on disc and the first two updated with the current values after the calculation is complete. The element volume is calculated by integrating the Jacobian matrix for the element.

When frictional restraints are present, part of the energy supplied to the body is dissipated through the frictional mechanism and the deforming load calculated by this method will underestimate the true load.

3.2.6.2 Forces on External Faces

The forces acting upon the faces of the external billet elements at any stage of the deformation can be calculated from equilibrium principles using the current state of stress in the body. For simplicity, the stress in a given element is assumed to be constant throughout its volume and equal to the centroid value.

Accurate estimation of the deforming load by this method requires that the calculated distribution of total stress is an accurate measure of the true state of stress in the body. For this reason, the hydrostatic component of stress should be calculated by the indirect method.

3.3 STRUCTURE OF PROGRAM

The functional structure of the finite-element program is illustrated in flow charts FC 1 - 13; FC 1 shows the overall structure, while the remaining flow charts depict the functioning of particular aspects of the program in greater detail. The program can be considered to be divided into three major stages, 1) preparation, 2) incremental solution and 3) output.

3.3.1 Preparation

If a new analysis is to be started, the data must be read in. This is extensively checked for consistency and contravention of the limits on the size of the problem. If errors are discovered, diagnostic messages are printed; the type of error determining whether the analysis continues. Many categories of information may be omitted if default values are required, thus simplifying data preparation.

After the input of the data, certain arrays are formed, expressing topological properties of the mesh and the order in which the nodes are to be eliminated from the frontal area of the solution, and frequently used elastic and other constants determined. It is at this stage that the matrices defining any rotated axes of prescribed displacement are formed.

If the analysis is a continuation from a previous program run, then the dumped information is retrieved from the magnetic tape used for storage and placed in the correct locations. Sufficient data is included so that the analysis can continue where it left off.

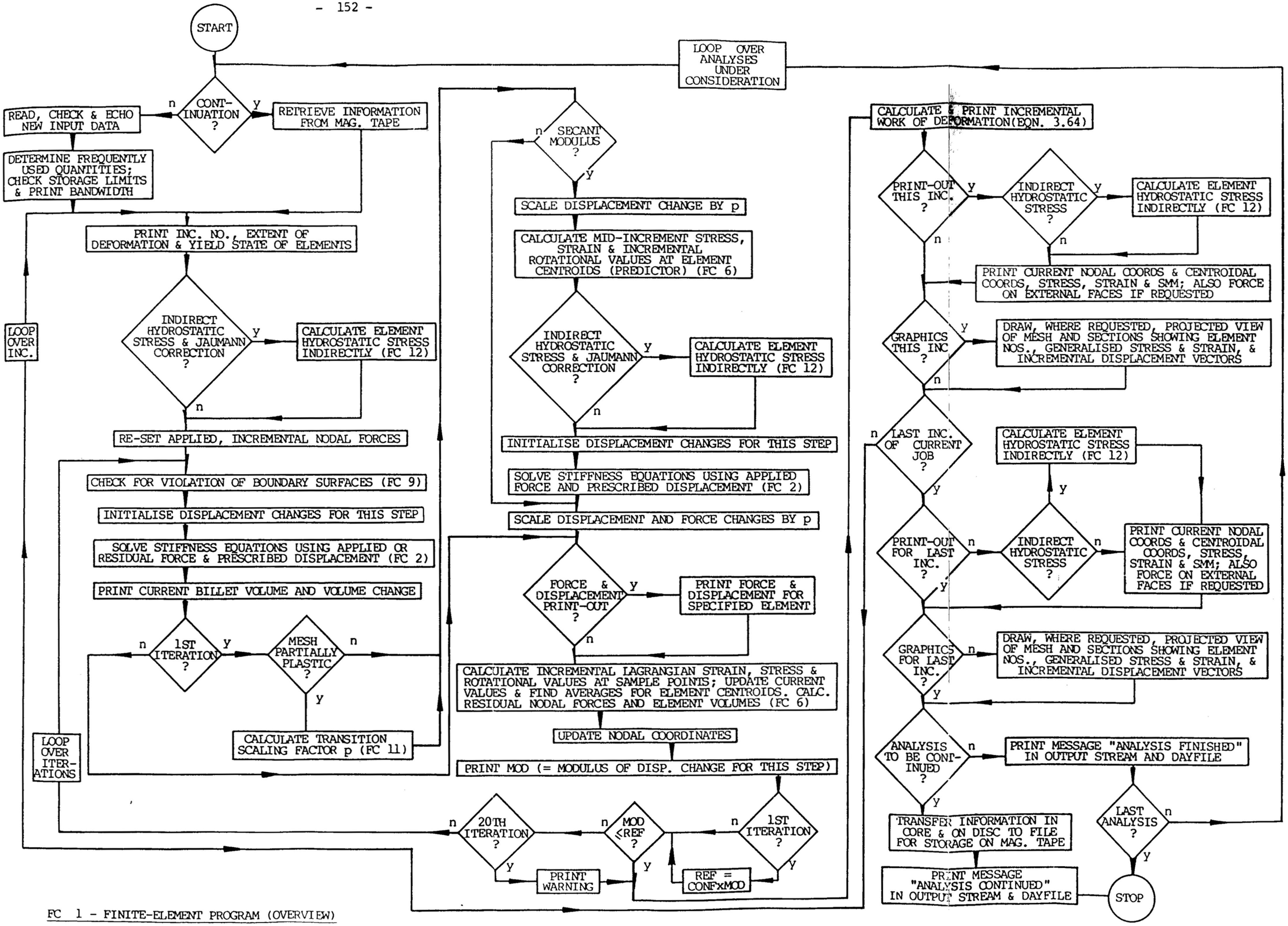

FC 1 - FINITE-ELEMENT PROGRAM (OVERVIEW)

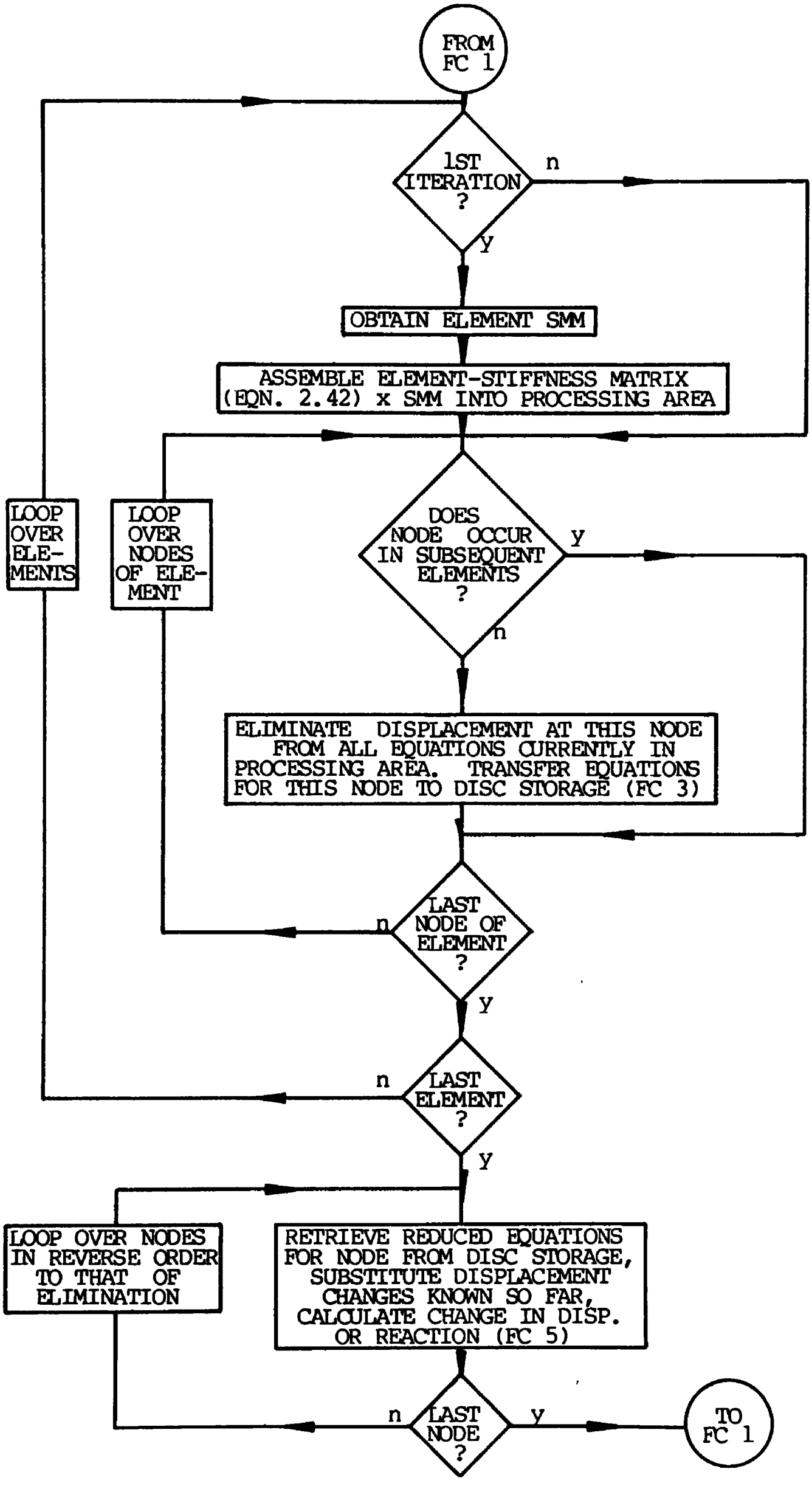

FC 2 - SOLUTION OF STIFFNESS EQUATIONS

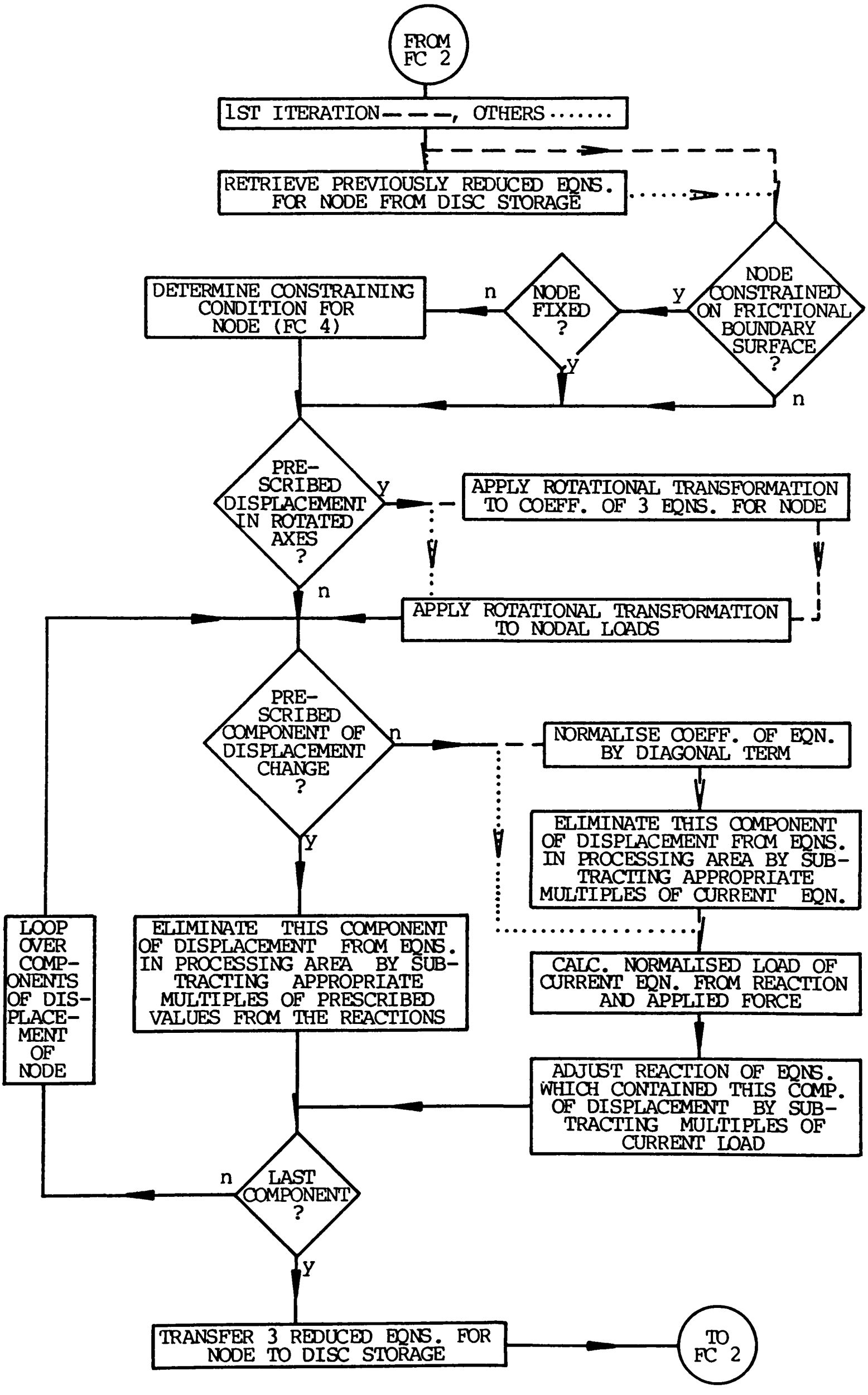

FC 3 - ELIMINATION OF DISPLACEMENT FROM STIFFNESS EQUATIONS

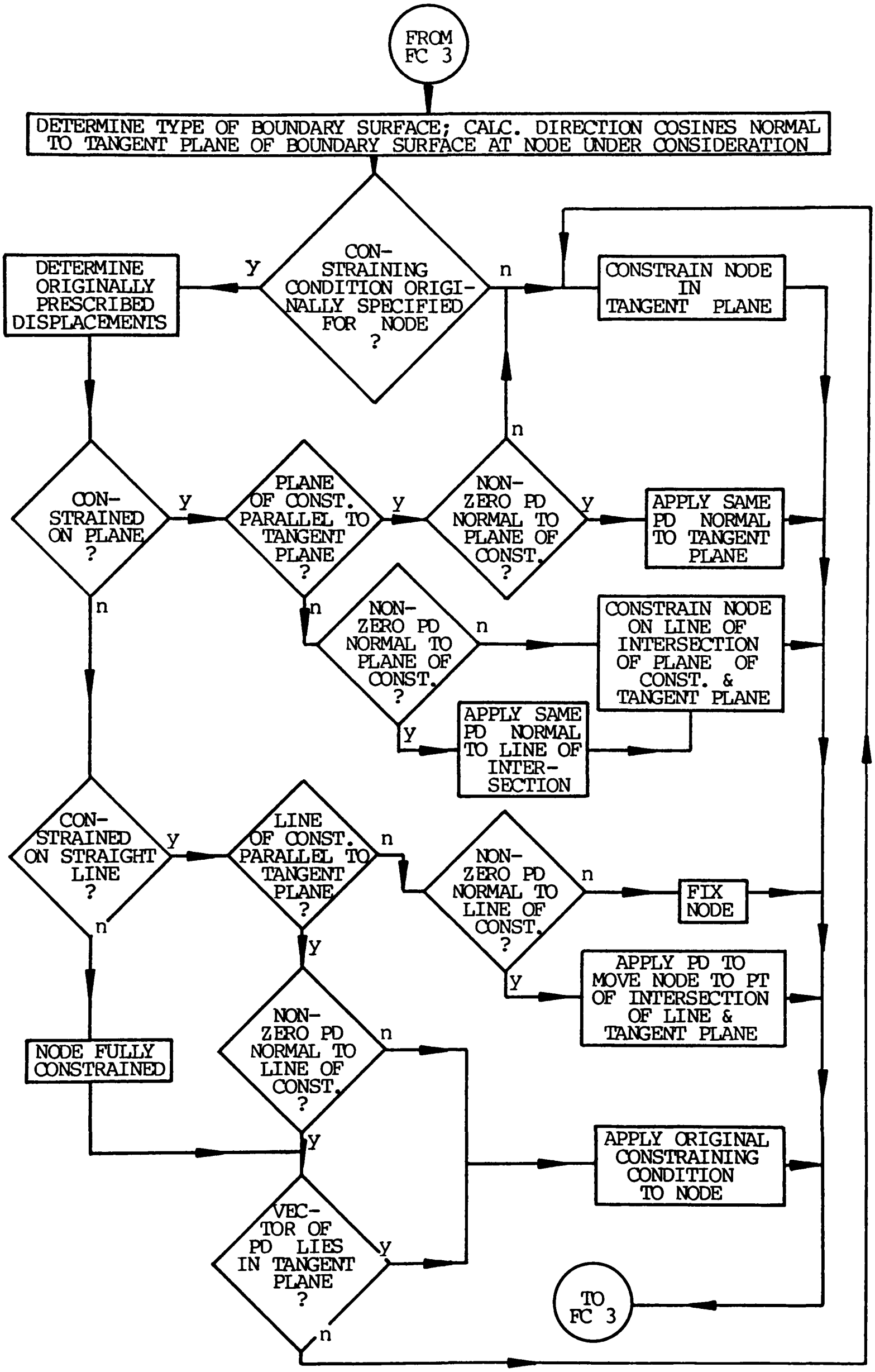

FC 4 - DETERMINATION OF CONSTRAINT FOR NODE ON BOUNDARY SURFACE

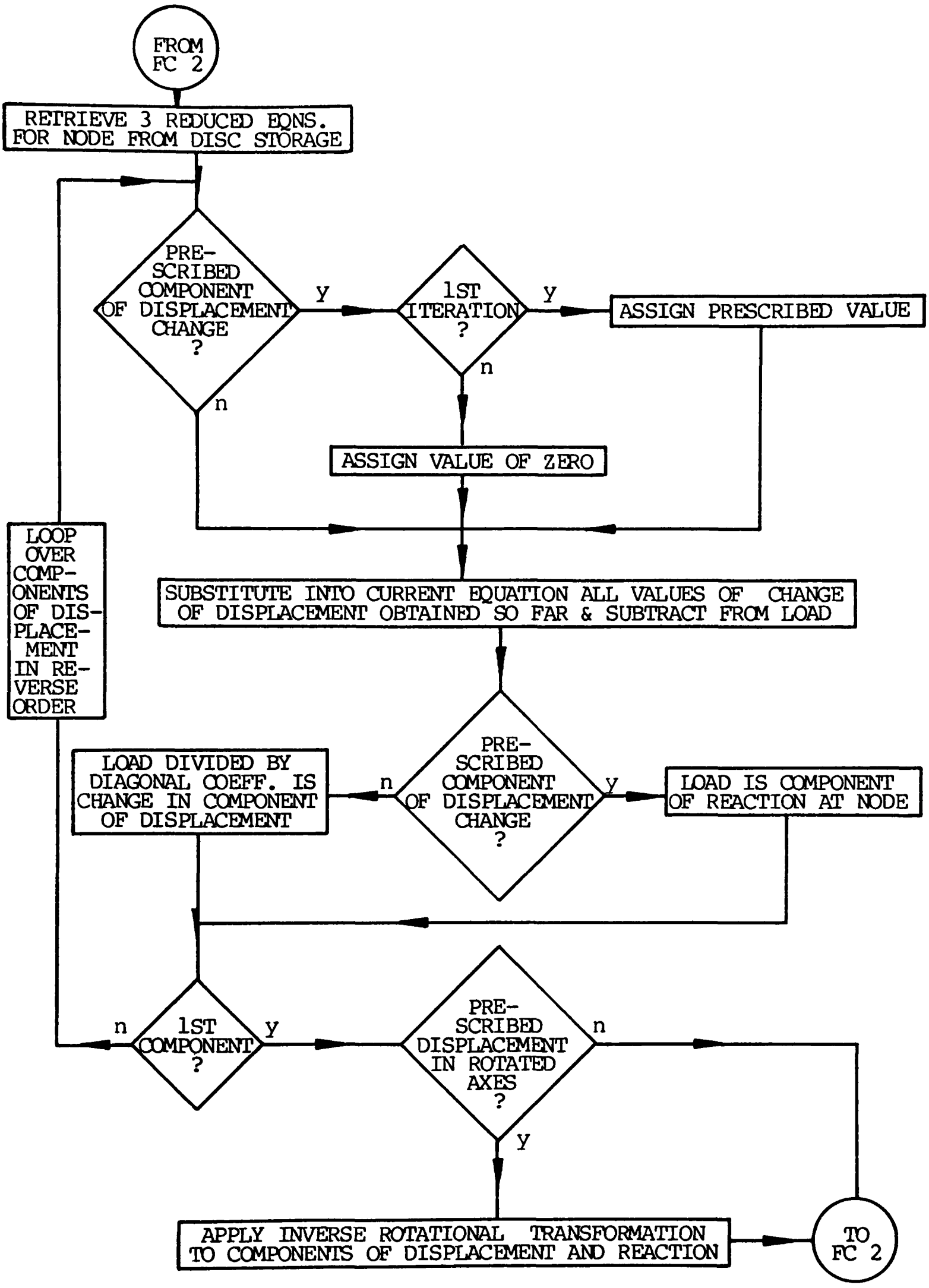

FC 5 - BACK-SUBSTITUTION INTO STIFFNESS EQUATIONS

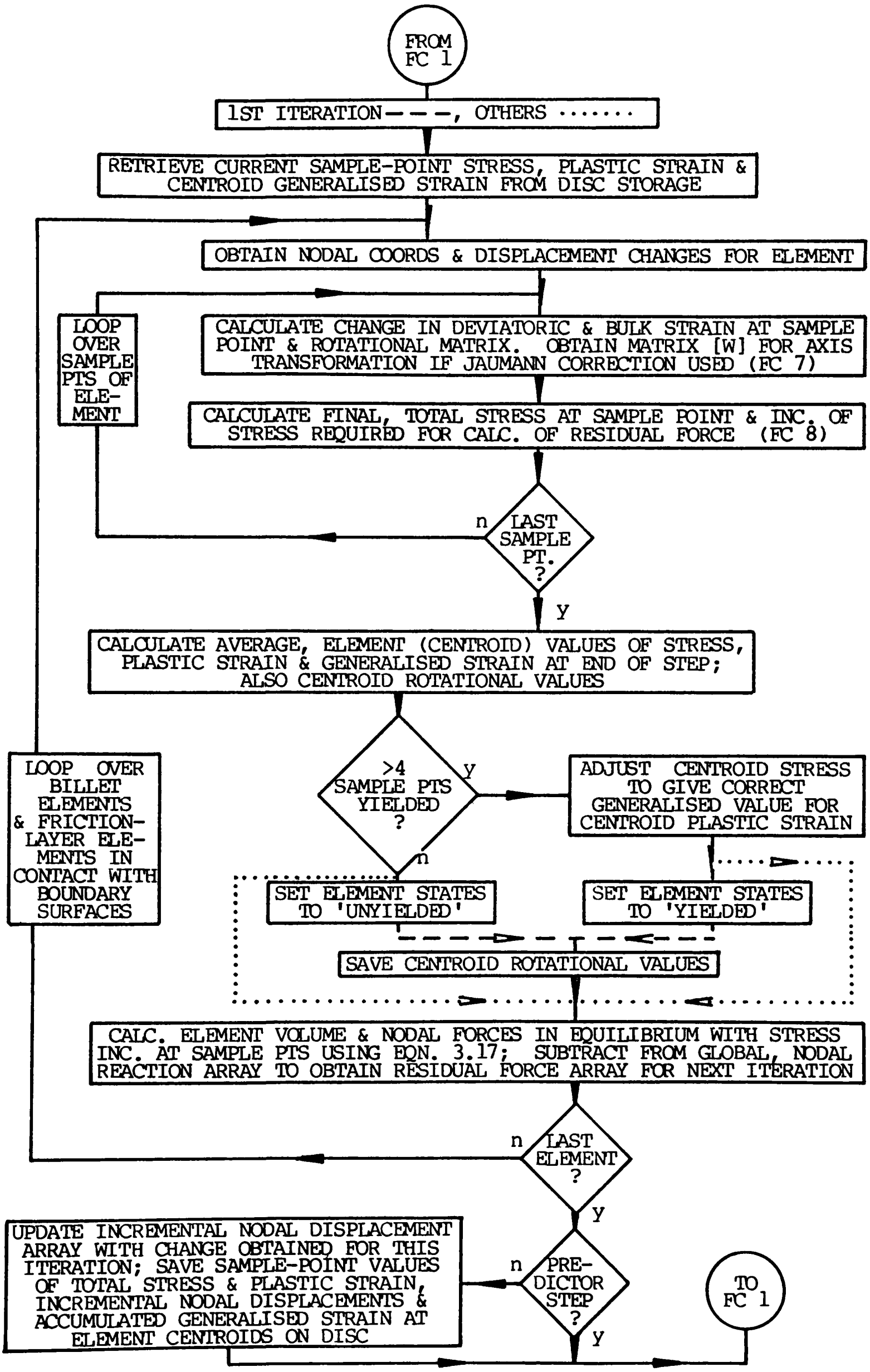

FC 6 - CALCULATION OF STRESS

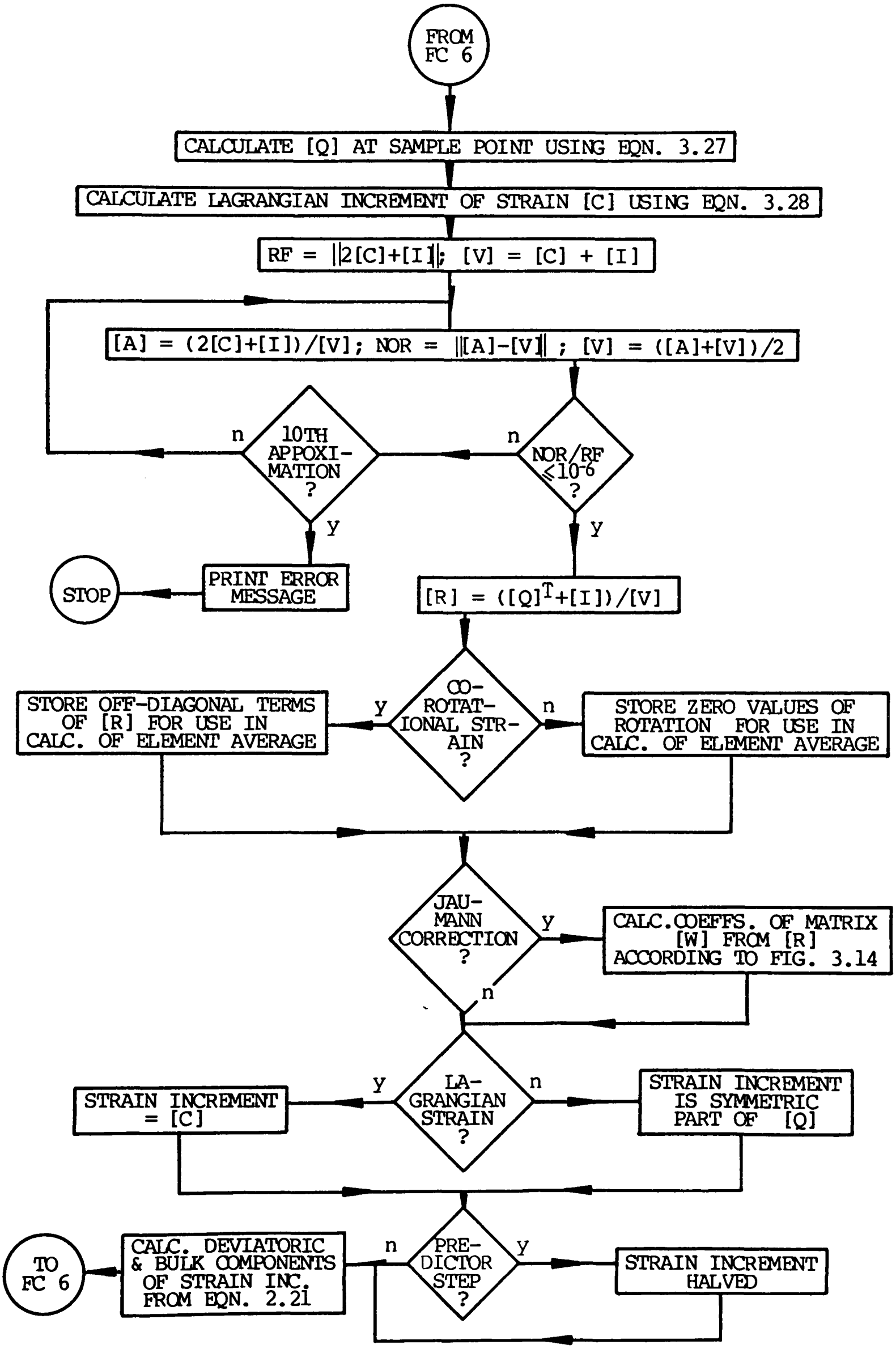

FC 7 - CALCULATION OF INCREMENT OF STRAIN AT SAMPLE POINT

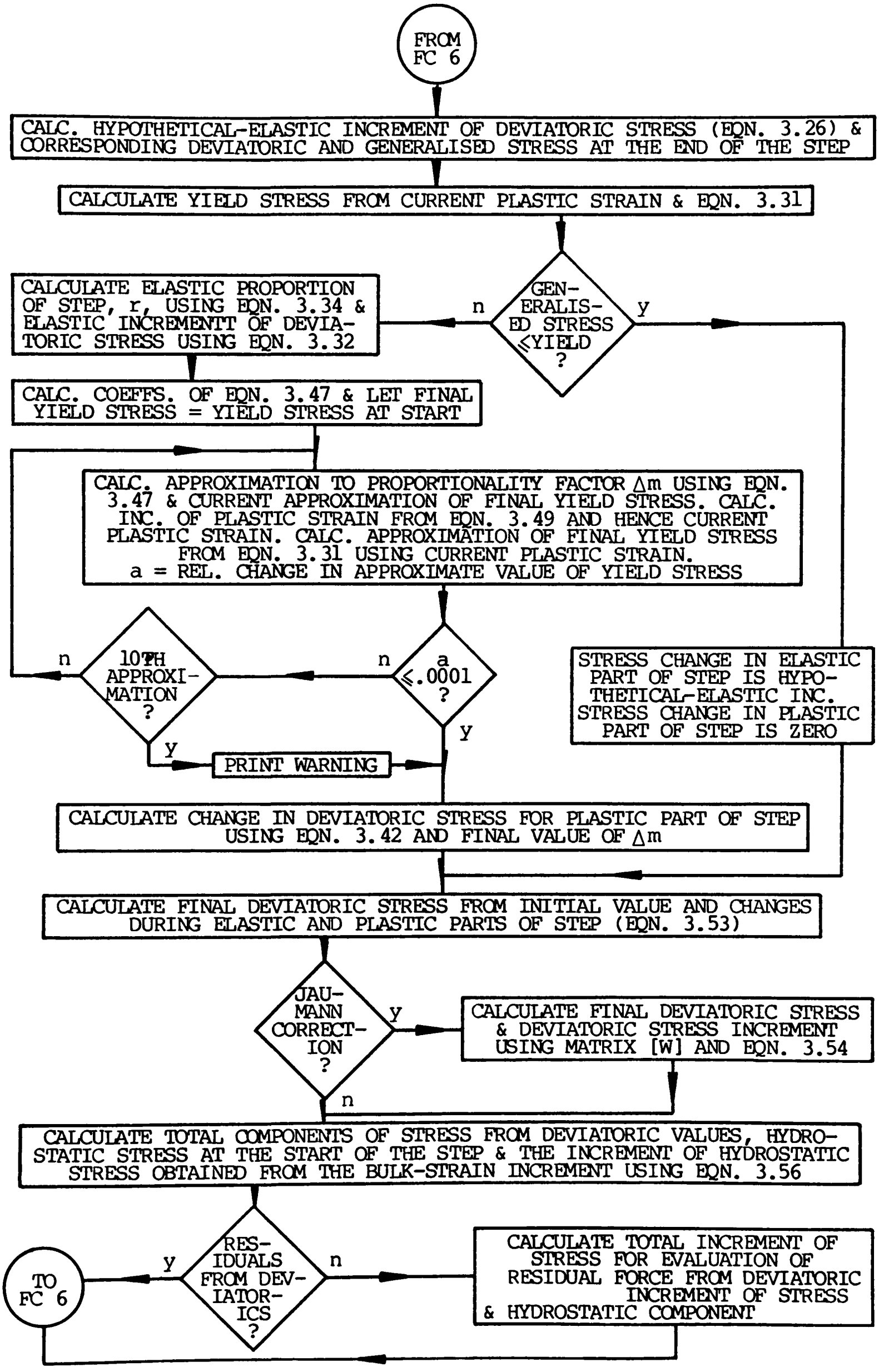

FC 8 - CALCULATION OF STRESS AT SAMPLE POINT

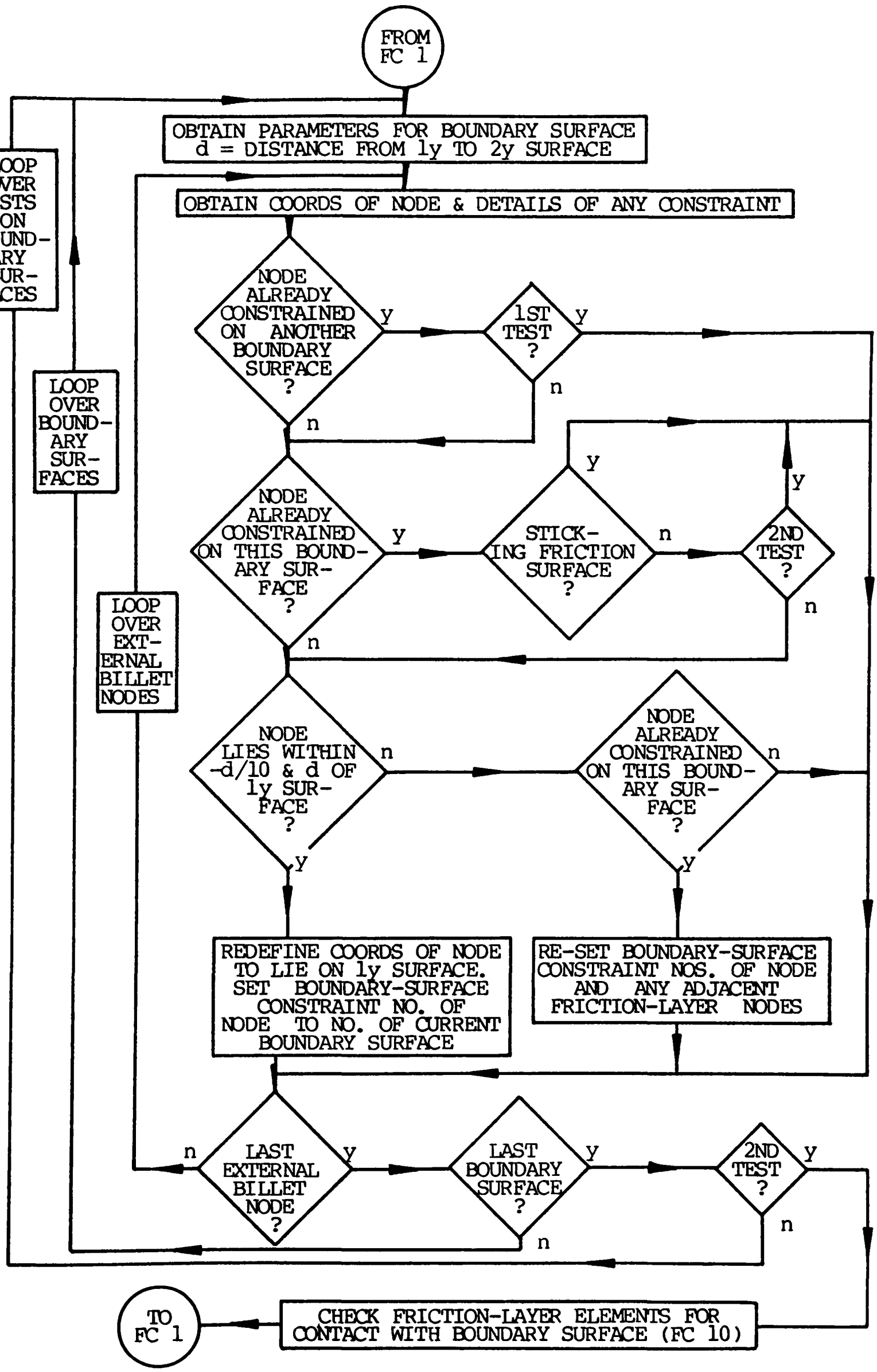

FC 9 - CHECK FOR VIOLATION OF BOUNDARY SURFACES

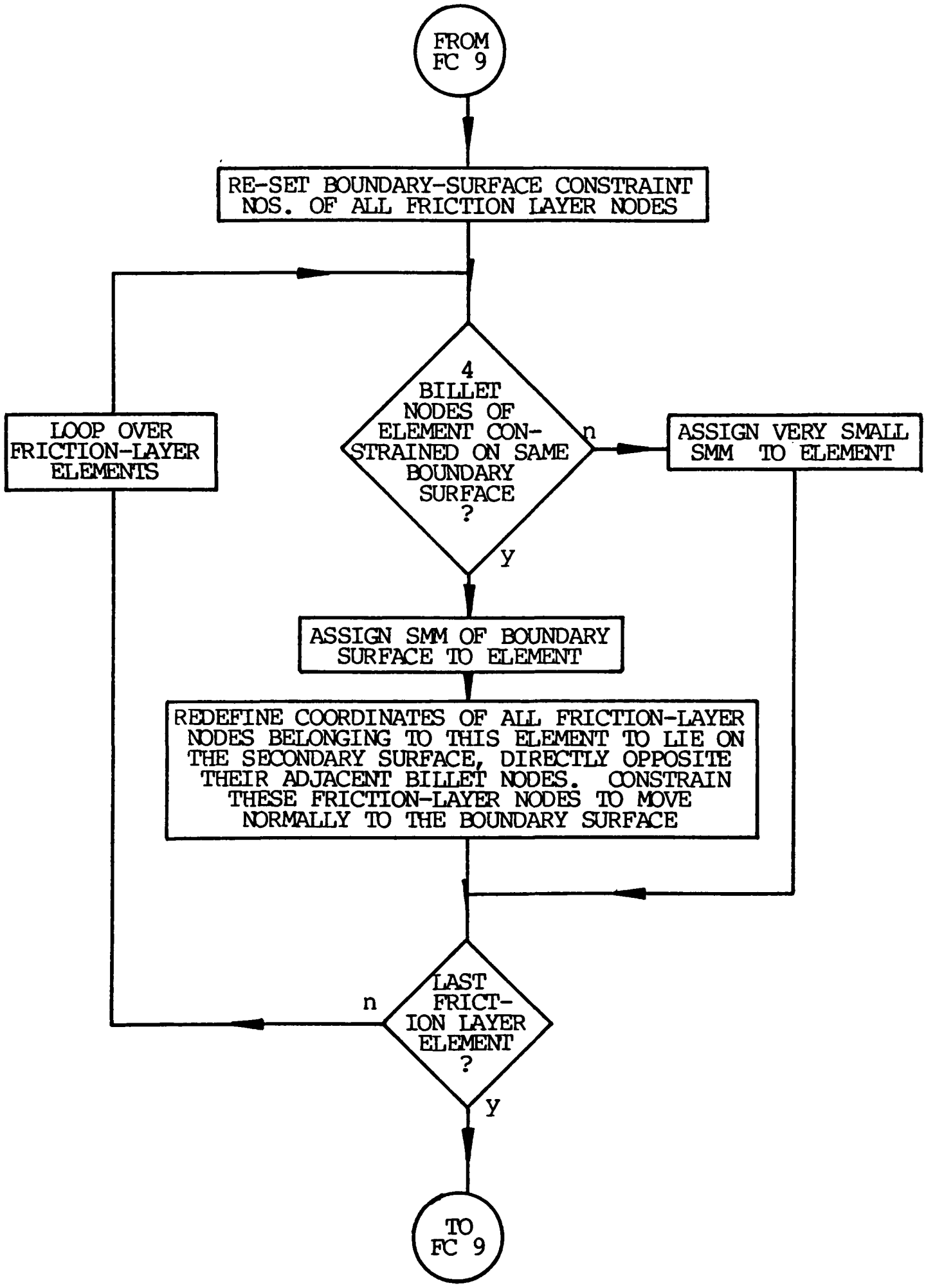

FC 10 - CHECK FOR CONTACT OF FRICTION-LAYER WITH BOUNDARY SURFACES

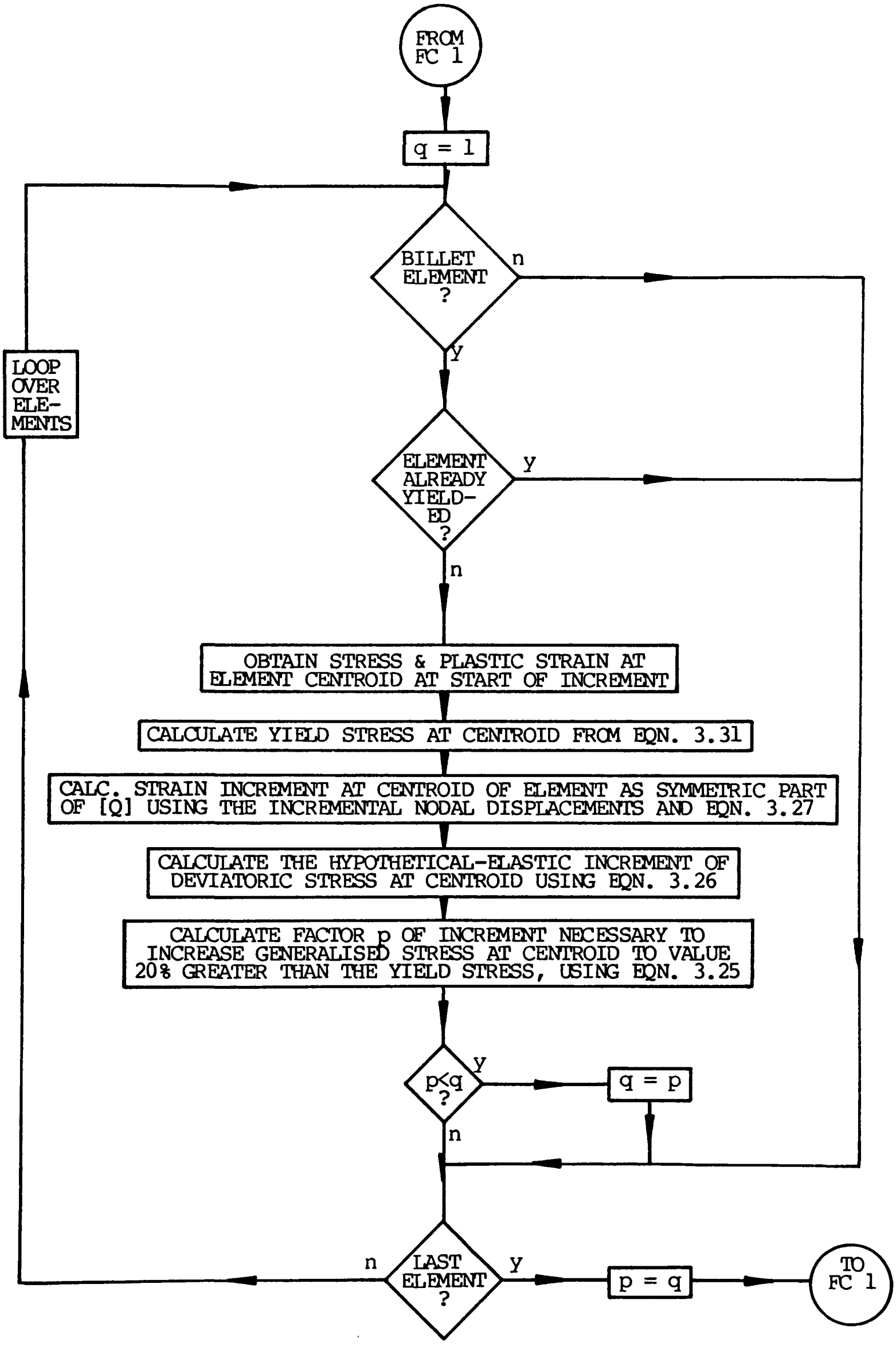

FC 11 - CALCULATION OF TRANSITION SCALING FACTOR p

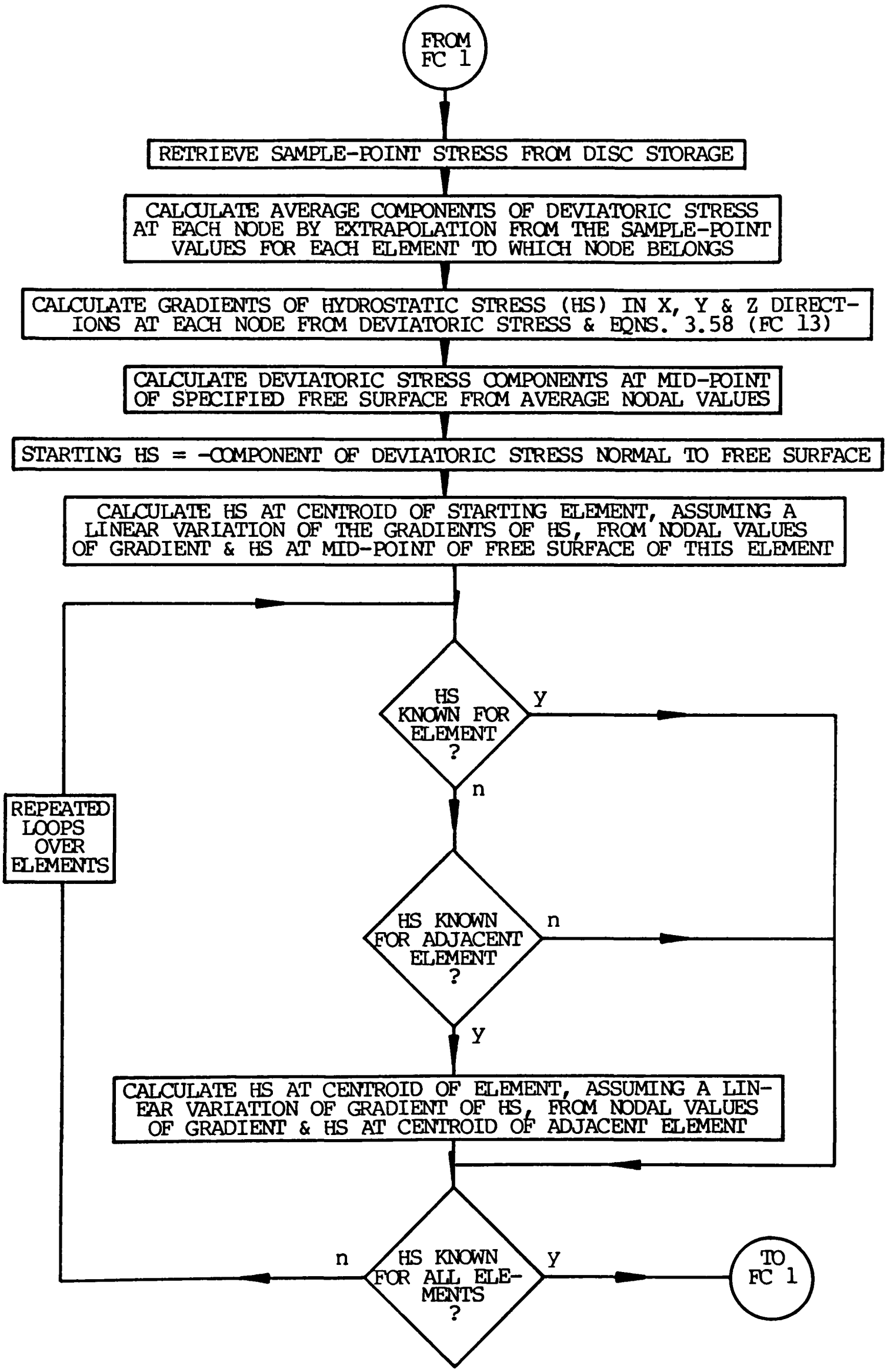

FC 12 - INDIRECT CALCULATION OF HYDROSTATIC STRESS

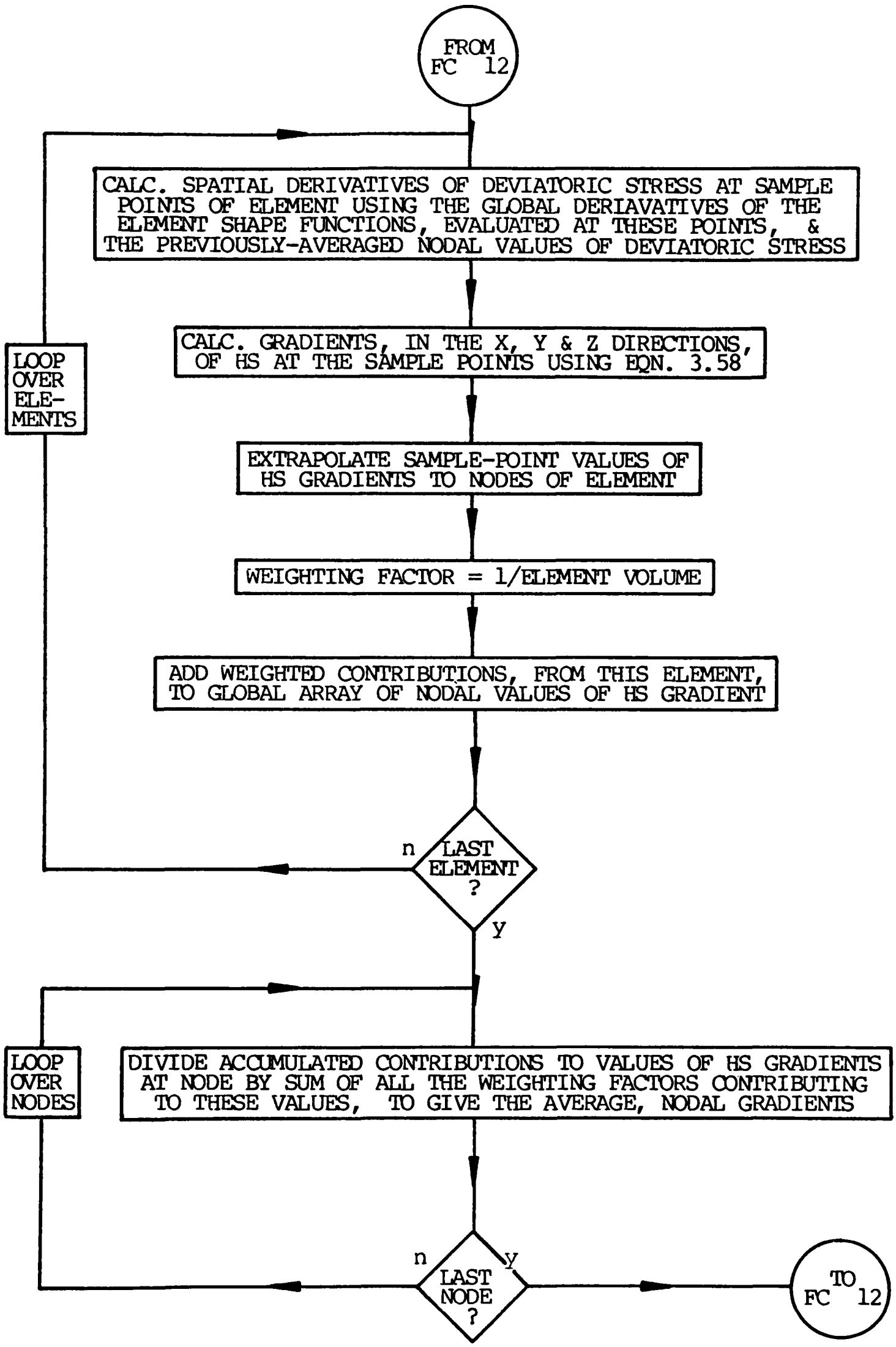

FC 13 - CALCULATION OF GRADIENTS OF HYDROSTATIC STRESS AT NODES

3.3.2 Incremental Solution

The deformation is applied in the specified number of increments, and iteration performed until the convergence criterion is satisfied to the required degree of accuracy. If this does not occur within 20 iterations, a warning is printed and the solution proceeds to the next increment.

During each iteration, a check is first performed to ensure that the nodes of the mesh have not passed through any specified boundary surfaces (FC 9 & 10), and then a displacement change array and a corresponding applied/residual force or reaction array are evaluated by solving the stiffness equations, as shown in the flow charts FC 2, 3, 4 and 5.

During the first iteration of each increment, this process can be repeated after having estimated the state of strain and stress in the elements halfway through the increment of deformation. Also, the displacement and force changes calculated for the first iteration may be scaled, when necessary, to facilitate the transition of elements from the unyielded to the yielded states (FC 11).

If the options of using the Jaumann correction and the indirect method of calculating hydrostatic stress have been selected, then the hydrostatic components of the stress at the centroids of the elements must be evaluated indirectly (FC 12 & 13) before the stress-dependent element-stiffness matrices can be calculated.

The nodal coordinates are then updated, and the corresponding changes in nodal strain and deviatoric or total stress found throughout the mesh. The nodal forces equilibrating the change in stress are evaluated, and subtracted from the previous applied or residual force array to give the residual force array for the next iteration. The new nodal and element-centroid values of stress

components, generalised stress and accumulated, plastic, generalised strain are also calculated. This is shown in flow charts FC 6, 7 and 8.

The current volume of the mesh, and the average, incremental work of deformation is found during each increment.

3.3.3 Output

The information produced during this stage of the program may be in numerical form, (nodal coordinates, element values of stress components, generalised stress and plastic strain and forces on the external faces of the mesh) or in the form of drawings, (projection of deformed mesh, or sections through the mesh showing generalised stress or plastic strain at the centroid positions or incremental-displacement vectors). The numerical or pictorial output may also be generated at specified intervals during the course of the calculation.

If the analysis is to be continued by another program, the information stored in core, or on backing disc, is transferred to a file for subsequent storage on magnetic tape.

CHAPTER FOUR

COMPARISON OF FINITE-ELEMENT AND EXPERIMENTAL RESULTS I. SIMPLE UPSETTING OF RECTANGULAR BLOCKS

4.0 INTRODUCTION

As part of the development of the finite-element program described in the previous chapters, numerous computer analyses were performed, in order to check aspects of the finite-element formulation and its implementation, using meshes with very few elements and modelling simple deformations such as compression, tension and shear.

The first full-scale analysis which was undertaken was an examination of the radial expansion of a thick tube under internal pressure, the results of which were compared with those of an established theoretical treatment. Excellent agreement was obtained providing certain precautions were taken. Full details may be found in reference 100, while a briefer account is given in appendix E of this thesis.

Since the radial expansion of a tube is an axisymmetric deformation, it was necessary to demonstrate the use of the program in examining a strictly three-dimensional forming operation. The process chosen was the simple upsetting of cubes of commercially-pure aluminium, and the deformations predicted by the finite-element program were compared with the results of an experiment in which the billets were compressed without lubrication (100). Agreement in this case was not close, chiefly because at that time the finite-element program did not include a method of modelling interfacial friction and the finite-element analysis had to be performed assuming sticking-friction conditions.

Another problem was that the aluminium cubes behaved anisotropically, possibly because of insufficient annealing of the material and the choice of billet shape; with a cube, slight variations of material properties with direction can cause changes in the geometry of the work-piece which tend to increase the anisotropic effects.

Therefore it was suggested that, for the next stage of the research, a method of modelling surface friction should be incorporated into the finite-element program, and the finite-element and experimental results for a forging operation which is not susceptible to slight material anisotropy should be compared.

This comparison is the subject of the present chapter. The process under consideration is the simple upsetting of rectangular 20x20x40mm blocks of commercially-pure aluminium in which one pair of the 20x40mm faces of each block is in unlubricated contact with the platens. The only previous three-dimensional finite-element analysis of this type of deformation appears to have been performed by Nagamatsu (76), who examined the upsetting of cubes, although results were only obtained for very small deformations with the cubes remaining partially elastic.

It is worth noting at this point that the results described in reference 100 were obtained using an earlier and simpler version of the finite-element program which lacked several of the features described in the previous chapters. So some of the conclusions and recommendations contained in this reference are subject to review, particularly the insistence upon using an iterative analysis. Subsequent work has shown that initial-stress iteration can lead to serious convergence problems with certain deformations. It was found, by contrast, that the secant-modulus technique described in section 3.2.3.2 gave reasonable results without these problems of convergence, and this approach has been used in all the analyses to be considered in this thesis.

4.1 EXPERIMENTAL PROCEDURE

4.1.1 Preparation of Blocks

Four rectangular blocks of nominal dimensions 20x20x40mm, were machined from 32mm diameter EC1 aluminium bar, and annealed at 410° C for one hour, before being allowed to cool in air. All the faces were polished, finishing with 1200 grit paper.

The four faces of each block which were not to be in contact with the platens were then photoetched with a grid pattern to aid interpretation of the photographs of the deformed shapes. The photoetching was carried out as follows.

The specimens were first degreased by application, in turn, of 5% sodium hydroxide solution and 35% nitric acid, then well washed in water and dried in warm air. The top and bottom surfaces of each block were masked with tape and, under darkroom conditions, with a yellow safety-light, the blocks were spun on a turntable and sprayed with a thin coating of KMER photo-resist medium, diluted 2.75:1 with its thinner. After being allowed to dry naturally, and still under yellow safety-light, the coated blocks were baked at 120°C for ten minutes. Masking tape was again used on each block to expose, in turn, one face out of the four to be etched which was illuminated with ultra-violet light through a grid transparency for about nine minutes, ensuring that there was no air-gap between the emulsion side of the transparency and the face of the block being exposed.

The specimens were immersed in KMER developer for two minutes and then washed in water, after which they were removed from the darkroom and baked at 120°C for a further ten minutes.

When cool, the blocks were swabbed with 10% sodium hydroxide to

etch the lines before being given a final wash in water.

4.1.2 Compression

4.1.2.1 Testing Machine

The blocks were compressed using an Avery-Denison 600 kN hydraulic press operating under constant fluid flow with dual input/output valves, which permitted precise control of the movement of the lower press platen. The upper platen was stationary during the tests, but could be set at any height by means of a hydraulically worked screw-mechanism. The applied load could be read to 0.5 kN.

4.1.2.2 Die-Set

It was important that the platens between which the blocks were compressed were always exactly parallel, of uniform surface finish and hard enough to resist damage. For these reasons, the upsetting was performed using the die-set shown, in use, in fig. 4.1 between the ram and top platen of the press.

The die-set consisted of a mild-steel outer barrel into the bottom of which was recessed and pegged (pegs not shown), and optionally bolted, a circular, hardened-steel platen. A similar platen was recessed in, and scewed to, the under-side of a partially-hollow, mild-steel plunger, which fitted closely inside the casing. Relative

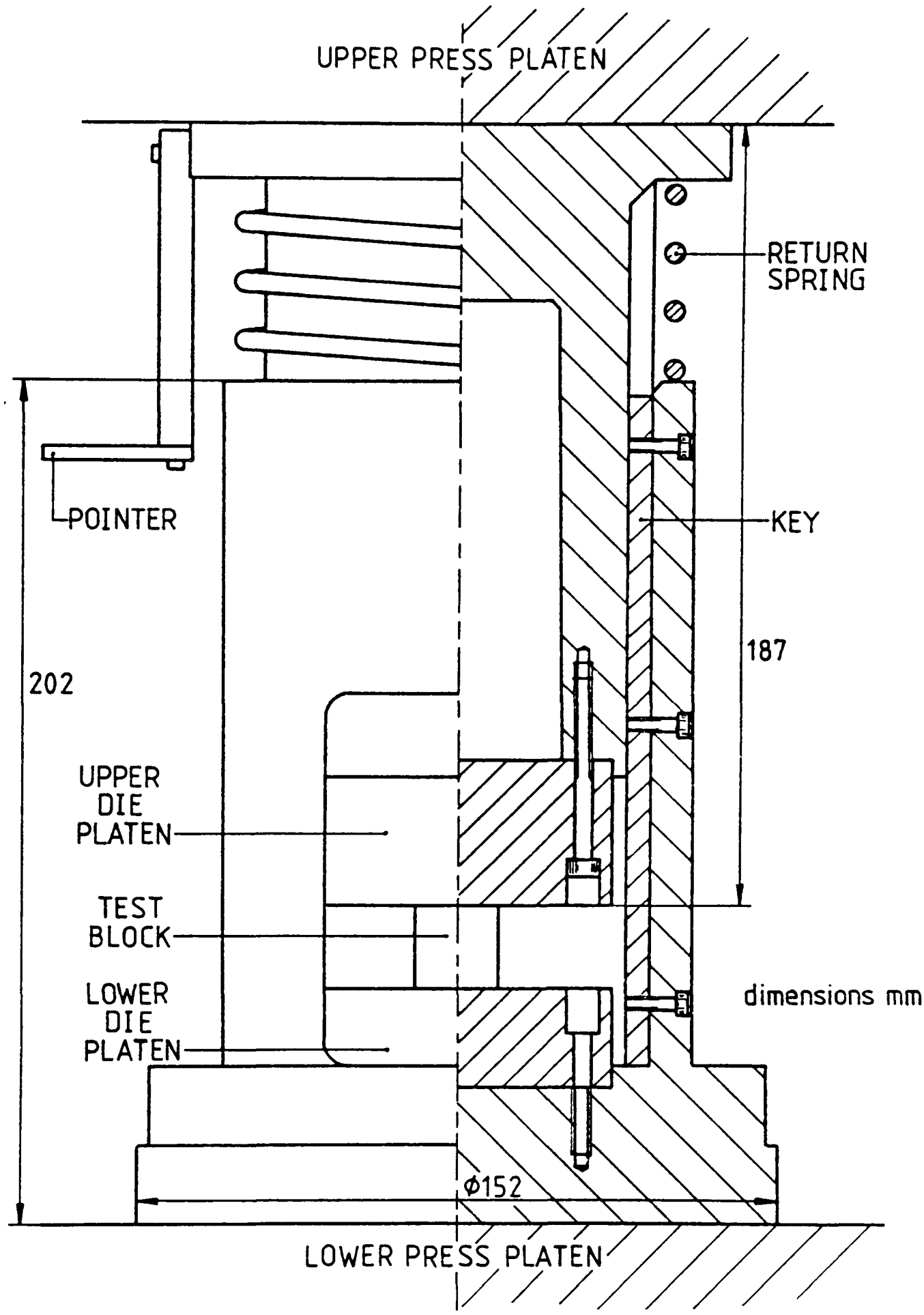

FIG. 4.1
DIE-SET IN USE

rotational movement of these two components was prevented by a vertical key, bolted to the inside of the barrel, which engaged with a slot, milled into the plunger.

The surfaces of the platens, which were to make contact with the blocks, were finely ground and made parallel to within about 25 μm across a diameter. Both of the die-platens were then heat-treated to a Rockwell C hardness of 60, which was sufficient to prevent their plastic deformation under the conditions of the experiment, but not high enough to risk cracking the centrally unsupported upper-die.

The test-blocks could be inserted in between the two platens through rectangular windows cut into the outer container wall, the spring lifting the plunger clear of the lower die when not actually being compressed by the testing machine. This spring was not stiff enough to affect the load registered by the press.

An approximate indication of the extent of the deformation could be obtained while the compression was under way, by means of a dial-gauge acting on the pointer attached to the plunger cap. The body of the gauge would normally be held in a free-standing clamp, resting on the lower ram of the press.

4.1.2.3 Method

The initial dimensions of the blocks were measured with a micrometer. They were then, in turn, degreased with acetone and placed between the similarly-degreased upper and lower platens of the die-set, which was in position on the lower ram of the press. The press was activated to bring the upper die-set platen into contact with the test-block, the dial-gauge was re-set to zero and positioned in contact with the

pointer, and then the test-block was slowly compressed to its final state, (typically taking about a minute), as indicated, approximately, by the dial-gauge.

The applied load was read from the hydraulic press, and after withdrawal of the lower ram, the height of the block was again measured with the micrometer. The four blocks were compressed, nominally, to 10, 20, 30 and 40% respectively.

4.1.3 Measurements

4.1.3.1 Deformed Shape of the Billets

The deformation of the free surfaces of the blocks was investigated by a combination of two techniques. The first measured the overall, deformed dimensions, and the second measured the shape of each of those faces relative to the reference points derived from the first.

4.1.3.1.1 Shadow Profile

The mid-height profiles of the blocks were examined using a Zeiss MP320 projector equipped with digital read-out. This was operated in the shadow-mode, and the mid-height profile was selected by focussing the microscope onto slip-gauges which had been previously placed at the correct height. The dimensions of the blocks in this plane were measured in two perpendicular directions across opposite faces.

4.1.3.1.2 Surface Profile

The shape of each of the free surfaces of the deformed blocks was measured using a modified Heidenhain XY table, shown diagrammatically in fig. 4.2.

The block being measured was attached to a small, lockable turntable (not shown) with double-sided tape. The turntable was then placed on the moveable part of the XY table, and rotated until the required face was parallel with the direction of travel of the table, (direction X in fig. 4.2). The Millitron probe was clamped, as shown, to a horizontal arm, which could be raised vertically, (direction Y). The Millitron transducer responded to movement of the tip, which was in contact with the surface of the block, (direction Z).

Thus the three-dimensional coordinates of any point on the deformed surface could be obtained; the X and Z values as a digital read-out, the Y coordinate from a dial-gauge acting upon the horizontal arm.

In practice, the Z values were sampled at the points of intersection of an imaginary 2mm grid lying in the XY plane. Firstly, the probe was positioned at the intersection of the diagonals of the face, and the reading zeroed. The probe was then moved horizontally across the block, at different heights, with the X and Z readings being recorded at the required intervals in X.

The probe had a modified tip, improvised from a ball-point pen nib. This gave a tip radius of about 0.5mm, which was small enough to avoid errors in measurement due to the curvature of the free surface, but large enough to eliminate spurious readings from surface irregularities.

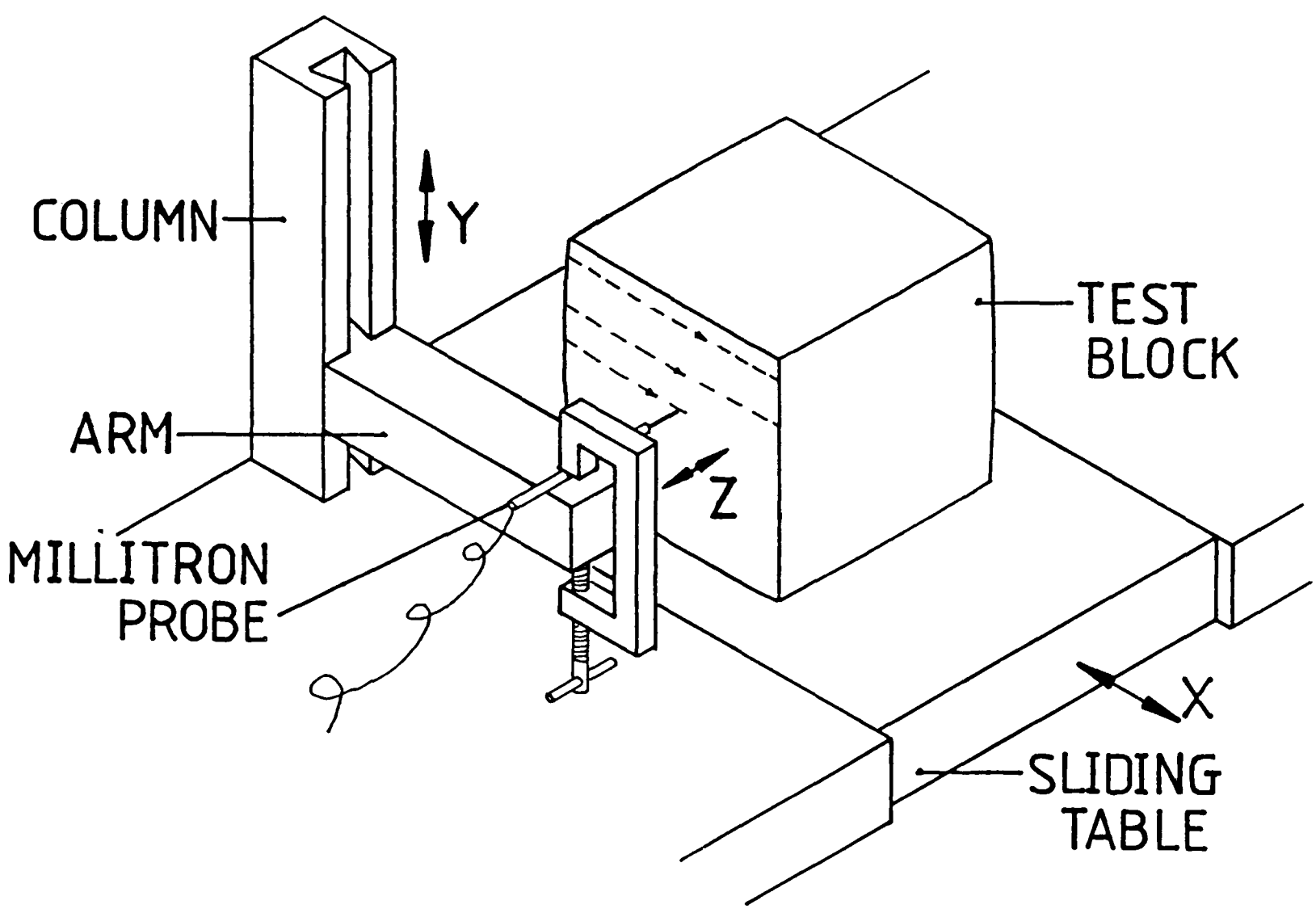

FIG. 4.2

SCHEMATIC REPRESENTATION OF
MEASUREMENT OF SURFACE PROFILE

4.1.3.2 Hardness Tests

The billet which had been deformed to a nominal strain of 40% was sectioned along its three planes of symmetry and the exposed surfaces polished. Hardness tests were then carried out on one quadrant of each of the cut surfaces using a Vickers pyramid indenter. The indentations were performed with a 5kg weight at the intersections of a 1.4mm grid.

4.2 FINITE-ELEMENT ANALYSIS

4.2.1 A Note on the Friction Technique

Since the analysis presented in this chapter was the first attempt to implement a friction technique in the program, the actual method used differed slightly from that which was eventually adopted (see section 3.2.1.2.2.2). For the present analysis, the changes in stress and plastic strain were calculated in friction-layer elements, which were therefore able to yield and deform plastically, the stiffness-matrix multiplier (SMM) applied to these elements was simply Hartley's beta factor $m/(1-m)$, where m is the friction factor of the interface, and the friction-layer elements were included in the procedure for evaluating the hydrostatic stress by the indirect method. (By contrast, in the final version of the program, the friction-layer elements always deformed elastically, the SMM was equal to the beta factor multiplied by the ratio H'/E, and friction-layer elements were ignored during the indirect calculation of hydrostatic stress.)

4.2.2 Finite-Element Model

The finite-element analysis was performed using a mesh of 432 elements in a rectangular 6x6x12 array modelling one eighth of a 20x20x40mm block (fig. 4.3). A frictional-boundary plane was defined to be in contact with the top of this mesh; an additional layer of friction elements (not shown in fig. 4.3) was specified at this surface.

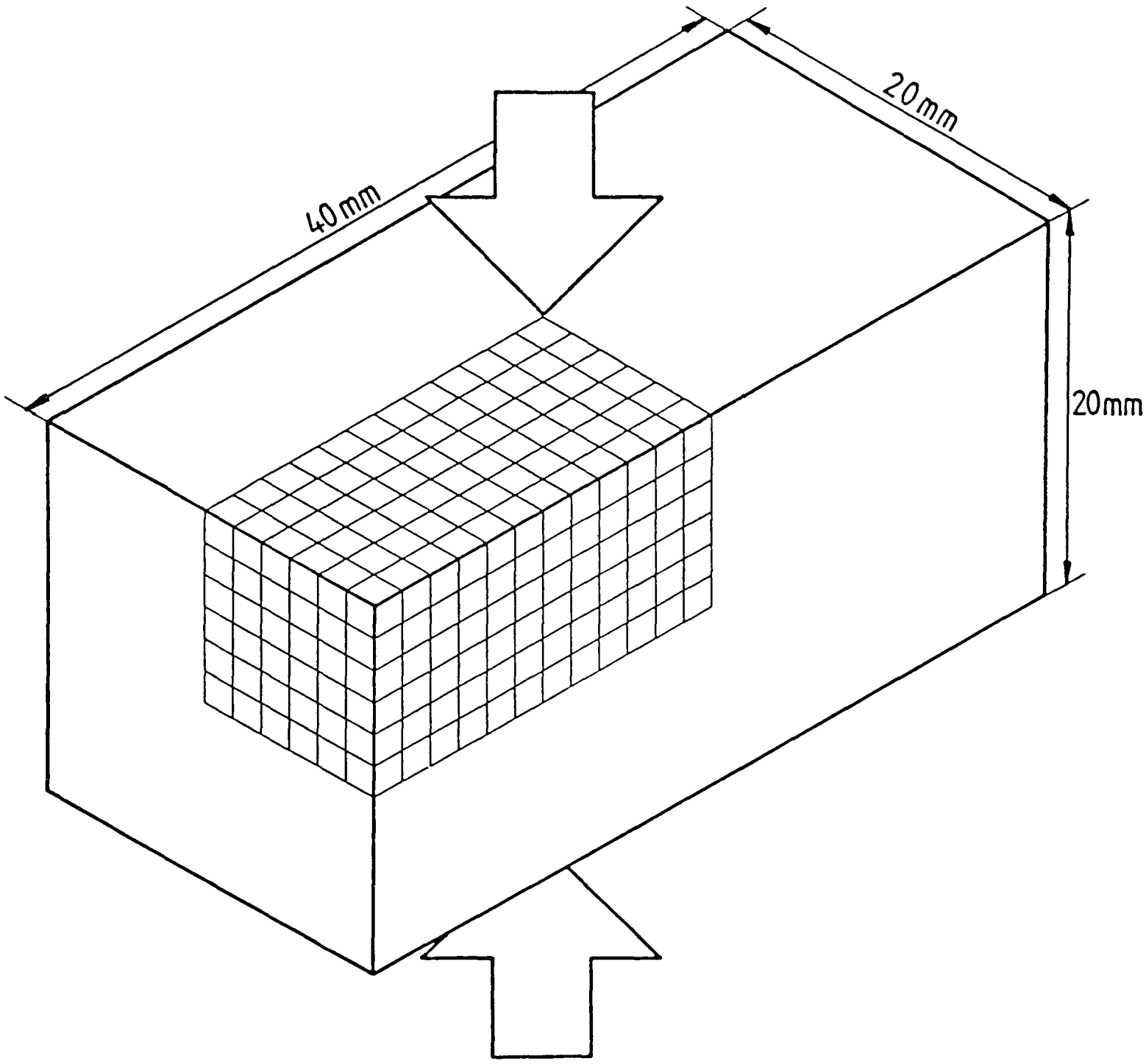

FIG. 4.3

RECTANGULAR BLOCK — FINITE-ELEMENT IDEALISATION

The friction factor m for this interface was 0.7, which previous work by Hartley et al (101) indicated was appropriate for simulating unlubricated contact.

The frictional-boundary plane had, necessarily, to be stationary, so the deformation was defined by specifying an incremental, upward displacement to the nodes on the bottom of the mesh, i.e. in the process modelled, the top platen was fixed and the lower platen moved upwards towards it. Since the bottom of the mesh represented a horizontal plane of symmetry of the billet, these nodes were free to move horizontally. The nodes on the two vertical planes of symmetry were similarly unconstrained within those planes but were prevented from moving perpendicularly to them.

During each increment, the lower surface of the mesh moved upwards by 0.2mm, giving a nominal engineering-strain increment of 2% at the start of the deformation.

4.2.3 Material Properties

The material properties of commercially-pure (EC1) aluminium were assumed for this analysis. Young's modulus was equal to 70GN/m^2 , Poisson's ratio (for the calculation of displacements in unyielded elements and the stress in all elements) was 0.34, while the material yielded initially at a generalised stress of 50MN/m^2 . The strain-hardening behaviour was modelled by the function:

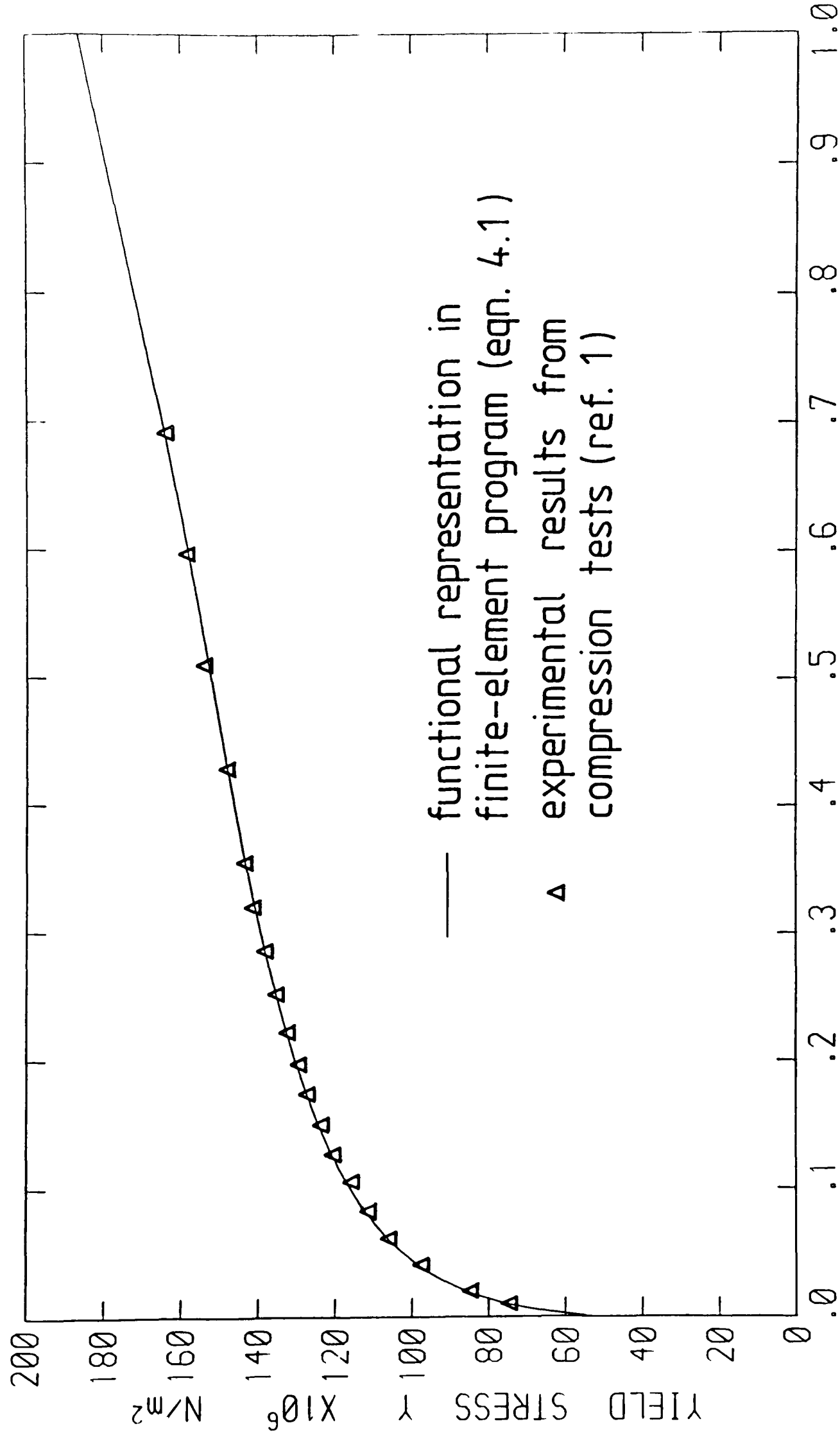

FIG. 4.4 VARIATION OF YIELD STRESS WITH GENERALISED PLASTIC STRAIN FOR COMMERCIALLY-PURE ALUMINIUM

$$Y = 50 + 21[\ln(\bar{\varepsilon}^p + .00465/.00465)] + 9e^{4.5(\bar{\varepsilon}^p - .6909)} \text{ MN/m}^2 \quad \bar{\varepsilon}^p \leq .7$$

$$Y = 164.8 + 72(\bar{\varepsilon}^p - .7) \text{ MN/m}^2 \quad \bar{\varepsilon}^p > .7 \quad (4.1)$$

the coefficients of which were chosen to fit the experimental data for commercially-pure aluminium obtained by Hartley (1) from compression tests using a Cook and Larke technique (102). Fig. 4.4 shows that the function fits the experimental points very well. Since the latter were only obtained up to a plastic strain of about 70%, the function assumed linear strain hardening after this point, which is indicated by the trend of the experimental results.

4.2.4 Method of Solution

As remarked earlier, the analysis was performed using the secant-modulus method of solving the non-linear stiffness relationships. The stiffnesses were calculated on the basis of the techniques described in Chapter Three, and included the Jaumann correction, LCR strain and constant dilatation modifications. To enforce volume constancy of the plastic region, a value of Poisson's ratio equal to 0.4999 was used in the evaluation of the stiffness matrices of yielded elements. The hydrostatic stress was calculated by the indirect method.

4.3 RESULTS

4.3.1 Deformation

The four experimental blocks were deformed to 10.1, 19.9, 29.8 and 40.3% reductions in height. A photograph of the most highly-deformed block is shown in fig. 4.5. Similar views of the finite-element mesh at stages throughout the deformation are presented in fig. 4.6, which also includes drawings of two sections of the mesh at the same intervals of the deformation. Note, due to the automatic scaling of pictures carried out in the program, these sections are not to exactly the same scale. Fig. 4.7 compares the finite-element predicted profiles of three sections through the billet at 40.9% deformation with the experimental results for 40.3% deformation (one quadrant only shown in each case).

The three experimental sections were the planes of symmetry of the billet; since the finite-element sections had to pass through the centroids of the elements, these sections lie approximately half an element (about 1mm) away from their respective planes of symmetry.

4.3.2 Hardness

The values of generalised stress (i.e. the current yield stress) were obtained at points of the finite-element sections of fig. 4.7 and converted to Vickers pyramid hardness numbers (VPN) according to the equation (103):

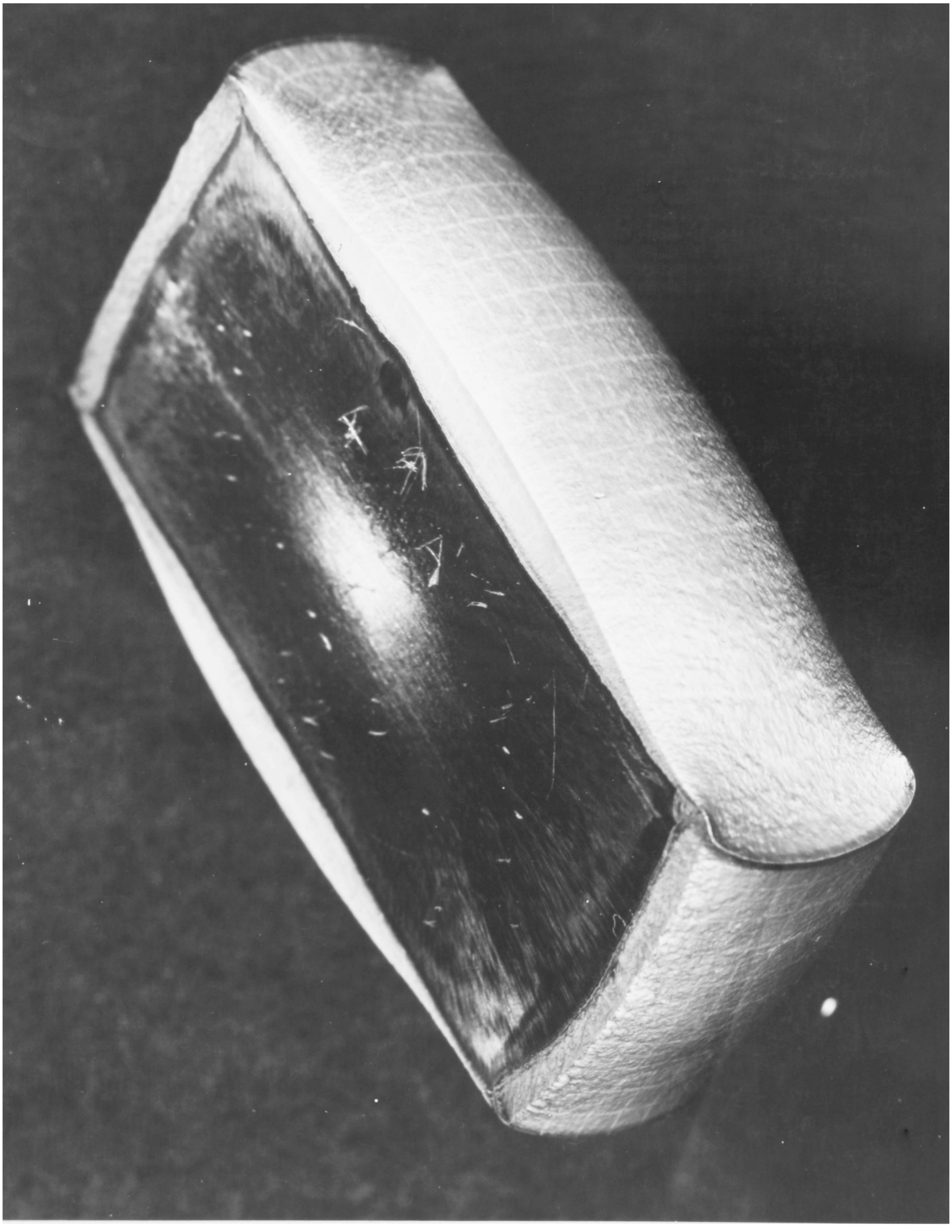

FIG. 4.5

RECTANGULAR (20x20x40mm) BLOCK OF COMMERCIALLY-PURE ALUMINIUM UPSET TO 40.3% REDUCTION IN HEIGHT WITHOUT LUBRICATION

FIG. 4.6

UPSETTING OF RECTANGULAR BLOCK —

FINITE-ELEMENT PREDICTED DEFORMATION

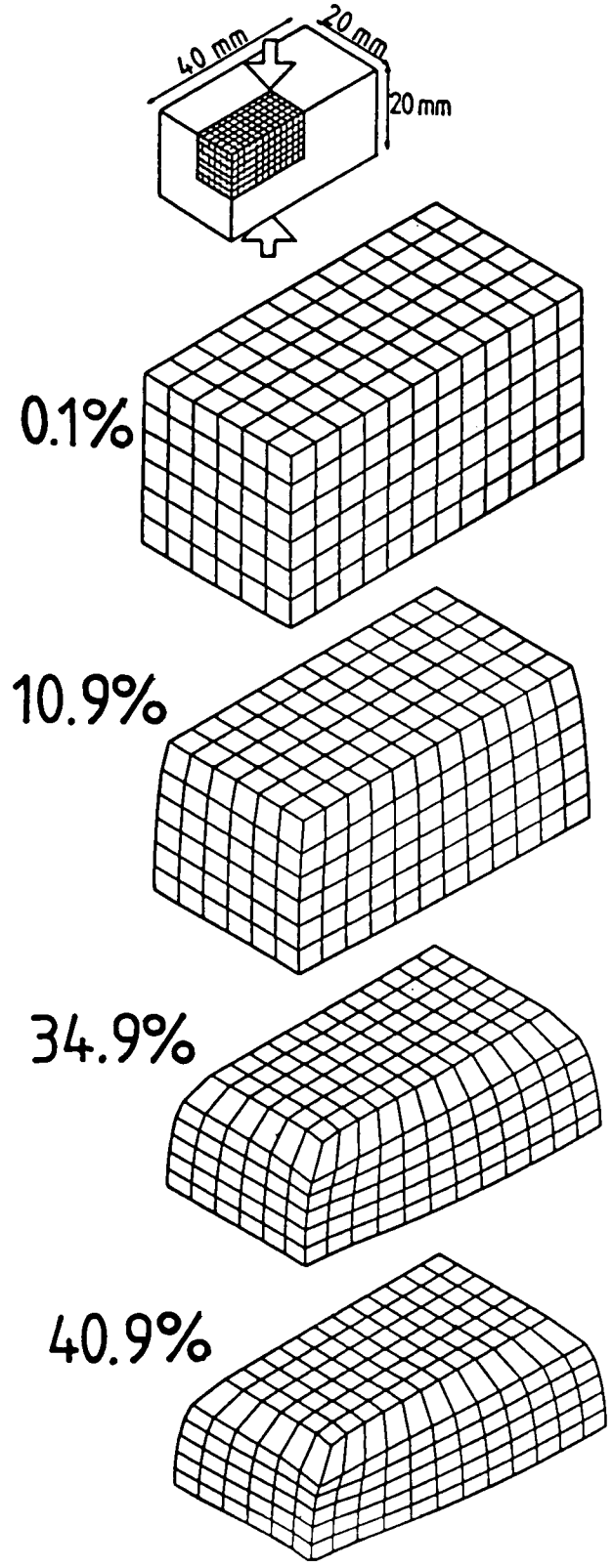

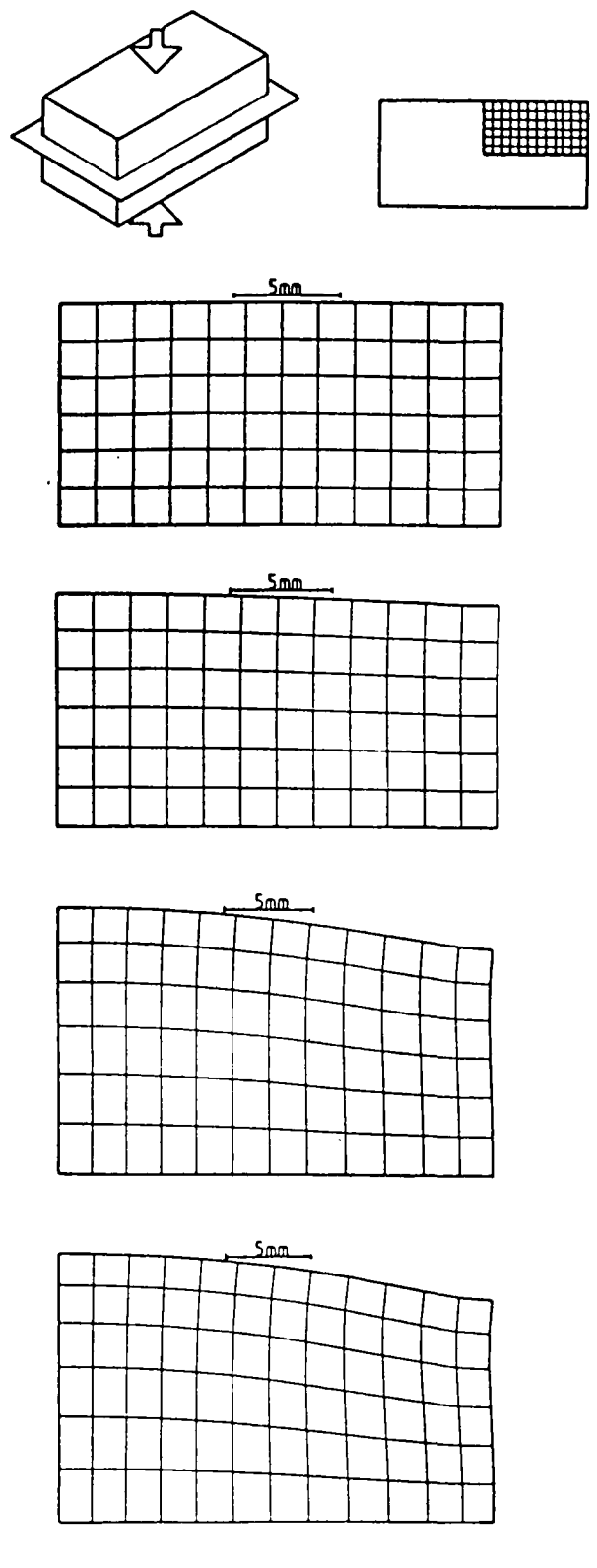

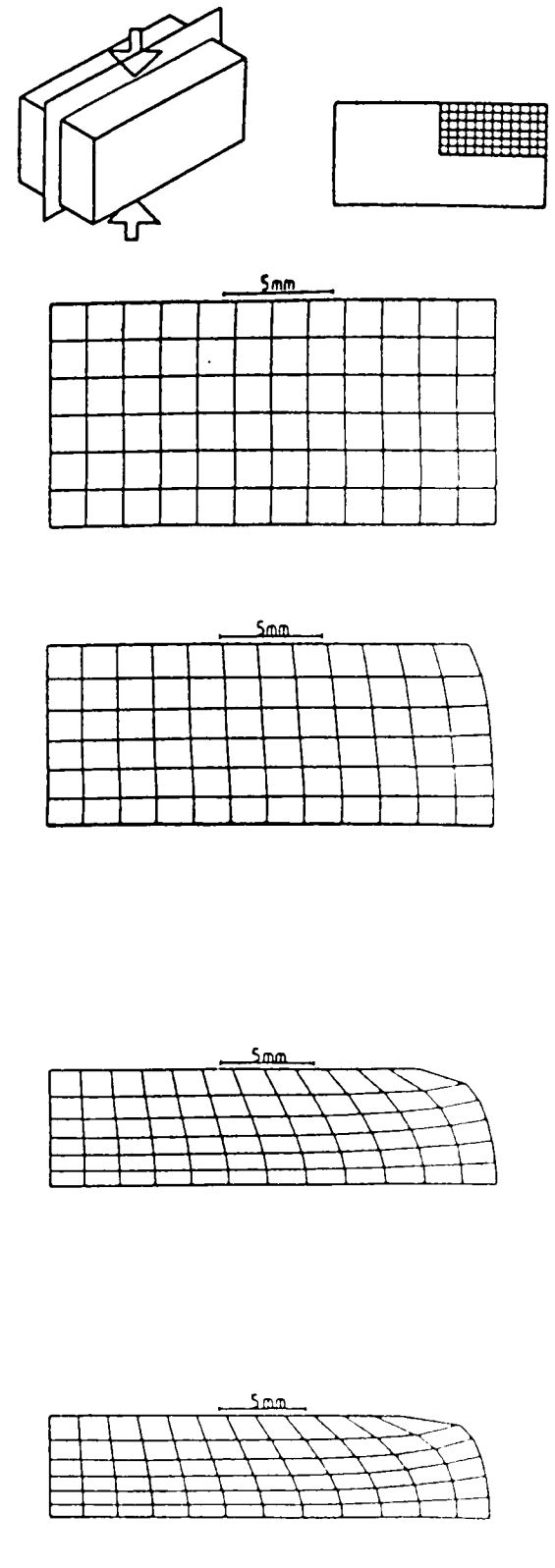

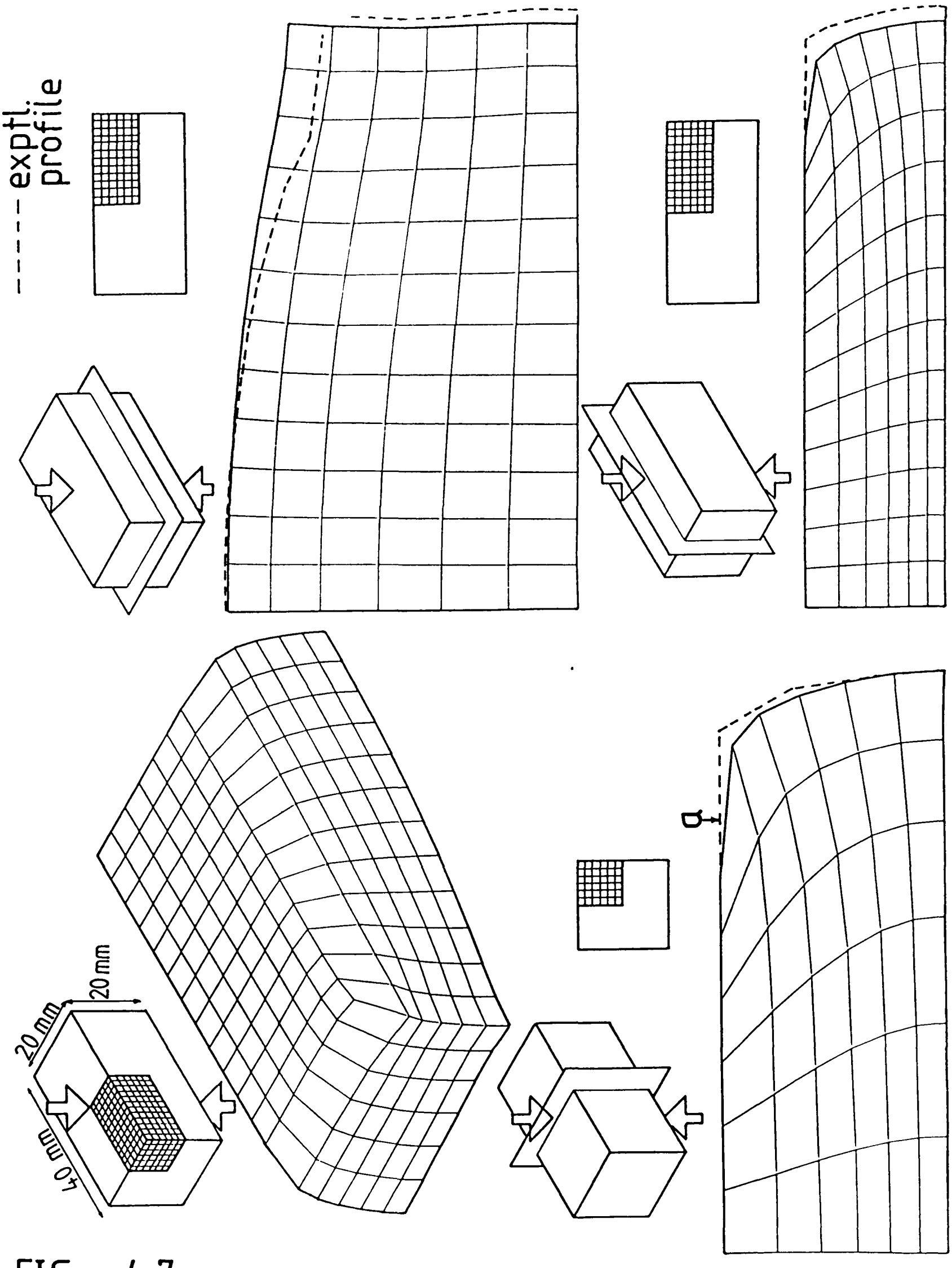

FIG. 4.7

COMPARISON OF F.E PREDICTED DEFORMATION (40.9%) WITH EXPERIMENTAL RESULTS (40.3%): GENERAL VIEW & SECTIONS CLOSE TO THREE PLANES OF SYMMETRY OF BLOCK

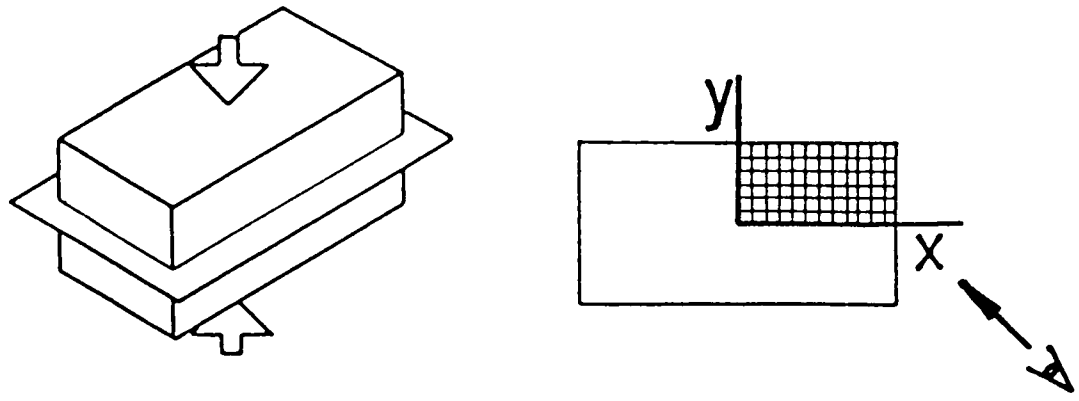

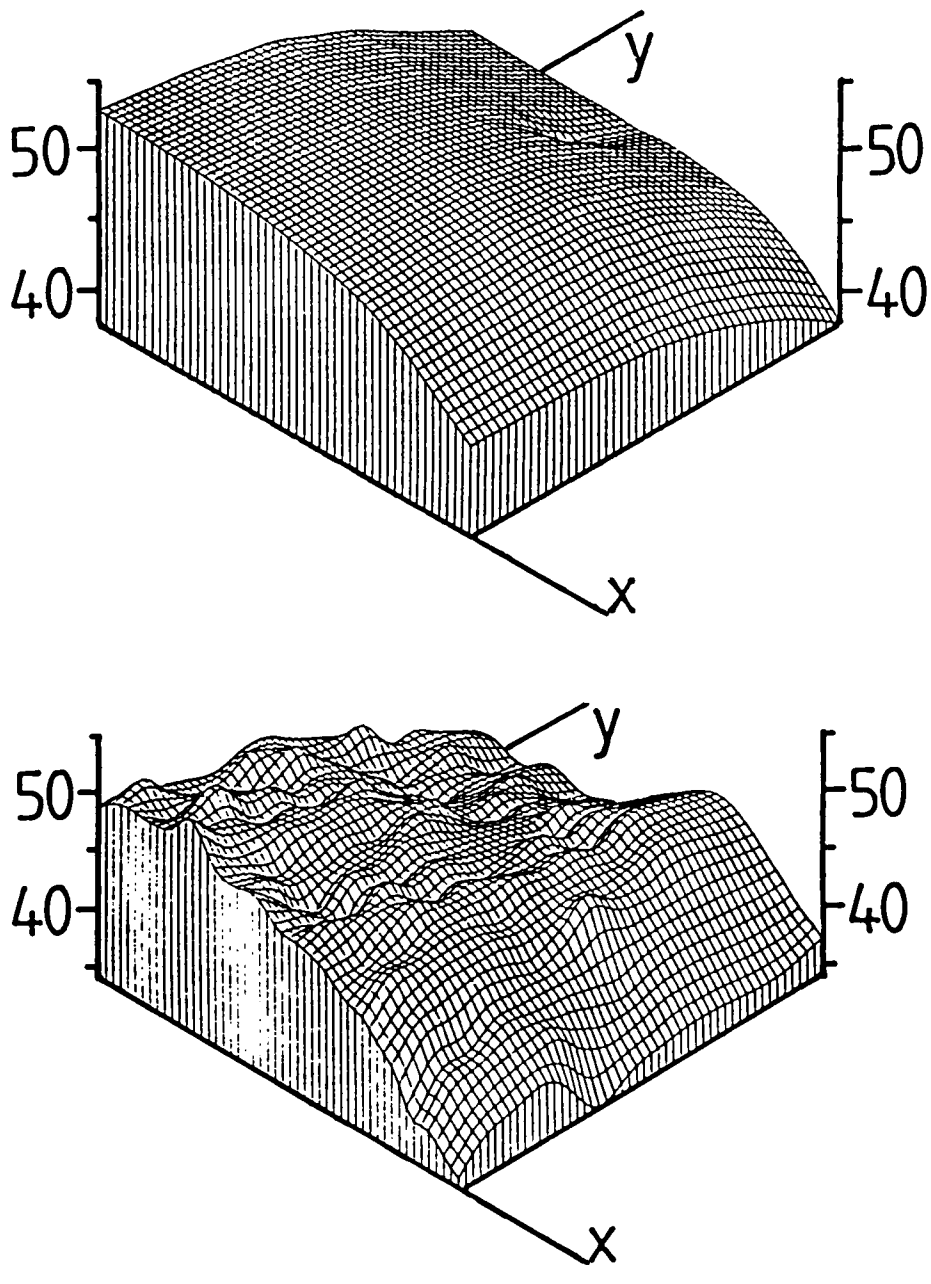

F.E.

EXPTL.

FIG. 4.8

COMPARISON OF F.E. PREDICTED WITH EXPERIMENTALLY MEASURED VICKERS PYRAMID HARDNESS DISTRIBUTIONS (kg f/mm^2) ACROSS ONE QUADRANT OF SECTION CLOSE TO HORIZONTAL PLANE OF SYMMETRY OF BLOCK

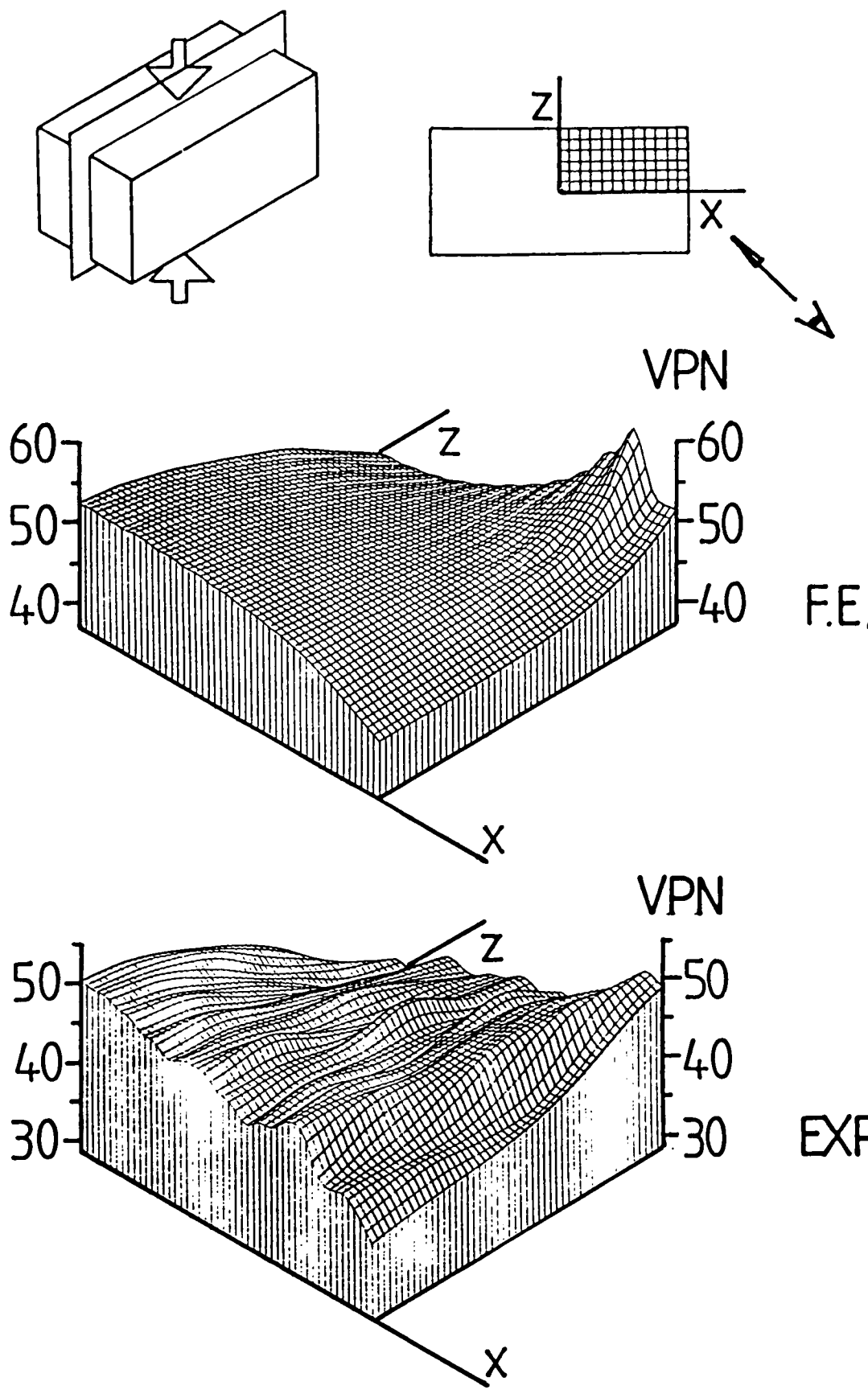

FIG. 4.9

COMPARISON OF F.E. PREDICTED WITH EXPERIMENTALLY MEASURED VICKERS PYRAMID HARDNESS DISTRIBUTIONS (kg f/mm^2) ACROSS ONE QUADRANT OF SECTION CLOSE TO VERTICAL PLANE OF SYMMETRY OF BLOCK (LONGER DIMENSION)

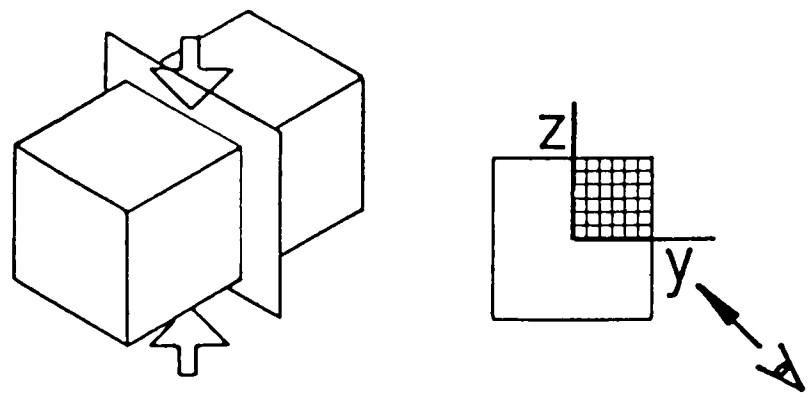

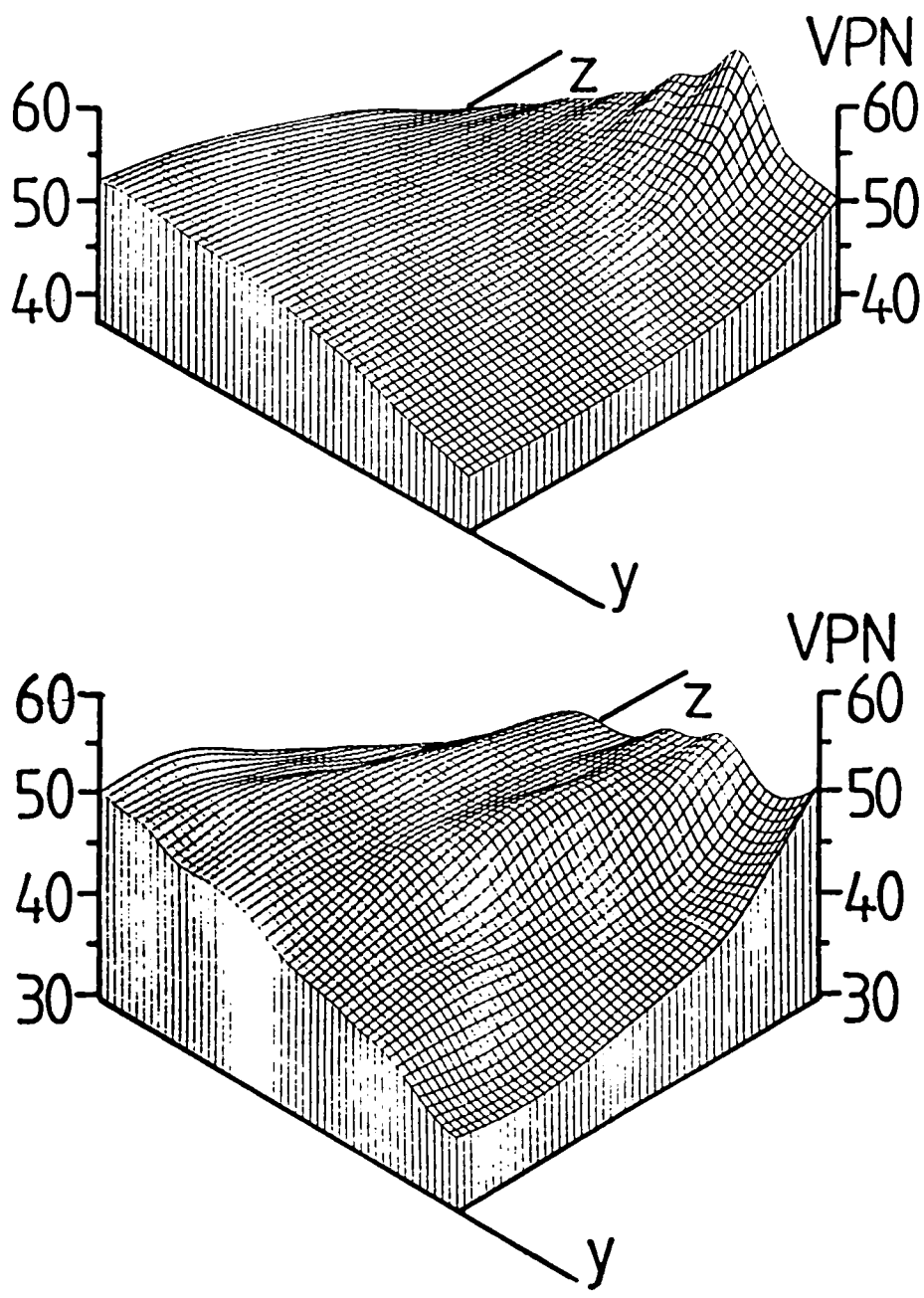

FIG. 4.10

COMPARISON OF F.E. PREDICTED WITH EXPERIMENTALLY MEASURED VICKERS PYRAMID HARDNESS DISTRIBUTIONS (kg f/mm^2) ACROSS ONE QUADRANT OF SECTION CLOSE TO VERTICAL PLANE OF SYMMETRY OF BLOCK (SHORTER DIMENSION)

$$VPN \simeq 0.302Y \qquad (4.2)$$

where VPN is measured in kg f/mm^2 and Y is measured in MN/m^2. The variations of these hardness values across these sections are shown as parametric surfaces in figs. 4.8-4.10. Also shown are the variations of the experimentally-determined Vickers hardness numbers. In each case, the domain over which the hardness is shown varying is a rectangle approximating one quadrant of the section under consideration; the computer package, used to draw the parametric surfaces, maps these rectangles onto squares.

4.3.3 Die-Interface Pressure

As mentioned previously, for this analysis the friction-layer elements were included in the procedure for calculating the hydrostatic stress indirectly. Since the stresses in friction-layer elements tend not to be typical of the rest of the billet, and because these values were used in the evaluation of the spatial gradients of stress in the top layer of billet elements, it was found that the components of stress calculated in these latter elements were completely unrealistic. Thus it was impossible to calculate the pressure across the die-interface directly from the values of stress in the top layer of billet-elements. Instead, this pressure was estimated by extrapolating values of stress from the two layers of elements just below the top one. The variation of the estimated pressure across the die interface is shown in fig. 4.11.

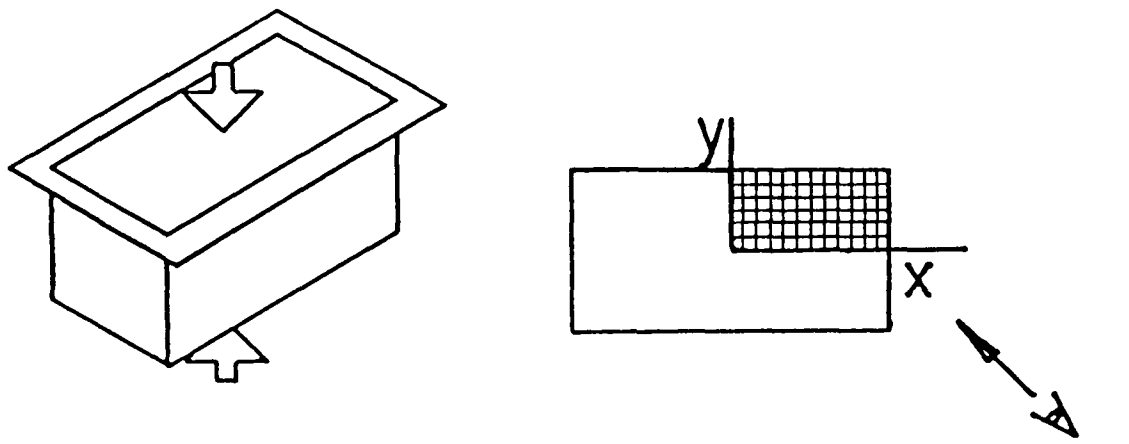

FIG. 4.11

FINITE-ELEMENT PREDICTION OF DISTRIBUTION OF PRESSURE (MN/m^2) ACROSS ONE QUADRANT OF THE INTERFACE BETWEEN THE DIE AND THE BLOCK

As before, the domain depicted in this figure represents a rectangular region approximating one quadrant of the die-interface, and this has been mapped onto a square.

Integrating the pressure distribution over the area of the interface gives the value of the deformation load, predicted by the finite-element program for 40.9% reduction in height, to be 120kN; the load recorded experimentally for 40.3% deformation was 220kN.

4.4 DISCUSSION

4.4.1 General

It was noted earlier that, as a computational convenience, the finite-element and experimental sections were separated by a small distance, of the order of 1mm. Examination of the projected view of the finite-element mesh in fig. 4.7 shows that the finite-element profiles at the positions of the planes of symmetry differ negligibly from those a half-element away (certainly to within the accuracy of the drawings of these sections). In the same way, it can be seen from the distributions of hardness given in figs. 4.8-4.10 that, on all three sections, the gradients of this quantity are small near the centre lines of the billet so the distributions of finite-element hardness plotted in these figures differ very little from the distributions to be found on the corresponding planes of symmetry.

Thus for the purposes of this chapter, it may be assumed that the sections through the finite-element mesh coincide with those actually made through the deformed experimental block.

It should also be noted that little error is introduced by comparing the finite-element results for 40.9% deformation with those for the experimental reduction in height of 40.3%.

4.4.2 Comparison of Deformation

Fig. 4.7 shows that the deformed shape of the finite-element mesh is not in good agreement with the experimentally-observed shape of the compressed block. In general, the faces of the finite-element mesh have spread too little while the corner has moved outwards too much.

This behaviour may be explained by comparing the horizontal displacement of the top surfaces of the experimental block and the finite-element mesh. The photograph of the former (fig. 4.5) shows that, in addition to the vertical faces of the billet folding onto the die, the increase in size of the top face of the experimental workpiece is also due to spread of the surface which was originally in contact with the die. The final position of the original edge of the billet is indicated by the arrow (a) on the section through the shorter vertical plane of symmetry in fig. 4.7. The top surface of the block has spread, across the shorter dimension, by some 15%. On the other hand, the top of the finite-element mesh has hardly spread at all in either direction, the edges moving outwards by only a fraction of a percent.

It appears, therefore, that despite using a friction factor of 0.7, the finite-element program, in the present analysis, imposed almost sticking-friction conditions: the friction technique adopted in this instance clearly did not work correctly, and required modification.

In spite of this, the general appearance of the deformed finite-element mesh indicates that the program obtained essentially the correct mode of flow. For instance, the overall shape predicted by the finite-element analysis is roughly similar to that observed experimentally, and in particular, the program predicted the formation of an 'ear' at the corner of the deformed billet which is

characteristic of the upsetting of prismatic blocks (13).

Also, unlike the previous analysis described in reference 100, the finite-element mesh correctly exhibited a tendency for the sides to fold onto the die interface; that this process was not quite complete at a deformation of about 40% is due solely to the coarseness of the discretisation, i.e. if the elements used were half the size, this fold-round would have occurred before this stage, as observed experimentally.

4.4.3 Comparison of Hardness Distributions

It can be seen from figs. 4.8-4.10 that the experimental hardness values are subject to considerable scatter, particularly those on the horizontal section. (Indeed, much of the scatter has been smoothed by the numerical techniques used to obtain the parametric surfaces.) In spite of this localised variation, the general shape of the experimental and finite-element distributions of hardness are in fairly good agreement. On the whole, the finite-element values are slightly higher than the experimental ones whereas the variations of the former are smaller, but except for some major discrepency near the edges of the sections, e.g towards the outer edge of the die interface in fig. 4.9, the finite-element program has predicted the correct type of distribution.

At first sight, this might seem surprising considering the poor correlation between the predicted and actual deformed shapes, but in fact it is in accordance with the conclusions made in the previous section, namely that the general shape is correct , but that there is

too little interfacial slip in the finite-element model. Thus, for the bulk of the material, the finite-element prediction of hardness is quite good, with the maximum discrepancy occurring in areas, such as near the die interface and the free surface, where the failure of the friction technique would be most apparent.

4.4.4 Die-Interface Pressure

Experimental measurement of the variation of the pressure across a die during a forging operation is extremely difficult to perform, particularly as the extent of deformation, and hence the pressure, is increased. It was felt that such measurement was outside the scope of the present programme of research, so the finite-element predictions of pressure will be discussed in the context of previous experimental results.

Nagamatsu and Takuma (4) measured the distribution of die pressure during the upset forging of rectangular aluminium-alloy blocks. They used a variety of billet geometries and found that when the height to width ratio of the specimens was small (less than about 0.5) the pressure exhibited a friction-hill distribution analagous to that predicted theoretically for plane-strain and axisymmetric upsetting (7), but that when the specimens were taller, this variation was reversed and the minimum pressure occurred at the centre of the interface. The pressure distribution obtained for the geometry under consideration here (20x20x40mm) is shown in fig. 4.12.

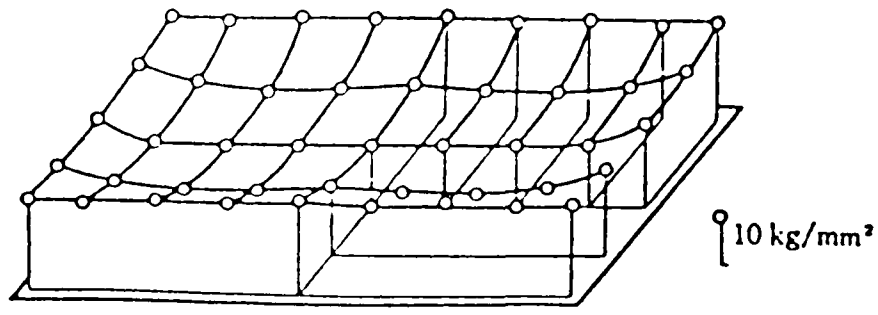

a)

Fig. 9 Pressure distribution on interface. Rectangular section (20 mm × 40 mm), $h_0=1$, No lubricant, $L=12$ ton.

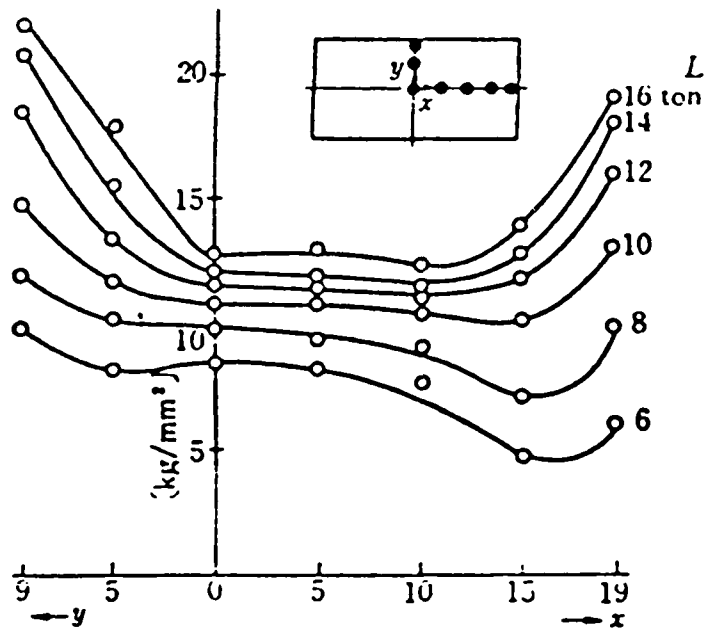

b)

Fig. 11 Pressure distribution on interface along central lines x and y (Effect of load L). Rectangular section (20 mm × 40 mm), $h_0=1$, No lubricant.

FIG. 4,12

EXPERIMENTALLY MEASURED DISTRIBUTION OF PRESSURE ACROSS THE TOP OF A 20x20x40 mm ALUMINIUM-ALLOY BILLET DURING SIMPLE UPSETTING WITHOUT LUBRICATION (REF. 4)

a) Distribution for Load of 12 tons

b) Variation along Centre Lines for Different Loads

Direct comparison between these results and fig. 4.11 is difficult because, judging by the loads quoted, Nagamatsu and Takuma's results would all seem to apply to smaller reductions in height than that corresponding to the finite-element distribution, and it has been observed that the shape of the pressure distribution changes as the deformation is increased during upset forging (14). However, some general remarks may be made.

The pressure distribution predicted by the finite-element program does show a friction depression of the sort observed experimentally, and the variation is of the right order (pressure is just greater than the average value at the outside and just over half this at the centre). The shape of the finite-element depression though does not agree with that obtained experimentally. For instance, except for the smaller loads, the experimentally-measured pressure increases monotonically from the centre of the interface to the middle of its longer edge, while the pressure predicted by the finite-element program attains a minimum in the middle of this line. It should be emphasised that the finite-element and experimental results refer to different stages in the deformation, so this is not conclusive evidence that the shape of the finite-element distribution is wrong.

However, the predicted values of pressure certainly appear to be too low, since they lead to a value of the deformation load which is much smaller than that measured as part of the present work.

Much of the discrepancy between the finite-element predicted and experimentally-measured distributions of pressure can probably be attributed to the fact that the former were calculated by a process of extrapolation from values inside the mesh. As mentioned earlier, this extrapolation was only necessary because the friction-layer elements were included in the indirect calculation of hydrostatic stress and resulted in the calculation of incorrect values in the adjacent layer

of billet elements. The final version of the program, used in the analyses considered in the rest of this thesis, does not include the friction-layer elements in the indirect calculation of hydrostatic stress, so that pressure may be calculated directly from the values of stress in the top layer of billet elements.

4.5 CONCLUSIONS

The general shape of the deformed billet predicted by the finite-element program is similar to that of the experimental block; the flow modes would therefore appear to be broadly the same. As a result, the finite-element program obtained values of material hardness which vary in a similar way to the experimentally measured values across the three planes of symmetry of the billet, although the finite-element hardnesses are in general slightly too high.

The profiles of the deformed finite-element mesh are not exactly the same as those observed experimentally - this appears to be the result of the particular form of the friction technique used for this analysis imposing too high a frictional restraint. Therefore, an attempt must be made to improve the method of modelling interfacial friction.

The distribution of die-interface pressure calculated by the finite-element program exhibits a friction depression. This agrees with the experimental results published previously (4). The actual shape though is not similar to the experimental results, and the values of pressure are too low. This was due to the process of extrapolation which was necessary for the evaluation of the pressure

in this analysis; future analyses will calculate the pressure without extrapolation and should give better estimates of the deforming load.

In general, the results examined in this chapter indicate that the finite-element program developed here can predict the behaviour of the work-piece during a fully three-dimensional forming process, providing the correct frictional restraint can be applied to the boundary surfaces. The development of the friction technique is the subject of the next chapter.

CHAPTER FIVE

DEVELOPMENT OF THE FRICTION TECHNIQUE

5.0 INTRODUCTION

It was shown in the previous chapter that the friction technique which was first used in the finite-element program imposed too high a restraint on the boundaries of the work-piece. It was clear that further work was necessary to examine and improve this technique. The development of the method of modelling interfacial friction in the finite-element program will be considered in this chapter.

In the analysis mentioned above, interfacial friction was modelled by defining an extra layer of elements (the friction layer) on the required surfaces. The outer layer of nodes thus introduced were prevented from moving, and the stiffness matrices of the friction-layer elements multiplied by the quantity $m/(1-m)$ (m is the interface-friction factor). By altering the value of m, the restraint offered to the tangential movement of the surface nodes of the mesh due to the shearing of the friction layer may be varied. This procedure has proved to work very well in an axisymmetric finite-element treatment (106), and, moreover, the required values of m agreed with those suggested by simple friction theory, in which the friction factor is usually assumed to be the ratio of the yield stresses of the lubricant layer (when present) and the billet material.

However, it was recognised that because of the fundamental differences between two- and three-dimensional formulations, this technique might not be suitable, without some modification, for a three-dimensional program. The results presented in the previous chapter prove this to be the case.

The most obvious way to modify the restraint imposed by the friction layer is by altering the multiplier of the stiffness matrices of the friction-layer elements. Various more complicated functions of m were tried, and some involving other variables such as plastic

strain. None proved to be completely satisfactory, and it became apparent that there was a basic problem with this friction technique, which was the dependence of the restraint on the strain history of the friction layer.

It is a fundamental precept of the friction-layer technique that this layer does not physically represent the lubricant film or any part of the billet; it is simply a mechanism for applying tangential force to a surface. As a result, the deformation occurring in this layer is completely fictitious - the more so since it is reformed at the start of each increment. It did not, therefore, seem reasonable to allow this deformation to affect the surface restraint through the influence of the stress and strain dependent $[D_n]$, $[T_n]$ and $[U_n]$ matrices in the stiffness formulation of the friction layer.

So it was decided to eliminate the strain-history dependence of the friction layer by setting the strain and stress in these elements to zero at the start of each increment. As a consequence, the stiffness matrices of the friction-layer elements will always be based upon the elastic $[D_n]$ matrix, and will therefore tend to be much stiffer than the billet elements with which they are in contact. To counteract this, the stiffness matrix of each friction-layer element needs to be multiplied by the ratio H'/E, where E is Young's modulus and H' is the slope of the yield stress vs plastic strain curve of the material for the current plastic strain in the adjacent billet element. The stiffness of the friction layer may then be modified, as before, by multiplying each element-stiffness matrix by the quantity $m/(1-m)$. The product of H'/E and $m/(1-m)$ which is used to modify the stiffness of a given friction-layer element is called the stiffness-matrix multiplier (SMM) of the element.

This modified friction technique, which is the one described in section 3.2.1.2.2.2, was found to model friction better than any other

method tried, on the basis of results of ring tests. These tests will be considered next.

5.1 DEMONSTRATION OF MODIFIED FRICTION TECHNIQUE - I. THE RING TEST

5.2.1 The Basis of the Ring Test

It has long been known that when a disc with a central, circular hole is compressed between parallel platens, the mode of deformation is very sensitive to the level of friction of the interfaces between the platens and the work-piece. Basically, if friction is high, the hole closes, whereas if friction is low the hole opens up. When the conditions are somewhere between the extremes of sticking and zero friction, the behaviour is slightly more complicated: for instance the hole may start by increasing in size, but then begin to contract as the deformation proceeds. The percentage change in the diameter of the hole may be plotted against the reduction in height of the ring, for different conditions of friction, to give calibration curves. Generally, the shape and disposition of these curves depend on the initial geometry of the billet and (to a certain extent) the stress-strain characteristics of the material. Investigations show that for any given calibration curve, the actual value of the friction factor m may vary throughout the deformation, and indeed, from place to place on the interface (104), but usually it is assumed to be constant for each such curve.

By standardising upon one particular ring geometry, and ignoring the dependence upon material properties, ring-test calibration curves

allow the friction factor for any given combination of surfaces and lubricants to be measured experimentally with relatively little effort (105). More recently, it has been recognised that these calibration curves offer a convenient and sensitive way of testing the friction models used in finite-element programs (36,37,101), and such curves have also been obtained using the present finite-element program as described below.

5.1.2 Finite-Element Analyses

Several finite-element analyses were conducted, modelling the simple upsetting of circular rings between parallel platens, and using the modified friction technique with the value of the friction factor m lying between 0.000001 and 0.7. The mesh, which contained 80 elements, represented the upper half of a five degree segment of a ring with outer diameter equal to 60mm, inner diameter equal to 30mm and with a height of 20mm (6:3:2 geometry). The finite-element mesh is shown in fig. 5.1. The properties of commercially-pure aluminium were assumed for the analyses (see section 4.2.3, fig. 4.4), the height of the mesh being reduced by 2% of its original value during each step of the calculation. As in the analysis examined in Chapter Four, a stationary boundary plane was defined to coincide with the top of the mesh, and the bottom of the mesh was moved upwards towards it. A layer of friction elements, having the same height as the rest of the elements, were specified on the top of the mesh. These friction-layer elements are not shown in fig. 5.1.

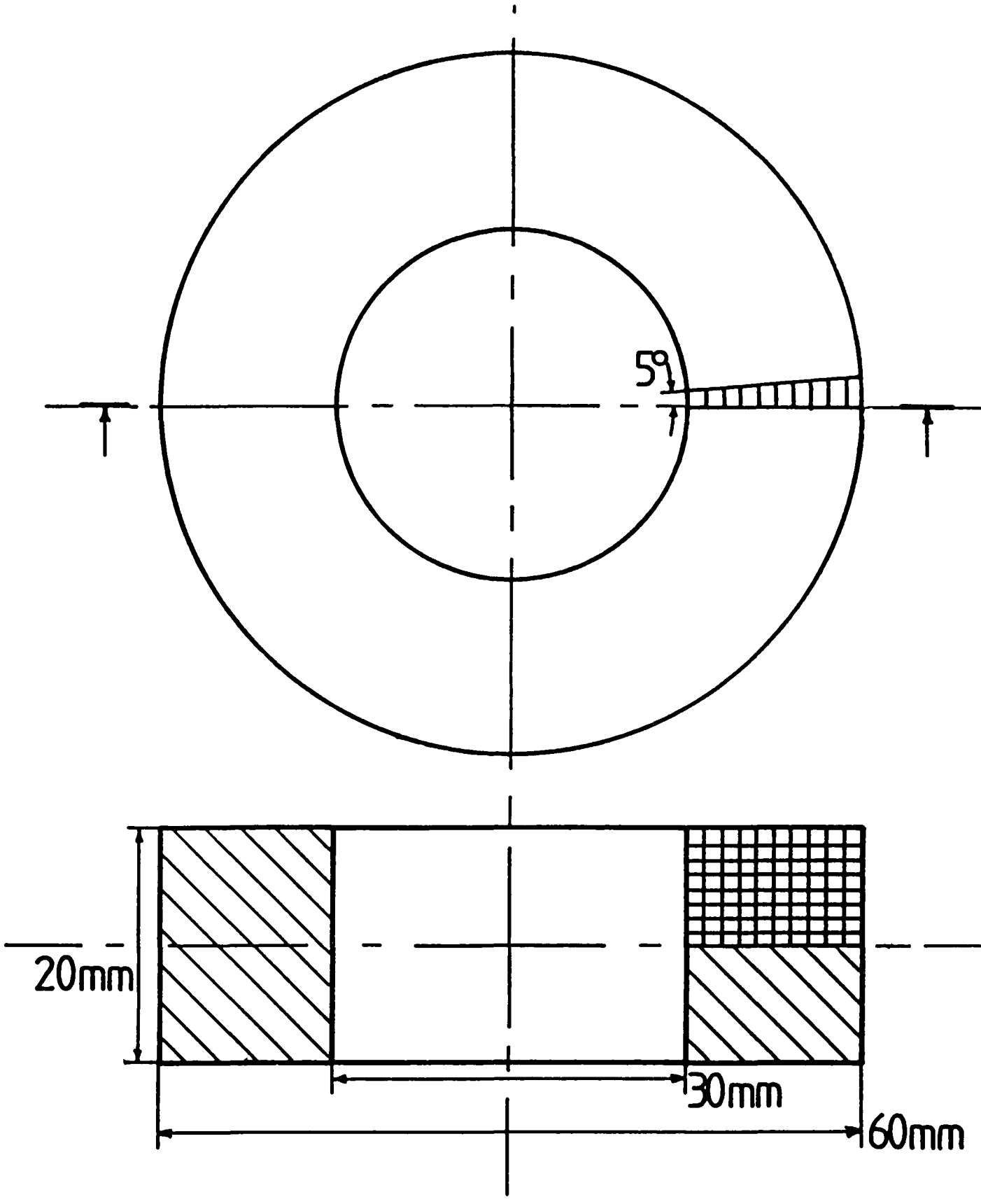

FIG. 5.1

RING-TEST SPECIMEN AND FINITE-ELEMENT IDEALISATION

The finite-element solutions were obtained using a secant-modulus technique with Jaumann correction, constant dilatation and the LCR strain definition. Volume constancy was enforced by specifying the value of Poisson's ratio in the plastic region to be 0.4999 for the evaluation of element stiffnesses.

5.1.3 Results

Some of the deformed finite-element meshes, obtained using various values of m, are shown in fig. 5.2. For each value of m, the length of the internal diameter of the mesh, averaged over the bore surface, was calculated at intervals throughout the deformation. The percentage changes in these diameters are plotted in fig. 5.3 as functions of the percentage reduction in height of the mesh. Also shown in this figure are the experimental results published by Hartley et al (106) for rings of commercially-pure aluminium with the geometry specified above and using a variety of lubricants. The ring-test calibration curve for graphite lubrication was obtained as part of the present work. The lubricant, DAG 580 suspension of graphite in alcohol, was allowed to dry on the billets before the compression tests were performed.

The continuous thick line in fig. 5.3 represents the calibration curve to be expected if a ring could be compressed with no friction at all. Equilibrium considerations show that such a billet must deform homogeneously, and the volume of the hole must remain constant throughout (apart from small elastic changes). Thus the change in the internal diameter in such a case may easily be calculated as a function of the reduction in height.

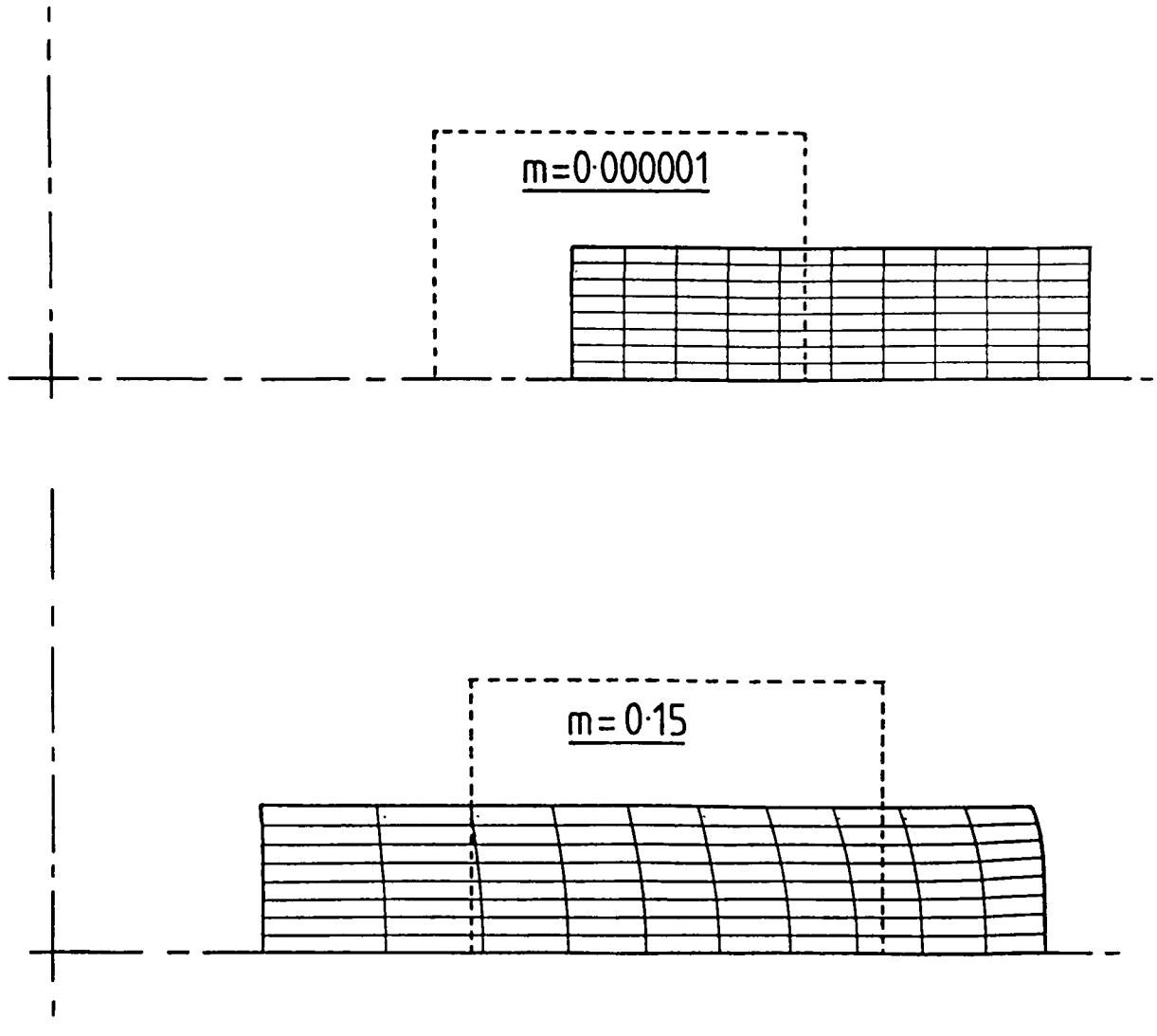

FIG. 5.2

RING TEST: DEFORMED FINITE-ELEMENT MESHES AT ABOUT 45% REDUCTION IN HEIGHT FOR DIFFERENT VALUES OF FRICTION FACTOR m

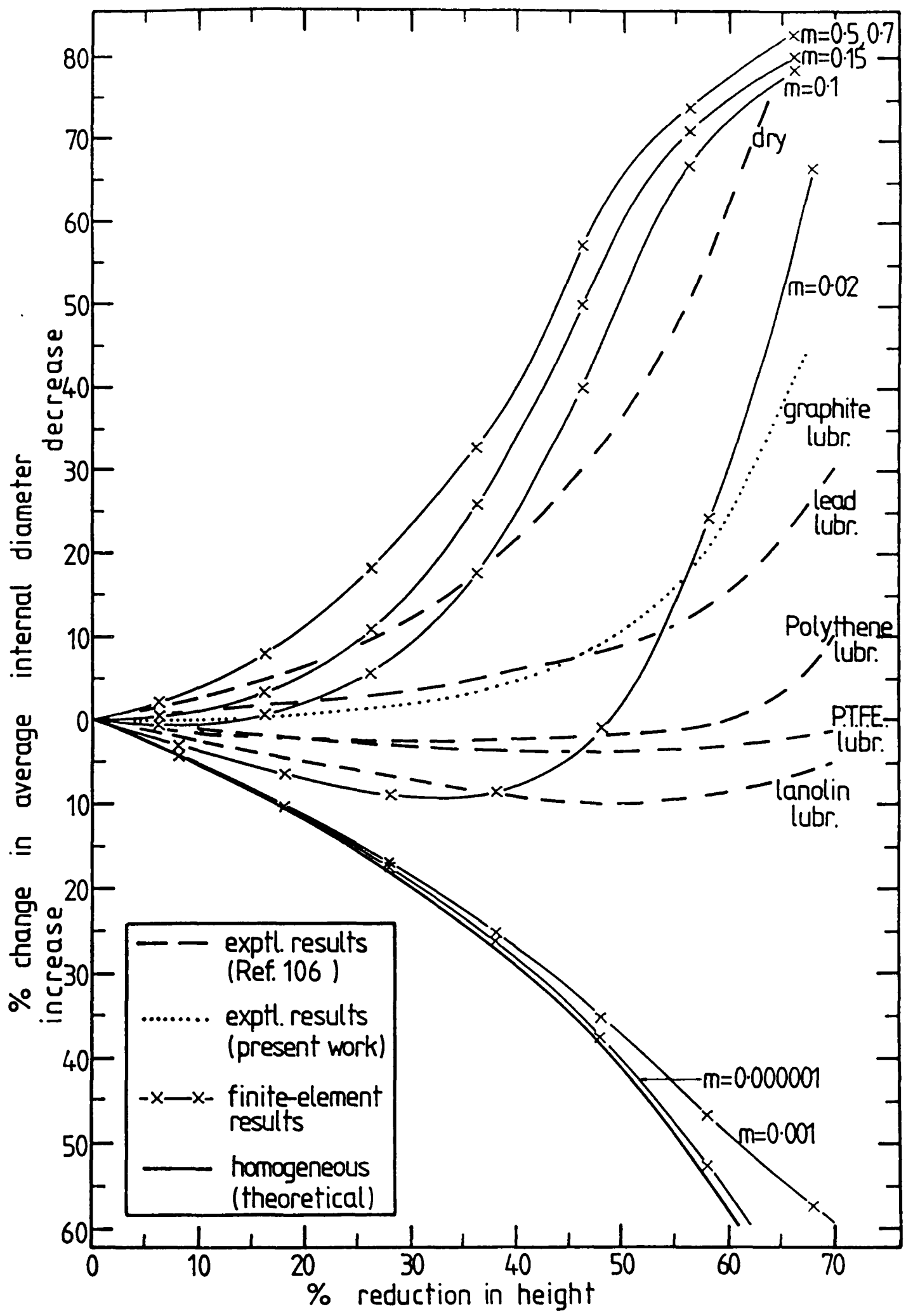

FIG. 5.3

RING-TEST CALIBRATION CURVES: VARIATION IN DIAMETER OF HOLE WITH EXTENT OF DEFORMATION. FINITE-ELEMENT AND EXPERIMENTAL RESULTS

5.1.4 Discussion of Ring-Test Results

It can be seen from fig. 5.3 that, using the modified friction technique, the finite-element program can model, in the ring test, the full range of frictional conditions which would be met in forming operations - at least when the deformation is not large. (The cross-over in the experimental curves for graphite and lead lubrication is probably due to the fact that the former lubricant was only applied at the start of the deformation whereas the lead foil was replaced at intervals in the work carried out for reference 106.)

Thus, the finite-element analysis with m equal to 0.02 gave broadly similar results to those observed experimentally when using lanolin as a lubricant, up to about 30% deformation; a value of m between 0.1 and 0.15 leads to a similar surface restraint to that provided by lead foil, but this time only up to a deformation of about 15%.

However, if the deformation is to proceed to a higher value, it is not possible to choose a suitable value of m to simulate an intermediate frictional condition. It would appear that the restraint imposed by the friction layer becomes progressively too large as the deformation continues. For instance, when a value m equal to 0.02 is used in the finite-element analysis of the ring test, the results agree initially with those obtained using lanolin lubrication, but when the deformation has reached about 60 or 70% reduction in height, the results are closer to those from the experimental test which used no lubricant.

As mentioned in the introduction to this chapter, many variations on the basic friction technique were tried, but none produced any better correlation between the finite-element and the experimental ring-test calibration curves than the method considered here. It is

apparent that the friction-layer technique which worked well in two-dimensional finite-element treatments is not so successful in a three-dimensional formulation at higher deformations and can only correctly model the required frictional restraint if the deformation is below 20 or 30%.

The reasons for the different effects of the friction technique in the two types of formulation are not immediately clear, although this behaviour is probably a result of the differences in the kind of flow existing in the two cases. Thus, in axisymmetric and plane-strain treatments, the friction layer need only restrain the surface of the mesh from moving in a straight line; in a three-dimensional formulation, the layer is influencing movement of the surface nodes within a plane. Certainly work is needed to examine this problem and to develop the technique in order to produce satisfactory results at higher deformations.

Providing the deformation is of a moderate size though, the ring-test results show that a range of frictional conditions can be modelled in the finite-element analysis, at least when considering axisymmetric material flow. It is necessary to show that a range of frictional conditions can also be applied in analyses of fully three-dimensional operations. This will be considered next.

5.2 DEMONSTRATION OF MODIFIED FRICTION TECHNIQUE - II. THREE-DIMENSIONAL FRICTION TEST

5.2.1 Choice of Configuration

In order to show that the friction technique is applicable to processes where flow is occurring in three dimensions, it is necessary to devise a three-dimensional friction test for which finite-element and experimental results may be compared.

The axisymmetric ring test has the advantage of being both a sensitive indicator of frictional conditions and relatively easy to perform, since the billet geometry and the deforming process are both quite simple. Since these characteristics would also be desirable in any three-dimensional friction test, it was natural to consider a strictly three-dimensional analogue of the simple upsetting of circular rings.

The proposed test involves the compression, between parallel platens, of a rectangular block containing a circular hole. The external dimensions of the block are 40x25x12.5mm, and the hole, which is 12.5mm in diameter, lies in the centres of the two 40x25mm faces. These faces are in contact with the platens during the upsetting. (fig. 5.4).

These billets can easily be machined to an acceptable tolerance, so the proposed test is readily reproducible, and preliminary compression tests showed that the size and shape of the hole in the deformed billet were sensitive to the conditions of interfacial friction.

Since the deformed hole generally assumes an oval shape, there are several parameters of the hole which could be measured. Changes in the lengths of the major and minor axes and the projected area of the

hole were examined. The variation in the length of the major axis was chosen as the ordinate of the calibration curves since this measurement displayed the greatest distinction between the experimental conditions of high and low friction.

5.2.2 Experimental Procedure

Blocks of commercially-pure aluminium were machined from round bar to the dimensions stated in the previous section. The central holes were then drilled and the blocks annealed at 410° C for an hour before being allowed to cool in the air. The faces of the blocks were then polished using 1200 grit paper, and the specimens thoroughly degreased with acetone.

The compression tests were carried out using the die-set described in section 4.1.2.2 (illustrated in fig. 4.1), and a 600kN Avery-Denison hydraulic press.

Two frictional conditions were used in the experimental tests, one produced by placing lead foil between the blocks and the platens of the die-set, and the other resulting from dry contact of these surfaces. The platens of the die-set were cleaned with acetone between each upsetting test; when the specimens were lubricated by lead, the foil was replaced at intervals during the deformation to prevent the extrusion of the lubricant.

The blocks were compressed to various reductions in height up to a maximum of 50%. After upsetting, the blocks were examined using a Zeiss MP320 projection microscope, operating in shadow mode. The longer dimensions of the holes were measured in the horizontal planes of symmetry of the blocks.

5.2.3 Finite-Element Analyses

The finite-element mesh contained 360 elements, and modelled one eighth of the proposed friction-test block as shown in fig. 5.4. The analyses used the material properties of commercially-pure aluminium as described in section 4.2.3 (fig. 4.4). A frictional-boundary plane was defined to be in contact with top surface of the mesh; additional friction elements were included on this surface (these elements are not shown in fig. 5.4). The nodes representing points on the two vertical planes of symmetry of the work-piece were constrained to remain in those planes throughout the deformation; the bottom layer of nodes was moved upwards towards the top surface, giving an initial reduction in height of 2% per increment.

The analyses were performed with a secant-modulus solution, using the Jaumann correction, constant dilatation and LCR strain. The volume of the plastic region was constrained to be approximately constant by specifying the value of Poisson's ratio used in the evaluation of displacements in yielded elements to be 0.4999.

Two levels of friction were modelled. The previous axisymmetric work (106) indicated that the conditions of unlubricated and lead-lubricated interfaces could be modelled with the friction-layer technique by using values of m equal to 0.7 and 0.1 respectively. Since there is some theoretical justification for these values, they are the ones used in the present finite-element analyses of the three-dimensional friction tests.

FIG. 5.4

THREE-DIMENSIONAL FRICTION TEST: GEOMETRY OF EXPERIMENTAL SPECIMENS AND FINITE-ELEMENT IDEALISATION

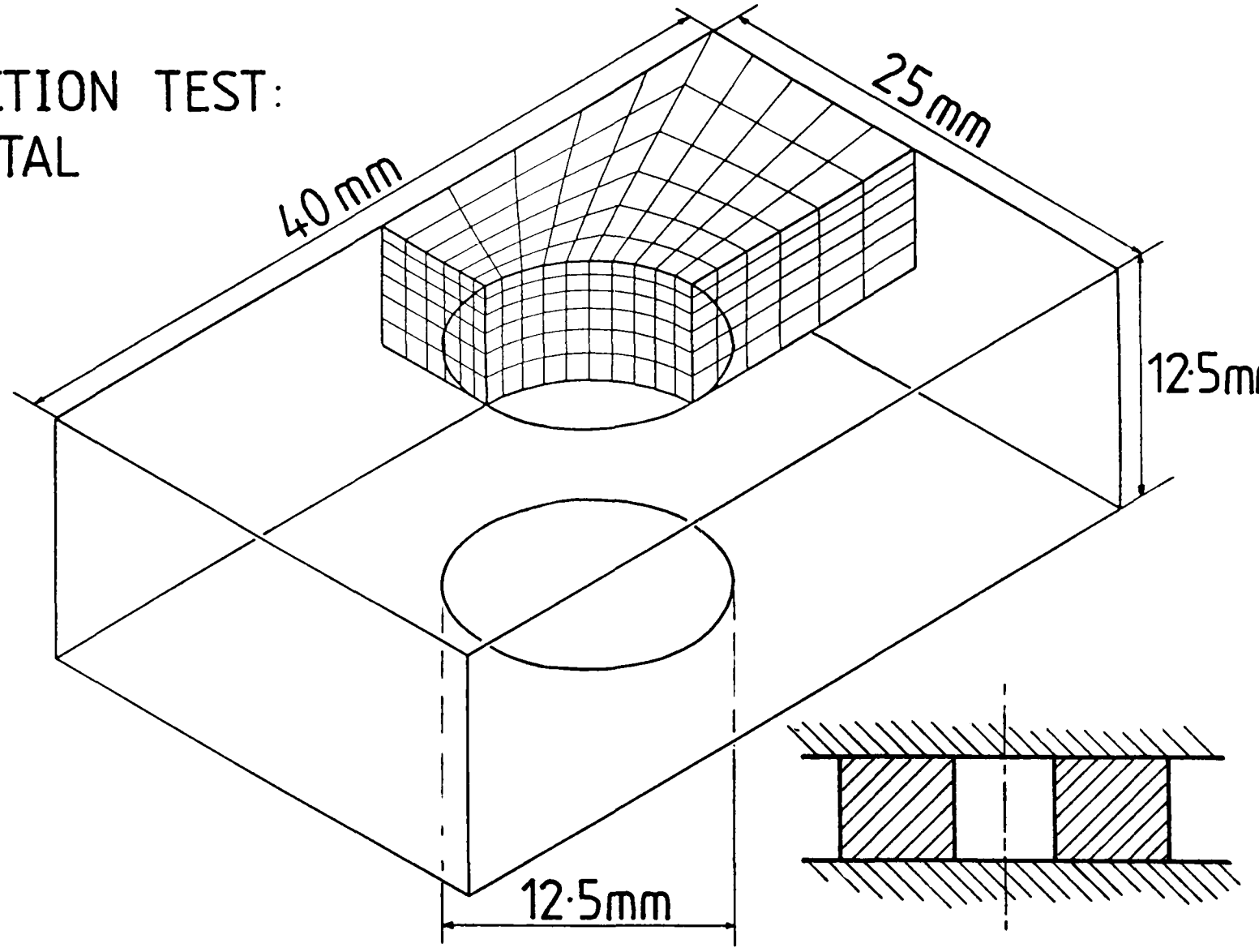

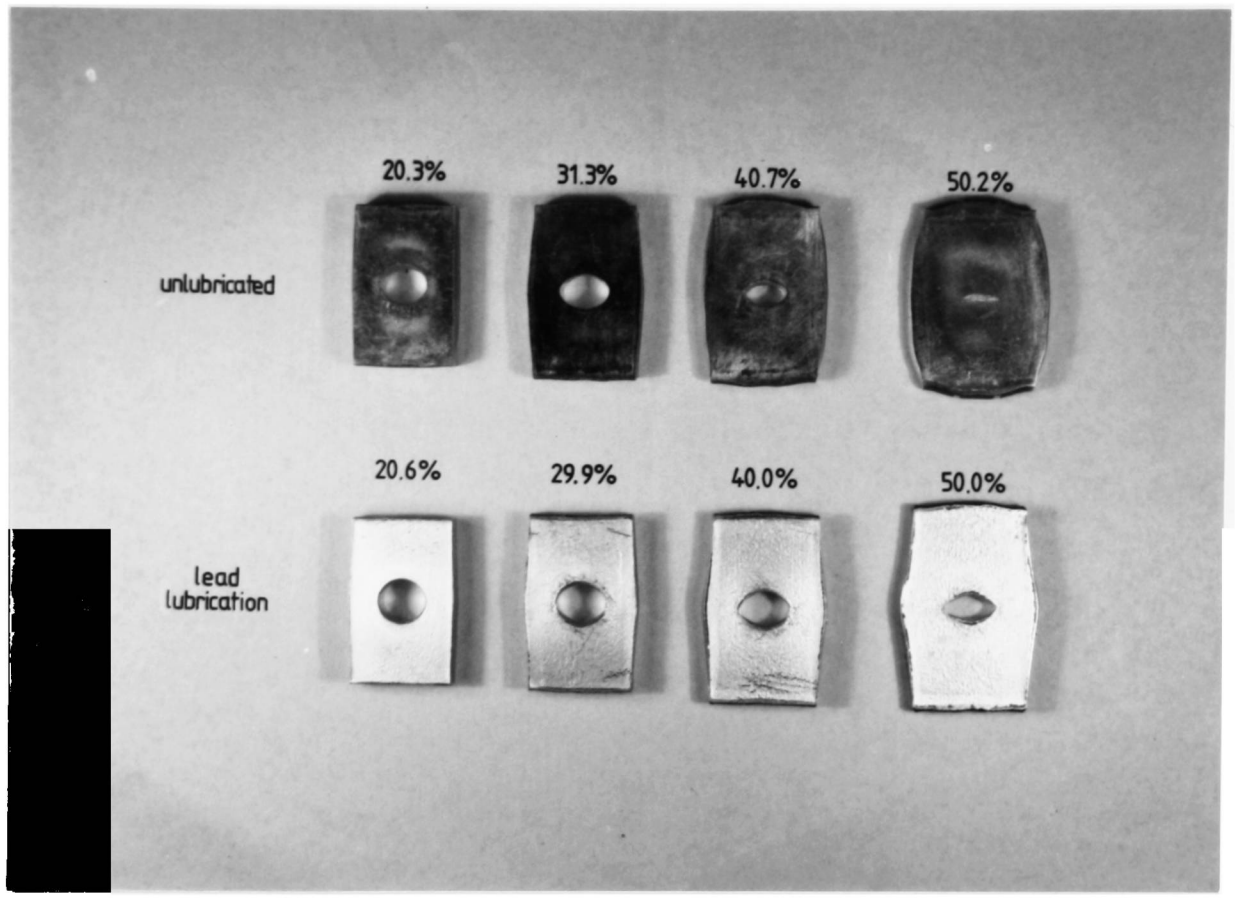

FIG. 5.5

COMMERCIALLY-PURE ALUMINIUM BLOCKS (INITIAL DIMENSIONS 40x25x12.5mm WITH CENTRAL HOLE 12.5mm DIAMETER) UPSET WITHOUT LUBRICATION AND WITH LEAD-FOIL LUBRICANT

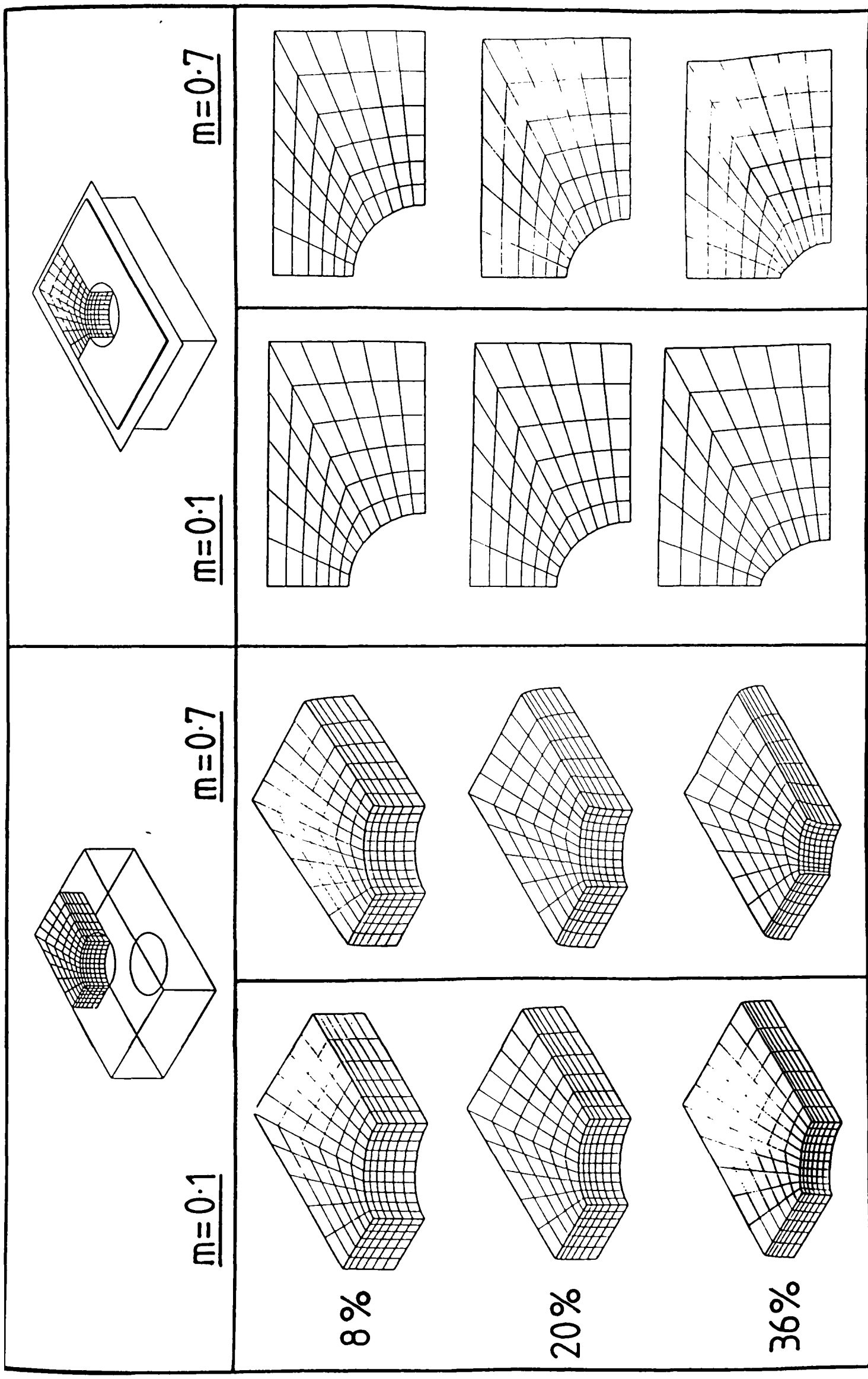

FIG. 5.6

THREE-DIMENSIONAL FRICTION TEST: DEFORMED FINITE-ELEMENT MESHES AT VARIOUS REDUCTIONS IN HEIGHT FOR TWO VALUES OF FRICTION FACTOR

5.2.4 Results

A photograph of the experimental specimens, upset by various amounts under the two conditions of friction, is shown in fig. 5.5

As a comparison, fig. 5.6 shows the finite-element meshes and horizontal sections through the top layer of elements, at stages throughout the deformation, for the two values of friction factor used in the analyses. Due to a computer-system fault, the sequences of jobs performing the analyses were halted after completing about 40% reduction in height and could not be re-started. There was no time to begin the whole analyses again, and fortunately the finite-element results obtained before the system failure are sufficient for the purposes of this chapter.

The changes in the lengths of the major axes of the holes in the experimental blocks and the finite-element meshes (measured in the horizontal plane of symmetry) are plotted in fig. 5.7 as functions of reduction in height of the specimens.

The variations, throughout the deformation, of the deforming load predicted by the two finite-element analyses (calculated by summation of the vertical forces acting on the top faces of the mesh, according to section 3.2.6.2) are compared with the loads measured experimentally in fig. 5.8.

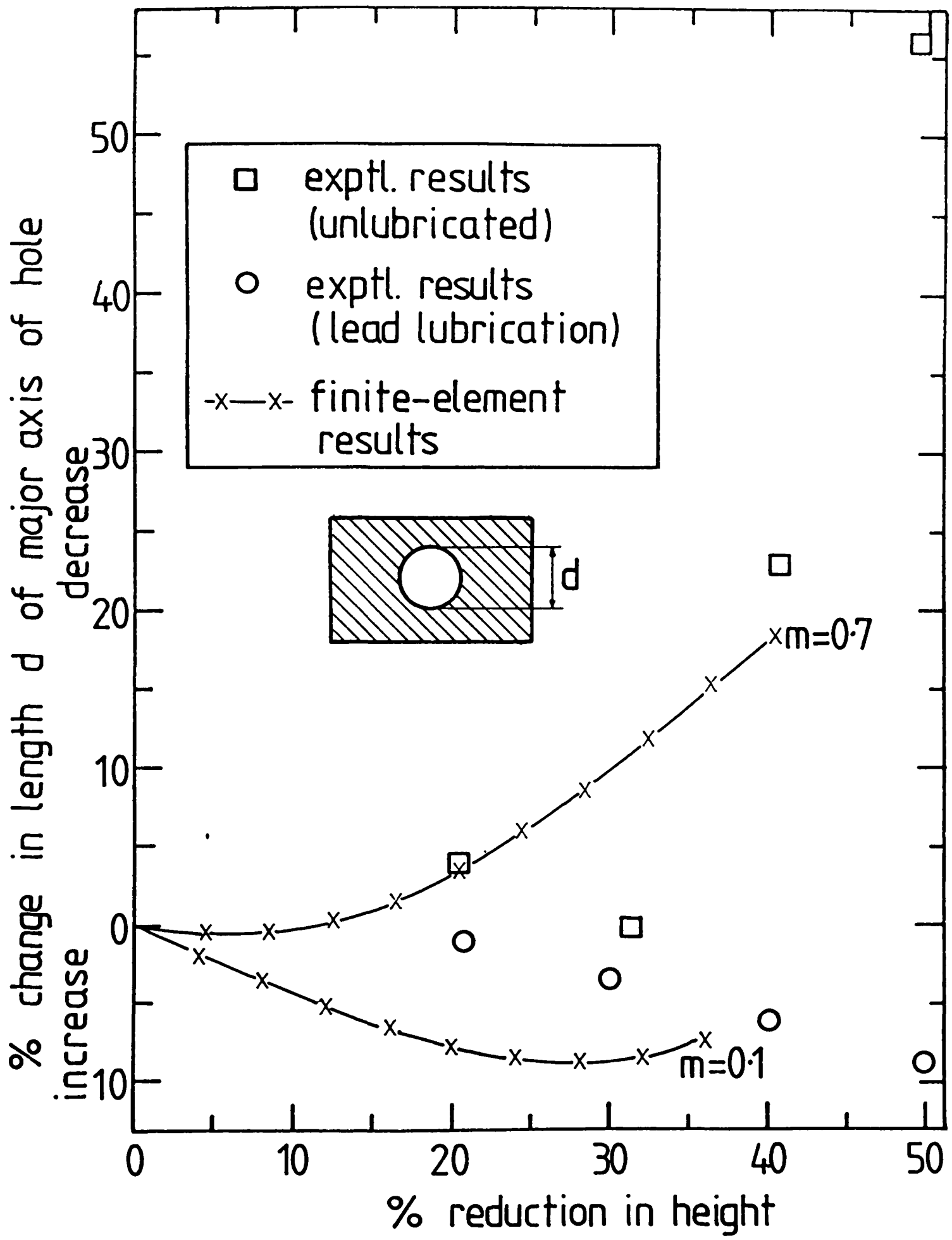

FIG. 5.7

CALIBRATION CURVES FOR THREE-DIMENSIONAL FRICTION TEST: VARIATION IN LENGTH OF MAJOR AXIS OF HOLE (MEASURED AT MID-HEIGHT OF BILLET) WITH EXTENT OF DEFORMATION. F.E. & EXPERIMENTAL RESULTS

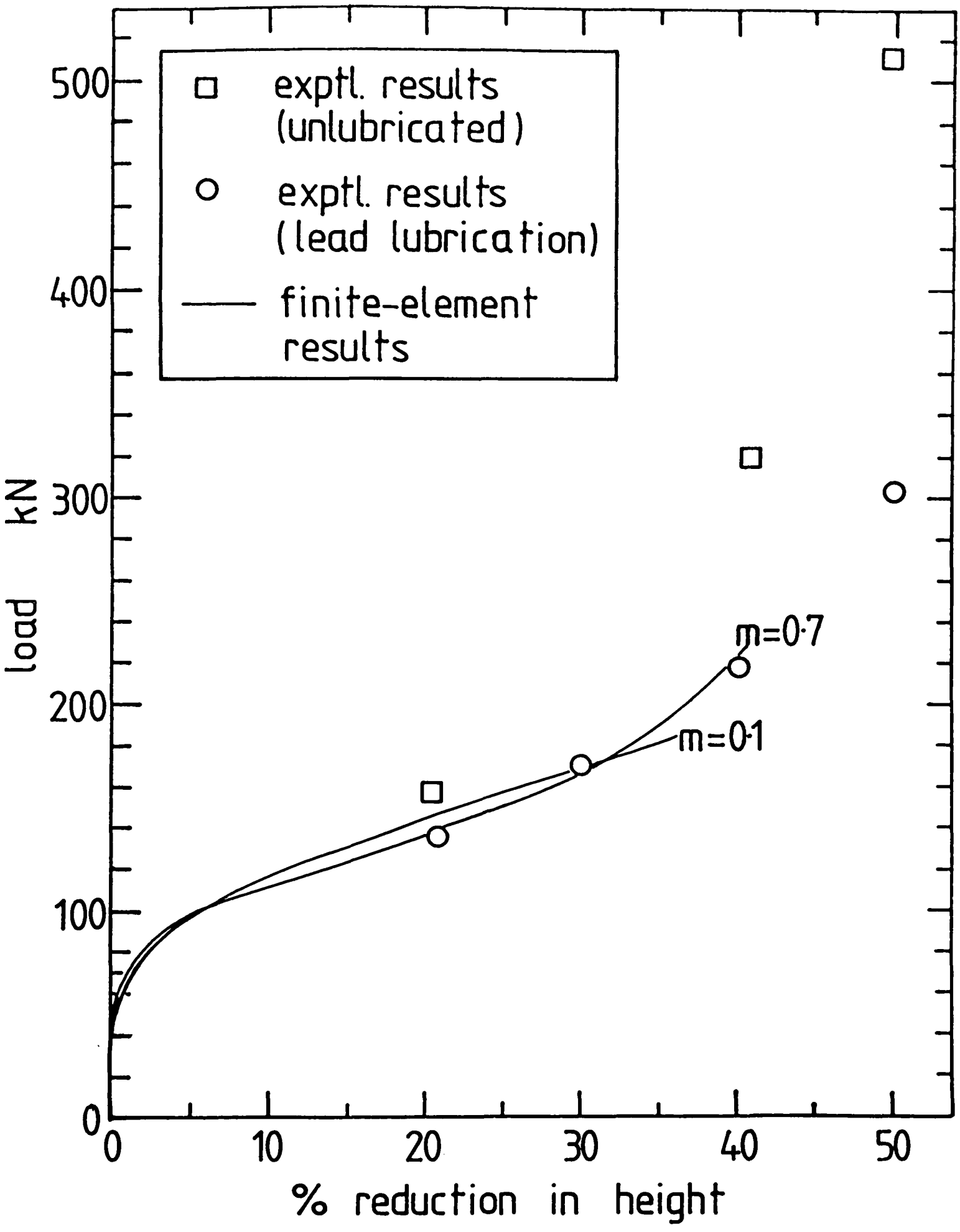

FIG. 5.8

VARIATION OF APPLIED LOAD WITH EXTENT OF DEFORMATION DURING THREE-DIMENSIONAL FRICTION TESTS: FINITE-ELEMENT PREDICTIONS AND EXPERIMENTAL MEASUREMENTS

5.1.5 Discussion of Three-Dimensional Friction-Test Results

It can be seen from fig. 5.5 that the modes of deformation of the experimental billets upset without lubrication are quite different to those of the billets for which lead was used as lubricant. For example, although the hole deforms into an oval shape under both frictional conditions (the longer axis of the the deformed hole lying at right angles to the longer axis of the whole billet), the size of the hole, for a given reduction in height, is not the same in the two cases. Thus the hole in the unlubricated billet has completely closed by 50% reduction in height whereas the hole in the specimen lubricated with the lead foil is still open at this stage. Also, there is a more pronounced bulge in the longer faces of the billets in the latter instance than in the former.

Thus the proposed three-dimensional friction test does distinguish satisfactorily between these two levels of friction. This distinction is quantified in fig. 5.7. It can be seen from this graph that the length of the major axis of the hole in an unlubricated billet decreases throughout the deformation, while the corresponding length in a lead-lubricated specimen increases. (The experimental result for the unlubricated specimen at around 30% deformation clearly does not agree with the other results for this condition of friction. This is most probably due to insufficient degreasing of the surfaces of the specimen or the platens, a supposition which is made more likely by the fact that this compression test was carried out some time after the others, when the experimental procedure may not have been as thorough. Although normally it would be inadvisable to ignore an experimental observation when the total number made is so small, in this instance other considerations suggest that the experimental result for the unlubricated specimen at 30% deformation may be

neglected as part of the present comparison.)

The finite-element results plotted in fig. 5.7 indicate that, by the use of suitable values of the friction factor, the friction technique can model high and low levels of friction, even when the material is flowing in a strictly three-dimensional way, at least for deformations up to about 20 or 30%. The finite-element analysis using m equal to 0.7 correctly predicts the variation in the length of the major axis of the hole in the unlubricated billets up to this stage. After this point, the finite-element treatment underestimates the rate of closure of the hole, but this may be a result of the coarseness of the discretisation and the inability of the mesh to assume the very complicated geometry of the central portion of the billet as the hole begins to close up.

Similarly, using a value of friction factor equal to 0.1 in the finite-element analysis results in a deformed mesh in which the major axis of the hole increases, once again up to around 30%. However, it can be seen that this represents a somewhat lower level of friction than that produced by lead lubrication.

Fig. 5.8 shows that the two finite-element analyses correctly predicted the deforming load in this process, once again up to around 30% deformation, to within the accuracy of the experimental results. Both the finite-element and the experimental results show that there is very little difference in the loads necessary to upset the specimens for quite a wide variation in the level of interfacial friction. It is only after about 30% reduction in height that the friction, in this simple forming process, becomes important in determining the required load.

This small variation of the deforming load with level of friction, for moderate deformations, is the cause of the anomaly observed in the finite-element predicted forces where, for part of the

deformation, the analysis with the higher friction factor appeared to predict a smaller load than that obtained using the lower value of m. Since the load in this instance is calculated to be in equilibrium with the stresses in the top layer of billet elements, and these stresses are dependent upon the indirectly-calculated values of hydrostatic stress, the load is very sensitive to small errors in the gradients of stress in the mesh. The apparent difference between the values of the load for the two values of m, up to 30% deformation, is well within the sort of error to be expected from this source. Notice that when the difference between the experimentally-measured loads for high and low levels of friction becomes appreciable, after 30% deformation, the finite-element analyses correctly predict higher loads when using m = 0.7 than when using m = 0.1.

5.3 CONCLUSIONS

The friction technique proposed by Hartley et al (106) used in a slightly modified form in the present finite-element treatment, is able to impose the full range of frictional conditions, from frictionless to sticking, in analyses of fully three-dimensional forming processes. Good correlation with experimentally-measured geometry and deforming load has been obtained up to deformations of about 20 or 30%. For higher deformations, the friction technique imposes too high a restraint in three-dimensional formulations; work is necessary to develop the friction technique in order to improve the finite-element predictions for higher deformations.

A three-dimensional friction test has been proposed to supplement

the observations carried out using the usual friction-ring test. The tests are easily performed and provide a sensitive indication of the level of friction in cases where the flow of the material at a die interface is in more than one direction.

CHAPTER SIX

COMPARISON OF FINITE-ELEMENT AND EXPERIMENTAL RESULTS

II. FORGING OF CONNECTING ROD

6.0 INTRODUCTION

In the previous chapters, the finite-element program which was developed as part of the present work has been used to examine various fairly simple three-dimensional forming processes and has been shown to give results which agree well with experimental observations. It is necessary, to conclude this work, to demonstrate that the program is capable of analysing more complicated and realistic three-dimensional deformations.

The forming process to be considered in this chapter is the forging of a stylised version of a connecting rod from an internal-combustion engine; the finite-element predictions for this process will be compared with the results of experiment. As far as the author is aware, no finite-element analyses of three-dimensional plastic deformations of comparable complexity have been attempted before.

Typically, con rods are forged, in pairs, in several stages. One such sequence of forgings, for an automobile con rod, is shown, from left to right, in fig. 6.1. The initial stock is square steel bar, and the first three stages convert this into a preform in which most of the material is concentrated in the part of the forging which will eventually form the big end of the con rod. The fourth stage deforms this to give a billet which has the basic outline of the con rod, and this is forged into the required shape in the fifth operation. This is followed by a coining operation, during which the dimensions of the work-piece change very little. All these operations are carried out in the hot state.

FIG. 6.1

SEQUENCE OF FORGINGS OF AUTOMOBILE CONNECTING ROD
(FORGINGS COURTESY OF AUSTIN-ROVER CARS)

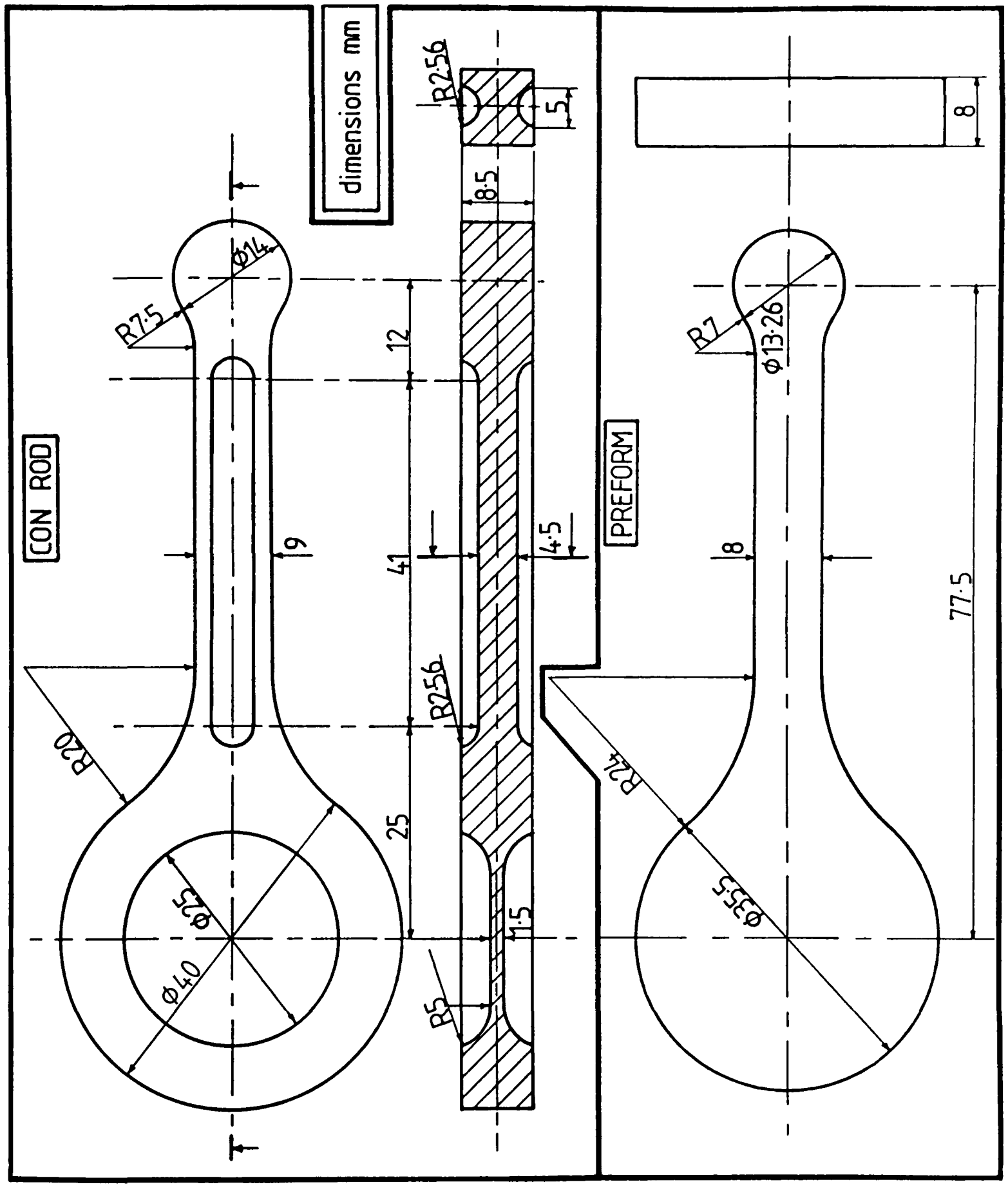

FIG. 6.2
CONNECTING-ROD
FORGING AND
CHOSEN PREFORM
GEOMETRY

For the purposes of this demonstration, it is only necessary to examine one stage of the typical forging sequence. The particular stage chosen is that between forgings four and five in the above sequence, since this step exhibits the most interesting features of the deformation.

Several simplifications were made for the comparison, which in no way invalidated the demonstration presented here. Firstly, the geometries of the connecting rod at stage five, and the preform at stage four were stylised. This was a matter of convenience only; in principle it would be possible to model the given operation exactly (to within the limits of finite-element discretisation), but at the expense of large computer-storage requirements and computer running time. Another important consideration was that the preform, which would have to be machined for the experimental tests, should not have too complicated a shape. The chosen geometries of the connecting rod and the preform are shown in fig. 6.2. It can be seen that the stylised form retains the essential features of the original such as the heavily indented big end and the cross section of the stem.

As mentioned above, the specimens in fig. 6.1 were forged from hot steel. Since it would be difficult to forge steel in the hot state under laboratory conditions, it was decided to conduct the experimental tests on commercially-pure aluminium con rods, deformed at room temperature.

Finite-element analyses of such a complicated process necessarily take a long time to complete, since the computer-installation limits mean that these analyses have to be conducted in a sequence of separate jobs, spread out over a period of weeks. As a result, the computer solutions considered in this chapter had to be started before the modifications to the friction technique described in Chapter Four could be implemented. Since, at the time, it was not possible to model

interfacial friction successfully, it was necessary to perform two analyses, one with zero-friction interfacial conditions, the other with sticking friction. Although these are obviously idealisations, it will be seen that a useful comparison can still be made between the results obtained and the experimental observations.

6.1 EXPERIMENTAL PROCEDURE

6.1.1 Manufacture of Dies and Preforms

The upper and lower dies used to forge the aluminium con-rod were made from Impax, a proprietory tool steel. Since the con rods were to be produced from relatively soft commercially-pure aluminium, it was possible to use this steel in its as-supplied state (with a Rockwell C hardness of about 30) without any subsequent hardening treatment.

The die cavities were spark eroded, the graphite electrodes being cut on a numerically-controlled milling machine from a tape prepared with the Modcon computer package developed at the University of Birmingham. The shape of the die cavities conformed to the impressions of the con-rod geometry given in fig. 6.2 except that a small draft was included on all the vertical surfaces to facilitate removal of the forgings from the dies, and the dies were designed to have a flash-gutter thickness of 1.5mm when fully closed.

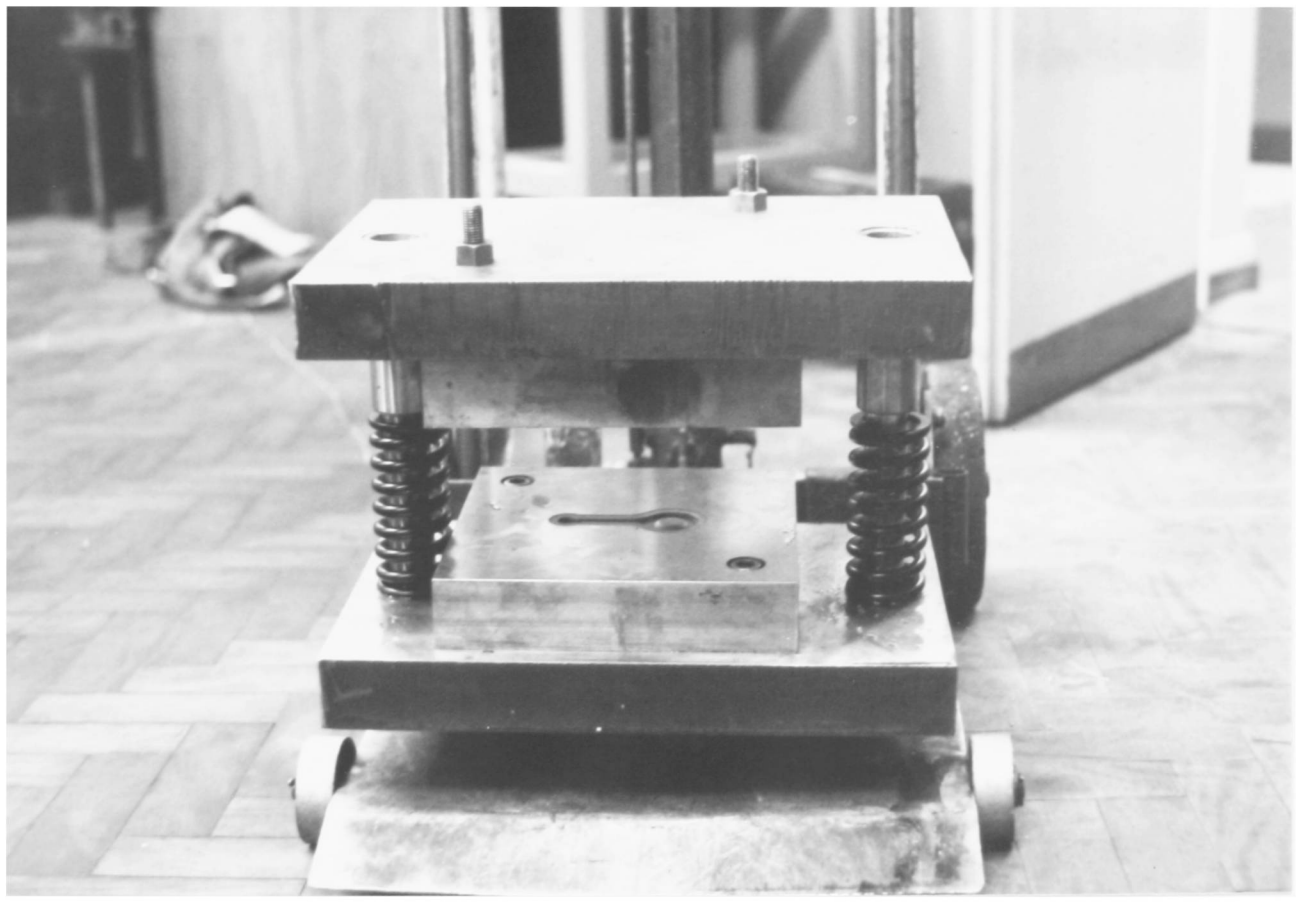

a)

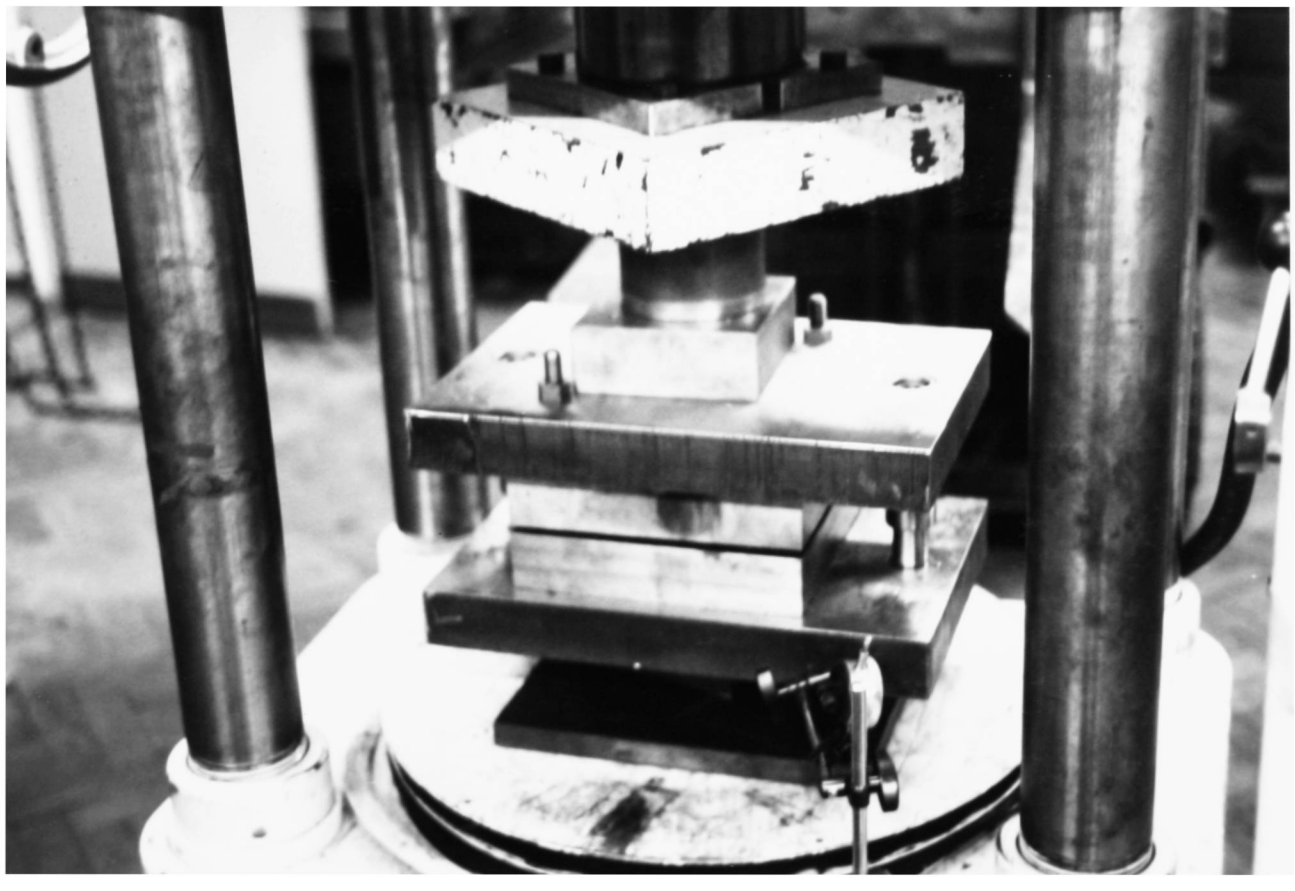

b)

FIG. 6.3

a) DIE-SET FOR FORGING OF CON ROD (THE SPRINGS WERE LATER REMOVED AND WERE NOT USED DURING THE TESTS)

b) GENERAL VIEW OF DIE-SET IN PRESS

The dies were drilled, and bolted to the inner faces of a two-pillar die-set as shown in fig. 6.3a. Care was taken to position the centres of the die cavities at the centres of the faces of the die-set to minimise the sideways thrust on the pillars during the forging stroke. The bolt holes were slightly over-size, allowing one of the dies to be moved slightly to obtain alignment with the other, prior to the final tightening of the bolts.

The preform billets were made from 32mm round commercially-pure aluminium bar. Sections of this were sawn off, and the billets dumped slightly to increase the width of the available material, before being annealed. The outline of the preform shape shown in fig. 6.2 was then cut out of each billet using the numerically-controlled miller, the control tape once again being prepared by the Modcon program. Finally, the specimens were milled to reduce their thickness to the specified value.

6.1.2 Forging of Specimens

The forging of the connecting-rod specimens was carried out using a 3000kN Denison hydraulic press. Fig. 6.3b shows the die-set in position in this press and the dial gauge which was used to measure the reduction in height of the specimens.

All the preform specimens and the die cavities were thoroughly degreased with acetone before being coated with DAG 580 graphite lubricant. This lubricant, in the form of a suspension of graphite in alcohol, was painted on with a brush and allowed to dry before the compression tests were made. After each forging operation, any bare

regions of the die cavity were re-coated with the lubricant.

The specimens were placed in turn in the lower die cavity, a small piece of Plasticine being used to retain them in the correct position, and the top of the die-set was lowered into position. The die-set was then compressed with the hydraulic ram to the required amount, as indicated by the dial gauge, the final load being recorded. In all cases, the strain rate was very low, the forging process typically taking about a minute. The specimens were deformed to various amounts up to the limit determined by die closure. After forging, the graphite remaining on the specimens was cleaned off with acetone.

6.1.3 Measurement of Deformed Specimens

The deformed con-rod specimens were sawn longtitudinally, to one side of the vertical plane of symmetry, and the larger portion machined back to the centre line. An extra specimen was obtained at 64% deformation, and this was milled to expose the horizontal plane of symmetry of the work-piece. The profile of this specimen and the profile of the longtitudinal section at the same deformation were measured using a Zeiss MP320 projection microscope operating in reflected mode. After polishing the surfaces, micro-hardness distributions were obtained using a Vickers pyramid indenter and a load of 100g.

6.2 FINITE-ELEMENT ANALYSES

The finite-element mesh used to model the preform billet contained 600 elements and represented one quarter of the con rod, as shown in fig. 6.4. The material properties of commercially-pure aluminium were used in the analyses (section 4.2.3, fig. 4.4) which was performed in steps of 0.5% reduction in height per increment.

Sixteen boundary surfaces were defined to model the shape of the experimental die cavity, and the finite-element mesh was deformed by moving the bottom layer of nodes upwards towards them. The nodes representing points on the vertical plane of symmetry of the con rod were constrained to remain within that plane. Nodes of the mesh coming into contact with any of the defined boundary surfaces were either fixed in position for the rest of the deformation (sticking-friction condition) or constrained to move tangentially to the contacted surface (zero-friction condition).

The analyses were performed using a secant-modulus technique, with Jaumann correction, constant dilatation, and LCR strain, and the hydrostatic stress was calculated indirectly. The volume of the plastic region was forced to be approximately constant by using a value of Poisson's ratio equal to 0.4999 for the evaluation of the stiffness matrices of yielded elements.

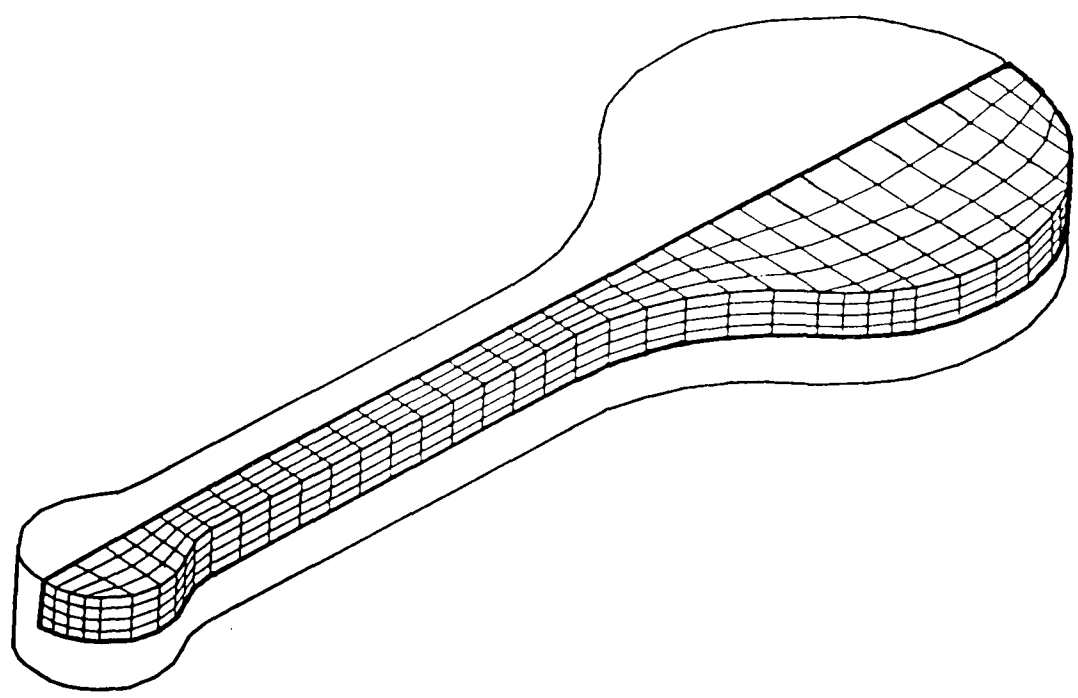

FIG. 6.4

FORGING OF CON ROD: FINITE-ELEMENT IDEALISATION OF PREFORM

6.3 RESULTS

The experimental specimens were forged to various extents up to a deformation of about 73% (for the rest of this chapter, any reference to percentage deformation means the percentage change in the thickness of the central portion of the big end). By this stage, the dies had almost closed and the flow was confined to the formation of the flash. The deformed aluminium con rods are shown in fig. 6.5, and the longtitudinal sections in fig. 6.6.

The two finite-element analyses were performed up to a deformation of about 64%. Projected views of the meshes obtained at various stages throughout the analysis, for the two boundary conditions are given in fig. 6.7. A more detailed comparison of the deformations predicted by the two finite-element analyses at about 64% deformation is presented in figs. 6.8 and 6.9, which show various sections through the deformed meshes.

The values of generalised stress at the centroids of elements lying on the vertical and horizontal planes of symmetry of the mesh were obtained and converted to Vickers pyramid hardness values according to eqn. 4.2. The distributions of hardness across the two planes of symmetry predicted by the zero- and sticking-friction finite-element analyses, at about 64% deformation, are compared with the experimentally-measured values in figs. 6.10 and 6.11. Note, a lack of experimental hardness measurements towards the small end of the longtitudinal section prevented contours being drawn in this region.

Fig. 6.12 shows values of pressure predicted by the two finite-element analyses across the portion of the die which was in contact with the meshes at 64% deformation. These pressures are taken from the values of normal vertical stress in the top layers of billet elements.

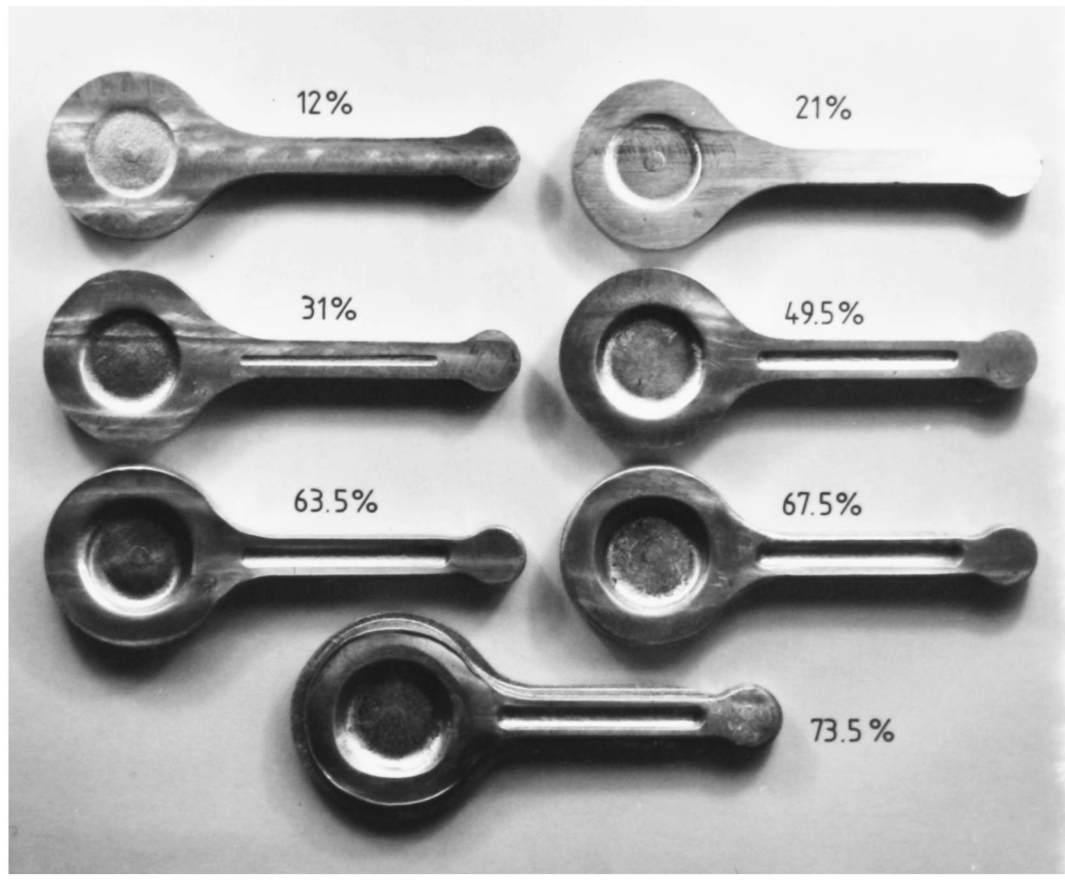

FIG. 6.5

FORGED COMMERCIALLY-PURE ALUMINIUM CONNECTING RODS AT VARIOUS DEFORMATIONS

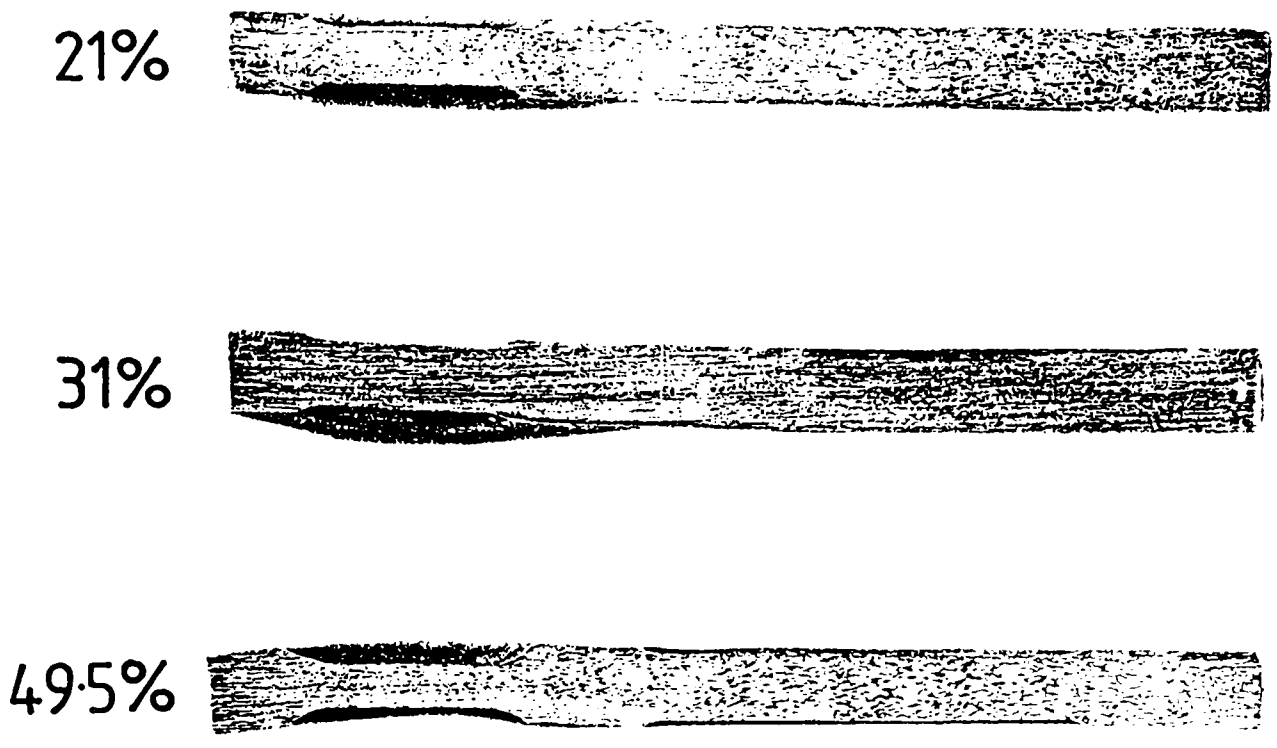

FIG. 6.6

FORGING OF CON ROD: LONGTITUDINAL SECTIONS THROUGH EXPERIMENTAL SPECIMENS AT VARIOUS DEFORMATIONS (ACTUAL SIZE)

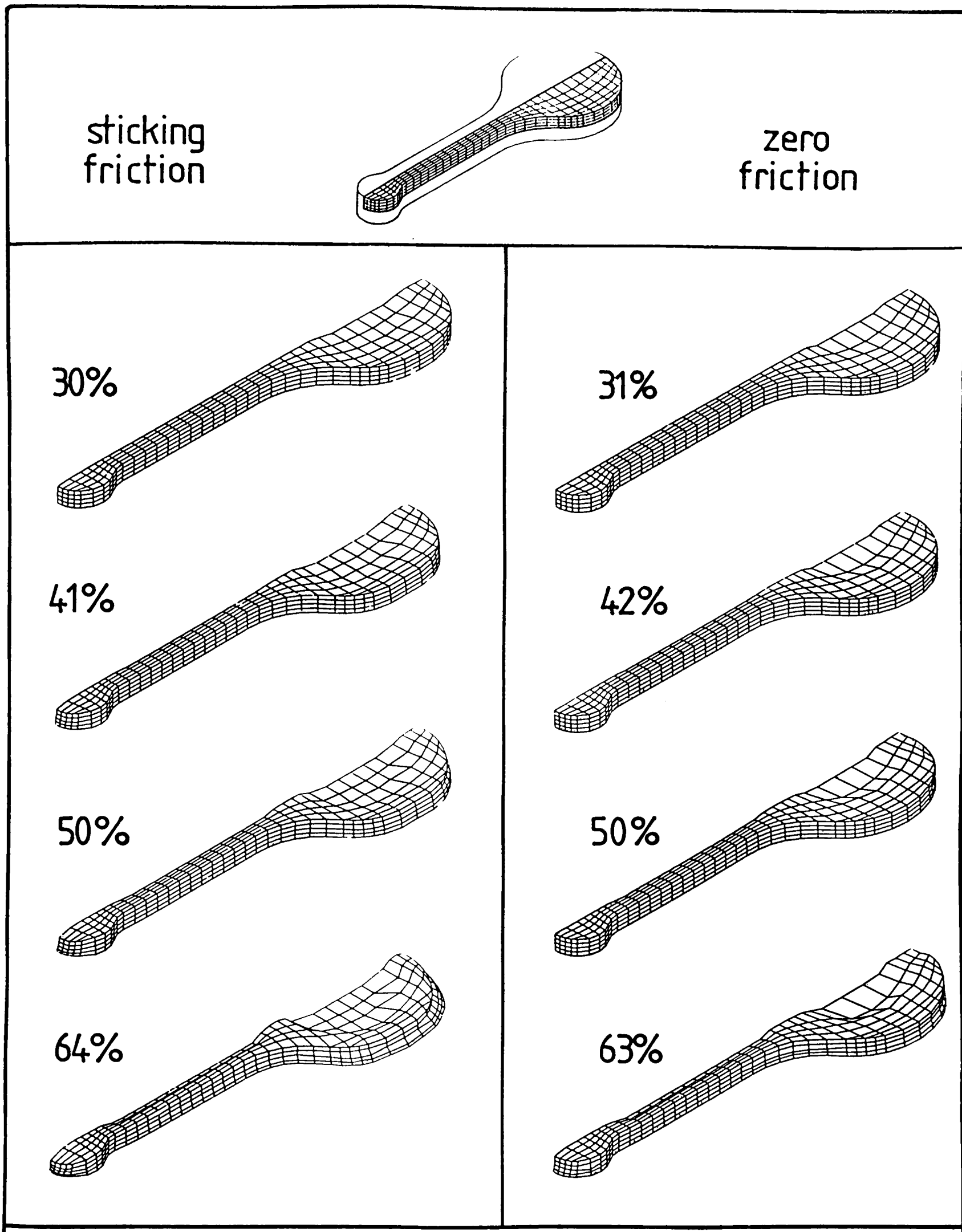

FIG. 6.7

FORGING OF CON ROD: FINITE-ELEMENT MESHES FOR TWO CONDITIONS OF FRICTION AT VARIOUS DEFORMATIONS

FIG. 6.8

SECTIONS THROUGH FINITE-ELEMENT MESHES AT ABOUT 64% DEFORMATION: COMPARISON OF TWO CONDITIONS OF FRICTION

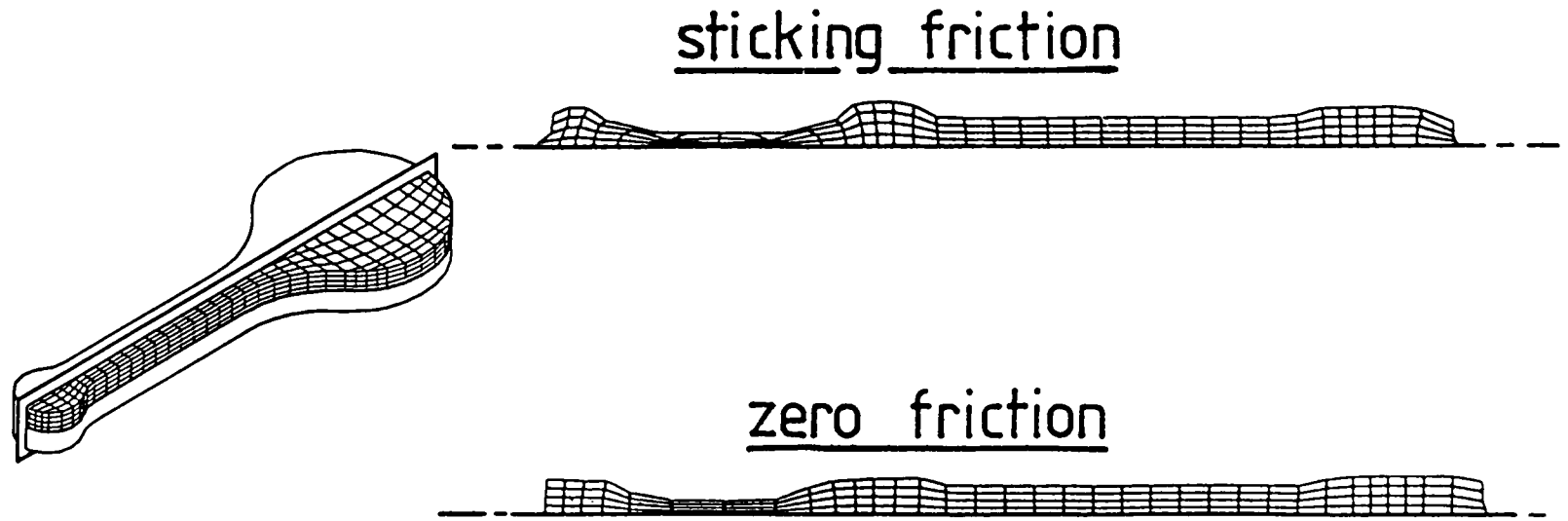

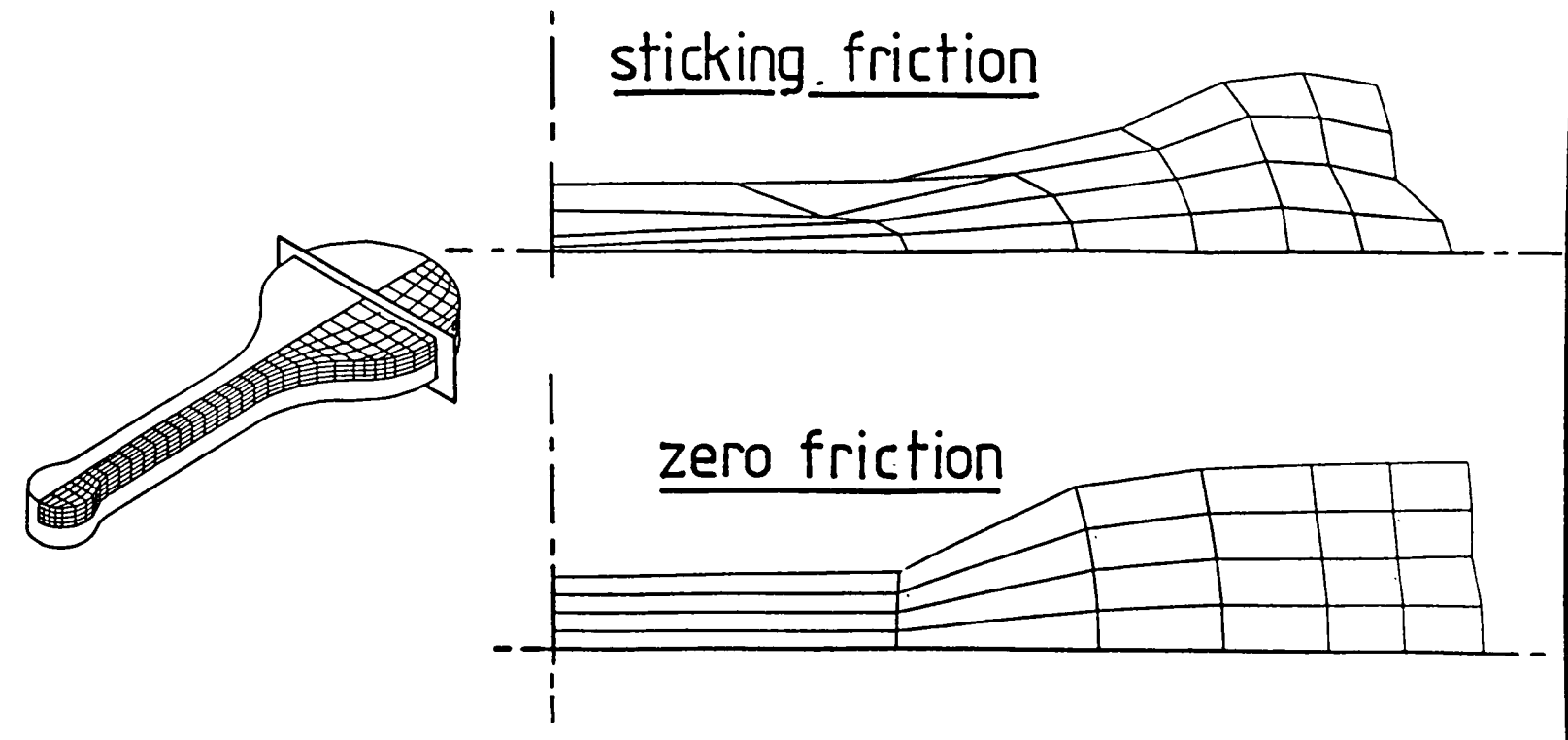

sticking friction

zero friction

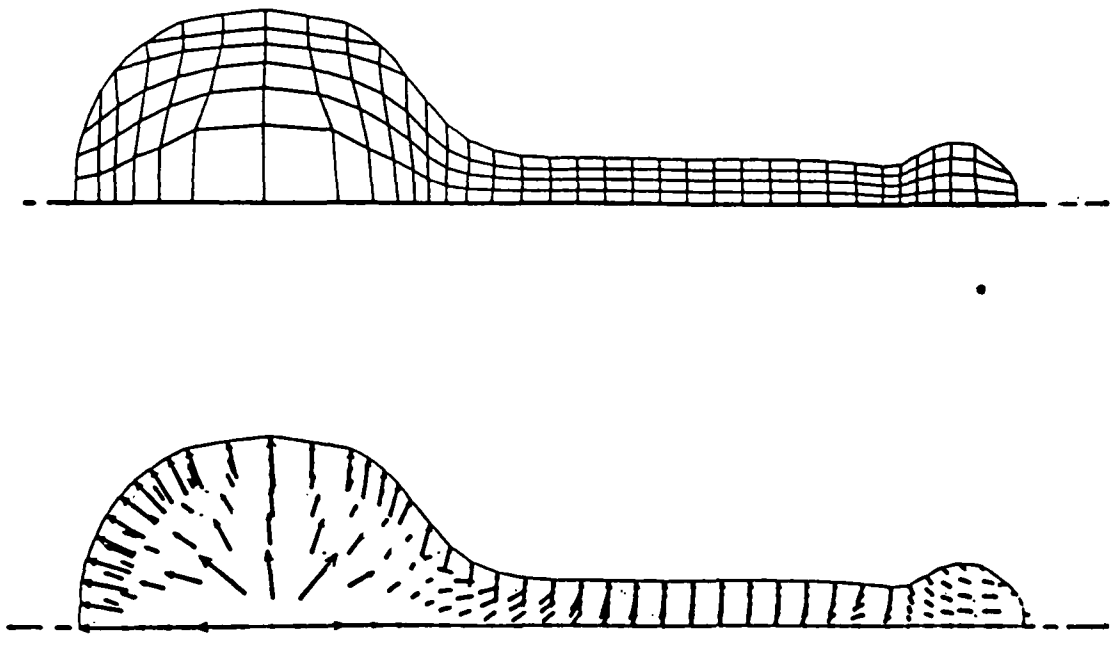

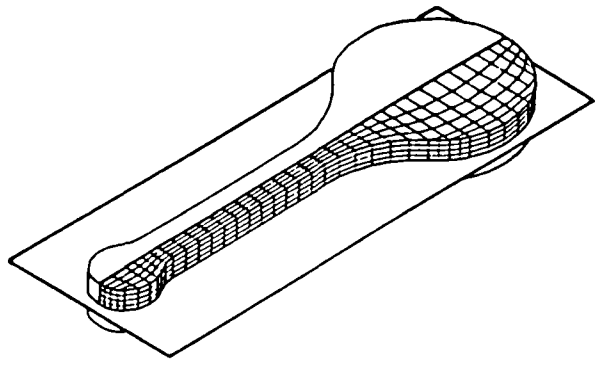

FIG. 6.9

SECTIONS THROUGH FINITE-ELEMENT MESHES AT ABOUT 64% DEFORMATION: COMPARISON OF DEFORMATION AND INCREMENTAL- DISPLACEMENT VECTORS OBTAINED ON HORIZONTAL PLANE OF SYMMETRY USING TWO CONDITIONS OF FRICTION

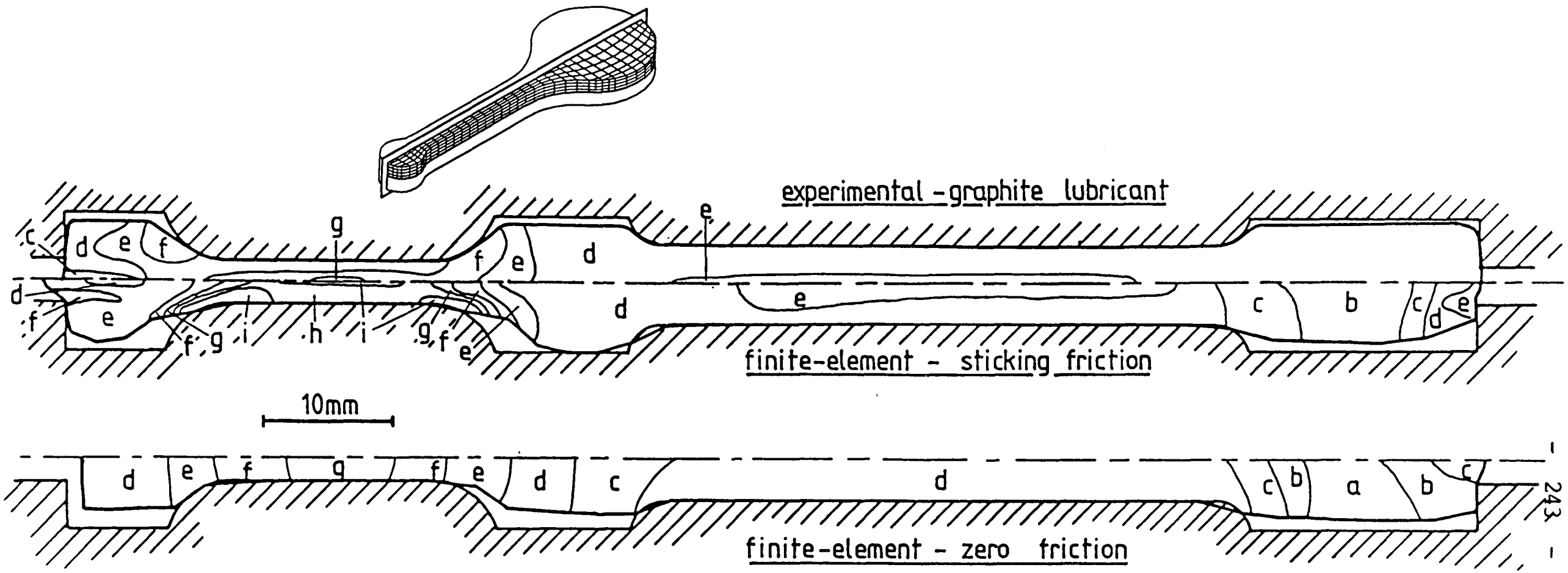

KEY: Vickers pyramid hardness numbers (kg f/m^2)		
a: 25 - 30	b: 30 - 35	c: 35 - 40
d: 40 - 45	e: 45 - 50	f: 50 - 55
g: 55 - 60	h: 60 - 65	i: > 65

FIG. 6.10

COMPARISON OF EXPERIMENTAL AND FINITE-ELEMENT HARDNESS VALUES ACROSS LONGTITUDINAL SECTION OF CON ROD AT ABOUT 64% DEFORMATION

KEY: as fig. 6.10

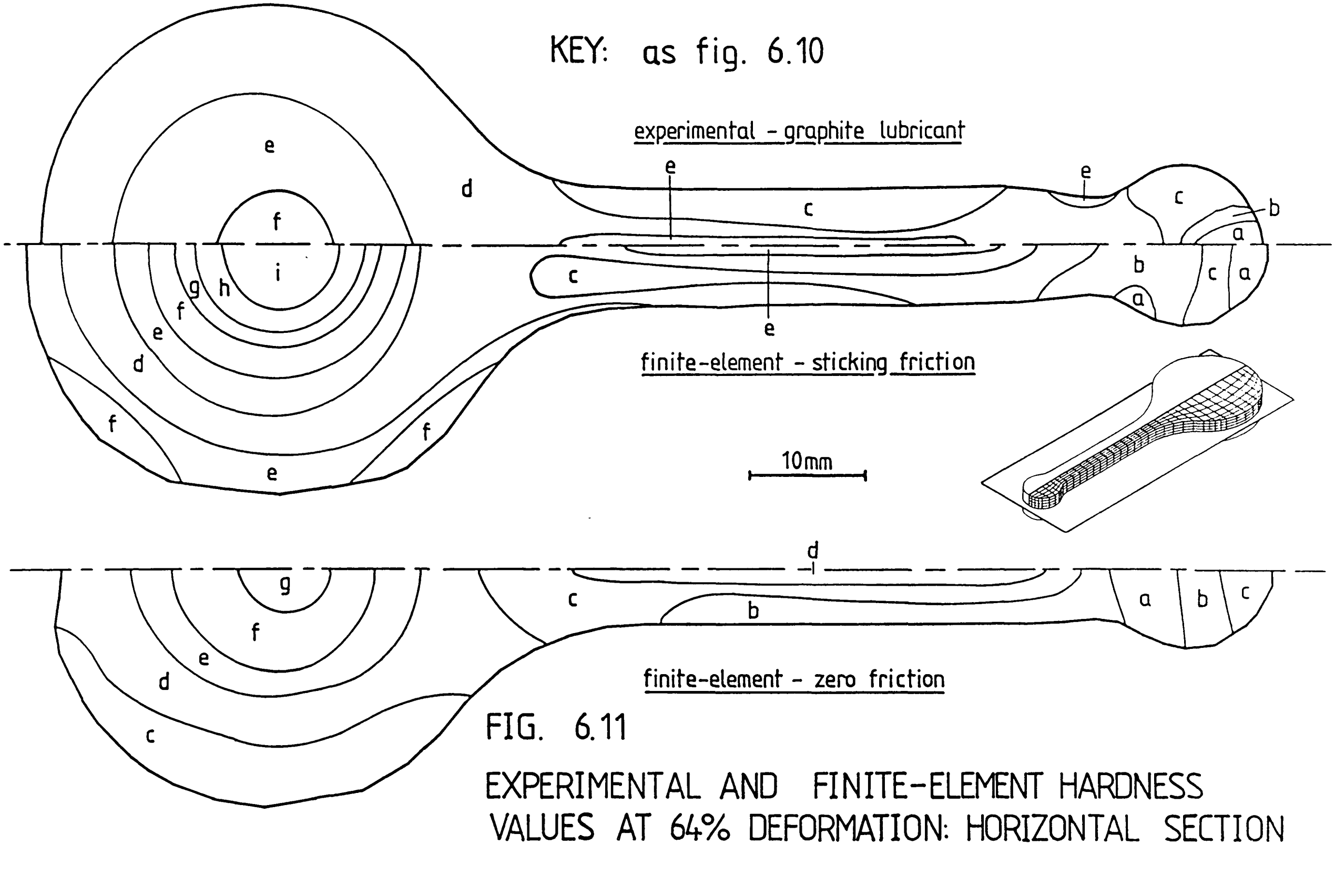

FIG. 6.11

EXPERIMENTAL AND FINITE-ELEMENT HARDNESS VALUES AT 64% DEFORMATION: HORIZONTAL SECTION

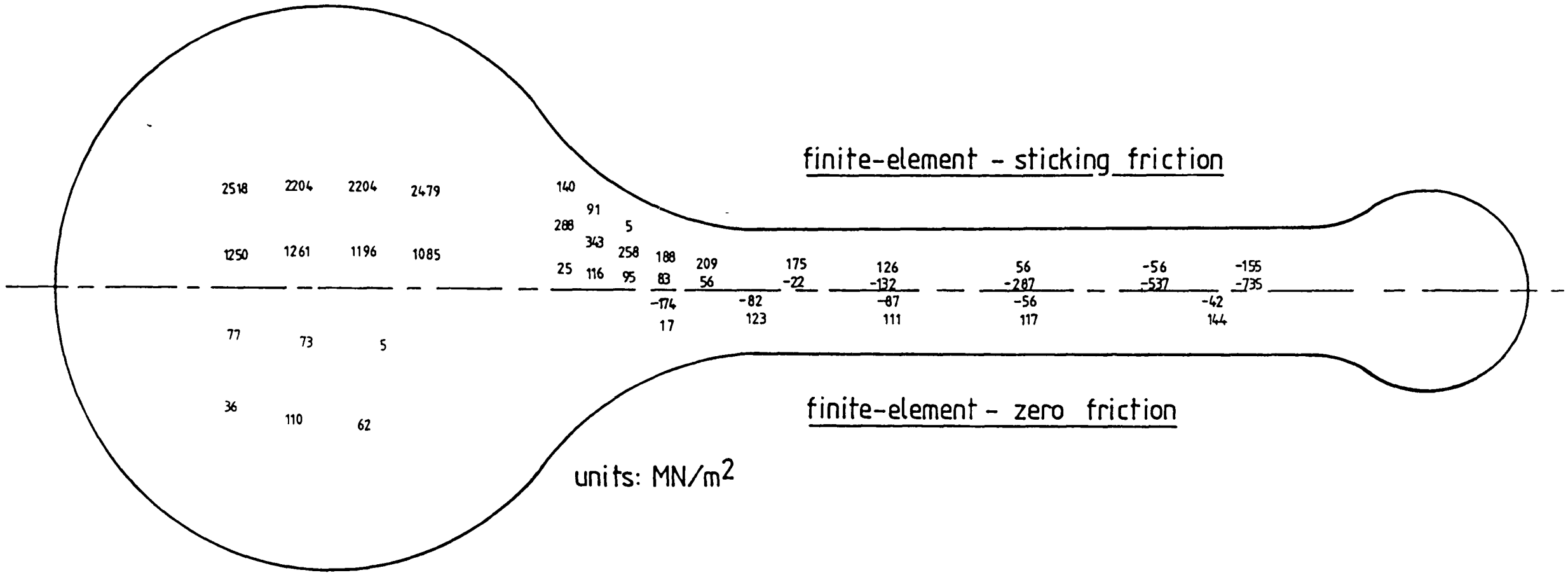

FIG. 6.12

DIE-CONTACT PRESSURE PREDICTED BY FINITE-ELEMENT ANALYSES: STICKING- AND ZERO-FRICTION CONDITIONS

For the reasons given later, reliable estimates of the total deforming load in the finite-element analyses could not be obtained from the values of force acting on the external faces of the meshes. Examination of the incremental work of deformation shows that at about 64% deformation, the finite-element program predicted a deforming load of 825kN with sticking friction and 227kN with zero friction. The load measured experimentally at this deformation was about 300kN.

6.4 DISCUSSION

6.4.1 Deformation

It can be seen from figs. 6.10 and 6.11 that the deformed profile predicted by the finite-element program at 64% for sticking-friction conditions is in quite good agreement with the experimentally-observed shape of the specimen. In particular, the sections through the horizontal plane of symmetry shown in fig. 6.11 indicate that the sticking-friction computer analysis correctly predicted a decrease in the width of the incipient flash at the neck of the small end, and the thickness of the rim of the big end predicted by this finite-element analysis is about the same as that measured experimentally (fig. 6.10). Much of the difference between the experimental and the sticking-friction finite-element profiles can be seen to be due to the coarseness of the mesh which had to be used for the computer analyses. This is apparent in the central portion of the big end in fig. 6.10, where the indented surface has tended to pull a considerable area of the surrounding mesh along with it. The relatively large size of the

elements used also explains why parts of the finite-element mesh appear to penetrate the die surfaces - in the program it is the nodes which are in contact with the surfaces, and if these are widely separated, the line joining them may appear to cross a convex surface. With a much finer mesh, the finite-element predicted profile would undoubtedly have conformed more closely to the surfaces of the die and produced better predictions of the shapes of the profiles.

At 64% deformation, the finite-element analysis with sticking friction predicted the existence of an appreciable flash round the horizontal profile. This is not evident in the aluminium specimen at this deformation, in which the flash had only just begun to form. This is almost certainly due to the differing conditions of friction in the two cases, since in a forging of this type, the extent of the flash is very sensitive to the level of friction in the die cavity and the flash gutter. In the lubricated experimental forging, flow can still take place within the die cavity at 64% deformation (i.e. before the dies are fully closed) whereas this flow is inhibited when the sticking-friction simplification is used, so that the material will tend to be extruded, to a greater extent, out of the die cavity.

Apart from this, the deformation predicted by the finite-element analysis with sticking friction agrees fairly well with that obtained experimentally using graphite lubrication. However, the finite-element deformation predicted assuming zero friction differs considerably from the experimental observations. The computer predictions for zero friction show much less flow of the material into the rim cavity of the big end, and less flow towards the die opening along the axis of the mesh. It can be seen from fig. 6.8 that the zero-friction finite-element mesh has remained remarkably homogeneous even at this advanced stage of the deformation. The different modes of flow produced by the two conditions of friction are clearly illustrated by the drawings of

the incremental-displacement vectors acting in the horizontal plane of symmetry (fig. 6.9). Whereas the material in the sticking-friction example is flowing almost radially outwards from the centre of the big end into the flash, the zero-friction flow is in a circumferential direction along much of the perimeter of the big end, and there is obviously little tendency for the flash to form.

These results indicate that although, as shown in the ring-test calibration curves in fig. 5.3, graphite is a moderately good lubricant, the deformation obtained experimentally was closer to the sticking-friction ~~ideal~~ simplification than it was to the zero-friction case. It would seem then that for most levels of friction, the pattern of deformation is broadly similar, differing only in degree with different values of friction; the pattern obtained when friction is removed altogether is totally different.

6.4.2 Hardness Values

Figs. 6.10 and 6.11 show that the distribution of hardness values predicted by the finite-element analysis with sticking friction is in general agreement with the experimentally-measured values. In particular, the finite-element program correctly predicts larger than average values of hardness under the two indentation zones (the big end and the stem) and also at the sides of the indented big-end region. Some of the detail picked out by the finite-element hardness maps (such as the two areas of increased hardness at the perimeter of the horizontal section of the big end) may be lost on the experimental sections due to an insufficient number of data points. In general, the

finite-element values are slightly too high, particularly at the centre of the big end, but this is probably a result of the more severe deformation produced with the sticking-friction condition and the coarseness of the finite-element mesh.

The hardnesses predicted by the finite-element analysis with zero friction are not in good agreement with the experimental results, indicating once again that the zero-friction idealisation is not a good approximation to actual interfacial conditions, even when the level of friction is quite low.

6.4.3 Die-Interface Pressure

The values of pressure shown in fig. 6.12 indicate the sort of information which can usefully be obtained from the finite-element analysis. Unfortunately, in this instance the values produced are of doubtful validity since some regions of the die appear to be subject to negative pressure. This is a result of the failure to calculate the hydrostatic component of stress correctly in certain parts of the finite-element mesh. In the analyses considered here, the hydrostatic stress change between adjacent elements was evaluated indirectly from the gradients of deviatoric stress, starting from the known value of hydrostatic stress at a free surface. The free surface used in these analyses was situated on the longtitudinal axis of the mesh at the left-hand end in fig. 6.12. Thus, calculating the hydrostatic stress in the region of the big end presented no problem. However, obtaining the value in elements towards the right-hand end of the mesh involved the calculation of the hydrostatic stress in the many elements lying

between the starting point and the element in question. Accumulation of error is quite likely under these circumstances, but in this particular deformation, the error was much greater because some of the intervening elements lay in regions of severe deformation (for example, at the centre of the big end) where the elements were grossly distorted. The effect of the accumulation of error is shown in the sticking-friction part of fig. 6.12 where the die pressure becomes progressively more negative in moving towards the small end of the mesh. (A similar trend is not shown in the zero-friction example because the deformation in the stem part of the mesh is not very severe.)

Two possible solutions to this problem present themselves. Firstly, the indirect calculation of hydrostatic stress could use more than one starting point, perhaps by evaluating the hydrostatic stress at the centroids of all elements with a free surface before the rest of the calculation is performed. This would generally avoid having the value of hydrostatic stress in any given element dependent upon the values in more than a few other elements, but would not solve the problems associated with the severe deformation of the mesh. A remedy for this would be to re-mesh the work-piece at intervals throughout the deformation, so that severely distorted elements are never formed. Such a re-meshing would not be easy to perform, automatically, in the three-dimensional processes examined by this program, but would, if accomplished, be generally beneficial. For instance, the ability of the mesh to flow round the corners of a die would be improved. A general re-meshing scheme should certainly be considered for the program in the long term. Once the problem with the calculation of hydrostatic stress is overcome, there should be no problem predicting the correct distribution of pressure across the die surface during the forging operation.

Because of the unreliability of the values of the total components of stress in this instance, it was not possible to calculate the deforming load in these finite-element analyses from the predicted values of force acting on the external faces of the mesh. However, the estimates of the load obtained from the incremental work of deformation appear to be of the right order, the value calculated for sticking friction being much larger than the value measured experimentally for the graphite lubricant, while the zero-friction prediction was slightly smaller.

6.5 CONCLUSIONS

The finite-element program developed here has been shown to be capable of examining an example of a complicated three-dimensional forging. The solution obtained assuming sticking-friction between the dies and the work-piece was in good agreement with the results of an experimental investigation in which graphite was used as a lubricant, the finite-element program predicting essentially the correct deformation pattern and distribution of hardness values. The finite-element analysis performed assuming zero-friction conditions was not in very good agreement with the experimental findings even though the level of friction produced by the graphite lubricant was quite small. It would seem, in general, that the deformation obtained by assuming precisely zero interfacial friction is quite different to that obtained when friction is present, whatever this friction might be.

Because of the severe deformation occurring in parts of the finite-element mesh in the process considered here, the method of

calculating hydrostatic stress indirectly from the equilibrium distributions of deviatoric-stress gradient appeared to produce incorrect values. This situation could be improved by increasing the number of points on the free surfaces from which the calculation is started and by re-forming the finite-element mesh at intervals during the deformation.

SUMMARY

A three-dimensional elastic-plastic finite-element program has been developed which incorporates a new measure of strain for deformations involving large rotation and a new strain-hardening improvement of the mean-normal (98) method of calculating increments of stress. This has been used to examine the unlubricated, simple upsetting of a rectangular block of commercially-pure aluminium. Good agreement was obtained between the finite-element predictions of deformation and hardness and experimental findings. The predicted shape of the distribution of pressure across the surface of the die also agreed with previous experimental results (4). However, the beta-stiffness technique (1) which was used in this analysis was found to impose too high a frictional restraint, and certain modifications had to be made.

The finite-element program with the modified friction technique was used to perform analyses of the axisymmetric friction-ring test and the results compared with experiment (106). The program was able to model the full range of interfacial conditions from zero to sticking friction, although good correlation with the experimental findings was only obtained for deformations up to about 30%.

A new friction test was proposed to demonstrate that the program could also model friction in situations where the flow is fully three-dimensional, within the above limit of deformation. This test, which consisted of the upsetting of a rectangular block containing a central, circular hole, was found to be a sensitive indicator of the level of interfacial friction. The finite-element predictions for this test, obtained using a friction factor equal to 0.7, were in good agreement with the results of the experimental tests performed without lubrication, up to about 30%, while the finite-element analysis which used a friction factor of 0.1 was found to give a somewhat smaller

frictional restraint than that obtained with lead lubrication.

Finally, finite-element analyses were obtained for the forging of aluminium con rods. In the absence, at that time, of a suitable friction technique, the finite-element analyses assumed the idealised boundary conditions of zero and sticking friction. The deformation and hardness predicted by the latter treatment agreed with the experimental observations of this complex three-dimensional forging, while it appeared that the mode of flow resulting from the zero-friction simplification differed substantially from that obtained experimentally, even though the experimental forgings were carried out using graphite lubrication.

Because of the gross distortion of the mesh in this analysis, the method of calculating hydrostatic stress, using the equilibrium distributions of deviatoric-stress gradient, produced incorrect results. Methods of overcoming this problem have been suggested.

The finite-element program developed here has been shown to be able to predict correctly the material flow and stresses in a variety of three-dimensional forgings and should prove to be a valuable analytical tool in the field of forging design.

SUGGESTIONS FOR FURTHER WORK

Several areas that require further investigation have become evident during the course of this work. Perhaps the most immediately important was mentioned in Chapter Five, namely the need to develop the existing friction technique in order to model correctly the boundary conditions in forging processes at deformations greater than 30% or so. This problem should receive urgent attention.

The failure of the present method of calculating hydrostatic stress indirectly, when gross deformation is taking place, became obvious when the program was used to examine the forging of the con rod in Chapter Six. The basic technique in this case is sound, and it should not be difficult to improve the calculation procedure to overcome this limitation.

In this context, it was suggested that a re-meshing technique would be useful, and some such modification will be necessary if the program is to be capable of modelling deformations where the geometry of the work-piece changes considerably during the process. (An example of this would be the formation of the flash in the con-rod forgings examined in Chapter Six, although in the analyses considered there, the solution was stopped before this became a problem.)

During these analyses it also became obvious that the solution would benefit from using a finer discretisation. This is largely a matter of computer-storage facilities, although increasing the number of elements also increases the the computational time, so work could usefully be devoted to improving the efficiency of the program in general, and of the matrix-solution technique in particular, perhaps with a view to using a computer with vector-processing capabilities.

Finally, little mention has been made in this work of the effects, on the flow and properties of the forging, of varying the

strain rate of the process, and the current program has no way of calculating , or allowing for, changes in temperature (spatial or temporal). In the context of this thesis, this has not been a problem since all the experimental comparisons have been carried out slowly, thus eliminating strain-rate effects and generating negligible change in the temperature. However, if the finite-element program is to be applied in general to practical forming problems, the ability to model strain-rate and temperature effects will become very important, and this should receive further consideration.

REFERENCES

(1) HARTLEY, P.
"Metal Flow and Homogeneity in Extrusion-Forging"
PhD Thesis, Birmingham (1979)

(2) NAGAMATSU, A., MUROTA, T. and JIMMA, T.
"On the Non-Uniform Deformation of Material in Axially Symmetric Compression Caused by Friction (Part 1)"
Bull. of JSME Vol. 14, No. 70, pp 331-338 (1971)

(3) NAGAMATSU, A., MUROTA, T. and JIMMA, T.
"On the Non-Uniform Deformation of Block in Plane-Strain Compression Caused by Friction (Part 2)"
Bull. of JSME Vol. 13, No. 66, pp 1396-1402 (1970)

(4) NAGAMATSU, A. and TAKUMA, M.
"Experimental Study of Pressure and Deformation of Rectangular Blocks in Compression" J. Jap. Soc. Tech. Plasticity (in Japanese), Vol. 14, No. 144, pp 49-57 (1973)

(5) DANESHI, G.H. and HAWKYARD, J.R.
"A Split-Platen Pressure Cell for the Measurement of Pressure Distribution in Upsetting Operations"
Int. J. of Mech. Sci. Vol 13, pp 355-371 (1971)

(6) BROUHA, M., de JONG, J.E. and VAN der WEIDE, K.J.A.
"Experimental Verification of Finite Element Analysis on Axisymmetric Deformation Processes" NAMRC 7

(7) ROWE, G.W.
"Principles of Industrial Metalworking Processes"
Arnold (1977)

(8) AMERICAN SOCIETY FOR METALS
"Forging Design Handbook" (1972)

(9) HARTLEY, P., STURGESS, C.E.N. and ROWE, G.W.
"Prediction of Deformation and Homogeneity in Rim-Disc Forging"
J. Mech. Working Tech. Vol. 4, pp 145-154 (1980)

(10) PEARSON, C.E. and PARKINS, R.N.
"The Extrusion of Metals" 2nd Ed.
Chapman & Hall, London (1961)

(11) GREEN, A.P.
"A Theoretical Investigation of the Compression of a Ductile Material between Smooth Flat Dies"
Phil. Mag. Vol. 42, pp 900-912 (1951)

(12) CHITHARA, N.R., JOHNSON, W. and UTTLEY, J.R.S.
"Ball Rolling: a Literature Survey and Some Experimental Results" Proc. 15th MTDR, Birmingham, pp 497-506(1974)

(13) AKU, S.Y., SLATER, R.A.C. and JOHNSON, W.
"The Use of Plasticine To Simulate the Dynamic Compression of Prismatic Blocks of Hot Metal" Int. J. of Mech. Sci. Vol. 9, pp 495-525 (1967)

(14) HARTLEY, P., STURGESS, C.E.N. and ROWE, G.W.
"Influence of Friction on the Prediction of Forces, Pressure Distributions and Properties in Upset Forging"
Int. J. of Mech. Sci. Vol. 22, pp 743-753 (1980)

(15) ANDRESEN, K.
"Threedimensional Forging of Rectangular Blocks"
Arch. Eisenhüttenwes (in German) Vol. 45, pp 297-300 (1974)

(16) KITAHARA, Y., OSAKADA, K., FUJII, S. and NARUTAKI, R.
"Analysis of Plane-Strain Metal Forming Problem with Linear Programming Method" Bull. JSME Vol. 22, No. 167, pp 763-768 (1979)

(17) OSMAN, F.H. and BRAMLEY, A.N.
"An Incremental Analytical Technique for Forging and Extrusion of Metals" in "Numerical Methods in Industrial Forming Processes" Ed. J.F.T. Pittman, R.D. Wood, J.M. Alexander and O.C. Zienkiewicz, Swansea, pp 333-342 (1982)

(18) ALTAN, T.
"Computer Simulation to Predict Load, Stress, and Metal Flow in an Axisymmetric Closed-Die Forging"
in "Metal Forming", Ed. A.L. Hoffmanner, Plenum Press, New York, pp 249-273 (1971)

(19) FINLAYSON, B.A. and SCRIVEN, L.E.
"The Method of Weighted Residuals - a Review"
App. Mech. Revs. Vol. 19, No. 9, pp 735-748 (1966)

(20) HILL, R.
"The Mathematical Theory of Plasticity"
Clarendon Press, Oxford (1950)

(21) FORD, SIR H. WITH ALEXANDER, J.M.
"Advanced Mechanics of Materials" 2nd Ed.
Ellis Horwood, Chichester (1977)

(22) KUNAR, R.R. and MINOWA, N.
"A Comparison between Finite Element and Finite Difference Formulations for Triangular and Quadrilateral Plane-Strain Elements" Int. J. Num. and Analytical Meth. in Geomechanics Vol. 5, pp 217-224 (1981)

(23) MARTI, J., KALSI, G., TRBOJEVIC, V.M. and ATTALLA, I.
"Three-Dimensional Dynamic Non-Linear Modelling of Reinforced Concrete under Impact Loads" Proc. Sym. "Concrete Structures under Impact and Impulsive Loading", W. Berlin (1982)

(24) MARTI, J., KALSI, G.S. and PRINJA, N.K.
"Three-Dimensional Non-Linear Analysis of Pipe-to-Pipe Impact" Proc. Conf. "ASCE Engineering Mechanics", Purdue University, West Lafayette, Indiana, USA (1983)

(25) MARTI, J., KALSI, G. and ATKINS, A.G.
"A Numerical and Experimental Study of Deep Elastoplastic Indentation" in "Numerical Methods in Industrial Forming Processes", Ed. J.F.T. Pittman, R.D. Wood, J.M. Alexander and O.C. Zienkiewicz, Swansea, pp 279-287 (1982)

(26) FADZIL, M., CHUAH, K.C., HARTLEY, P., STURGESS, C.E.N. and ROWE, G.W.
"Metal-Forming Analysis on Desk-top Microcomputers Using Non-Linear Elastic-Plastic Finite Element Techniques"
22nd MTDR Conf., pp 533-539 (1981)

(27) ZIENKIEWICZ, O.C.
"The Finite Element Method: from Intuition To Generality"
App. Mech. Reviews Vol. 23, pp 249-256 (1970)

(28) ZIENKIEWICZ, O.C.
"The Finite Element Method" 3rd Ed.
McGraw-Hill (1977)

(29) MITCHELL, A.R. and WAIT, R.
"The Finite Element Method in Partial Differential Equations"
Wiley, London (1977)

(30) KUDO, H. and MATSUBARA, S.
"Joint Examination Project of Validity of Various Numerical Methods for the Analysis of Metal Forming Processes"
in "Metal Forming Plasticity(Int. Union of Theor. and App. Mechanics)", Ed. H. Liepmann, Spinger-Verlag (1979)

(31) LEE, C.H. and KOBAYASHI, S.
"New Solutions to Rigid-Plastic Deformation Problems Using a Matrix Method" Trans. ASME J. Engg. for Industry Vol. 95, pp 865-873 (1973)

(32) ZIENKIEWICZ, O.C. and GODBOLE, P.N.
"Flow of Plastic and Visco-Plastic Solids with Special Reference To Extrusion and Forming Processes" Int. J. for Num. Meth. in Engg. Vol. 8, pp 3-16 (1974)

(33) PRICE, J.W.H. and ALEXANDER, J.M.
"The Finite Element Analysis of Two High Temperature Metal Deformation Processes" 2nd Int. Symp. on Finite Elements in Flow Problems, Santa Margherita Ligure, Italy (1976)

(34) ZIENKIEWICZ, O.C., JAIN, P.C. and ONATE, E.
"Flow of Solids During Forming and Extrusion: some Aspects of Numerical Solutions" Int. J. of Solids and Structures Vol. 14, pp 15-38 (1973)

(35) OH, S.I., REBELO, N. and KOBAYASHI, S.
"Finite Element Formulation for the Analysis of Plastic Deformation of Rate Sensitive Materials in Metalforming" in "Metal Forming Plasticity (IUTAM)", Ed. H. Lippmann, Springer-Verlag, pp 273-291 (1971)

(36) CHEN, C.C. and KOBAYASHI, S.
"Rigid Plastic Finite Element Analysis of Ring Compression" ASME publication, AMD Vol. 28, "Applications of Numerical Methods to Forming Processes", pp 163-174 (1978)

(37) PRICE, J.W.H. and ALEXANDER, J.M.
"Specimen Geometries Predicted by Computer Model of High Deformation Forging" Int. J. of Mech. Sci. Vol. 21, pp 417-430 (1979)

(38) DUNG, N.L., KLIE, W. and MAHRENHOLTZ, O.
"Analysis of Plastic Flow with a Simplified Finite Element Method" Mech. Res. Comm. Vol. 7, pp 33-38 (1980)

(39) KLIE, W., LUNG, M. and MAHRENHOLTZ, O.
"Axisymmetric Plastic Deformation Using Finite Element Method" Mech. Res. Comm. Vol. 1, pp 315-320 (1974)

(40) SHARMAN, F.W.
"Analysis of Metal Deformation-Extrusion" Electricity Council Research Centre M537 (1972)

(41) SHARMAN, F.W.
"Hot Bar Extrusion and the Effect of Radial Temperature Profiles in the Billet" Electricity Council Research Centre R851 (1975)

(42) CORNFIELD, G.C. and JOHNSON, R.H.
"Theoretical Predictions of Plastic Flow in Hot Rolling Including the Effect of Various Temperature Distributions Proc. Iron and Steel Inst. Conf."Mathematical Process Models in Iron and Steelmaking" Amsterdam (1973)

(43) SHAH, S.N. and KOBAYASHI, S.
"Rigid-Plastic analysis of Cold Heading by the Matrix Method" Proc. 15th MTDR, Birmingham, England, pp 603-610 (1974)

(44) MARCAL, P.V. and KING, I.P.
"Elastic-Plastic Analysis of Two-Dimensional Stress Systems by the Finite Element Method" Int. J. of Mech. Sci. Vol. 9, pp 143-155 (1967)

(45) YAMADA, Y., YOSHIMURA, N. and SAKURAI, T.
"Plastic Stress-Strain Matrix and Its Application for the Solution of Elastic-Plastic Problems by the Finite Element Method" Int. J. of Mech. Sci. Vol. 10, pp 343-354 (1968)

(46) NAGAMATSU, A., MUROTA, T. and JIMMA, T.
"On the Non-Uniform Deformation of Material in Axially Symmetric Compression Caused by Friction (Part 2)"
Bull. of JSME Vol. 14, No. 70, pp 339-347 (1971)

(47) NAGAMATSU, A., MUROTA T. and JIMMA, T.
"On the Non-Uniform Deformation of a Block in Plane-Strain Compression Caused by Friction (Part 3)" Bull. of JSME Vol. 14, No. 70, pp 314-321 (1971)

(48) NAGAMATSU, A., MUROTA, T. and JIMMA, T.
"On the Non-Uniform Deformation of a Block in Plane-Strain Compression Caused by Friction (Part 4)" Bull. of JSME Vol. 14, No. 70, pp 322-330 (1971)

(49) LEE, C.H. and KOBAYASHI, S.
"Analyses of Axisymmetric Upsetting and Plane Strain Side-Pressing of Solid Cylinders by the Finite Element Method" Trans. ASME, J. Engg. for Industry, pp 445-454 (1971)

(50) LEE, C.H., MASAKI, S. and KOBAYASHI, S.
"Analysis of Ball Indentation"
Int. J. of Mech. Sci. Vol. 14, pp 417-426 (1972)

(51) IWATA, K., OSAKADA, K. and FUJINO, S.
"Analysis of Hydrostatic Extrusion by the Finite Element Method" Trans. ASME J. Engg. for Industry, Vol. 94, pp 697-703 (1972)

(52) LEE, E.H., MALLETT, R.L. and McMEEKING, R.M.
"Stress and Deformation Analysis of Metal Forming Processes" in "Num. Modelling of Manufacturing Processes" PVP-PB-025, Ed. R.F. Jones Jr., H. Armen and J.T. Fong, ASME (1977)

(53) GORDON, J.L. and WEINSTEIN, A.S.
"A Finite Element Analysis of the Plane Strain Drawing Problem" Proc. 2nd NAMRC, Wisconsin, USA (1974)

(54) ZIENKIEWICZ, O.C., VALLIAPPAN, S. and KING, I.P.
"Elasto-Plastic Solutions of Engineering Problems 'Initial Stress', Finite Element Approach" Int. J. for Num. Meth. in Engg. Vol. 1, pp 75-100 (1969)

(55) BARNARD, A.J. and SHARMAN, P.W.
"The Elasto-Plastic Analysis of Plates Using Hybrid Finite Elements" Int. J. for Num. Meth. in Engg. Vol. 10, pp 1343-1356 (1976)

(56) DESAI, C.S. and PHAN, H.V.
"Three-Dimensional Finite Element Analysis including Material and Geometric Nonlinearities" in "Computational Methods in Nonlinear Mechanics" Ed. J.T. Oden, North-Holland, pp 205-224 (1980)

(57) LEE, E.H. and McMEEKING, R.M.
"Concerning Elastic and Plastic Components of Deformation"
Int. J. of Solids and Structures Vol.16, pp 715-721 (1980)

(58) LUBARDA, V.A. and LEE, E.H.
"A Correct Definition of Elastic and Plastic Deformation and its Computational Significance" SUDAM No. 80-1, Metal Forming Rep. #7, Div. of App. Mech., Dept. of Mech. Engg., Stanford (1930)

(59) LEE, E.H.
"Some Comments on Elastic-Plastic Analysis" SUDAM Rep. No. 80-5, Metal Forming Rep. #9, Div. of App. Mech., Dept. of Mech. Engg., Stanford (1980)

(60) THOMAS, T.Y.
"On the Structure of the Stress-Strain Relations"
Proc. Nat. Acad. Sci. Vol. 41, pp 716-720 (1955)

(61) THOMAS, T.Y.
"Combined Elastic and Prandtl-Reuss Stress-Strain Relations" Proc. Nat. Acad. Sci. Vol. 41, pp 720-726 (1955)

(62) THOMAS, T.Y.
"Combined Elastic and Von Mises' Stress-Strain Relations" Proc. Nat. Acad. Sci. Vol. 41, pp 908-910 (1955)

(63) PRAGER, W.
"An Elementary Discussion of Definitions of Stress Rate" Quart. App. Math. Vol. 19, pp 403-407 (1961)

(64) RICE, J.R.
"A Note on the 'Small Strain' Formulation for Elastic-Plastic Problems" Tech. Rep. No. N00014-67-A-0191-0003/8, Div. of Engg. Brown University (1970)

(65) LEE, E.H.
"The Basis of an Elastic-Plastic Code" SUDAM Report No. 76-1, Div. of App. Mech., Dept. of Mech. Engg., Stanford (1976)

(66) HIBBITT, H.D., MARCAL, P.V. and RICE, J.R.
"A Finite Element Formulation for Problems of Large Strain and Large Displacement" Int. J. of Solids and Structures Vol. 6, pp 1069-1086 (1969)

(67) OSIAS, J.R. and SWEDLOW, J.L.
"Finite Elasto-Plastic Deformation - I Theory and Numerical Examples" Int. J. of Solids and Structures Vol. 10, pp 321-339 (1974)

(68) YAMADA, Y., WIFI, A.S., and HIRAKAWA, T.
"Analysis of Large Deformation and Stress in Metal Forming Processes by the Finite Element Method" in "Metal Forming Plasticity (Int. Union of Theor. and App. Mech.)" Ed. H. Lippmann, Springer-Verlag (1979)

(69) MALLETT, R.L.
"Finite-Element Selection for Finite Deformation Elastic-Plastic Analysis" SUDAM Rep. No. 80-4, Metal Forming Rep. #8, Div. of App. Mech., Dept. of Mech. Engg., Stanford (1980)

(70) NAGTEGAAL, J.C. and de JONG, J.E.
"Some Computational Aspects of Elastic-Plastic Large Strain Analysis" in "Computational Methods in Nonlinear Mechanics" Ed. J.T. Oden North-Holland Pub. Co., pp 303-339 (1980)

(71) WEBSTER, W.
"A Three-Dimensional Analysis of Extrusion and Metalforming by the Finite Element Method" PhD Dissertation, University of Missouri-Rolla, USA (1978)

(72) BAYNHAM, J.M.W.
"Finite Element Analysis of Three-Dimensional Extrusion" Seminar Presented at 21st MTDR, Swansea (1980)

(73) SEBASTIAN, M.A., RODRIGUEZ, P. and SANCHEZ, A.M.
"A Method of Discretisation and an Approach to Three-Dimensional Deformation Analysis of Extrusion by the Finite Element Method" in Numerical Methods in Industrial Forming Processes", Swansea, pp 227-236 (1982)

(74) MORI, K. and OSAKADA, K.
"Simulation of Three-Dimensional Rolling by the Rigid-Plastic Finite Element Method" in "Numerical Methods in Industrial Forming Processes" Ed. J.F.T. Pittman, R.D. Wood J.M. Alexander & O.C. Zienkiewicz, Swansea, pp 747-756 (1982)

(75) SUN, J. LI, G., and KOBAYASHI, S.
"Analysis of Spread in Flat-Tool Forging by the Finite Element Method" NAMRC 11, pp 224-231 (1983)

(76) NAGAMATSU, A.
"Analysis of Contact Pressure and Deformation of Square Blocks in Elastic-Plastic Compression by the Finite Element Method" J. Jap. Soc. Tech. Plasticity (in Japanese) Vol. 14, No. 146, pp 220-229 (1973)

(77) HINTON, E. and OWEN, D.R.J.
"Finite Element Programming"
Academic Press, London (1977)

(78) CHEUNG, Y.K. and YEO, M.F.
"A Practical Introduction To Finite Element Analysis"
Pitman (1979)

(79) OWEN, D.R.J. and HINTON, E.
"Finite Elements in Plasticity: Theory and Practice"
Pineridge Press (1980)

(80) McMEEKING, R.M. and RICE, J.R.
"Finite-Element Formulations for Problems of Large Elastic-Plastic Deformation" Int. J. of Solids and Structures Vol. 11, 601-616 (1975)

(81) NAGTEGAAL, J.C.
"Some Recent Developments in Combined Geometric and Nonlinear Finite Element Analysis" in "Recent Advances in Non-Linear Mechanics" Ed. E. Hinton, D.R.J. Owen and C. Taylor, Pineridge Press, pp 87-117 (1982)

(82) HILL, R.
"Some Basic Principles in the Mechanics of Solids Without a Natural Time" J. Mech. and Phys. of Solids Vol. 7, pp 209-225 (1959)

(83) ERINGEN, A.C.
"Nonlinear Theory of Continuous Media"
McGraw-Hill, New York (1962)

(84) LEIGH, D.C.
"Nonlinear Continuum Mechanics"
McGraw-Hill, New York (1968)

(85) BRICKELL, F.
"Matrices and Vector Spaces"
Allen and Unwin, London (1972)

(86) NAGTEGAAL, J.C., PARKS, D.M. and RICE, J.R.
"On Numerically Accurate Finite Element Solutions in the Fully Plastic Range" Computer Methods in App. Mechanics and Engg. Vol. 4, pp 153-177 (1974)

(87) STARK, P.A.
"Introduction To Numerical Methods"
Macmillan, New York (1970)

(88) DRUCKER, D.C.
"A More Fundamental Approach To Plastic Stress-Strain Relations" Proc. 1st Nat. Cong. on App. Mechanics, pp 487-491 (1951)

(89) IRONS, B. and AHMAD, S.
"Techniques of Finite Elements"
Ellis Horwood, Chichester (1980)

(90) MORI, K., SHIMA, S. and OSAKADA, K.
"Analysis of Free Forging by Rigid-Plastic Finite Element Method Based on the Plasticity Equation for Porous Metals" Bull. of JSME Vol. 23, No. 178, pp 523-529 (1980)

(91) KOBAYASHI, S. and LEE, C.H.
"Deformation Mechanics and Workability in Upsetting Solid Circular Cylinders" Proc. 1st NAMRC, McMaster University, Canada, pp 185-204 (1973)

(92) OH, S.I.
"Finite Element Analysis of Metal Forming Processes with Arbitrarily Shaped Dies" Int. J. of Mech. Sci. Vol. 24, No. 8, pp 479-493 (1982)

(93) WEBSTER, W.D., Jr. and DAVIS, R.L.
"Development of a Friction Element for Metal Forming Analysis" Trans. ASME J. Engg. for Industry Vol. 1104, pp 253-256 (1982)

(94) SAADA, A.S.
"Elasticity Theory and Applications"
Pergamon (1974)

(95) ALEXANDER, J.M. and PRICE, J.W.H.
"Finite Element Analysis of Hot Metal Forming"
18th MTDR Conf., pp 267-274 (1977)

(96) McCRACKEN, D.D. and DORN, W.S.
"Numerical Methods and Fortran Programming"
Wiley (1965)

(97) NAYAK, G.C. and ZIENKIEWICZ, O.C.
"Elasto-Plastic Stress Analysis. a Generalisation for Various Constitutive Relations Including Strain Softening" Int. J. for Num. Meth. in Engg. Vol. 5, pp 113-135 (1972)

(98) RICE, J.R. and TRACEY, D.M.
"Computational Fracture Mechanics" in "Numerical and Computer Methods in Fracture Mechanics", Ed. S.J.Fenves, N. Perrone, A.R. Robinson and W.C. Schnobrich, Academic Press, New York, pp 585-623 (1973)

(99) SANTIAGO, J.M. and WISNIEWSKI, H.L.
"Implementing the Besseling-White Plasticity Model in the ADINA Finite-Element Program" in "Numerical Methods in Industrial Forming Processes" Ed J.F.T. Pittman, R.D Wood J.M. Alexander & O.C. Zienkiewicz, Swansea, pp 435-447 (1982)

(100) PILLINGER, I.
"The Prediction of Metal Flow and Properties in Three-Dimensional Forgings Using the Finite Element Method"
MSc(qual) Thesis, Birmingham (1982)

(101) HARTLEY, P., STURGESS, C.E.N. and ROWE, G.W.
"Friction in Finite-Element Analyses of Metalforming Processes" Int. J. Mech. Sci., Vol. 21, pp 301-311 (1979)

(102) COOK, M. and LARKE, E.C.
"Resistance of Copper and Copper Alloys To Homogeneous Deformation in Compression" J. of Inst. of Metals Vol. 71, pp 371-390 (1945)

(103) BOWDEN, F.P. and TABOR, D.
"The Friction and Lubrication of Solids" Part II,
Clarendon Press, Oxford (1964)

(104) HWANG, S.M. and KOBAYSHI, S.
"A Note on Evaluation of Interface Friction in Ring Tests"
NAMRC 11, pp 193-196 (1983)

(105) MALE, A.T. and COCKCROFT, M.G.
"A Method for the Determination of the Coefficient of Friction of Metals under Conditions of Bulk Plastic Deformation" J. Inst. Metals Vol. 93, pp 38-46 (1964)

(106) HARTLEY, P., STURGESS, C.E.N. and ROWE, G.W.
"An Examination of Frictional Boundary Conditions and their Effect in an Elastic-Plastic Finite Element Solution"
Proc. 20th MTDR Conf., Birmingham, pp 157-163 (1979)

APPENDICES

APPENDIX A

EFFECT OF JAUMANN CORRECTION

In order to demonstrate the necessity of including the Jaumann correction into the finite-element formulation, two finite-element analyses of an idealised deformation were performed, one using the Jaumann increment of Cauchy stress in the constitutive stress-strain relations, (i.e. with Jaumann correction), and the other using the increment of nominal stress in these relations (i.e. without Jaumann correction).

In both analyses, a single-element cube, length of edge 1 cm, which was initially aligned with the xyz axes, was rotated about the z axis by one degree per increment, the axis system (x', y', z') rotating with the element. At the same time, the element was extended by 0.000158844mm per increment, in the current x' direction. The other two dimensions of the element were reduced in accordance with a value of Poisson's ratio equal to 0.34. The element, which started the deformation with a tensile stress of 100 MN/m^2 acting in the x direction, was assumed, for simplicity, to remain elastic throughout with Young's modulus equal to 70 GN/m^2. The stress acting at any stage of the deformation could therefore be calculated by classical elasticity theory.

At any instant, the total value of the tensile strain in the x' direction is $\ln(1+0.0000158844a)$ where a is the current angle of

rotation, in degrees. Thus by Hooke's law, the normal stress in this direction, σ, is given by:

$$\sigma = 100 + 70000 \ln(1+0.0000158844a) \quad MN/m^2 \quad (A.1)$$

which includes the initial value of tensile stress in the body.

Using Mohr's circle, the normal stress in the x direction is found to be:

$$\sigma_{xx} = \sigma\cos^2 a \quad (A.2)$$

while the shear stress in the xy plane is:

$$\sigma_{xy} = \sigma\sin a.\cos a \quad (A.3)$$

The force f which must be acting in the x' direction to cause this state of stress is obtained from eqn. A.1 by multiplying the normal stress by the current area of the face which is perpendicular to this stress. Since the dimensional changes of the element are very small, this area can be taken to be equal to the original area of one face of the cube. Thus:

$$f = 0.0001\sigma \quad (A.4)$$

and the component of force in the x direction is:

$$f_x = f.\cos a \quad (A.5)$$

The change in the x component of force during an increment, Δf_x is the difference between f_x evaluated for angles a and a-1.

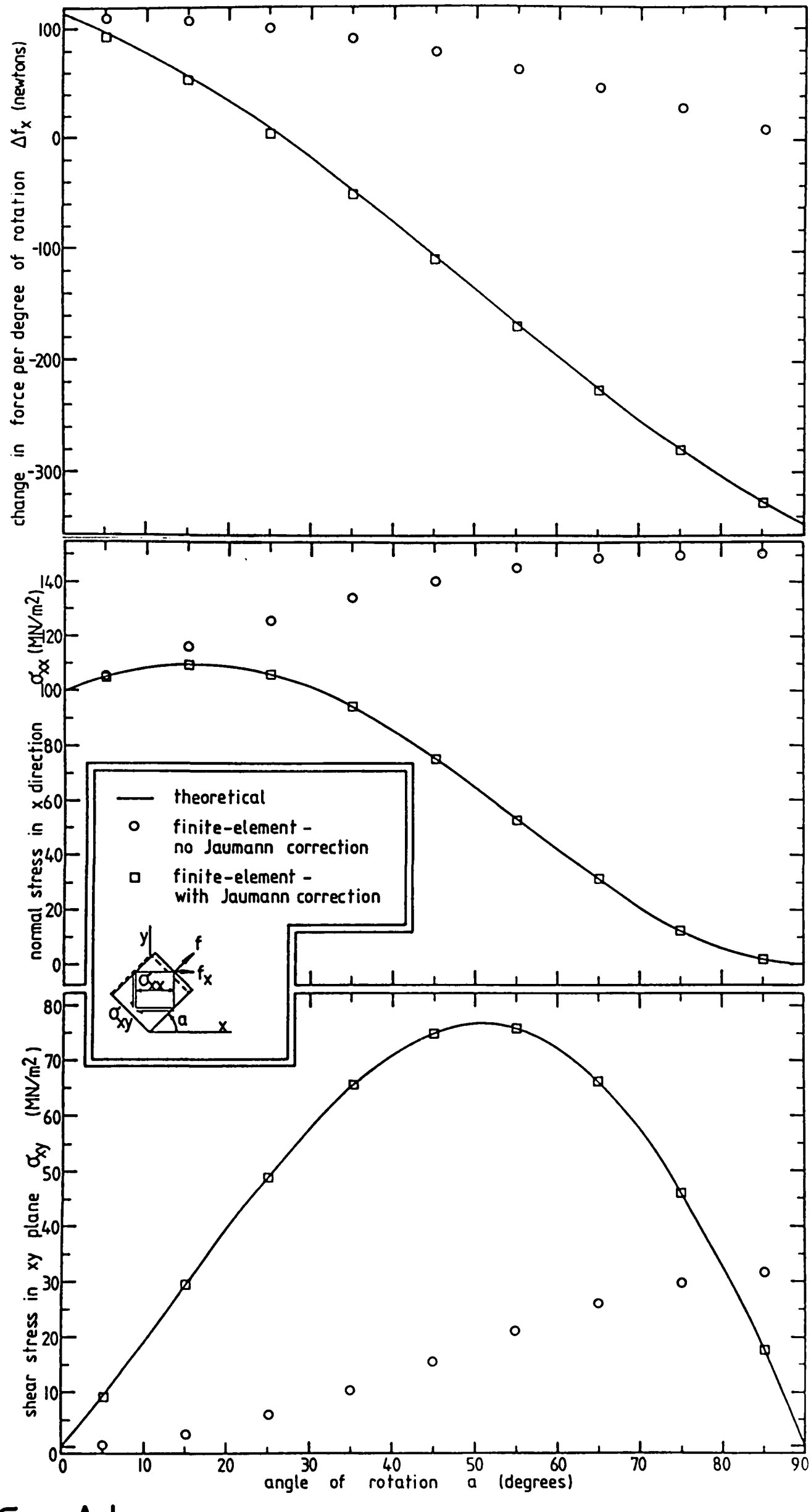

FIG. A.1

EFFECT OF JAUMANN CORRECTION ON COMBINED EXTENSION AND ROTATION OF PRE-STRESSED BODY

Fig. A.1 shows the variation of Δf_x, σ_{xx} and σ_{xy} with angle of rotation a as predicted by the above analysis, by the finite-element treatment without the Jaumann correction and by the finite-element treatment with the Jaumann correction.

The three graphs clearly illustrate that when the nominal stress is used in the the constitutive equations, (no Jaumann correction), the predicted values of incremental force and total stress are greatly in error; the finite-element treatment with the Jaumann correction gives components of incremental force and total stress which are in excellent agreement with the true values.

The size of the elastic extension in this example was chosen so that it gave a final tensile stress of the same order as the stresses obtained in the elastic-plastic forming processes examined by the finite-element program. The angular increment of one degree was also the order of rotation to be expected in these processes. Thus the above results show that the use of the Jaumann increment of Cauchy stress in the stress-strain relationships is essential if flow and stress are to be accurately predicted in metal-forming processes.

APPENDIX B

STRAIN DURING FINITE INCREMENTS OF DEFORMATION

B.1 Introduction

In section 2.1.1.3 it was stated that the infinitesimal strain tensor $([Q]+[Q]^T)/2$ which appears in the virtual work relationship is not an accurate representation of incremental strain when the material is rotating, even if the deformation is quite small. It was explained that the correct type of strain to use for the present formulation is the Lagrangian measure, but that this could not easily be incorporated into the governing equations because it is a quadratic function of incremental-displacement gradients. A new type of incremental strain was therefore defined, called linearised co-rotational (LCR), which, as its name implies, is a linear function of these quantities and is approximately independent of any material rotation. It was stated that providing the strain increment is small, LCR incremental strain is a good approximation to the Lagrangian value, even when the angular velocity of the material is an order of magnitude larger than the strain rate. Incorporation of LCR strain into the virtual-work expressions requires that the incremental angles of rotation be estimated using the values obtained from the previous step of the calculation, and it was further stated that even though the correct angles will not, in general, be predicted, LCR strain with such

estimated rotations is far more accurate than infinitesimal strain providing the estimates are of the right sort of order.

It is the purpose of this appendix to demonstrate the inadequacy of the infinitesimal definition of strain for metal-forming analysis, to illustrate the close agreement between the LCR and Lagrangian definitions of strain increment when this strain increment is small and to justify the use of the LCR expression with estimated rotational coefficients in the present treatment.

B.2 Requirements and Assumptions

The equations describing the behaviour of a plastically-deforming body are non-linear, not only because the geometry of this body changes with the extent of deformation, but also because the material properties are functions of strain and stress. Thus the analysis of a process where extensive yielding takes place has to be carried out incrementally, whatever strain measure is used.

However, the metal-forming operations to be examined by the present program may involve plastic strains of the order of one or more, and it is important, in order to make best use of the computer resources, that the analysis is performed in as few increments as possible and use of strain increments of about one or two percent is a reasonable compromise under these circumstances. Thus the first requirement is that the definition of strain used in the program must give acceptably-accurate values for increments of deformation of this sort of size.

Metal-forming operations may involve gross deformation of the

work-piece and considerable rotation of the material. But, bearing in mind the size of the increments to be used in the present analyses, the angular increments of rotation would not be expected to exceed about ten degrees. Thus the second requirement is that the strain definition used is acceptably accurate even when material rotations of this order are occurring.

As a corollary, it may be assumed for the purposes of the present work that the incremental strains and rotations do not exceed, to any large extent, those values specified above.

B.3 Example Deformation

The following simple deformation will be considered in order to illustrate the different definitions of incremental strain mentioned in section B.1.

The unit cube in fig. B.1 is initially aligned with the xyz axes. It is first deformed by simple tension, being extended in the x direction by a small amount e (for simplicity, the material is assumed to be incompressible, so that the strains in the y and z directions are e/2), and then rotated by a small angle a about the z axis in an anti-clockwise direction. The edges of the deformed body are now aligned with the x'y'z' axes.

The x, y and z components of incremental displacement of a point of the undeformed body with coordinates (x, y, z) are:

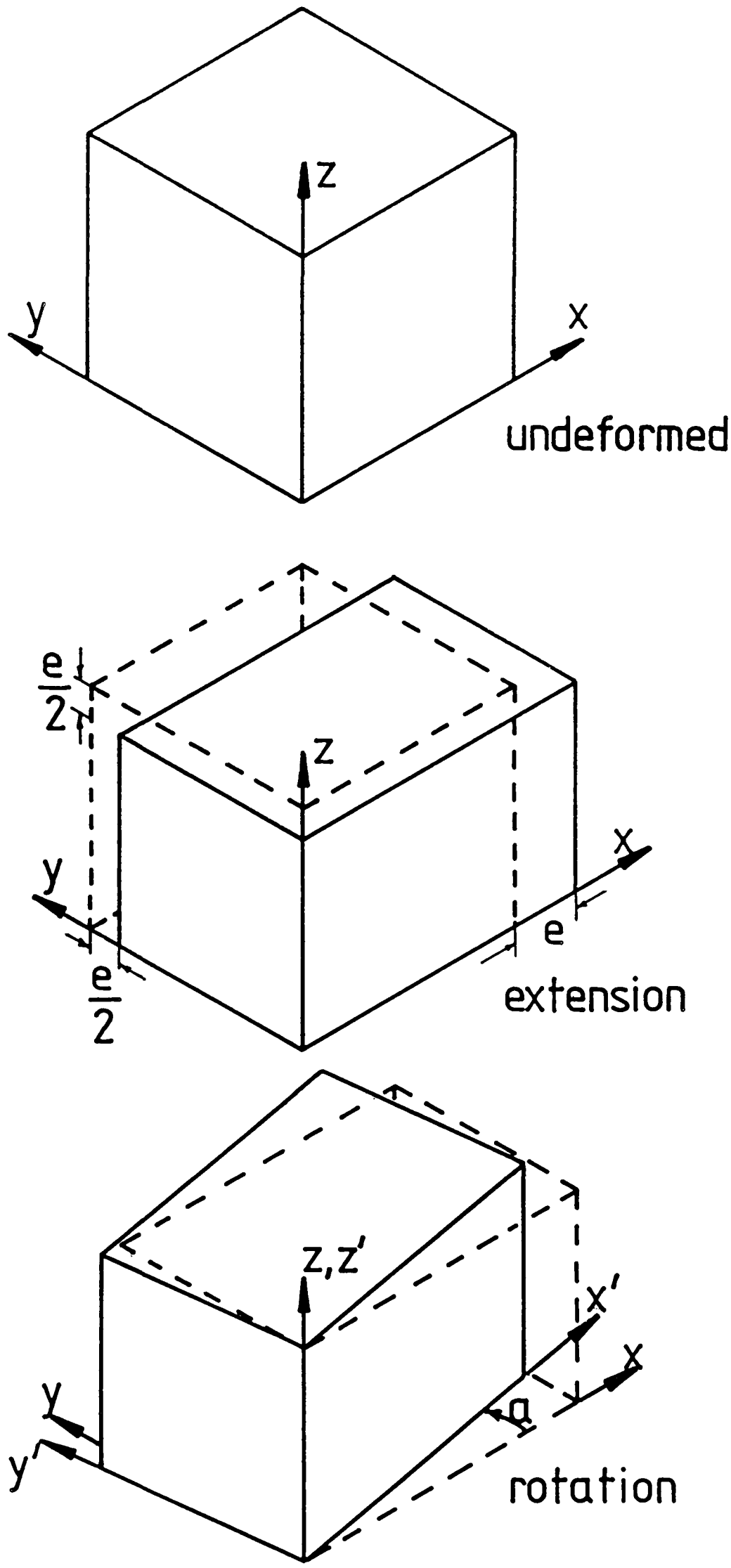

FIG. B.1

COMBINED EXTENSION AND ROTATION OF CUBIC ELEMENT

$$\Delta u_x = ((1+e)\cos a - 1)x - (1-e/2)\sin a.y \qquad (B.1A)$$

$$\Delta u_y = (1+e)\sin a.x + ((1-e/2)\cos a - 1)y \qquad (B.1B)$$

$$\Delta u_z = -(e/2)z \qquad (B.1C)$$

Taking the partial derivatives of eqns. B.1 and substituting into eqn. 2.2 gives that the incremental-displacement gradient tensor for this deformation is:

$$[Q] = \begin{bmatrix} (1+e)\cos a-1 & (1+e)\sin a & 0 \\ -(1-e/2)\sin a & (1-e/2)\cos a-1 & 0 \\ 0 & 0 & -e/2 \end{bmatrix} \qquad (B.2)$$

Using the definition given in section 2.1.1.3.1, the Lagrangian increment of strain is therefore given by:

$$[\Delta\varepsilon^L] = \begin{bmatrix} e + e^2/2 & 0 & 0 \\ 0 & -e/2 + e^2/8 & 0 \\ 0 & 0 & -e/2 + e^2/8 \end{bmatrix} \qquad (B.3)$$

B.4 Infinitesimal Definition

Substituting eqn. B.2 into the expression given in section B.1, the increment of strain for this deformation according to the infinitesimal definition is:

$$[\Delta\varepsilon^{\infty}] = \begin{bmatrix} (1+e)\cos a - 1 & (3e.\sin a)/4 & 0 \\ (3e.\sin a)/4 & (1-e/2)\cos a - 1 & 0 \\ 0 & 0 & -e/2 \end{bmatrix} \qquad (B.4)$$

comparing eqns. B.3 and B.4, and expanding the trigonometric quantities, the absolute errors in the normal x and y components of the infinitesimal increment of strain are, to a first approximation, both equal to $-a^2/2$, while the absolute error in the xy shear component is approximately 0.75e.a (with a measured in radians).

Thus, for example, if e is 0.01 (i.e. the tensile strain increment is 1%) and the angular increment a is five degrees, the relative error in the normal component of incremental strain in the x direction, using the infinitesimal definition, is about -38%; if the value of a is ten degrees, the error rises to about -150%.

Clearly, the infinitesimal strain is grossly inaccurate when the material is rotating, even when the rotations are fairly small.

B.5 Linearised Co-rotational (LCR) Strain

Let the estimated value of the angular increment for this deformation be b. The rotational matrix [R] is then:

$$[R] = \begin{bmatrix} \cos b & -\sin b & 0 \\ \sin b & \cos b & 0 \\ 0 & 0 & 1 \end{bmatrix} \qquad (B.5)$$

Using the definition given in eqn. 2.16, the LCR increment of strain for this deformation may be expressed as:

$$[\Delta\varepsilon] = \begin{bmatrix} ((1+e)\cos a-1)\cos b + (1/2 + 7e/8)\sin a.\sin b & (3e.\sin(a-b))/4 & 0 \\ (3e.\sin(a-b))/4 & ((1-e/2)\cos a-1)\cos b + (1/2 - 5e/8)\sin a.\sin b & 0 \\ 0 & 0 & -e/2 \end{bmatrix} \qquad (B.6)$$

In order to demonstrate that LCR strain is a good approximation to Lagrangian strain, assume that the angular increment has been correctly estimated, i.e. b=a, then:

$$[\Delta\varepsilon] = \begin{bmatrix} ((1+e)\cos a-1)\cos a + (1/2 + 7e/8)\sin a & 0 & 0 \\ 0 & ((1-e/2)\cos a-1)\cos a + (1/2 - 5e/8)\sin a & 0 \\ 0 & 0 & -e/2 \end{bmatrix} \qquad (B.7)$$

Comparison of eqns. B.7 and B.3 shows that the LCR definition of incremental strain gives the correct, zero value of the xy shear component, irrespective of the values of e and a. The normal x and y components though include errors which are functons of these two quantities.

Fig. B.2 depicts the variation, with respect to a and e, of the absolute error in the normal component of LCR incremental strain in

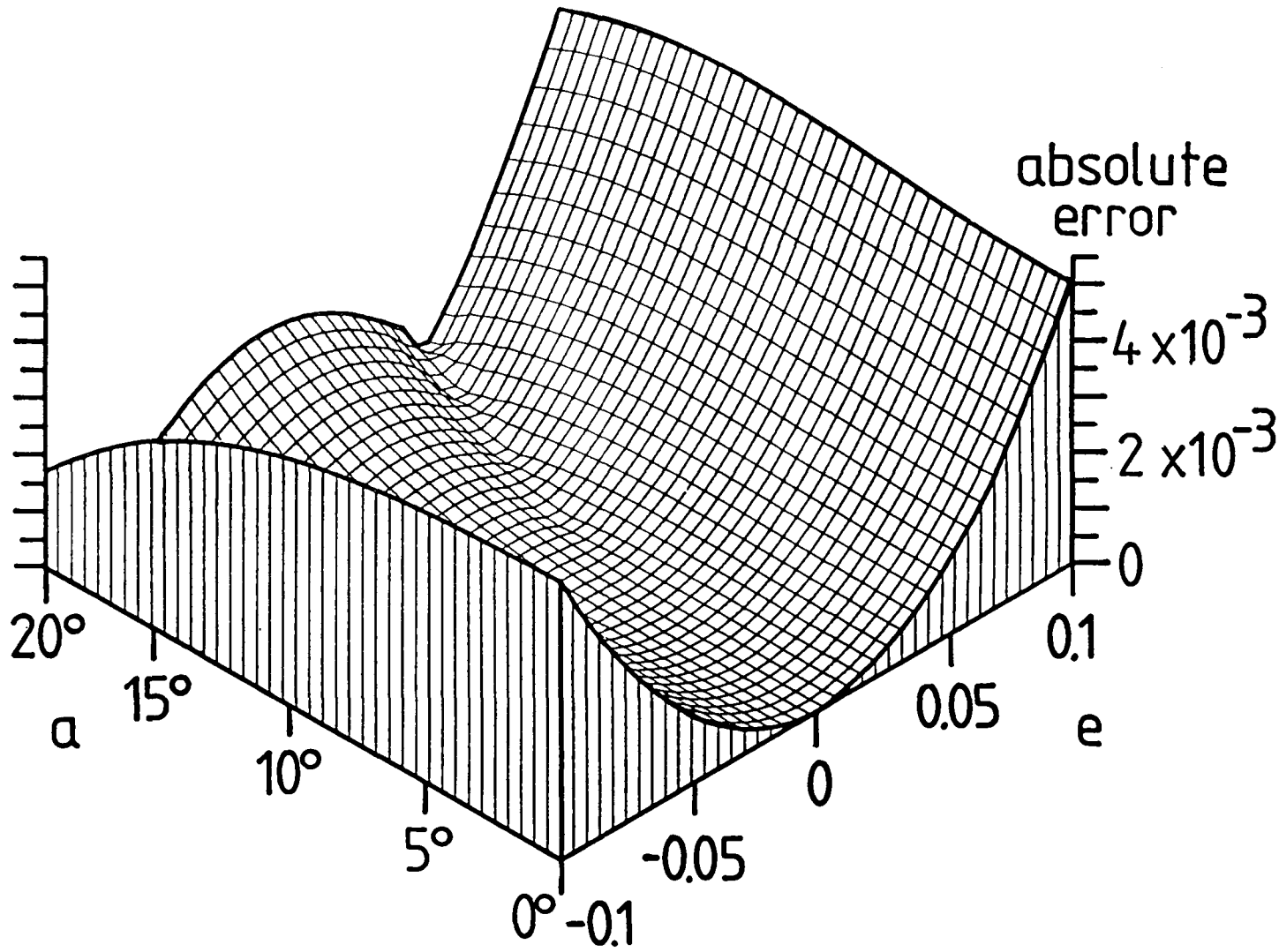

FIG. B.2

VARIATION OF THE ABSOLUTE ERROR IN THE x COMPONENT OF LINEARISED CO-ROTATIONAL STRAIN WITH ANGULAR INCREMENT α AND EXTENSION e FOR THE COMBINED TENSION/ COMPRESSION AND ROTATION OF A BODY

the x direction, over the domain of normal strain and angular increment of interest in the present case. It can be seen that providing the magnitude of the strain is less than two or three percent, the absolute error in this component of LCR strain is very small, and that this is true even for values of a up to about ten degrees. The relative error in the x component of incremental strain in this region is of the order of one percent or less, which is certainly an acceptable order of accuracy. (Strictly, the relative error will tend to infinity as e tends to zero, for all a not equal to zero, and the above error bound only applies when the magnitude of the strain increment is greater than a fraction of a percent. However, since it is the absolute error in the strain which is important if the true value of the strain is zero, and the absolute error in the present case is very small, being approximately proportional to the fourth power of a when e is zero, this behaviour may be safely ignored.)

Thus for this simple deformation, the LCR increment of strain is a very good approximation to the Lagrangian measure for the required range of strain and angular increment.

B.6 LCR Strain with Estimated Rotational Coefficients

In order to incorporate LCR strain into the finite-element formulation, the coefficients of the matrix [R] are estimated to be equal to those calculated for the previous increment or step of the analysis. Thus in general, in the present simple example, b is not exactly equal to a.

However, it is reasonable to assume that the estimate of b does not differ too greatly from a, so that a-b, a and b, are all fairly small. In this case, eqn. B.6 may be rewritten to give, approximately:

$$[\Delta\varepsilon] \simeq \begin{bmatrix} -(a.\sin(a-b))/2 + e.\cos(a-b) & (3e.\sin(a-b))/4 & 0 \\ (3e.\sin(a-b))/4 & -(a.\sin(a-b))/2 - (e.\cos(a-b))/2 & 0 \\ 0 & 0 & -e/2 \end{bmatrix} \quad (B.8)$$

providing b is not very close to a (in which case the error analysis set out in section B.5 would apply). Comparing eqn. B.8 with eqn. B.3 gives the following relative errors, after neglecting higher-order terms:

$$err(\Delta\varepsilon_{xx}) = a(b-a)/2e - e/2 \quad (B.9A)$$

$$err(\Delta\varepsilon_{yy}) = a(b-a)/e - e/4 \quad (B.9B)$$

and the absolute error:

$$abs.err(\Delta\varepsilon_{xy}) = 3e(a-b)/4 \quad (B.9C)$$

Thus, for this simple deformation, all three errors are linear functions of the error in the estimated angle of rotation b-a.

The infinitesimal increment of strain may be considered to be the same as the LCR definition but with the angular increment estimated to be zero i.e. with 100% error in the estimated angle. Thus providing, as is most likely, the finite-element program gives a better estimate

of the angular increments than this, the strain increments calculated from the LCR definition will be more accurate than those obtained from the infinitesimal expression. In many situations the rate of rotation of the material changes little from one increment to the next, and in these cases LCR strain with estimated rotational coefficients will agree very well with the Lagrangian measure.

This is illustrated in fig. B.3. This compares the results of two finite-element analyses of the combined rotation and elastic extension of the single element described in appendix A with the analytical results presented there. This time, the two finite-element treatments were identical except that one used the infinitesimal strain increment definition in the formulation, and the other used the LCR definition with estimated rotational values. The values of incremental force in the x direction and normal stress in the x direction are in excellent agreement with the theoretical results; the infinitesimal definition of strain leads to gross errors in these quantities.

B.7 A Note on the Chosen Example

For simplicity of calculation, this appendix has examined a deformation in which there is only one axis of rotation. Under these circumstances the off-diagonal terms of the matrix [R] are exactly equal and opposite in sign to the terms in the corresponding transpose positions, (eqn. B.5), which in general is only approximately true, and then only for small angles of rotation. Thus the chosen example is in this respect a special case. However, numerical examination of other examples of deformation with strictly triaxial rotation leads to

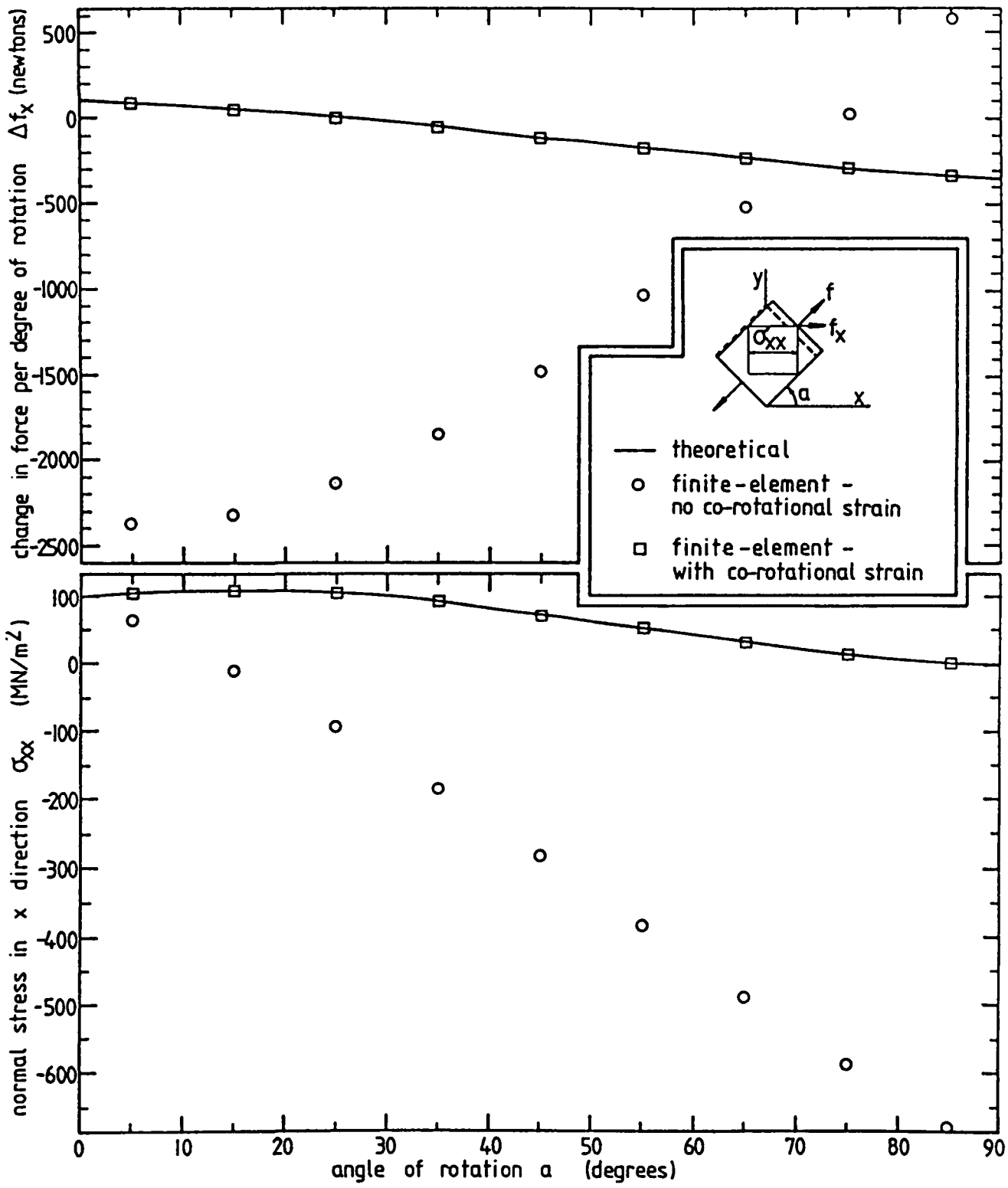

FIG. B.3

EFFECT OF CO-ROTATIONAL STRAIN ON COMBINED EXTENSION AND ROTATION OF PRE-STRESSED BODY

similar conclusions concerning the relative merits of infinitesimal and LCR strain and the errors involved in their use, although, for the sake of conciseness, these results will not be presented here.

B.8 Conclusions

1. The infinitesimal strain tensor is not an accurate representation of incremental strain when the deformation involves rotation, even small values.
2. The expression for the linearised co-rotational increment of strain given in eqn. 2.16 predicts values which are very close to the true values of incremental strain providing the rotational matrix [R] is evaluated correctly.
3. When [R] is not known exactly, the LCR definition of strain gives values which are much closer to the true values of incremental strain than those obtained from the infinitesimal expression, providing [R] is estimated to be of the correct order of magnitude. Therefore, the technique developed for this program, in which the co-rotational strain increment is incorporated into the stiffness formulation using the rotational matrices calculated for the previous increment, is justified.

APPENDIX C

BANDWIDTH

In section 2.2 it is stated that the stiffness matrix [K] is symmetric (assuming the vectors of incremental displacement and force refer to nodes in the same order) and banded, i.e. all the non-zero terms lie within a band about the leading diagonal, and that only the coefficients in the upper (or lower) band need be stored.

The maximum number of coefficients in a row of the band is called the bandwidth; the maximum number in a row of the stored upper band is the semi-bandwidth (strictly (bandwidth+d)/2, where d is the number of degrees of freedom per node - three in the present analysis). The nodal bandwidth and the nodal semi-bandwidth are obtained from these quantities by dividing by d.

The value of the bandwidth depends upon the order in which the nodes are considered in the force and displacement vectors. It is important to minimise the bandwidth so that the storage requirements of the computer are as small as possible for a given total number of degrees of freedom. The strategy adopted when setting up the finite-element mesh under these conditions is to number the nodes so that the maximum difference between the numbering, of any pair of nodes which belong to the same element, is minimised. In practice this may be a complicated procedure, but the principle is straightforward.

However, when a frontal solution is adopted, the above approach

is no longer valid since the ordering of nodes in the rows and columns of the stiffness matrix is no longer the same as the node numbering but instead depends upon the numbering of the elements and the order in which nodes are specified in defining the vertices of elements.

As a general rule, the elements should be numbered and defined so that the maximum difference in the numbering of any pair of elements with a common node is minimised. However, this does not guarantee that the nodal semi-bandwidth is within the limits, stated in section 3.1, of the current finite-element program.

Algebraic expressions can be obtained for nodal semi-bandwidth when the mesh consists of a rectangular array of elements numbered in a regular fashion. In other situations it must be calculated from first principles.

The following equivalent definitions may be helpful.

Firstly it should be noted that the stiffness matrices of elements are assembled into the global stiffness matrix (or that part of it currently forming the front) in order of increasing element number.

Secondly, a node is said to be introduced when the stiffness matrix of the first element to contain that node is assembled.

Thirdly, a node is said to be eliminated after the stiffness matrix of the last element to contain that node is assembled.

Definition 1: the semi-bandwidth is the maximum number of equations of the stiffness matrix which need to be stored in the computer main memory at any one time.

This is not a very useful criterion, but it is the one used by the finite-element program.

Definition 2: define the span of a node n to be the total number of nodes which, at the time node n is eliminated, have been introduced but not yet eliminated. The nodal semi-bandwidth is the maximum span of any node.

This is still slightly impractical as definition, but it leads naturally to the third definition, which is actually an algorithm for the calculation of nodal semi-bandwidth.

Definition 3: construct a running total as follows.

1. Running total is zero to start with.
2. Consider elements in numerical order. For each element increase running total by one for every node which has not been encountered in any element so far, then decrease it by one for every node which will not be encountered in any subsequent element.
3. Nodal semi-bandwidth is the maximum value attained by the running total during the above process.

For large meshes, the calculation of nodal semi-bandwidth by hand is lengthy. The finite-element program developed here automatically prints the value of this quantity (even when it exceeds the program limit) and so can be used to check whether a given mesh is suitable for analysis.

APPENDIX D

DEMONSTRATION OF MEAN-NORMAL TECHNIQUE

Fig. D.1 shows deformed meshes predicted by two finite-element analyses of the simple upsetting of a cube of commercially-pure aluminium with zero friction at the interface between the die and the billet. For the purposes of this demonstration, the two finite-element meshes contained 27 elements and each modelled one eighth of their respective billets. In both cases, the pictures show the results after 50.075% reduction in height, the tangent-modulus solutions being undertaken with 1% reduction in height per increment.

The first picture illustrates the deformed mesh obtained by a technique in which the increment of stress at sample points was calculated using the elastic-plastic stress-strain matrix (evaluated at the start of the increment) followed by a correction to the yield surface (tangent-D-matrix method); the second picture results from an analysis which used the mean-normal method of calculating the increment of stress described in section 3.2.4.2.2. The two analyses were otherwise similar.

With zero interfacial friction, the cube should deform homogeneously with strain and stress constant throughout the body. In the axis system shown, the three shear components of stress should be zero and the x and y normal components of stress should be equal. It is easily established that with a 50% reduction in height, the accumulated generalised strain should be everywhere equal to 0.69.

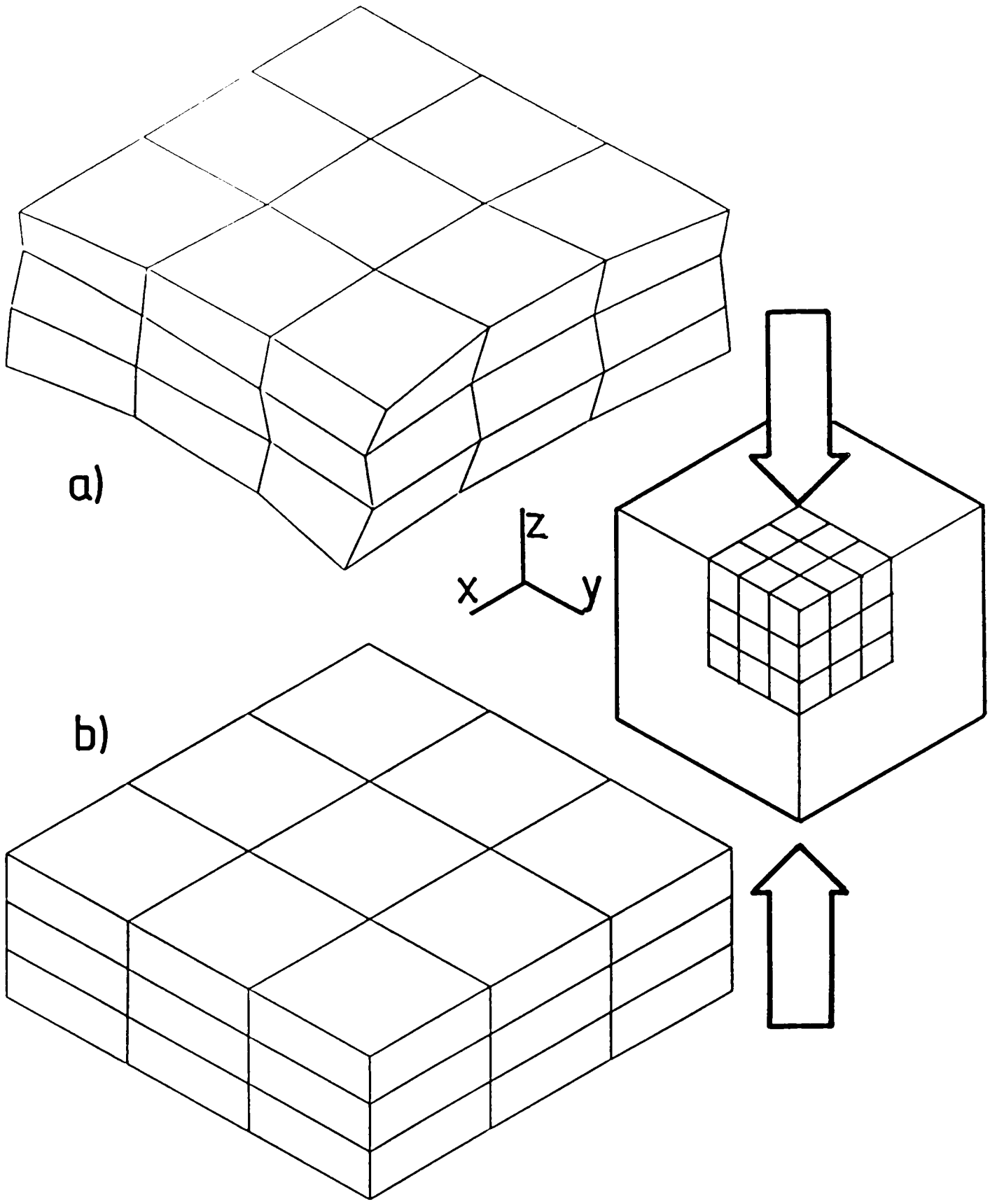

FIG. D.1

FINITE-ELEMENT PREDICTIONS OF SIMPLE UPSETTING OF A CUBE OF ECI AL WITH ZERO INTERFACIAL FRICTION.
(1/8 CUBE MODELLED; 50.075% DEFORMATION)
a) STRESS FROM TANGENT D-MATRIX & CORRECTION
b) STRESS FROM MEAN-NORMAL METHOD

It can be seen from fig. D.1a that the tangent-D-matrix method of calculating stress leads to a highly inhomogeneous, deformed mesh. The stress and strain in this case vary considerably throughout the body, and large values of shear stress were predicted. In addition, the calculated generalised strain is generally too low, varying from 0.46 to 0.61.

The deformed mesh predicted by the analysis which used the mean-normal technique is homogeneous to within the number of figures of the printed values of nodal coordinates (i.e. to within 0.01%). The stress and strain calculated in this case are similarly constant throughout the body, all shear stresses are zero and the x and y components of stress are equal. The predicted value of generalised strain of 0.71 is very close to the theoretical value.

These results show that the tangent-D-matrix method of calculating stress leads to incorrect deformation patterns even when the stress is corrected to the yield value, while the mean-normal method results in correct displacements and very good values of stress and strain.

APPENDIX E

PUBLISHED WORK

PILLINGER, I., HARTLEY, P., STURGESS, C.E.N. and ROWE, G.W.

"An Elastic-Plastic Finite-Element Analysis of the Radial Expansion of a Thick-Walled Hollow Cylinder and Analytical Validation"
in "Numerical Methods in Industrial Forming Processes",
Ed. J.F.T. Pittman, R.D. Wood, J.M. Alexander and O.C. Zienkiewicz,
Swansea, pp 123-133 (1982)

AN ELASTIC-PLASTIC FINITE-ELEMENT ANALYSIS OF THE RADIAL EXPANSION OF A THICK-WALLED HOLLOW CYLINDER AND ANALYTICAL VALIDATION

by
I.Pillinger, P.Hartley, C.E.N.Sturgess and G.W. Rowe

Department of Mechanical Engineering
University of Birmingham

ABSTRACT

A three-dimensional elastic-plastic finite-element formulation has been developed and checked by comparing the stress distributions predicted for the partially plastic radial expansion of a tube with those of a conventional analytical solution. Finite-element analyses were carried out to investigate the effects of (i) relaxing the incompressibility conditions of yielded elements, (ii) the method of calculating hydrostatic stress and (iii) the use of a new method of obtaining convergence by calculating residual forces from deviatoric stress increments.

Excellent agreement was obtained with the results of the theoretical analysis, providing plastic volume constancy was strictly enforced and hydrostatic stress was calculated from the deviatoric stress distributions after iteration was complete. Solutions failed to converge when plastic incompressibility was not enforced. Accurate determination of hydrostatic stress directly from the bulk strain was possible only if plastic volume change was optimised. The new iteration method was found to give results which were as accurate as those of the previous method, for this deformation.

The incorporation of work hardening into the finite-element analysis led to stress distributions which were appreciably different to those predicted by the non-workhardening analytical solution.

1. INTRODUCTION

Finite-element formulations are often tested by comparing the results with experiment *[1-4]*, but no check can then be made of the stress components in the body of the material. The validation described here is for the finite-element

124

analysis of one of the few examples of plastic deformation which allow analytical determination of stress component distributions, namely that of the radial expansion of a tube by internal pressure.

The comparisons between the finite-element and the theoretical results for this process also made possible an investigation into the effects, on the finite-element solutions, of relaxing the assumed incompressibility of yielded elements, of the methods of obtaining convergence and of the methods of calculating the hydrostatic stress.

Various authors have proposed solutions for the stress distributions in partially plastic, radially expanded non-workhardening tubes, using different yield criteria, plastic flow rules and end conditions. The radial and tangential stress components can be calculated explicitly as functions of position and extent of deformation if the Tresca criterion is used *[5-10]*, while a closed form expression for the axial stress in the plastic region can only be obtained by assuming either complete incompressibility of the yielded portion *[11]*, or the disappearance of the plastic axial strain *[12]*. In other cases, a numerical technique must be adopted *[13]*. Solutions have been extended to cover workhardening materials *[14]*, and also to deal with the fully plastic range *[11,15]*. A more complete survey of the theoretical treatments of this problem is given in *[16]*.

2. FINITE-ELEMENT FORMULATION

Finite-element theory is well documented, both in general terms *[17,18]*, and as applied to plasticity *[11,20]*, and the following are only brief notes on those aspects relevant to the technique under discussion.

2.1 Solution technique

A mixed incremental/iterative analysis is used. For the j^{th} iteration of the i^{th} increment *[21]*,

$$\Delta\underline{\delta}_j^i = \{K^i\}^{-1}\Delta\underline{F}_j^i \qquad (1)$$

where $\Delta\underline{\delta}_j^i$ is the increment in the nodal displacement; $\{K^i\}$ is the global stiffness matrix, based on stress-strain relationships derived from the Prandtl-Reuss flow rule *[20]* and Von Mises' yield criterion, at the start of the increment; $\Delta\underline{F}_j^i$ is the applied nodal force vector for the increment and $\Delta\underline{F}_j^i$ $j>1$, is the residual force vector defined by,

$$\Delta\underline{F}_j^i = \Delta\underline{F}_{j-1}^i - \Delta\underline{F}_{j-1}^{i*} \qquad (2)$$

where $\Delta\underline{F}_{j-1}^{i*}$ is the nodal force vector which is in equilibrium with the calculated stress increment distribution at the

end of the $j-1^{th}$ iteration.

Equation (1) is solved using a frontal technique [18]. Iteration is repeated until $\Delta\underline{\delta}_j^i$ decreases to a specified level.

2.2 Enforcement of incompressibility

The amount of elastic bulk strain of yielded elements can be controlled by varying the value of Poisson's ratio, ν_p, used in the stress-strain relationships applying to those elements. Values close to 0.5 are required to enforce incompressibility.

2.3 Methods of calculating residual forces

i) $\Delta\underline{F}_{j-1}^{i*}$ calculated to be in equilibrium with the total stress increments at the end of each iteration, ii) a new method in which, for yielded elements, the residual forces are calculated to be in equilibrium with the deviatoric components of these stresses.

2.4 Calculation of stress

(a) Deviatoric components; The strain increments are obtained as displacement gradients from $\Delta\underline{\delta}_j^i$. The increments in deviatoric stress for each iteration are calculated from the deviatoric strain increments using the current stress-strain relationships.

(b) Hydrostatic components; The increments in hydrostatic stress are calculated either from bulk strain increments at each iteration (direct method), or, for yielded elements, from the deviatoric stress values after the iteration is complete by means of the stress equilibrium equations [22], (indirect method).

3. THEORETICAL ANALYSIS USED FOR VALIDATION

The stress components predicted by the finite-element technique were compared with an analytical treatment using Prandtl-Reuss and Tresca equations, based on that of Hill, Lee and Tupper for plane strain [17]. It was modified to use values of Poisson's ratio in the elastic (ν) and plastic (ν_p) regions, corresponding to the values of Poisson's ratio used in the finite element analysis. For this deformation, the Tresca criterion approximates that of Von Mises to within 3% [16].

4. FINITE ELEMENT ANALYSIS

The finite-element mesh consisted of 210 8-node isoparametric brick elements (fig.1). The plane-strain expansion of the tube was simulated by prescribing a total displacement of 0.04mm to the bore surface, divided into 16 increments. Material properties of annealed EC1 aluminium were assumed [21],

130

hardening material differ from the non-workhardening analytical values, particularly the tangential component.

5.3 Computational time

One increment of a convergent, iterative solution (cases 4-9) took 17 seconds of processor time on a CDC 7600, compared to 14 seconds for a non-iterative solution (case 3).

6. DISCUSSION

6.1 Finite-element validation

The results from cases 5,6 and 8 show that, with the appropriate amount of plastic incompressibility, the finite-element treatment can give values of total stress components which are in excellent agreement with the previous analytical solution due to Hill et al. The finite-element formulation is therefore validated for this deformation and may be extended to configurations for which no analytical solution exists.

6.2 Calculation of hydrostatic stress

Cases 7 and 8 gave the same deviatoric stress distributions, and so the inaccurate total stresses obtained by the former analysis were due to calculating the hydrostatic components of stress directly from the bulk strain increment, the maximum error in this component being 170% at the bore at full yield. Thus when values of ν_p which are very close to 0.5 are used, it is necessary to calculate the hydrostatic stresses by the indirect method after iteration is complete.

Cases 5, 6 and 7 indicate that accurate hydrostatic stress values can only be obtained directly from the bulk strain increments if a value of ν_p is used in the finite-element analysis which is less than 0.495, for this configuration. This limiting value may vary according to the type of deformation and would not, in general, be known. The calculation of hydrostatic stress indirectly is not subject to a limiting value of ν_p and therefore may be used as part of a predictive technique in analysing geometries for which no previous solutions are available.

6.3 Methods of iteration

Iterative finite-element solutions failed to converge when elastic values of ν_p were used for yielded elements, whether the residual forces were calculated from deviatoric (new method) or from total stress increments (previous method), while both methods predicted correct deviatoric stress when volume constancy was strictly enforced (cases 7 and 8).

Thus, for this small-strain deformation, the two methods of iteration produce similar results, although the new method has an advantage when used with the indirect technique for calculating hydrostatic stress, in that the increments of

127

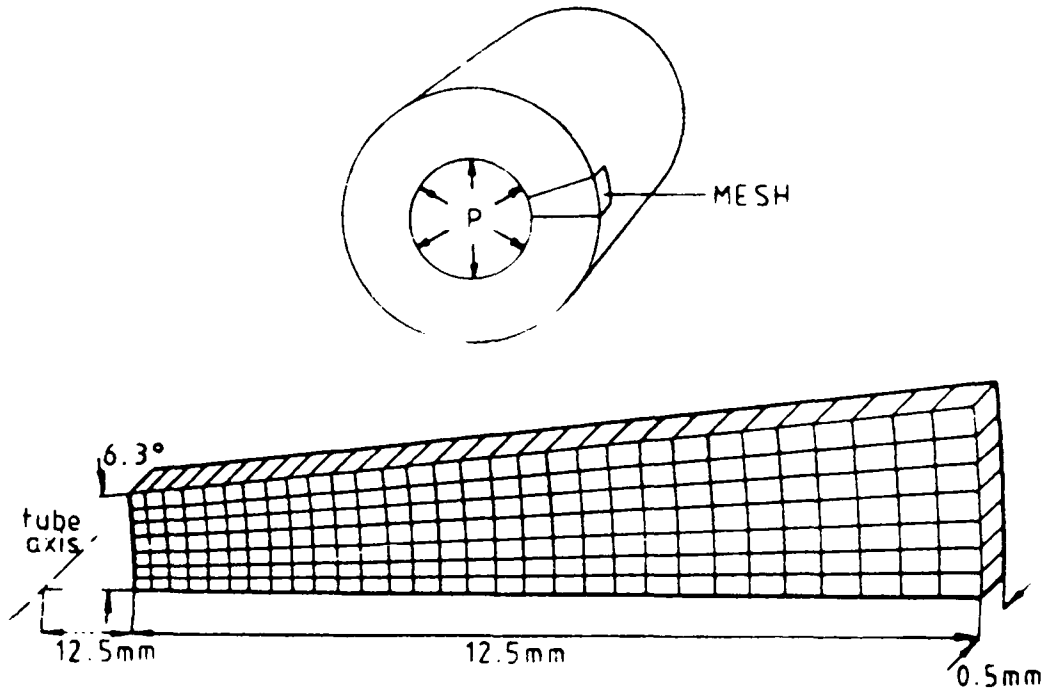

Fig.1. TUBE AND FINITE-ELEMENT MESH

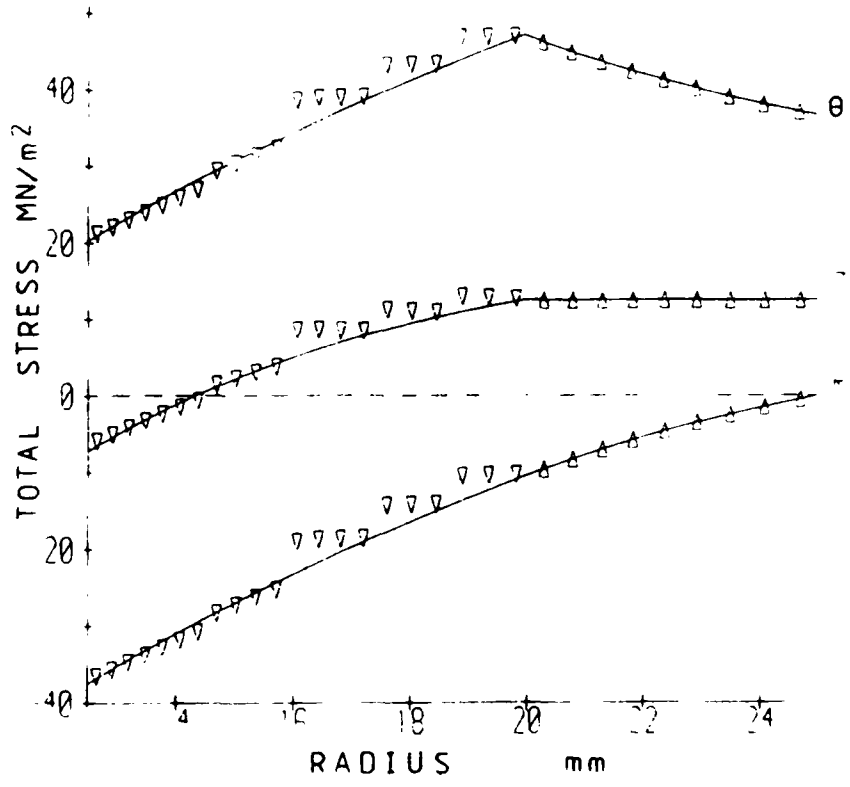

Fig.2. TOTAL STRESS DISTRIBUTIONS (θ tangential, Z axial, R radial) for case 3 from analysis (——), finite-element (∇ yielded, Δ unyielded)

128

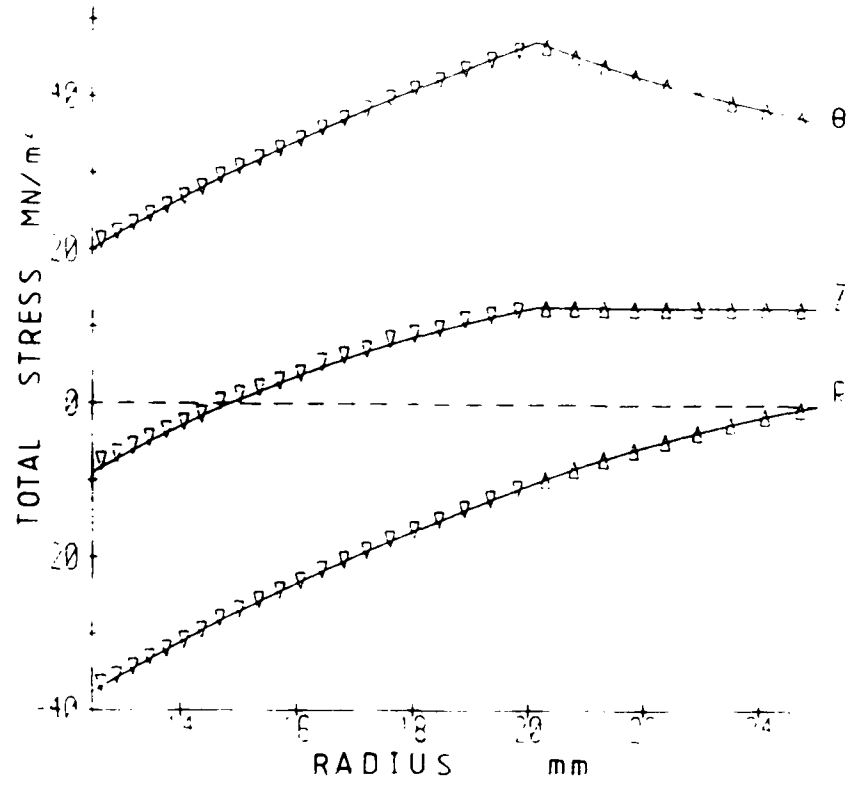

Fig 3 TOTAL STRESS DISTRIBUTIONS FOR CASE 5

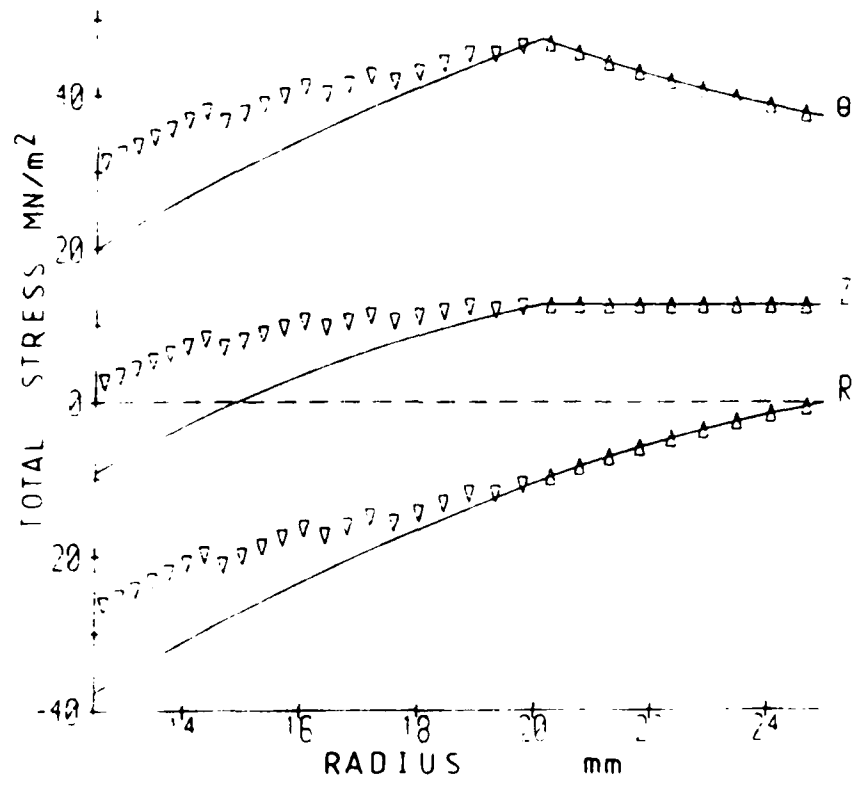

Fig.4. TOTAL STRESS DISTRIBUTIONS FOR CASE 7

129

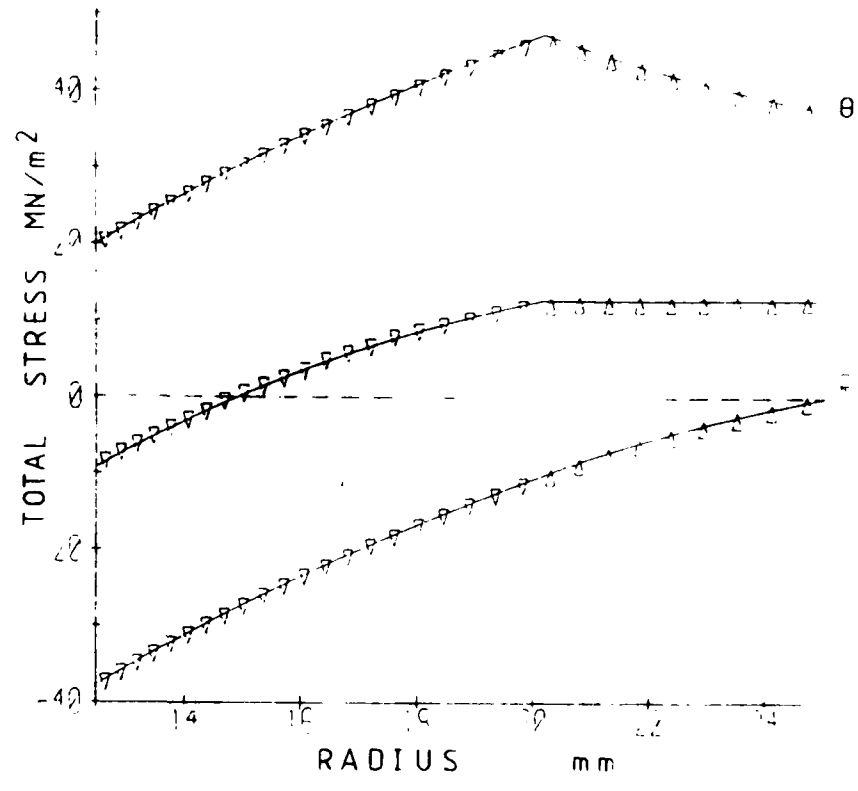

Fig.5. TOTAL STRESS DISTRIBUTIONS FOR CASE 8

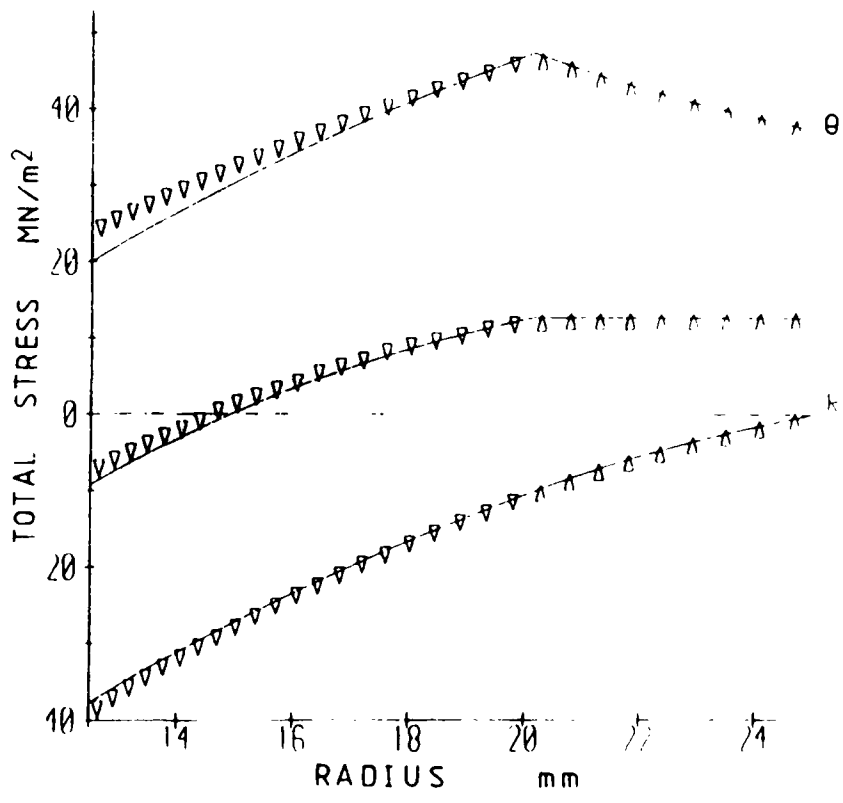

Fig.6. TOTAL STRESS DISTRIBUTIONS FOR CASE 9

126

with E = 70.8 GN/m^2, ν = 0.34, initial yield stress = 50 MN/m^2 and work hardening obeying the relationship,

$$Y = 50 + 21.2 \ln\left(\frac{\bar{\varepsilon}_p + 0.00465}{0.00465}\right) \qquad (10)$$

The examples considered are described in table 1.

Case	Residual Forces from	Calculation of Hydrostatic Stress	ν_p	Work Hardening
1.	total stress	direct	0.34	No
2.	dev. stress	indirect	0.34	No
3(a)	———	direct	0.34	No
4.	total stress	direct	0.475	No
5.	total stress	direct	0.485	No
6.	total stress	direct	0.495	No
7.	total stress	direct	0.4999	No
8.	dev. stress	indirect	0.4999	No
9(b)	dev. stress	indirect	0.4999	Yes

Table 1.
Specification of Finite-Element Analyses

Notes:
(a) No iteration carried out
(b) Finite-element analysis compared with non-workhardening theoretical results.

5. RESULTS

5.1 Convergence

The iterative solutions failed to converge in cases 1 and 2 immediately after initial yield, and in case 4 just before the mesh became fully plastic.

5.2 Comparison of stresses

Figs. 2-6 show the comparisons between the finite-element and analytical solutions when the radius of the elastic/plastic interface, c , was approximately 20mm.

(a) Case 3 (fig.2). With no iteration correlation was poor except in the elastic region and near the inner surface.

(b) Cases 4, 5 (fig. 3) and 6. show that the results were in good agreement throughout the tube wall.

(c) Case 7 (fig.4). The finite-element distributions of stress differed from the analytical values.

(d) Case 8 (fig.5). Comparison between the finite-element and the analytical total stress distributions was very good.

(e) Case 9 (fig.6). The finite-element stresses for the work-

hydrostatic stress do not have to be evaluated for each iteration. However, current research [16] shows that for large-strain deformations, convergence is only possible is the new method of iteration is adopted.

6.4 Effect of incorporating work hardening

Even though only small plastic strains were considered in the present analysis (< 0.3%), the stress distributions resulting from the finite-element treatment using the work-hardening characteristics of EC1 aluminium differed from those predicted by the non-workhardening theoretical solution, the discrepancy in the tangential stress reaching 35% at the bore at full yield (case 9). When applied to the autofrettage of a tube, the non-hardening theoretical treatment would underestimate the bore pressure required to produce a given position of the elastic/plastic interface, and so err on the side of safety. If accurate values of stress components are required, the strain hardening of the material should be taken into account.

7. CONCLUSIONS

(1) Convergence is not obtained for the finite-element solutions if a value of Poisson's ratio less than 0.475 is used for yielded elements.

(2) Providing a convergent solution is obtained, the finite-element deviatoric stresses agree with analytical predictions for this deformation, whether iteration is carried out by evaluating residual forces from the total or from the deviatoric stress increments.

(3) Accurate calculation of hydrostatic stress values directly from bulk strain increments requires that Poisson's ratio in yielded elements is less than a limiting value which, for this deformation, lies in the range 0.495-0.4999.

(4) Hydrostatic stresses may be calculated accurately from the distributions of deviatoric stress for values of Poisson's ratio in yielded elements up to 0.4999 and this method appears to be more suitable for application to other types of deformation.

(5) A non-workhardening analytical treatment does not accurately calculate the stress distributions in a tube of work-hardening material, even for the small strains of this deformation.

(6) The three-dimensional elastic-plastic finite-element formulation incorporating the Prandtl-Reuss flow rule, developed here, has been validated for the partially plastic, radial expansion of a tube under plane-strain end conditions and appears to be suitable for application to other types of

132
deformation.

ACKNOWLEDGEMENTS

We wish to thank the SERC for financial support and the Staff of the Centre for Computing and Computer Science, Birmingham, and the University of Manchester Regional Computer Centre for use of facilties.

REFERENCES

1. CHEN,C.C. and KOBAYASHI,S.-Rigid Plastic Finite Element Analysis of Ring Compression, Winter Meeting ASME, California, 1978.
2. PRICE,J.W.H. and ALEXANDER, J.M.-Specimen Geometries Predicted by Computer Model of High Deformation Forging, Int.J.Mech.Sci, Vol 21, pp 417-430, 1979.
3. DUNG,N.L. KLIE,W, and MAHRENHOLTZ,O.-Analysis of Plastic Flow with a Simplified Finite Element Method, Mech.Res. Comm., Vol 7, pp 33-38, 1980.
4. HARTLEY,P, STURGESS, C.E.N. and ROWE, G.W. -Influence of Friction on the Prediction of Forces, Pressure Distributions and Properties in Upset Forging, Int.J.Mech.Sci., Vol 22, pp 743-753, 1980.
5. TURNER,L.B. -The Stresses in a Thick Hollow Cylinder Subjected to Internal Pressure, Trans.Camb.Phil.Soc. Vol 21, pp 377-396, 1909.
6. COOK,G.-The Stresses in Thick-Walled Cylinders of Mild Steel Overstrained by Internal Pressure, Proc.Instn. Mech.Engrs., Vol 126, pp 407-455, 1934.
7. HILL,R, LEE,E.H. and TUPPER,S.J. - The Theory of Combined Plastic and Elastic Deformation with Particular Reference to a Thick Tube under Internal Pressure, Proc.Roy.Soc., A Vol 191, pp 278-303, 1947.
8. HILL,R, LEE,E.H. and TUPPER,S.J. - Plastic Flow in a Closed Ended Tube with Internal Pressure, Proc.1st Nat. Cong.App.Mech. Chicago, pp 561-567 1951.
9. ALLEN,D.N. DE G. and SOPWITH, D.G. - The Stresses and Strains in a Partially Plastic Thick Tube under Internal Pressure and End Load, Proc.Roy.Soc. A Vol 205, pp 69-83 1951.
10. THOMAS,D.G.B. -The Autofrettage of Thick Tubes with Free Ends, J.Mech.Phys.Solids, Vol 1, pp 124-133, 1953.
11. NADAI,A.- Theory of Flow and Fracture in Solids, McGraw-Hill, New York, 1950.
12. KOITER,W.T. -On Partially Plastic Thick-Walled Tubes, Anniversary Vol. on App.Mech.Dedicated to C.B.Biezeno, N.V de Technische Uitgeverij H. Stam, Haalem, 1953.
13. HODGE,P.G. and WHITE,G.N. - A Quantitative Comparison of Flow Deformation Theories of Plasticity, J.App.Mech, Vol 17, pp 180-184, 1950.
14. MACGREGOR,C.W. COFFIN,L.F. and FISHER,J.C. -Partially Plastic Thick-Walled Tubes, J.Franklin Inst. Vol 245, pp 135-158, 1948.

15. MANNING,W.R.D. -The Overstrain of Tubes by Internal Pressure, Engineering, pp 101-102, 183-184, 1945.
16. PILLINGER,I. -The Prediction of Metal Flow and Properties in Three Dimensional Forgings Using the Finite Element Method, MSc(Qual) Thesis, Birmingham, 1982.
17. ZIENKIEWICZ,O.C. -The Finite Element Method, McGraw-Hill, 1977.
18. CHEUNG,Y.K. and YEO,M.F.- A Practical Introduction to Finite Element Analysis, Pitman, 1979.
19. MARCAL,P.V. and KING,I.P.- Elastic-Plastic Analysis of Two-Dimensional Stress Systems by the Finite Element Method, Int.J.Mech.Sci. Vol 9, pp 143-155, 1967.
20. YAMADA,Y. YOSHIMURA,N. and SAKURAI,T.- Plastic Stress-Strain Matrix and Its Application for the Solution of Elastic-Plastic Problems by the Finite Element Method, Int.J.Mech.Sci. Vol 10, pp 343-354, 1968.
21. ZIENKIEWICZ,O.C. VALLIAPPAN,S. and KING,I.P. -Elasto-Plastic Solutions of Engineering Problems, 'Initial Stress' Finite Element Approach, Int.J.Num.Meth.Eng., Vol 1, pp 75-100, 1969.
22. ALEXANDER,J.M. and PRICE,J.W.H.- Finite Element Analysis of Hot Metal Forming, 18th MTDR Conf., pp 267-274, 1977.